CERN-LHCC-2008-014
ALICE-TDR-014
1 September 2008

A L I C E

Electromagnetic Calorimeter

Technical Design Report

Cover design by CERN Desktop Publishing Service.

Cover:

Printed at CERN
September 2008.

ISBN 978-92-9083-320-8

ALICE Collaboration

Alessandria, Italy, Dipartemento di Science e Tecnologio Avanzale dell'Università del Piemonte Orientale and Sezione INFN:
P. Cortese, G. Dellacasa, R. Gemme, L. Ramello and M. Sitta.

Aligarh, India, Department of Physics, Aligarh Muslim University:
A. Ahmad, N. Ahmad, M. Danish Azmi, M. Irfan, A. Kamal and M. Khan.

Amsterdam, The Netherlands, National Institute for Nuclear and High Energy Physics (NIKHEF):
A. Bilandzic, M. Botje, I. Kraus, M. Krzewicki, P. Kuijer, R. Snellings and N. Van Der Kolk.

Athens, Greece, University of Athens, Physics Department:
A. Belogianni, P. Christakoglou, M. Fragkiadakis, P. Ganoti, S. Potirakis, M. Spyropoulou-Stassinaki, C. Tagridis, E. Tsilis and M. Vassiliou.

Bari, Italy, Dipartemento Interatenco di Fisica 'M. Merlin' and Sezione INFN:
G. E. Bruno, G. D'Erasmo, D. Di Bari, C. Di Giglio, E. M. Fiore, B. Ghidini, A. Mastroserio, F. Minafra, F. Navach, D. Perrino, F. Posa, R. Romita, R. Santoro and I. Sgura.

Bari, Italy, Sezione INFN:
D. Elia, R. Fini, V. Lenti, V. Manzari, E. Nappi, M. Nicassio, V. Paticchio and G. Volpe.

Beijing, China, China Institute of Atomic Energy:
S. Hu, X. Li, S. Lu, Q. Wen and S. Zhou.

Bergen, Norway, Department of Physics, University of Bergen:
J. Alme, S. Bablok, K. Kanaki, A. Klovning, D. T. Larsen, J. Nystrand, G. Ovrebekk, B. Pommeresch, M. Richter, D. Röhrich, K. Ullaland, B. Wagner and H. Yang.

Bergen, Norway, Bergen University College:
H. Helstrup, K. Hetland, B. Kileng and K. Røed.

Berkeley, U.S.A., Lawrence Berkeley National Laboratory:
S. Blyth, H. Gray, M. Horner, P. Jacobs, G. Odyniec, M. Ploskon, J. Symons and M. van Leeuwen.

Bhubaneswar, India, Institute of Physics:
A. Dash, S. Dash, C. Jena, D. Mahapatra, S. Rath and Y. Viyogi.

Birmingham, United Kingdom, School of Physics and Space Research, University of Birmingham:
A. Bhasin, M. Bombara, D. Evans, G.T. Jones, P. Jones, P. Jovanović, A. Jusko, M. Krivda, C. Lazzeroni, R. Lietava, R. Platt, H. Snow, D. Tapia Takaki and O. Villalobos Baillie.

Bologna, Italy, Dipartimento di Fisica dell'Università and Sezione INFN:
A. Alici, S. Antinori, S. Arcelli, M. Basile, L. Cifarelli-Strolin, D. Falchieri, M. Masetti, R. Preghenella, G. Scioli, A. Silenzi and A. Zichichi.

Bologna, Italy, Sezione INFN:
P. Antonioli, G. Cara Romeo, F. Cindolo, F. Costa, D. Hatzifotiadou, G. Laurenti, M. Luvisetto, A. Margotti, R. Nania, F. Noferini, A. Pesci, E. Scapparone, C. Williams and C. Zampolli.

Bratislava, Slovak Republic, Comenius University, Faculty of Mathematics, Physics and Informatics:
V. Černý, V. Fekete, R. Janik, M. Pikna, M. Siska, B. Sitár, P. Strmeň and I. Szarka.

Bucharest, Romania, National Institute for Physics and Nuclear Engineering:
C. Andrei, I. Berceanu, V. Catanescu, A. Herghelegiu, M. Petris, M. Petrovici, A. Pop and C. Schiaua.

Bucharest, Romania, Institute of Space Sciences ISS:
D. Felea, A. Gheata, M. Haiduc, D. Hasegan, C. Mitu, A. Sevcenco, I. Stan and I. Zgura.

Budapest, Hungary, KFKI Research Institute for Particle and Nuclear Physics, Hungarian Academy of Scinences:
G. Barnäfoldi, L. Boldizsár, E. Dénes, G. Hamar, P. Lévai, L. Molnar and T. Tolyhy.

Cagliari, Italy, Dipartemento di Fisica dell'Università and Sezione INFN:
A. De Falco, M. Floris, G. Puddu, S. Serci and G. L. Usai.

Cagliari, Italy, Sezione INFN:
B. Becker, C. Cicalo, A. Masoni, E. Siddi and H. Woehri.

Campinas, Brazil, Universidade Estadual de Campinas (UNICAMP):
D. Dobrigkeit-Chinella and J. Takahshi.

Cape Town, South Africa, University of Cape Town, Physics Department:
J. Cleymans, D. de Vaux, R. Fearick, A. Szostak and Z. Vilakazi.

Catania, Italy, Dipartimento di Fisica dell'Università and Sezione INFN:
R. Barbera, F. Blanco, N. Giudice, P. La Rocca, F. Noto, C. Petta, A. Pulvirenti and F. Riggi.

Catania, Italy, Sezione INFN:
A. Badalà, F. Fichera, A. Grimaldi, F. Librizzi, A. Palmeri, G. S. Pappalardo, S. Urso and R. Vernet.

CERN, Switzerland, European Organisation for Nuclear Research:
G. Aglieri Rinella, G. Anelli, F. Antinori, A. Augustinus, J. Baechler, J. Belikov, L. Betev, M. Boccioli, G. Bruckner, R. Brun, P. Buncic, I. Cali, R. Campagnolo, M. Campbell, F. Carena, W. Carena, F. Carminati, S. Chapeland, C. Cheshkov, V. Chibante Barroso, P. Chochula, A. Colla, G. de Cataldo, J. de Groot, A. Di Mauro, R. Divi, C. W. Fabjan, F. Formenti, U. Fuchs, M. Gheata, J.-F. Grosse-Oetringhaus, R. Grosso, P. Hristov, L. Jirden, S. Kapusta, C. Klein-Bösing, A. Kluge, F. Lackner, L. Leistam, C. Lippmann, I. Makhlyueva, P. Martinengo, M. Meoni, A. Morsch, H. Müller, L. Musa, M. Oldenburg, F. Osmic, D. Perini, A. J. Peters, A. Rademakers, J.-P. Revol, P. Riedler, W. Riegler, P. Rosinský, S. Rossegger, F. Roukoutakis, K. Šafařík, R. Salgueira Dominques da Silva, K. Schossmaier, J. Schukraft, R. Shahoyan, C. Soos, G. Stefanini, D. Swoboda, M. Tadel, H. Taureg, M. Tavlet, C. Torcato de Matos, H. Tydesjo, P. Vande Vyvre and L. Wallet,

Chandigarh, India, Physics Department, Punjab University:
M. Aggarwal, A. Bhati, L. Kumar and N. Kumar.

Clermont-Ferrand, France, LPC, Université Blaise Pascal, CNRS/IN2P3:
A. Baldit, V. Barret, N. Bastid, A. Blanchard, G. Blanchard, J. Castor, P. Crochet, A. Devaux, P. Dupieux, P. Force, R. Guernane, J. Lecoq, X. Lopez, L. Manceau, F. Manso, P. Rosnet and P. Saturnini.

Columbus OH, U.S.A., NSF, Department of Physics, Ohio State Univeristy:
T. Humanic, A. Kisiel, M. Lisa, B. Nilsen and D. Truesdale.

Copenhagen, Denmark, University of Copenhagen, Niels Bohr Institute:
I. Bearden, H. Bøggild, C. Christensen, J.-J. Gaardhøje, K. Gulbrandsen and B. S. Nielsen.

Cracow, Poland, Henryk Niewodnicznski Institute of Nuclear Physics, High Energy Physics Department:
J. Bartke, E. Kornaś, M. Kowalski, A. Matyja and A. Rybicki.

Culiacan, Mexico, Universidad Autónoma de Sinaloa:
I. Leon Monzon.

Darmstadt, Germany, GSI, Gesellschaft für Schwerionenforschung GmbH:
S. Altinpinar, A. Andronic, R. Bailhache, A. Bercuci, E. Berdermann, P. Braun-Munzinger, B. Doenigus, P. Foka, U. Frankenfeld, J. Garabatos, H. Gutbrod, M. Ivanov, P. Malzacher, A. Marin, S. Masciocchi, D. Miśkowiec, C. Schmidt, H. Schmidt, K. Schwarz, D. Soyk, D. Vranic and J. Wiechula.

Darmstadt, Germany BMBF, Institut für Kernphysik, Technische Universität Darmstadt:
H. Oeschler.

Detroit, U.S.A., Wayne State University:
R. Bellwied, T. Cormier, Q. Li, J. Mlynarz, A. Pavlinov, V. Petrov, F. Pompei, C. A. Pruneau, A. Rumbers and S. Voloshin.

Frankfurt, Germany BMBF, Institut für Kernphysik, Johann-Wolfgang-Goethe Universität Frankfurt:
K. Antipin, D. Antonczyk, H. Appelshäuser, C. Blume, H. Buesching, M. Hartig, M. Kliemant, S. Kniege, F. Kramer, M. Ploskon, R. Renfordt and W. Sommer.

Frascati, Italy, Laboratori Nazionali di Frascati, INFN:
N. Bianchi, G. P. Capitani, A. Casanova Diaz, G. Conesa Balbastre, L. Cunqueiro, M. Del Franco, P. Di Nezza, A. Fantoni, D. Hasch, V. Muccifora, A. R. Reolon, F. Ronchetti A. Orlandi, W. Pesci, R. Vieira and A. Viticchie.

Gatchina, Russia, Petersburg Nuclear Physics Institute:
Y. Berdnikov, V. Ivanov, A. Khanzadeev, E. Kryshen, V. Nikulin, V. Polyakov, V. Samsonov, A. Zalite and M. Zhalov.

Grenoble, France, LPSC, Université Joseph Fourier Grenoble 1, CNRS/IN2P3, Institut Polytechnique de Grenoble:
O. Bourrion, C. Furget, S. Gadrat, R. Guernane, S. Kox, J. F. Muraz and J. Real.

Havana, Cuba, Centro de Aplicaciones Tecnológias y Desarrollo Nuclear (CEADEN):
A. Abrahantes Quintana, K. Shtejer and E. López Torres.

Heidelberg, Germany BMBF, Kirchhoff Institute für Physik, Ruprecht-Karls-Universität Heidelberg:
T. Alt, V. Angelov, S. Böttger, J. De Cuveland, S. Gorbunov, S. Kalcher, U. Kebschull, I. Kisel, C. Lara, V. Lindenstruth, R. Panse, C. Reichling, F. Rettig, R. Schneider, T. Steinbeck, J. Thäder and G. Tröger.

Heidelberg, Germany BMBF, Physikalisches Institut, Ruprecht-Karls Universität Heidelberg:
O. Busch, M. de Gaspari, D. Emschermann, P. Glässel, N. Herrmann, M. Kweon, J. Mercado Perez, K. Oyama, S. Radomski, I. Rusanov, R. Schicker, K. Schweda, H. Soltveit, R. Soualah, J. Stachel, G. Tsiledakis, Y. Wang and B. Windelband.

Helsinki/Jyväskylä, Finland, University of Jyväskylä:
J. Äysto, M. Bondila, R. Díaz Valdes, D. Kim, T. Malkiewicz, M. Oinonen, J. Rak and W. Trzaska.

Hiroshima, Japan, Hiroshima University:
T. Horaguchi, K. Shigaki, T. Sugitate and H. Torii.

Houston, U.S.A., Physics Department, University of Houston:
D. M. M. Don, B. Mayes and L. Pinsky.

Jaipur, India, Physics Department, University of Rajasthan:
R. Raniwala and S. Raniwala.

Jammu, India, Physics Department, University of Jammu:
R. Bala, A. Gupta, A. Mahajan, B. Potukuchi, S. Sambyal and S. Sharma.

JINR, Russia, Joint Institute for Nuclear Research:
B. Batyunya, L. Jančurová, M. Kutovsky, P. Nomokonov, T. Pocheptsov, G. Shabratova, M. Vala, A. Vodopianov, Y. Zanevskiy and A. Zinchenko.

Kangnung/Pohang, Republic of Korea, Kangnung National University:
Y. Baek, H. Jung, W. Jung, E. Kang, D. S. Kim, D. W. Kim, H. N. Kim, J. S. Kim, M. Kim, K. S. Lee and S. C. Lee.

Kharkov, Ukraine, Scientific Research Technology Institute of Instrument Engineering:
V. Borshchov.

Kiev, Ukraine, Bogolyubov Institute for Theoretical Physics:
B. Grynyov and G. Zinovjev.

Knoxville, U.S.A., University of Tennessee:
I. Garishvili, J. Hamblen, D. Hornback, I. Martashvili, K. F. Read and S. P. Sorensen.

Kolkata, India, Saha Institute of Nuclear Physics:
S. Bose, S. Chattopadhyay, I. Das, S. Pal, P. Roy and T. Sinha.

Kolkata, India, Variable Energy Cyclotron Centre:
Z. Ahammed, S. Chattopadhyay, M. Dutta Majumdar, M. Ganti, B. Mohanty, M. Mondal, T. Nayak, S. Pal, S. Prasad, J. Saini, R. Singaraju, V. Singhal and B. Sinha.

Köln, Germany BMBF, Fachhochschule Köln:
T. Krawutschke.

Košice, Slovak Republic, Institute of Experimental Physics, Slovak Academy of Sciences and Faculty of Science, P.J. Šafárik University:
J. Bán, I. Králik, A. Kravčáková, B. Pastirčák, L. Šándor, J. Urbán and J. Vrláková.

Legnaro, Italy, Laboratori Nazionali di Legnaro, INFN:
A. Dainese, R. A. Ricci and L. Vannucci.

Livermore, U.S.A., Lawrence Livermore National Laboratory:
A. Glenn and R. Soltz.

Lund, Sweden, Division of Experimental High Energy Physics, University of Lund:
P. Christiansen, A. Dobrin, P. Gros, H.-A. Gustafsson, A. Oskarsson, L. Österman, I. Otterlund and E. Stenlund.

Lyon, France, IPNL, Université de Lyon, CNRS/IN2P3:
B. Cheynis, L. Ducroux, J.-Y. Grossiord, F. Nendaz, R. Tieulent and Y. Zoccarato.

Madrid, Spain, Centro de Investigaciones Energeticas Medioambientales y Tecnologicas (CIEMAT):
A. Acero, F. Blanco, M. Cardenas-Montes, P. Gonzales-Zamora, P. Ladron de Guevara, E. Montes, J. Perez Griffo. A. Rubio, M. Rubio and E. Serradilla.

Mexico City and Mérida, Mexico, Centro de Investigación y de Estudios Avanzados (CINVESTAV):
E. Camacho, J. Contreras, A. Gago, G. Herrera Corral, L. Montaño Zetina, C. Perez and A. Zepeda.

Mexico City, Mexico, Instituto de Fisica, Universidad Nacional Autónoma de Mexico:
R. Alfaro, A. Anzo, E. Belmont-Moreno, L. H. Gonzales-Trueba, V. Grabski, H. Leon, A. Menchaca-Rocha and A. Sandoval.

Mexico City, Mexico, Instituto de Ciencias Nucleares, Universidad Natcional Autónoma de Mexico:
E. Cuautle, L. Diaz, I. Domínguez, I. Maldonado Cervantes, A. Ortiz Velázquez, G. Paić, D. Perez Astudillo, P. Podesta, L. Serkin and O. Sokolov.

Moscow, Russia, Institute for Nuclear Research, Academy of Science:
V. Feshchenko, V. Gorlychev, F. Guber, T. Karavicheva, E. Karpechev, A. Kurepin, A. N. Kurepin, A. Maevskaya, I. Pshenichnov and A. Reshetin.

Moscow, Russia, Institute for Theoretical and Experimental Physics:
A. Akindinov, Y. Grishuk, S. Kiselev, D. Mal'Kevich, P. Polozov, E. Sharkov, I. Vetlitskiy, K. Voloshin and B. Zagreev.

Moscow, Russia, Russian Research Center Kurchatov Institute:
D. Aleksandrov, D. Blau, V. Dobretsov, S. Fokin, M. Ippolitov, A. Kazantsev, K. Kozlov, Y. Kucheriaev, V. Manko, T. Moukhanova, A. Nianine, S. Nikolaev, S. Nikulin, D. Peresunko, E. Ryabinkin, Y. Sibiriak, A. Vasiliev, A. Vinogradov and I. Yushmanov.

Moscow, Russia, Moscow Engineering Physics Institute:
A. Bogdanov, V. Grigoriev, V. Kaplin, N. Kondratieva and V. Loginov.

Mumbai, India, Indian Institute of Technology:
B. Nandi, P. Pujahari and R. Varma.

Münster, Germany BMBF, Institut für Kernphysik, Westfälische Wilhelms-Universität Munster:
B. Bathen, C. Baumann, T. Dietel, R. Glasow, H. Gottschlag, M. Rammler, K. Reygers, R. Santo, J. Wessels and A. Wilk.

Nantes, France, SUBATECH, Ecole des Mines de Nantes, Université de Nantes, CNRS/IN2P3:
L. Aphecetche, G. Batigne, L. Benhabib, G. Bourdaud, S. Bouvier, J. Cussonneau, H. Delagrange, M. Dialinas, M. Estienne, C. Finck, M. Germain, C. Hadjidadkis, R. Ichou, N. Le Bris, F. Lefévre, L. Luquin, G. Martínez Garcia, P. Pillot, C. Roy, Y. Schutz, J.S. Stutzmann, A. Tournaire and F. Yermia.

New Haven, U.S.A., Yale University:
T. Aronsson, S. Baumgart, E. Bruna, H. Caines, J. W. Harris, M. Heinz, A. Knospe, C. Nattrass, J. Putschke and N. Smirnov.

Novosibirsk, Russia, Budker Institute for Nuclear Physics:
A. Frolov and Y. Pestov.

Oak Ridge, U.S.A., Oak Ridge National Laboratory:
T. C. Awes, A. Enokizono, P. W. Stankus, D. Silvermyr and G. R. Young.

Omaha, U.S.A., Creighton University:
M. Cherney and Y. Gorbunov.

Orsay, France, IPNO, Université Paris-Sud, CNRS/IN2P3:
L. Bimbot, V. Chambert, A. Charpy, B. Espagnon, I. Hřivnáčová, V. Lafage, Y. Le Bornec, M. Malek, J. Peyré, J. Pouthas, S. Rousseau, C. Suire and N. Willis.

Oslo, Norway, Department of Physics, University of Oslo:
K. Aamodt, I. Arsene, L. Bravina, P. Hille, H. Kvaerno, G. Løvhøiden, J. Milosevic, A. Nyiri, B. Skaali, T. Tveter, K. Tywoniuk and J. Wikne.

Padova, Italy, Dipartemento di Fisica dell'Università and Sezione INFN:
M. Lunardon, M. Morando, S. Moretto, F. Scarlassara, G. Segato and G. Viesti.

Padova, Italy, Sezione INFN:
C. Bombonati, D. Fabris, J. Faivre, A. Pepato and R. Turrisi.

Prague, Czech Republic, Czech Technical University of Prague CTU:
J. Bielčík, M. Pachr, V. Petráček, V. Pospíšil and V. Wagner.

Prague, Czech Republic, Academy of Sciences of the Czech Republic (ASCR), Institute of Physics:
J. Mareš, K. Polák and P. Závada.

Protvino, Russia, Institute for High Energy Physics:
M. Bogolyubsky, Y. Kharlov, V. Onuchin, B. Polichtchouk, S. Sadovsky, A. Soloviev and P. Stolpovsky.

Puebla, Mexico, Benemérita Universidad Autónoma de Puebla:
A. Férnandez Téllez, R. López-Ramírez, M. I. Martínez, J. Munoz, S. Román López and G. Tejeda Muñoz.

Řež u Prahy, Czexh Republic, Academy of Science of the Czech Republic, Nuclear Physics Institute:
D. Adamov, J. Bielčíková, J. Kapitan, S. Kushpil, V. Kushpil and M. Šumbera.

Roma, Italy, Dipartemento di Fisica dell'Università 'La Sapenza' and Sezione INFN:
F. Meddi.

Roma, Italy, Sezione INFN:
S. Di Liberto, M. A. Mazzoni and G. M. Urciuoli.

Saclay, France, CEA, Centre d'Études Nucléaires DAPNIA:
A. Baldisseri, H. Borel, J. Castillo Castellanos, J. L. Charvet, F. Orsini, H. Pereira and F. Staley.

Salerno, Italy, Dipartemento di Fisica 'E.R. Caianiello1 dell'Università and Sezione INFN:
A. De Caro, D. De Gruttola, S. De Pasquale, M. Fusco Girard, C. Guarnaccia, P. Pagano, G. Russo and T. Virgili.

San Luis Obispo, U.S.A., California Polytechnic State University:
B. Boswell, C. R. Brown, A. Donoghue, J. L. Klay, S. Lewis and R. M. Ward.

Santiago de Compostela, Spain, IGFAE, Universidad de Santiago de Compostela:
N. Armesto, E. Gonzales-Ferreiro, and C. Pajares.

São Paulo, Brazil, Universidade de São Paulo (USP):
A. Depmann, M.G. Munhoz, A.A.P. Suaide and A. Szanto-de-Toledo.

Sarov, Russia, Russian Federal Nuclear Center (VNIIEF):
V. Basmanov, D. Budnikov, V. Demanov, S. Filchagin, R. Ilkaev, A. Kuryakin, A. Mamonov, S. Nazarenko, G. Nazarov, A. Punin, V. Punin, O. Vikhlyantsev and Y. Vinogradov.

Seoul, Republic of Korea, Sejong University, Department of Physics:
D. S. Hwang and S. Kim.

Split, Croatia, Technical University of Split FESB:
S. Gotovac, E. Mudnic and L. Vickovic.

St. Petersburg, Russia, V. Fock Institute for Physics, St. Petersburg State University: A. Asryan, M. Braun, D. Derkach, G. Feofilov, A. Ivanov, R. Kolevatov, A. Kolojvari, V. Kondratiev, V. Vechernin, L. Vinogradov and A. Zarochentsev.
Strasbourg, France, IPHC, Université Louis Pasteur, CNRS/IN2P3:
D. Bonnet, J.-P. Coffin, B. Hyppolite, C. Kuhn, J.-R. Lutz, A. Michalon and H. Ricaud.

Tokyo, Japan, University of Tokyo:
H. Hamagaki.

Torino, Italy, Dipartimento di Fisica Sperimentale dell'Università and Sezione INFN:
S. Beolé, E. Chiavassa, O. Cobanoglu, A. Ferretti, M. Gagliardi, M. Gallio, A. Marzari Chiesa, M. Masera, F. Poggio, S. Senyukov, D. Stocco and E. Vercellin.

Torino, Italy, Sezione INFN:
B. Alessandro, R. Arnaldi, P. Cerello, E. Crescio, N. De Marco, P. Giubellino, M. Monteno, A. Musso, C. Oppedisano, A. Piccotti, F. Prino, L. Riccati, E. Scomparin and F. Tosello.

Trieste, Italy, Dipartimento di Fisica dell'Università and Sezione INFN:
M. Bregant, P. Camerini, E. Cattaruzza, G. Contin, G. V. Margagliotti, A. Rossi, R. Rui and M. Venaruzzo.

Trieste, Italy, Sezione INFN:
E. Fragiacomo, N. Grion, A. Rachevski and A. Vacchi.

Tsukuba, Japan, University of Tsukuba:
Y. Miake.

Utrecht, The Netherlands, Subatomic Physics Department:
A. De Haas, C. Ivan, R. Kamermans, A. Mischke, G. Nooren, C. Oskamp, T. Peitzmann, E. Simili and A. Van Den Brink.

Warsaw, Poland, Soltan Institute for Nuclear Studies:
A. Deloff, T. Dobrowolski, I. Ilkiv, P. Kurashvili, K. Redlich, T. Siemiarczuk, G. Stefanek and G. Wilk.

Warsaw, Poland, Warsaw University of Technology:
D. Kikola, T. Pawlak, W. Peryt, J. Pluta, M. Szuba and T. Traczyk.

West Lafayette, U.S.A., Purdue University:
R. Scharenberg and B. Srivastava.

Worms, Germany BMBF, Fachhochschule Worms Zentrum für Technologietransfer und Telekommunikation ZTT:
R. Keidel and B. Schockert.

Wuhan, China, Hua-Zhong Normal University:
X. Cai, H. Ding, Y. Mao, R. Wan, Y. Wang, C. Xu, C. Yang, Z. Yin and D. Zhou,

Wuhan, China, Hua-Zhong University of Science and Technology:
X. Cao, Y. Liu and G. Su.

Yerevan, Armenia, Yerevan Physics Institute:
A. Grigoryan, H. Gulkanyan, A. Harutyunyan, A. Hayrapetyan, M. Poghosyan and T. Poghosyan.

Zagreb, Croatia, Rudjer Bošković Institute:
T. Antičić, V. Nikolic and T. Susa,

Contents

1 Introduction

1.1 Physics Motivation

ALICE (A Large Ion Collider Experiment) at the LHC contains a wide array of detector systems for measuring hadrons, leptons, and photons. ALICE is designed to carry out comprehensive measurements of high energy nucleus–nucleus collisions, in order to study QCD matter under extreme conditions and to study the phase transition between confined matter and the Quark-Gluon Plasma (QGP). Discussion of the full ALICE physics program can be found in [1, 2].

The interaction and energy loss of high energy partons in matter provides a sensitive tomographic probe of the medium generated in high energy nuclear collisions ("jet quenching") [3–6]. Jet quenching measurements have played a key role at the Relativistic Heavy Ion Collider (RHIC) [7–10] and will be central to the study of nuclear collisions at the LHC.

This Technical Design Report describes a large acceptance Electromagnetic Calorimeter (EMCal) that will be installed in the ALICE central detector. The EMCal enhances ALICE's capabilities for jet quenching measurements. The addition of the EMCal enables triggering on high energy jets, reduces significantly the measurement bias for jet quenching studies, improves jet energy resolution, and augments existing ALICE capabilities to measure high momentum photons and electrons. Combined with ALICE's excellent capabilities to track and identify particles from very low p_{t} to high p_{t} the EMCal enables an extensive study of jet quenching at the LHC.

1.1.1 Jet Quenching in Nuclear Collisions

Hard (high Q^2) scatterings occur in the initial stage of a high energy nucleus–nucleus collision, producing high E_{T} partons that must traverse the bulk matter generated in the collision before fragmenting in vacuum into a jet of hadrons. The scattered partons interact with the matter, losing energy through both radiative [3–5] and elastic channels [11–13], with the magnitude of the energy loss depending strongly on the density of the medium. The energy loss effectively softens the fragmentation of the jet, resulting in suppression of high p_{t} hadrons and enhancement of the soft jet multiplicity. The jet structure may in addition be broadened, and its shape may be deformed by interaction with the flowing matter. Measurements of jet quenching effects have the potential to probe the medium at the hottest, densest stage of the collision.

However, jet measurements in high energy nucleus–nucleus collisions must contend with the large background of soft hadrons in the underlying event. Jet measurements in nuclear collisions at RHIC have therefore concentrated until recently mainly on high p_{t} hadrons and their correlations (although we remark below on recent developments at RHIC regarding full jet reconstruction in heavy ion collisions). Figure 1.1, left panel, shows the large suppression of the high p_{t} inclusive hadron yield in central 200 GeV Au-Au collisions, together with the lack of similar suppression for direct photons [14]. This contrast, as well as comparison to hadron production in d–Au collisions [15–18], shows that the suppression arises from final state interaction of high energy partons with dense matter generated in the collision. The curve in the left panel of the figure is the result of a radiative energy loss calculation in the few-scattering GLV approximation, which reproduces the measured suppression for initial gluon density $dN^g/dy \sim 1100$, about 30 times the density of cold nuclear matter [19]. The figure suggests that large $p_{\mathrm{t}} > 6$ GeV/c is required to separate QCD radiative effects from non-perturbative phenomena. Measurements of particle-identified yields have also shown a large enhancement in the yield of baryons relative to mesons in the intermediate p_{t} region $\sim 2-5$ GeV/c at RHIC [20, 21]. This has been interpreted in a parton coalescence picture, indicating an interplay between the fragmentation of hard scattered partons

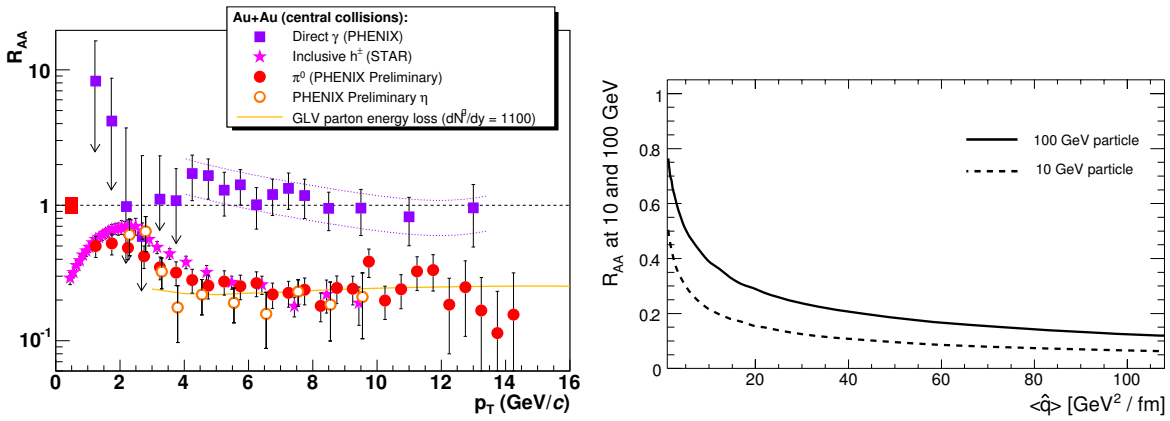

Figure 1.1: Inclusive hadron suppression at RHIC. Left: Hadron and direct photon yields in central 200 GeV Au-Au collisions normalized by p–p collision yields [14]. Right: hadron suppression as a function of transport coefficient $\hat{q}$ [25].

and the hadronization of the bulk medium [22–24].

Figure 1.1, right panel, shows a calculation of inclusive hadron suppression based on a multiple soft collision approximation to radiative energy loss [25, 26]. In this approach the medium is parametrized by a transport coefficient $\hat{q} = \mu^2/\lambda$, where μ is the typical momentum transfer and λ is the gluon mean free path [27]. The transport coefficient is related to the energy density ε of the medium via $\hat{q} = c\varepsilon^{3/4}$, with $c \sim 2-10$ [27]. Comparison of data in the left panel to the curve for 10 GeV particles requires $\hat{q} \sim 10$ GeV^2/fm. However, the inclusive suppression is seen to have little sensitivity to $\hat{q}$ over a very large range: for a sufficiently opaque medium, the inclusive yield is dominated by jets suffering relatively little energy loss, which are those jets generated at the periphery of the collision zone and headed outwards [27–29]. This bias fundamentally limits the sensitivity of inclusive hadron measurements as a probe of the medium.

Expectations for inclusive hadron suppression at the LHC can also be derived from the figure by scaling $\hat{q}$ with the expected increase in initial gluon density from RHIC to the LHC, giving $\hat{q}_{LHC} \sim 70$ GeV^2/fm [27]. A large variation in suppression is not predicted, despite the large variation in initial density. Comparison of the suppression for 10 and 100 GeV particles shows that a large range in p_t is needed to study the logarithmic QCD evolution, which is only possible at the LHC. Overall, inclusive hadron suppression has only weak sensitivity to properties of the medium, and much more information can be gleaned from detailed study of jet structure.

Additional evidence for jet quenching is seen in Fig. 1.2, which shows RHIC measurements of the azimuthal distribution of high p_t hadron pairs [18]. The back-to-back correlation expected from di-jets is seen in p–p and d–Au collisions, while the di-jet correlation is strongly suppressed in central Au-Au collisions. In this measurement the "trigger" hadron likewise has a surface bias, meaning that the jet recoiling against the trigger is directed towards the dense core of the collision zone. The high p_t fragments of the recoiling jet are seen to be strongly suppressed, also indicating substantial partonic energy loss in the medium. Its energy and momentum must be conserved, however, and indeed an enhanced correlation of low p_t hadrons is seen for the recoil in central Au-Au collisions [30], with features suggesting that the energy lost to the medium has to a large extent been equilibrated.

These measurements show clear evidence for jet quenching but the physics reach of such leading-hadron observables is limited, since they bias towards the subset of jets that has *not* interacted in the dense medium. More sensitive measurements of jet quenching, and qualitatively new observables, can be obtained by means of reconstruction of the full jet energy. This is a difficult task in the complex environment of heavy ion collisions, but recent theoretical progress has identified practical implementations

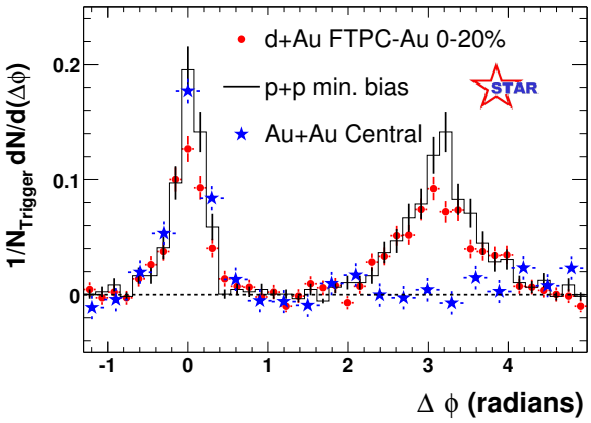

Figure 1.2: Back-to-back high p_t hadron pairs at RHIC [18].

for background subtraction and (approximately) infrared-safe jet reconstruction even in such an environment [31]. The STAR experiment at RHIC has applied these algorithms to the measurement of jets in Au-Au collisions at $\sqrt{s_{NN}} = 200$ GeV, with first results reported at a recent conference [32]. These studies, though preliminary, suggest that unbiased jet reconstruction may be achievable even in heavy ion collisions.

Progress towards full jet reconstruction raises the possibility of new ways of measuring jet quenching, including jet structure observables such as the medium-induced modification of sub-jet distributions [33]. RHIC is beginning to explore these possibilities, though its jets studies are constrained kinematically to E_T less than 50 GeV or so.

Nuclear collisions at the LHC will extend the measurement of jet quenching into a qualitatively new regime. The factor 30 increase in $\sqrt{s_{NN}}$ relative to RHIC corresponds to a huge increase in kinematic and statistical reach for hard probes, and additional measurement channels become available. There is copious production of high energy jets that are clearly distinguishable over background, and robust event-wise jet reconstruction will be possible. The resulting jet sample will give a much more detailed and complete view of partonic energy loss and the medium-induced modifications of jet fragmentation.

Guidance for the p_t scale of hadron production from high E_T jets arising from medium-induced radiation can be obtained from a recent calculation which incorporates medium effects into the Modified Leading Logarithmic Approximation (MLLA) [34]. Figure 1.3, left panel, shows the hadron multiplicity distribution plotted as a function of the scaling variable ξ=log$(1/x)$, with $x = (p_t^{hadron}/E_T^{jet})$. Large effects are seen in both the low p_t and the high p_t regions, with suppression of hard fragments (low ξ) and a marked enhancement for the softest fragments (high ξ). The medium-induced excess for jets with $E_T \sim 100$ GeV is predicted to be large for $p_t \sim 1$–5 GeV$/c$, matching well the unique ALICE momentum reconstruction and PID capabilities.

Partonic energy loss will be reflected in the modification of jet observables such as jet shapes and multiplicity distributions. Calculations suggest that the broadening of the jet multiplicity distribution provides a sensitive probe of the matter [35]. Figure 1.3, right panel, shows the gluon multiplicity distribution within a jet cone radius $R = 0.3$ as a function of momentum k_t perpendicular to the jet direction. The distribution from fragmentation in vacuum is shown, together with its broadening due to interactions in the medium. A significant medium-induced enhancement is seen at $k_t \sim$ few GeV$/c$, calculated both in the "single hard" and "multiple soft" collision approximations for radiative energy loss, $\omega_c = \frac{1}{2}\hat{q}L^2$, where L is the path length in medium, ω_c is the effective cutoff of the radiated spectrum and is proportional to the total energy loss $\Delta E \sim \alpha_s \omega_c$.

Potentially the most detailed investigation of jet quenching utilizes the coincidence of a jet recoiling from a direct photon. The colorless photon does not interact with the medium, providing a measurement of

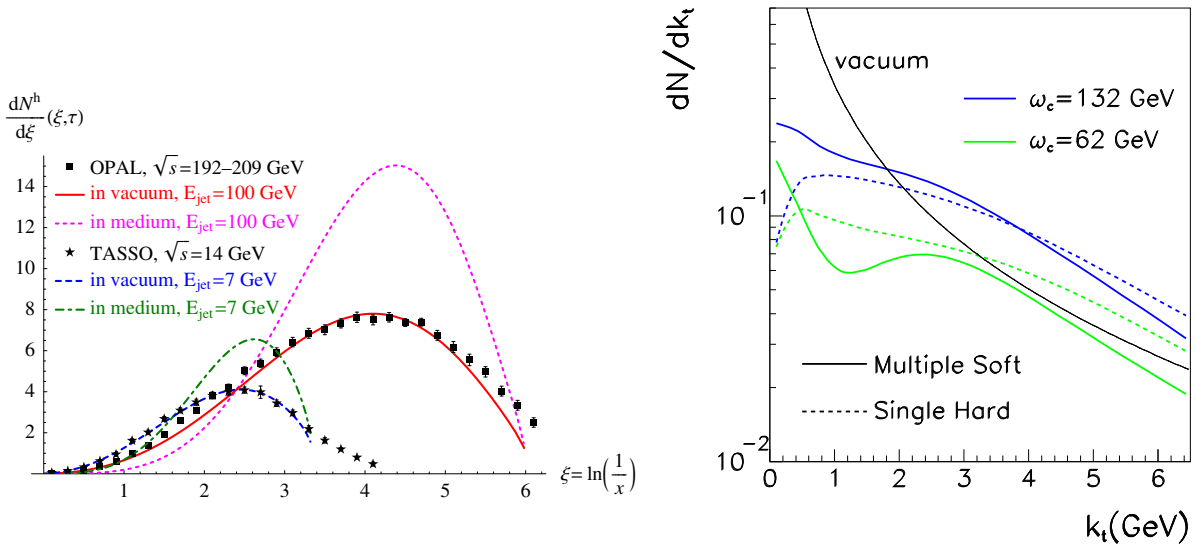

Figure 1.3: Left: MLLA calculations of the single inclusive hadron distribution as function of $\xi=\log(1/x)$ for vacuum fragmentation compared to e^+e^- data and for a medium-modified jet. ξ=4 corresponds to $p_t^{hadron} \sim 2$ GeV for $E^{jet} = 100$ GeV. Right: Gluon multiplicity distribution in a jet cone of radius $R = 0.3$ in vacuum and in the medium.

the recoiling jet energy [36]. The fragmentation function can then be studied in detail on an inclusive basis using charged particle tracking.

1.2 The ALICE Electromagnetic Calorimeter

ALICE is designed for measurements in the high multiplicity environment of heavy ion collisions and is well suited for jet quenching studies. It has excellent momentum resolution for charged particles from 100 MeV/c to 100 GeV/c, covering nearly the full range of fragment momentum for the highest energy jets accessible in heavy ion collisions. ALICE has a wide array of particle identification capabilities which, as demonstrated at RHIC, will be crucial to understand the mechanisms of particle production from jet fragmentation and hadronization of the bulk medium.

The EMCal will complete ALICE's capabilities to measure jet quenching. The most important features of the EMCal are an efficient and unbiased fast trigger (Level 0/1) for high energy jets, and measurement of the neutral portion of jet energy. Jet measurements based solely on charged particle reconstruction are subject to large measurement biases. This bias puts severe limitations on jet quenching studies, since it is precisely the modification of jet structure that is the observable. The addition of the EMCal allows measurement of a large fraction of jet energy, thereby reducing the sensitivity of jet reconstruction to specific jet structure and enabling a comprehensive study of jet quenching. The EMCal will also improve jet energy resolution, and enhance ALICE capabilities to measure high p_t photons, neutral hadrons, and electrons, of particular importance for tagging heavy flavor jets.

Figure 1.4 shows the annual yield for various hard processes in the EMCal acceptance, for minimum bias Pb–Pb collisions at nominal luminosity[1]. The EMCal kinematic reach for inclusive jets extends beyond 200 GeV, while for di-jets with a trigger jet in the EMCal and the recoiling jet in the TPC acceptance it is about 170 GeV. The γ–jet rate is statistically robust for $p_t \leq 40$ GeV/c. The yield for electrons from

[1]Due to the scaling of hard process cross sections and LHC luminosity with system size, similar annual yields are also expected for lighter collision systems.

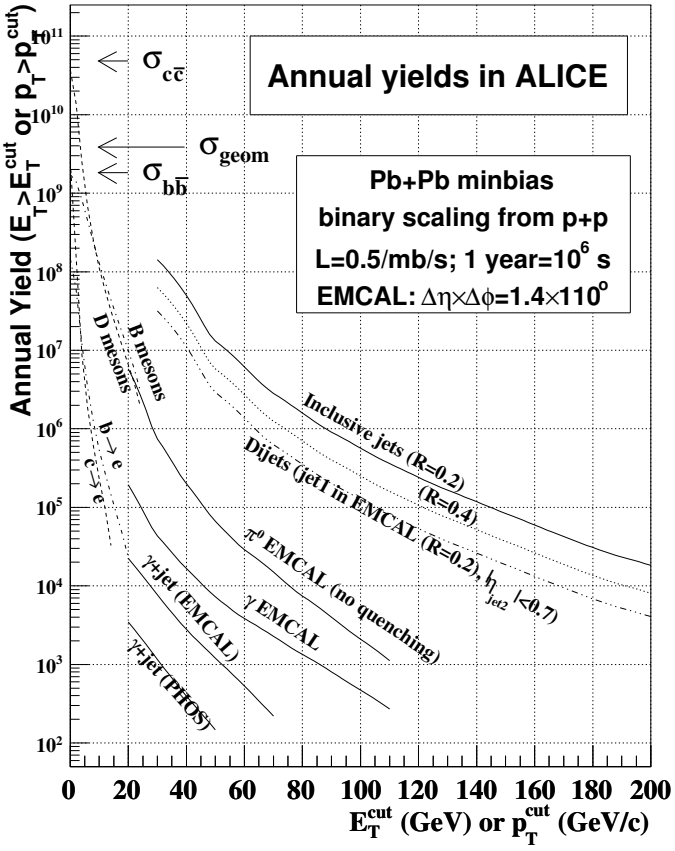

Figure 1.4: Expected annual yields in the EMCal acceptance for various hard processes for minimum bias Pb–Pb collisions at 5.5 TeV.

semi-leptonic decays of b and c extends to $p_{\mathrm{t}} \sim 25\ \mathrm{GeV}/c$, corresponding to heavy quark jet energies out to 80 GeV.

ALEPH [37] and STAR [38] have shown that jet measurements based on EM calorimetry and charged particle tracking have similar energy resolution to EM and hadronic calorimetry. Indeed, our analysis shows, charged particle tracking is in fact superior to hadronic calorimetry for suppressing backgrounds to jet measurements in the high multiplicity environment of heavy ion collisions. The EMCal is therefore an important addition to ALICE for jet quenching studies.

Full exploitation of jets as a probe of QCD matter at the LHC requires both broad kinematic reach of jet energy and detailed measurement of jet structure, from the hardest hadronic fragments to very soft fragments. Much of the interesting physics may indeed be carried by low p_{t} hadrons, which have the greatest sensitivity to the jet interaction with the medium. In light of RHIC measurements [20, 21], particle identification is expected to be critical in elucidating the physics of jet quenching. The EMCal acceptance, triggering and measurement capabilities, combined with the excellent tracking and particle identification capabilities of ALICE, enable extensive measurements of jet quenching at the LHC.

2 Detector Design

2.1 Design Overview

The overall design of the EMCal is heavily influenced by its integration within the ALICE [1] magnet. The EMCal is to be located inside the large room temperature solenoidal magnet of ALICE within a cylindrical integration volume approximately 110 cm deep in the radial direction sandwiched between the ALICE space-frame, which supports the entire ALICE central detector, and the ALICE magnet coils. The PHOton Spectrometer (PHOS) carriage below the ALICE TPC and the the High Momentum Particle IDentifier (HMPID) above the ALICE TPC, define the azimuthal space available for the EMCal. These constraints limit the EMCal to a region of about 110 degrees in azimuth. As discussed in Section 2, this EMCal acceptance is well matched to ALICE physics goals.
The conceptual design of the electromagnetic calorimeter for the ALICE experiment is based on the Shashlik technology as implemented in the PHENIX experiment [2] at RHIC, HERA-B [3] at HERA, and LHCb [4] at the CERN. The scope and basic design parameters of the proposed calorimeter have been chosen to match the physics performance requirements of the proposed ALICE high p_{t} physics program.

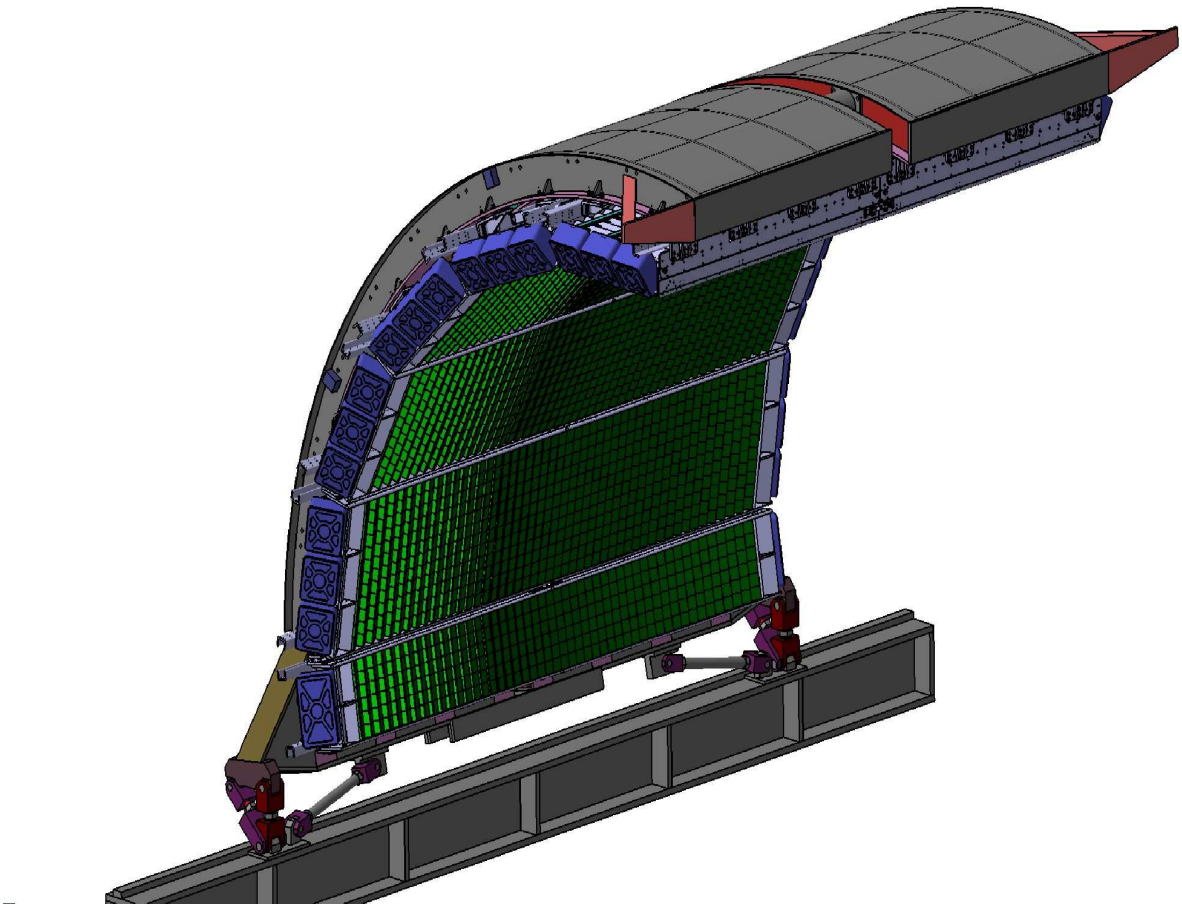

Figure 2.1: The array of super modules shown in their installed positions on the support structure.

Figure 2.1 shows the EMCal super modules, the basic structural units of the calorimeter, mounted in their

installed positions on the support structure. These are the units handled as the detector is moved below ground and rigged during installation into their final resting place in the ALICE magnet. A continuous arch of super modules, each full super module spanning ∼20 degrees in azimuth, is indicated. The EMCal is positioned to provide partial back-to-back coverage with the PHOS calorimeter. Small azimuthal gaps (∼ 3.0 cm) are provided between super modules to facilitate installation and alignment. These gaps are positioned in line with the TPC sector boundaries. Along these sector boundaries there is substantial additional structural material required for the support of the TPC and other ALICE detectors that would significantly degrade any electromagnetic measurements made in these gaps. Thus, the gaps create no additional loss of electromagnetic acceptance. Detailed simulations further show that these gaps have no significant influence on the measured jet energy or jet resolution.

The chosen technology is a layered Pb-scintillator sampling calorimeter with a longitudinal pitch of 1.44 mm Pb and 1.76 mm scintillator[1] with longitudinal wavelength shifting fiber light collection (Shashlik). The full detector spans η = -0.7 to η = 0.7 in pseudo-rapidity with an azimuthal acceptance of $\Delta\phi$ = 107°. The detector is segmented into 12,288 towers, each of which is approximately projective in η and ϕ to the interaction vertex.

The towers are grouped into super modules of two types: full size which span $\Delta\eta$ =0.7 and $\Delta\phi$ = 20°, and one-third size which span $\Delta\eta$ = 0.7 and $\Delta\phi$ = 7°. There are 10 full size and 2 one-third size super modules in the full detector acceptance (see Fig. 2.1).

Each full size super module is assembled from $12 \times 24 = 288$ modules arranged in 24 strip modules of 12×1 modules each. Each one-third size super module is assembled from $4 \times 24 = 96$ modules. Each module has a fixed width in the ϕ direction and a tapered width in the η direction with a full taper of 1.5°. The resultant assembly of stacked strip modules is approximately projective in η with an average angle of incidence at the front face of a module of less than 2° in η and less than 5° in ϕ.

A module is a single self-contained detector unit. Each module is comprised of four independently read out towers, each spanning $\Delta\eta \times \Delta\phi = 0.014 \times 0.014$. In the following sections we present the mechanical and optical design of the EMCal modules, the motivation for this design, and their assembly into strip modules and super modules.

2.2 EMCal Detector Modules

Each individual module, the smallest building block of the calorimeter, contains $2 \times 2 = 4$ towers built up from 76 alternating layers of 1.44 mm Pb (Natural Pb - standard mill spec.) and 77 layers of 1.76 mm polystyrene base, injection moulded scintillator (BASF143E + 1.5%pTP + 0.04%POPOP) with an intrinsic light output of 50% Anthracene [5]. White, acid free, bond paper serves as a diffuse reflector on the scintillator surfaces and provides friction between layers. The scintillator edges are treated with TiO_2 loaded reflector to improve the transverse optical uniformity within a single tower and to provide tower to tower optical isolation at $> 99\%$. The total thickness of the 3 layers of paint applied to the scintillator edges is 80 μm.

The Pb-scintillator stack in a module is secured in place by the static friction between individual layers under the load of an internal pressure of ∼1.1 kg/cm^2. The module is closed by a skin of 150 μm thick stainless steel on all four transverse surfaces. Flanges are laser welded to the ends of the stainless steel skin (straps) to permit secure attachment to the front and back plates of the module. This thin stainless skin, plus the optical treatment of the scintillator edges, is the only inert material between the active tower volumes. The internal pressure in the module is stabilized against thermal effects, mechanical relaxation, and long term flow of the Pb and/or polystyrene by a customized array of 5 non-linear spring sets per module. In this way, each module is a self-supporting unit with a stable mechanical lifetime of more than 30 years when held from its back surface in any orientation, as when mounted in a strip module.

[1] To best account for inactive materials in the space immediately before the calorimeter, the first layer of the detector is scintillator.

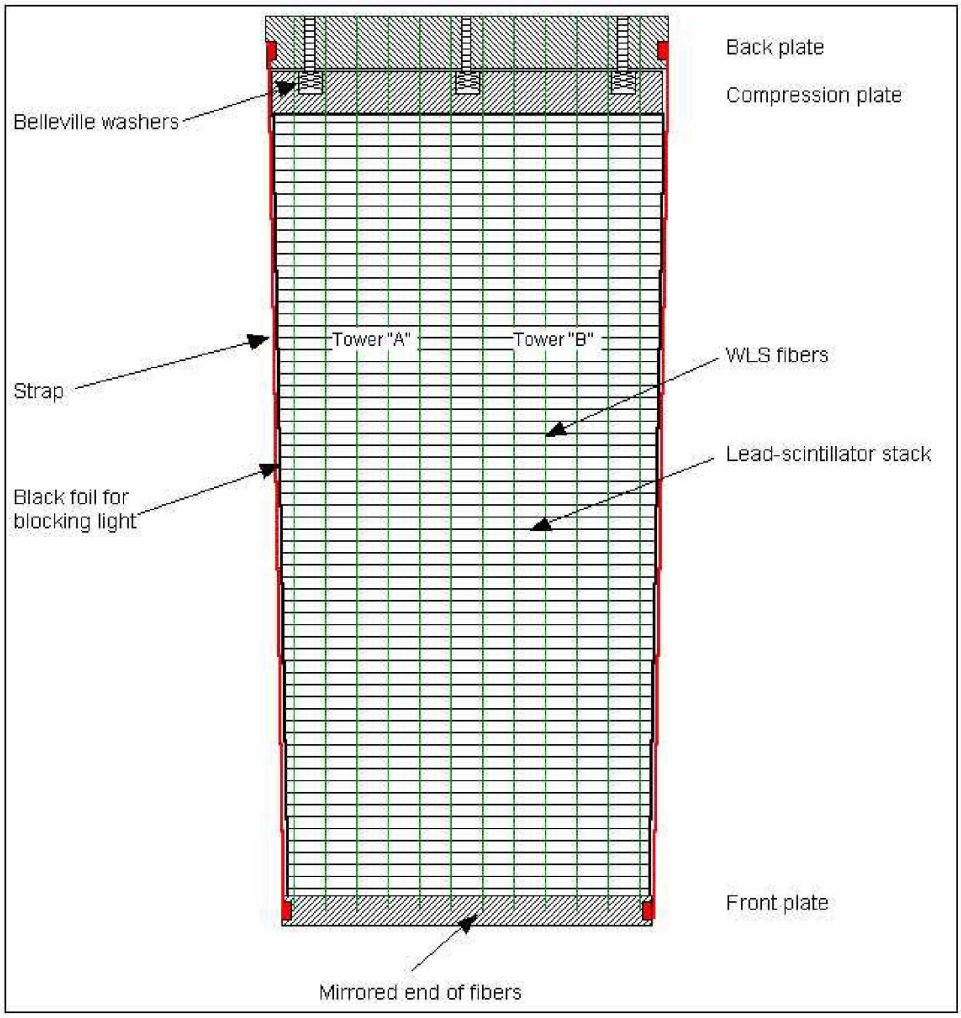

Figure 2.2: A cross section of the scintillator/Pb stack of one module identifying the main mechanical components.

All modules in the calorimeter are mechanically and dimensionally identical. The front face dimensions of the towers are $\sim 6 \times 6\,\mathrm{cm}^2$ resulting in an individual tower acceptance of $\Delta\eta \times \Delta\phi \sim 0.014 \times 0.014$ at η=0. The mechanical aspects of module construction are discussed in more detail below in Section 2.2.2.

2.2.1 Sampling Fraction

The calorimeter design incorporates a moderate detector average active volume density of $\sim$5.68 g/cm^3 which results from a $\sim 1 : 1.22$ Pb to scintillator ratio by volume. This results in a compact detector consistent with the EMCal integration volume at the chosen detector thickness of ~ 20 radiation lengths. In simulations, this number of radiation lengths gives a maximum deviation from linearity (due mainly to shower leakage) of $\sim$2.8% for the most probable energy response in the range up to 100 GeV photons, which is deemed acceptable.
The energy resolution of an electromagnetic calorimeter can be parameterized as

$$\sigma/E = a/\sqrt{E} \oplus b \oplus c/E \,, \tag{2.1}$$

where E is the shower energy and the first term characterized by the parameter a arises from stochastic fluctuations due to intrinsic detector effects such as energy deposit, energy sampling, light collection

efficiency, etc. The constant term, b, arises from systematic effects, such as shower leakage, detector non-uniformity or channel-by-channel calibration errors. The third term, c, arises from electronic noise summed over the towers of the cluster used to reconstruct the electromagnetic shower. The three resolution contributions add together in quadrature as indicated in Eq. 2.1. Over the lower half of the energy range of interest in ALICE, the stochastic term dominates with the constant term increasing in significance only at the highest energies.

The energy resolution for a given sampling frequency in an electromagnetic calorimeter varies with the sampling frequency approximately as $\sigma/E \sim \sqrt{d_{\mathrm{Sc}}/f_{\mathrm{s}}}$ where d_{Sc} is the scintillator thickness in mm and f_{s} is the sampling fraction for minimum ionizing particles. For optimum resolution in a given physical space and total radiation lengths, there is thus a desire to have the highest possible sampling frequency. Practical considerations, including the cost of the total assembly labour, suggest reducing the total number of Pb/scintillator layers thus decreasing the sampling frequency. Using the 1:1.22 Pb to scintillator ratio described above as a compromise - a sampling geometry of Pb(1.44 mm)/Scint(1.76 mm) - detailed GEANT3 simulations yield $a/\sqrt{E} \oplus b\%$ with fit results $a = (6.90 \pm 0.09)\%$ and $b = (1.44 \pm 0.03)\%$ over the range $p_{\mathrm{t}} = 5$ to 100 GeV$/c$. The simulation results are shown in Fig. 2.3. These results are based on energy deposition only and do not include photon transport efficiencies or the electronic noise contribution. Systematic contributions to the resolution arising from calibration and related systematic uncertainties are ignored.

Some increase in the constant a is to be expected from photon transport and related effects. This has been studied in a series of test beam measurements of prototypes of this detector with various sampling frequencies including - Pb(1.6 mm)/Scint(1.6 mm) also shown in Fig. 2.3 - and preliminary results are consistent with a small increase in a as discussed in Chapter 7.

The value of the constant term b is dominated by shower leakage in these calculations. Other systematic effects which arise during detector fabrication and from the tower-by-tower calibration uncertainties will increase b. The latter effect is itself of the order of 1% typically. Results from the analysis of the test beam measurements performed at PS and SPS at CERN with the final prototype modules are described in Chapter 7.

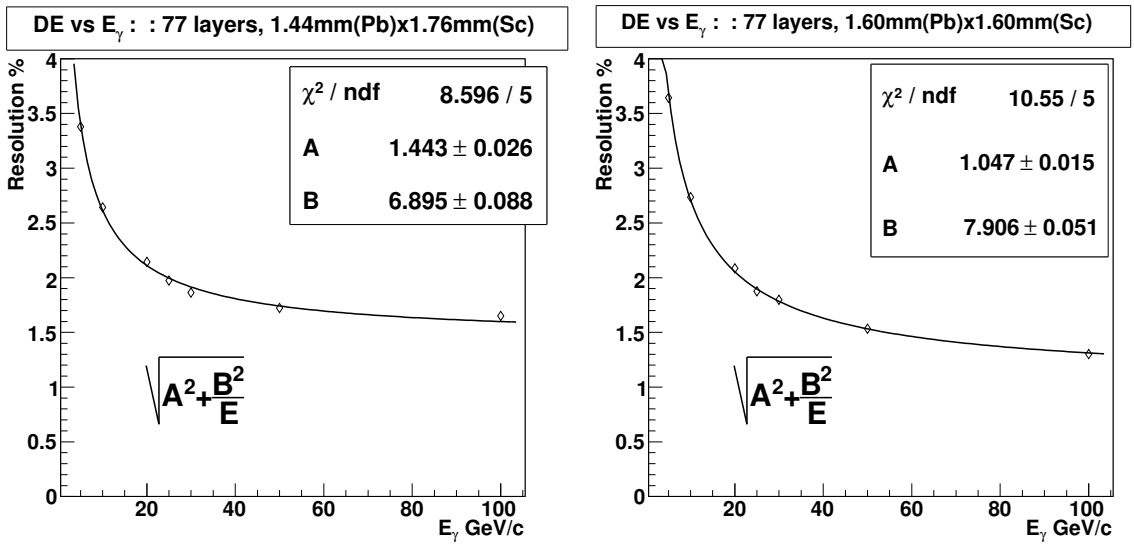

Figure 2.3: GEANT3 simulations of the EMCal module resolution. Left: Proposed production module. Right: Prototype test module.

The impact of detector energy resolution on the proposed physics program has been studied. Given the nature of the proposed physics, and in particular, the main focus on jet physics, there is no sharp cutoff on the required energy resolution for isolated electromagnetic clusters. Simulations show that a

resolution of the order of $\sim 15\%/\sqrt{E} \oplus 2\%$ is sufficient for the jet physics program and this is fixed as the minimum detector requirement. The electron and photon physics programs will benefit from better resolution. Based on simulations and test beam results it is expected that the EMCal minimum performance requirements will be readily met and we project an ultimate performance of better than $\sim 12\%/\sqrt{E} \oplus 1.7\%$. This is discussed further in connection with the prototype module test beam results in Chapter 7.

The physical characteristics of the EMCal are summarized in Table 2.1. An exploded view drawing of the module showing all single components is shown in Fig. 2.4

Table 2.1: The EMCal Physical Parameters.

Quantity	Value
Tower Size (at η=0)	$\sim$6.0 $\times$ $\sim$6.0 $\times$ 24.6 cm^3 (active)
Tower Size	$\Delta\phi \times \Delta\eta = 0.0143 \times 0.0143$
Sampling Ratio	1.44 mm Pb / 1.76 mm Scintillator
Number of Layers	77
Effective Radiation Length X_o	12.3 mm
Effective Moliere Radius R_M	3.20 cm
Effective Density	5.68 g/cm^3
Sampling Fraction	10.5
Number of Radiation Lengths	20.1
Number of Towers	12,288
Number of Modules	3072
Number of Super Modules	10 full size, 2 one-third size
Weight of Super Module	$\sim$7.7 metric tons (full size)
Total Coverage	$\Delta\phi$ = 107^o, -0.7 $< \eta <$ 0.7

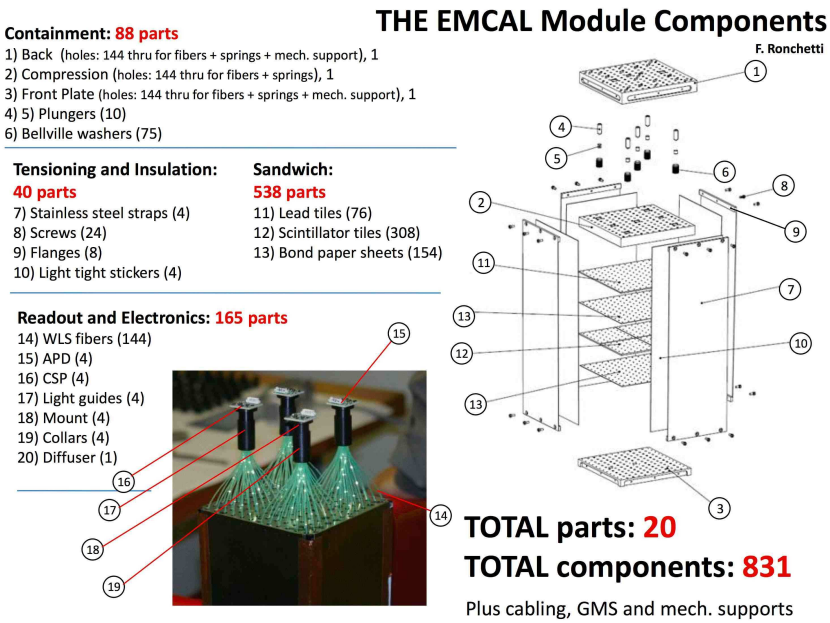

Figure 2.4: Exploded view drawing of EMCal module showing all components.

2.2.2 Module Mechanical Details

Each module has a radial slice rectangular cross section in the ϕ direction and a trapezoidal cross section in the η direction with a full taper of 1.5 degrees. The structural members of each module in the final design are: back plate, compression plate, paper-Pb-paper-scintillator stack, front plate and 4 straps; the dimensions and materials used are listed in Table 2.2

Table 2.2: Materials and dimensions of the components used for the construction of a single EMCal ALICE module.

Component	Quantity	η width (mm)	ϕ width (mm)	Thickness (mm)	Material
Back plate	1	127.41	119.47	15	aluminum, 6082 T6
Compression plate	1	126	119	14	aluminum, 6082 T6
Lead absorber	76	min 119.80	119.54	1.44	Natural Lead
		max 126.49			
Scintillator tile	308 = 4x77	as for Lead	119.54	1.76	Polystyrene
Paper	154 = 2x77	as for Lead	119.54	0.1	Bond, acid free
Front Plate	1	119.80	119.54	10	aluminum, 6082 T6
Straps	4	100	100	0.150	Stainless Steel 316 L

A compressed design has been adopted for the EMCal modules in order to provide the module with self-supporting mechanical stability. Figure 2.5 shows a cross section of the module illustrating the straps, the back plate, the compression plate, and the Belleville washer stacks. The front and back plates of a module are held precisely in place by the four stainless steel straps. These straps align the back and front plates and permit a compressive force to be applied to the stack. The mass of each module is ~ 20.5 kg and the different layers of the stack are held in place in any orientation by the inter-layer static friction that appears when a compressive force is applied via the compression plate. Tests have established the coefficient of static friction for every pair of materials in the module stack. The minimum coefficient was found to be 0.33, corresponding to the bond paper-scintillator interface. The minimum compressive force needed for stability of the stack is 5×141 N. A final compressive force of 5×311 N was adopted after a program of tests with mechanical prototypes, and applying safety factors and contingencies. The resultant pressure in the stack is $\sim$ 1.1 kg/cm^2 when this force is applied.

The compressive force is transferred to the stack through the compression plate (see Fig. 2.5). This is a 14 mm thick aluminum plate that is situated between the back plate and the stack and has freedom for axial displacement while it is restrained for lateral movement. The load is transferred to this plate by 5 sets of Belleville washers compressed by setscrews from the back plate or alternatively through 5 load cells used to measure the compression force at initial assembly. These washers are characterized by a rather flat, nonlinear relationship between load and deflection. A series-parallel configuration of washers can be arranged to allow large deflection of the stack with relatively small change in load. The chosen Belleville washer design will permit a total stack deflection of ~ 1.3mmwhile sustaining a mechanically stable compression within 50% of its initial value.

The long term value of the compressive force within the module is determined by the response of the Bellville washers in response to creep, or flow, of the module components as well as the long term relaxation of the components as they continue to flatten over time. The effect of Lead flow under compression has been analyzed in order to predict long-term structural stability of the modules. According to J.R. Riddington and M.K. Sahota, it is safe to assume, provided tensile or shear stresses are limited to 1.72 MN/m^2 (250 psi) in normal conditions, that no measurable creep for lead of 99.9% purity will be observed. In conditions of purely compressive stress the "safe stress" figure may be increased to 2.75 MN/m^2 (400 psi).

By design, therefore, the EMCal modules are not expected to show measurable creep of the lead tiles. The compressive load is more than a factor of 10 smaller than the value for which measurable creep is observed. Thus, flow of the lead over the lifetime of the module is not an issue. Similar measurements of stacks of paper or polystyrene scintillator under compression show a very rapid (hours) approach to the equilibrium stack height. Therefore the most significant issue for the lifetime of the compressive load in a module is the slow approach to flatness of the module component layers under the compressive load, and the resultant decrease in the height of the module stack. The single largest contributer within the module to the flatness relaxation is the lead plates which invariably are slightly deformed by handling in the module fabrication process.
The nonlinear response of the Belleville washer system allows 0.400 mm of creep of the module during the estimated lifetime of the module, with a 10% loss of compressive load. A 1.30 mm shortening of the module stack will lead to a 50% loss of compressive load and 1.75 mm of creep would lead to 100% loss of compressive load. Experimental tests have shown that 100% loss of compressive load does not lead to failure of the module structure. In this case the lead tiles ”slide” down onto the straps and thus some compressive load is restored. The mechanical design is thus ”failsafe” although complete loss of compressive load might result in damage to some WLS fibers.
In order to stabilize the module and to avoid more than 0.400 mm of creep during the anticipated lifetime of the EMCal, a higher than nominal compression load is applied during the first 3 days after the module is stacked and prior to transfer of the compressive load to the Belleville washers. The module pressure is tracked with load cells over this period and adjusted early in the process wen the pressure drop and module shortening occurs quickly. It is assumed that a module is stabilized when no measurable change in the stack height occurs in a 24 hour period.

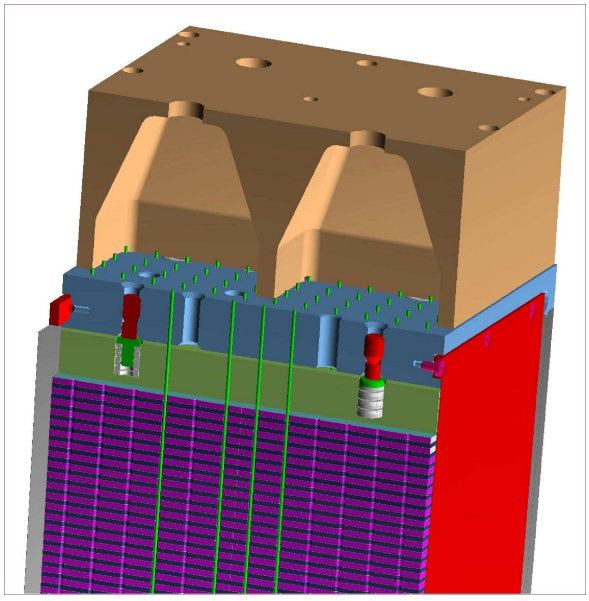

Figure 2.5: A cut-away view of the module stack showing the structure of the straps, the back plate, the compression plate and the Belleville washer stacks. A section of the strong-back that binds modules into strip modules is also shown.

Other activities associated with module production include pre-machining the taper in the scintillator, processing the Wave Length Shifting (WLS) fibers to the final bundle configuration, treating the scintillator edges and quality control. For the machining of the scintillator tiles to their final size the complete set required for one tower is stacked, compressed, and machined as a unit to the final taper dimensions. The machined tiles are kept in stacked order until they are ready for module assembly.
The WLS fiber preparation begins with the cutting of the fibers to the proper length and polishing the

ends with a high precision wheel with 3 cutters (2 carbide and 1 diamond). The fibers are cooled to liquid N_2 temperature for the cut-polish process. Once the fibers are polished, the next step is to sputter an aluminum mirror on one end (see Fig. 2.6)

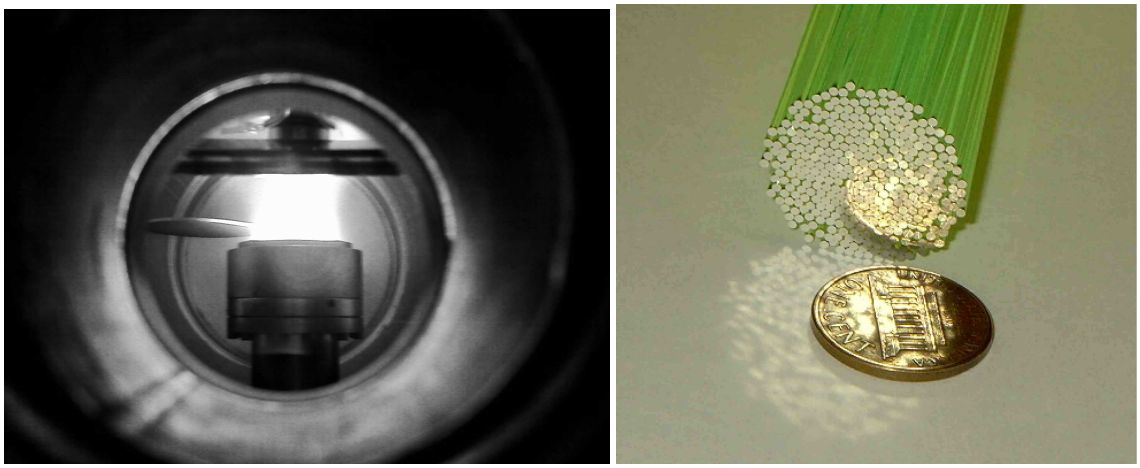

Figure 2.6: A picture of the Ar ion plasma used to sputter Al on the polished fiber end to form a high quality mirror. A bundle of approximately 400 fibers can be treated at one time.

After the fibers are aluminized the bundles are prepared using a fixture (see Fig. 2.7) which positions the fiber bundle into the correct convergent configuration from the rectangular matrix that samples the volume of the tower into the circular cross section required to mate to the light guide/diffuser. The converged fiber bundle passes through a plastic cylinder where the cut and polished fiber ends are secured with optical epoxy. After curing, the optical epoxy surface is polished. This surface ultimately makes contact with the light-guide that removes spatial correlations (a diffuser) and transfers the light to the Avalanche PhotoDiode (APD) photo sensor (see Section 2.2.4).

Figure 2.7: A fixture used to position the WLS fibers into the correct convergent shape that transitions from the uniform sampling of the tower volume to the small circular diameter required to mate to the light guide/diffuser.

2.2.3 Module Assembly

During the module prototyping period efforts were made to scale-up the facilities and handling equipment for the full scale production requirements of the Shashlik modules. The dimensional tolerances of individual modules are critical to the successful assembly of modules into strip modules and their integration into super modules. A module stacking fixture used to control tolerances in the process of assembling the hundreds of parts that go into a module is shown in Fig. 2.8 and Fig. 2.9 during various stages of module assembly.

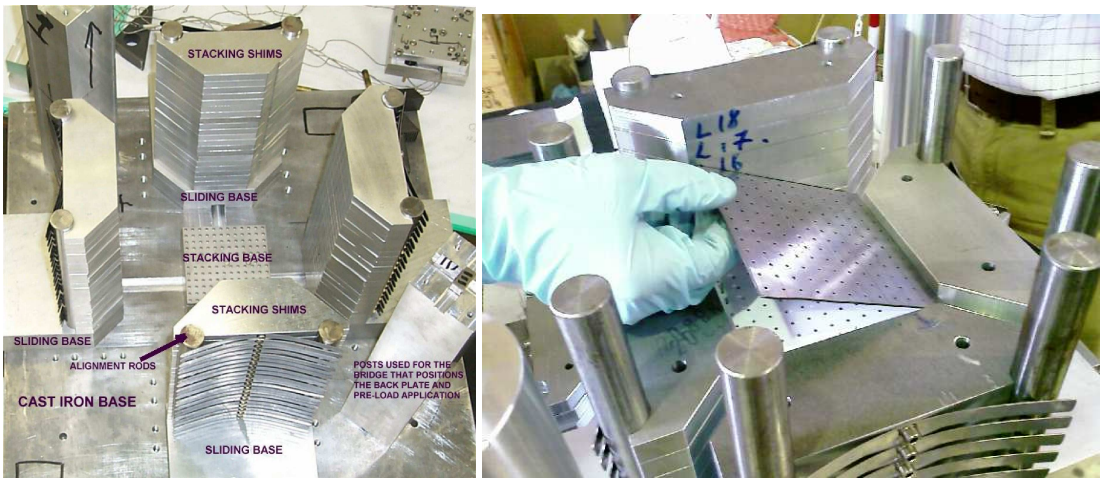

Figure 2.8: Left: Stacking fixture prior to the insertion of any EMCal components. Right: Stacking fixture during the assembly of a prototype module.

Figure 2.9: Left: Assembled module on the assembly station after removing the stacking fixture, and with the load cells and the crossbeam installed. Right: The module during the installation of the black light-blocking foil.

The module stacking fixture is mounted on a precision cast iron base. Four laterally sliding alignment towers are attached to the cast iron table. The shape of these towers correspond precisely to the desired shape of the module. A set of 16 precision wires (4 per tower), aligned with the fiber holes of the stack are mounted in a mechanism under the stacking base which allows them to be increased in length in a way that follows the increasing height of the stacked module.
When all layers of a module have been stacked in place, a crossbeam is attached to the uprights of the stacking fixture in order to fix the module front and back plates precisely with respect to each other. A compression is then performed loading the compression plate to a total of 350 pounds. This force, adjusted as necessary, is applied over a period of three days until satisfactory stability is reached. At that

time, the module is wrapped in a light tight enclosure; the external straps are attached and the module is removed from the assembly station ready for integration into the strip module.

2.2.4 Optical System and Photo Sensors

Scintillation photons produced in each tower are captured by an array of 36 Kuraray Y-11 (200 M), double clad, wavelength shifting (WLS) fibers that run longitudinally through the Pb/scintillator stack. Each fiber within a given tower terminates in an aluminized mirror at the front face of the module and is integrated into a polished, circular group of 36 fibers at the photo sensor end at the back of the module. Because the tower transverse shape deviates slightly from square as a function of longitudinal depth, we choose a fiber pattern which has exactly the same aspect ratio as the mechanical tower shape at a depth close to shower maximum. This has the effect of making the fiber pattern uniform across tower boundaries when weighted by the shower energy deposition. The properties of the selected fibers are given in Table 2.3.
The fiber bundles are pre-fabricated and inserted into the towers after the module mechanical assembly is completed. A prototype fiber bundle is shown in Fig. 2.10. The 36 individual fibers for a single tower are packed into a circular array 6.8 mm in diameter and held in place inside a custom injection moulded grommet by Bicron BC-600 optical cement. An optical quality finish is applied to the assembled bundle using a diamond polishing machine. At the other end of the bundle, individual fibers are similarly polished and mirrored with a sputtered coat of aluminum as described above.

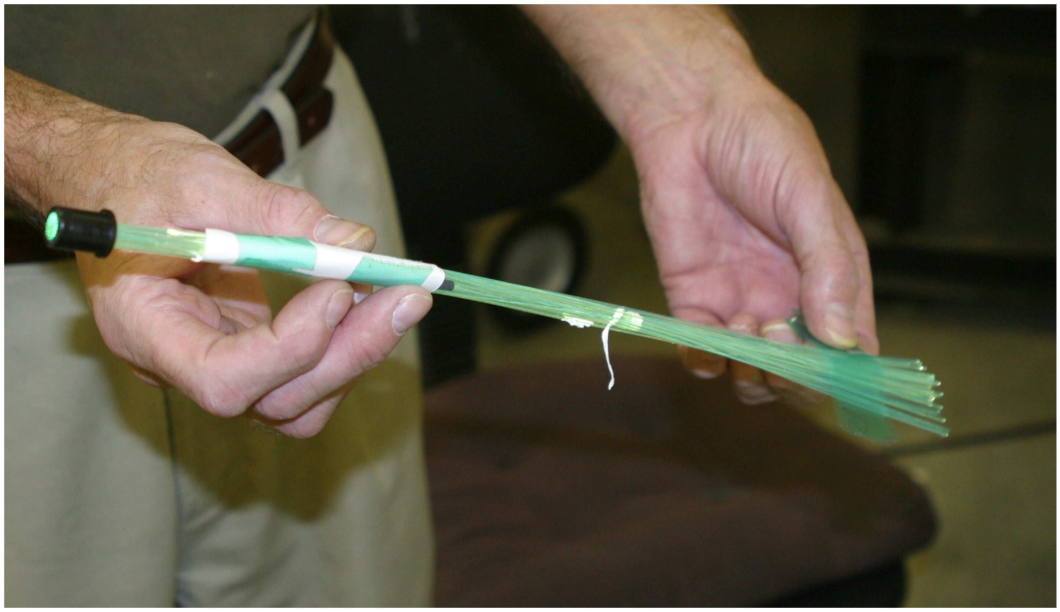

Figure 2.10: A prototype EMCal fiber bundle of 36 fibers.

A number of optical studies have been completed to assess the light transmission through individual fibers and the efficacy of the mirror applied to the fiber end at the front face of the calorimeter. In these tests, a single optical fiber connected to a UV LED light source was used to inject light of fixed amplitude at varying positions along the fiber. Tests were made with and without mirroring applied to the polished fiber end and transmitted light was recorded with an Avalanche Photo Diode (APD) photosensor as a function of position of the light injection point. Typical results are shown in Fig. 2.11 for a single mirrored fiber. In this figure, the APD sits at zero distance and the front face of the calorimeter, in a full detector assembly, would sit at the distance of approximately 37 cm. The curve shows the light transmission efficiency in arbitrary units as a function of distance from the APD. The response is quite flat in the vicinity of shower maximum (i.e., the location of the highest density energy deposition for an

electromagnetic shower). The shower maximum occurs at about 26 cm on the distance scale of Fig. 2.11. This number accounts for material immediately in front of the EMCal in ALICE (which ranges between 0.4 and 0.8 radiation lengths) and assumes a total of 5.5 - 6.0 radiation lengths for shower maximum for 10 GeV photons. At this depth in the detector, the mirrored fiber response is very uniform and does not contribute significantly to the non-linearity of the detector as a whole.
Measurements studying direct transmission through fibers, including long ones, reveal three attenuation lengths for these WLS fibers associated with the fiber core and cladding layers: 2.2 cm, 20.6 cm, and 340 cm. The fit in Fig. 2.11 assumes these attenuation lengths and varies the source strengths and reflection coefficients independently for each of the attenuation lengths. We note that the reflection coefficient for the long attenuation length (P6) component is $\sim 73\%$ while the short attenuation length components are not effectively reflected (consistent with zero) by our mirror.

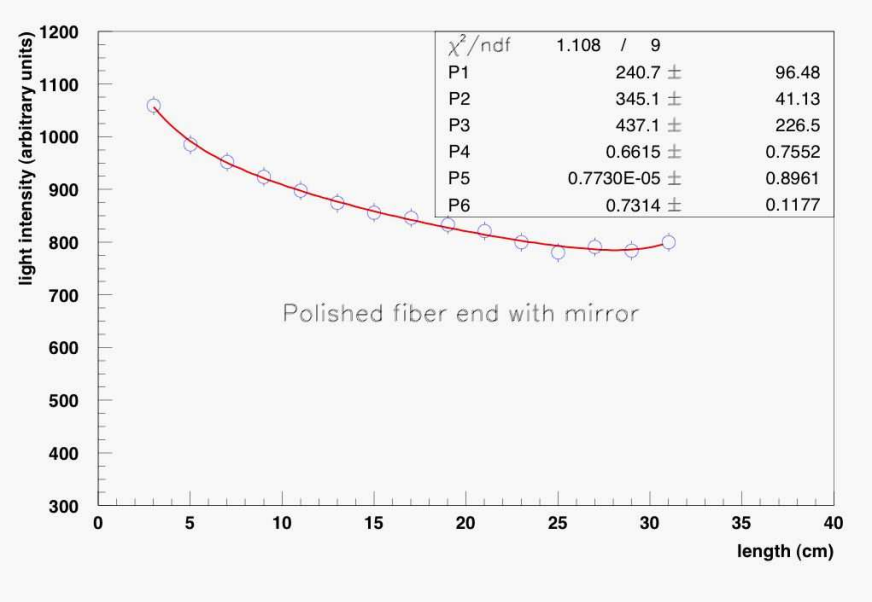

Figure 2.11: Light transmission efficiency in arbitrary units versus distance of propagation for Kuraray Y-11 fibers with aluminized mirrored end. The fitted curve is discussed in the text.

Other factors that can significantly impact the performance of the calorimeter include scintillator edge treatment, the density of the wavelength shifting fiber readout pattern, and the material chosen for the interlayer diffuse reflector. For scintillator edge treatment and fiber density, we were able to take advantage of the extensive studies made by the LHCb collaboration for their ECAL [4]. Given that we use the same scintillator with virtually identical towers size to the LHCb "middle modules", we were able to adopt their procedures for scintillator edge treatment and fiber density after a series of relatively simple checks. In particular, we have adopted a diffuse reflector edge treatment such as that obtained with Bicron Titanium Dioxide loaded white paint (BC622A) and a total fiber density of about one fiber per cm^2. In the case of the interlayer diffuse reflector, we have to deviate from LHCb and use a white, acid free, bond paper in place of the Teflon based commercial TYVEK. While TYVEK produces slightly better surface reflectivity, its coefficient of friction is too low to permit its use in this design where the module's mechanical stability depends on the interlayer static friction. The white paper used in the EMCal prototypes has been previously studied for aging effects in connection with the STAR calorimeter project [6].
The 6.8 mm diameter fiber bundle from a given tower connects to the APD through a short light guide/diffuser with a square cross section of 7 mm $\times$ 7 mm that tapers slowly down to 4.5 mm $\times$ 4.5 mm as it mates (glued) to the 5 mm $\times$ 5 mm active area of the APD.
Figure 2.12 shows 4 pre-fabricated fiber bundles inserted into the towers of a single prototype module.

Table 2.3: Characteristics of the selected wavelength shifting fibers.

Quantity	Value
WLS fiber	Y-11 (200) M-DC
Manufacturer	Kuraray
WLS Fluor	K27 200 mg
Absorption Peak	430 nm
Emission Peak	476 nm
Decay Time	7 ns
Core material	PS
Refractive Index	1.59
Inner Cladding	PMMA
Refractive Index	1.49
Outer Cladding	FP
Refractive Index	1.42
Long fiber Attenuation Length	3.5 m
fiber Diameter	1.0 mm

Figure 2.12: Fiber bundles with attached APD and preamplifier of four towers of an EMCal prototype module.

In this picture all of the module rear enclosing and structural elements are omitted so the wavelength shifting fibers may be seen as they converge to the light guide (inside the black plastic tube) and finally to mate with the APD and charge sensitive preamplifier. The APD and preamplifier are discussed at length in Chapter 3. Here we will mention briefly their optical characteristics. The selected photo sensor is the Hamamatsu S8664-55 avalanche photodiode. This photodiode has a peak spectral response at a wavelength of 585 nm compared to an emission peak of 476 nm for the Y-11 fibers. However, both the

spectral response and the quantum efficiency of the APD are quite broad with the latter dropping from the maximum by only ∼5% at the WLS fiber emission peak. At this wavelength, the manufacturer's specification gives a quantum efficiency of 80%.

2.3 Mechanical Assembly

2.3.1 Strip Module

2.3.1.1 Design

Twelve detector modules and a structural strong-back form a strip module which is the final product of the module assembly site from whence they are shipped to the super module assembly and calibration site. A fully assembled strip module is shown in Fig. 2.13. Like the module, the strip module is a self-supporting unit. A collection of 24 strip modules forms a super module. The functions of the strong-back, in addition to the mechanical support for modules, include a role as the principle structural component of the super module crate as well as protection for the optical fibers, a structural mount for the light guide, APD, and charge sensitive preamplifier, and a light-tight enclosure for all these elements. At the top of the strong-back are 3 printed circuit boards (the so-called Transition cards, or T-cards) whose function is to provide the interface between the charge sensitive preamplifiers and the flat ribbon cables that transport the analog signals along the length of the super module to the FEE crates. Each detector module is fixed onto the strong-back by four 5 mm diameter stainless steel screws.

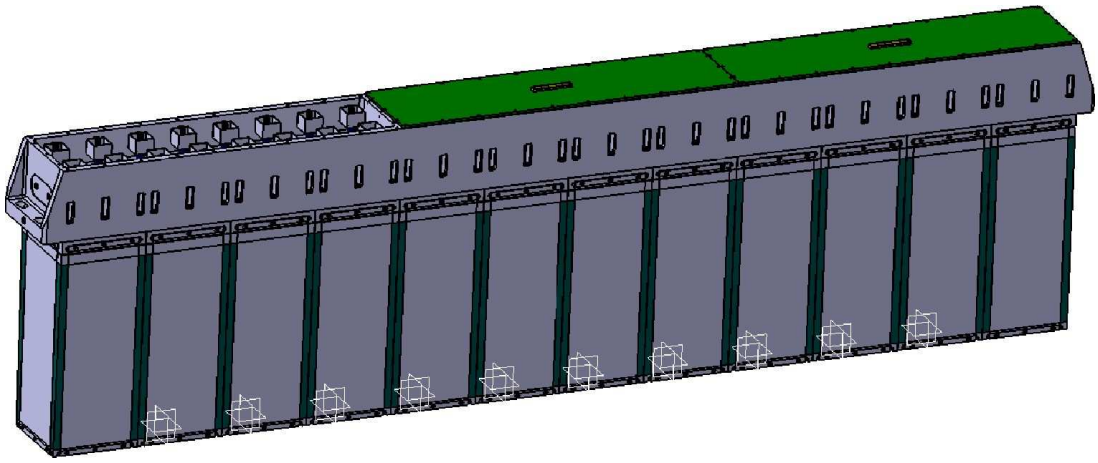

Figure 2.13: Fully assembled strip module showing 12 modules integrated onto their strong-back.

2.3.1.2 Description

The strong-back is 1494 mm long, 130 mm wide, and 100 mm thick with a weight of 15 kg. The strong-back is designed thick enough to provide sufficient inertia and mechanical stiffness with a small deflection for the 272 kg load of 12 detector modules. The weight of a fully equipped strip module is estimated at 293 kg.

2.3.1.3 Fabrication

The strong-back is made from sand cast aluminum, with 48 pyramidal cavities along its length where the optical fibers from 12 modules emerging from towers converge toward the photo sensor. The casting process is well suited to form these cavities and the overall structure of the strong-back, saving considerable raw material cost and machining time. The raw material will be aluminum alloy (AC-42000) chosen for

its magnetic properties and its ability to be easily cast and machined. Figure 2.14 shows the front and the back side of a cast strip module strong-back.

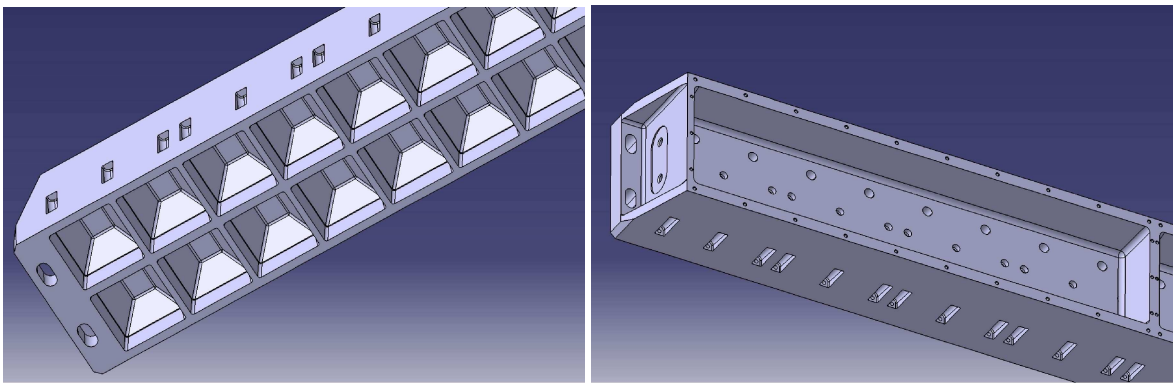

Figure 2.14: Front (left) and back (right) side of a module strong-back.

2.3.1.4 Design and Fabrication Status

A prototype sized for 4 modules was machined for qualification of the strip module concept and the strong-back design. These 4-module prototype versions of the strong-back were used for the second beam test modules where a 4×4 module ($8 \times 8 = 64$ tower) prototype was tested. Figure 2.15 shows the machined version of the strong-back prototype suitable for the beam test. As this document is written, the first several full size strong-backs have been cast and machined.

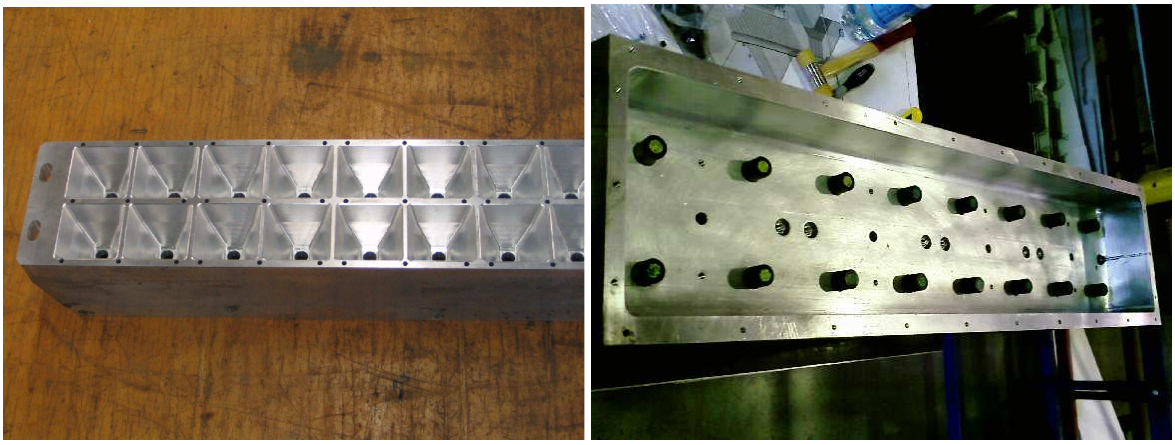

Figure 2.15: Prototype of strong-back for beam test without (left) and with (right) modules mounted on it.

2.3.1.5 Finite Element Analysis

Detailed Finite Element Analysis (FEA) of the strong-back design has been conducted. Safety coefficients in the FEA analysis were used following the ENV 1993-1-1 norm, Eurocode 3, which specifies a safety coefficient of 1.1 on yield strength of material, and 1.35 safety coefficient on static load. For strip modules at the 12 o'clock location in the ALICE magnet, the maximum deflection of the present strong-back design is found to be 0.32-0.35 mm with clamped ends as the boundary condition. The corresponding maximum stress is 28-30 MPa for 180 MPa yield strength of the raw material. The maximum stress occurs on the 5 mm diameter holes located near ends of the strip module used for fixation of

modules onto the strong-back. Figure 2.16 shows the mesh model of the strong-back used in the FEA calculations. Figure 2.17 shows the deflection pattern and the distribution of stress in the strong-back.

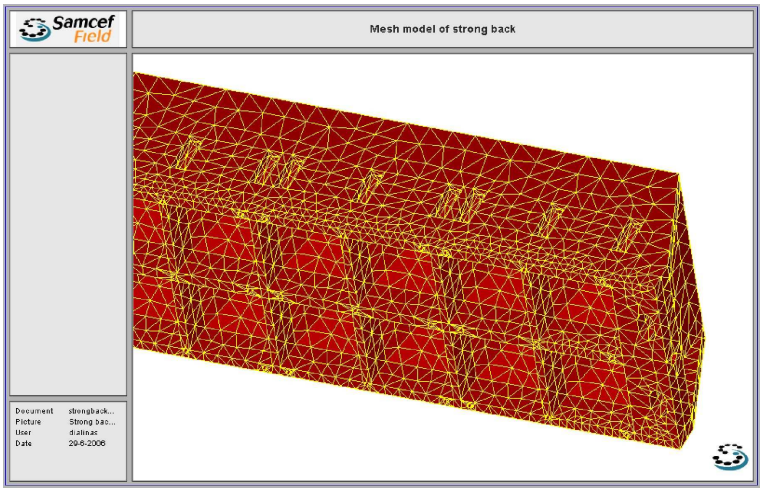

Figure 2.16: Mesh model of strong-back.

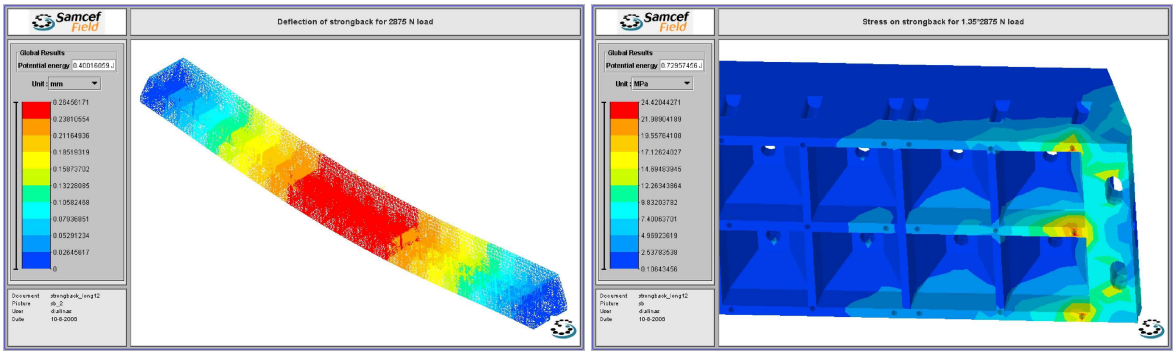

Figure 2.17: Left: Deflection of strong-back. Right: Location of maximum stress on strong-back.

2.3.2 Super Module

The super module is the basic building block of the calorimeter and is the final unit which is handled for movement into the underground cavern and installation into the ALICE magnet. Given the 288 individual detector modules which are rather compact and heavy, the main engineering task was to design a stiff super module structure that performs with small deflections in any orientation yet does not require extensive, heavy external stiffening components that would reduce the available volume for the active detector. The basic structure of the ALICE central detector suggests that the EMCal super modules should have an azimuthal size of approximately 20 degrees to correspond to the primary structural periodicity of the ALICE TPC and the other detectors of the ALICE central detector. This defines the natural size and weight range of the super module to meters and several tons.

2.3.2.1 Design of Super Module Crate

The concept adopted for the ALICE EMCal is to develop a super module crate which functions not as a box for holding the individual modules, but rather an integrated structure in which the individual strip module elements contribute to the overall stiffness. In the present design, the super module crate is a

large I-beam in which the flanges are the longitudinal sides of the crate and the 24 transverse rows of strip modules together form the web of the I-Beam, as shown in Fig. 2.18. The two extreme positions of the super module in the ALICE magnet ($\sim$12 and $\sim$9 o'clock) stress the super module in the two principal perpendicular directions. With 1444 mm spaced flanges, this configuration gives the super module a very good stiffness for the $\sim$9 o'clock location. To limit deflections of the super module when positioned in the 12 o'clock orientation, the super module crate features a 1 mm thick stainless steel forward sheet (traction loaded), which controls the bending moment at the root of the strip modules which would otherwise tend to open the crates longitudinal sides in the 12 o'clock position. By controlling the tendency of the super module crate to open in the 12 o'clock position, this forward sheet helps to limit deflection of strip modules for the 12 o'clock location.

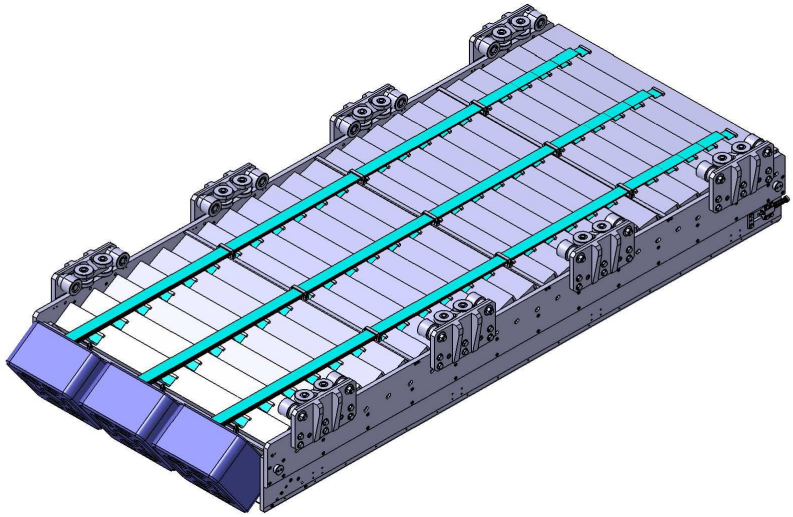

Figure 2.18: A fully equipped super module.

The intrinsic stiffness given by the I-beam concept allows the use of non-magnetic aluminum alloys for most parts of the super module crate. Unlike austenitic stainless steels, light alloys are easy to machine, helping to limit both cost and weight. The two main sides (flanges of the I-beam) of the crate are assembled from 2 plates, each 25 mm thick, bolted together and arranged in order to approximately follow the taper of the 20 degree sector boundary. Parts of the super module crate are made mainly from laminated 2024 aluminum alloy plates. Ridges are provided on side plates to allow accurate angular alignment of the strip modules. Strip modules are stacked together in contact - without any clearance. This allows a limit on machining costs of the ridges and to avoid serious dead areas for the physics. In order to limit machining time, the crate is mainly made from 25 mm thick plates bolted together instead of a whole 50 mm thick machined plate. Only one of these plates (the one with ridges for strip module alignment) receives any significant milling, the other is mainly just drilled.

2.3.2.2 Dimensions and Weight of Super Modules

The super module crate is 3400 mm long, 1600 mm wide, and 530 mm high. The estimated weight of the super module crate, without strip modules but including the roller system is 482 kg. The estimated weight of a fully fitted, full size, super module is 7514 kg.

2.3.2.3 Finite Element Analysis of Super Module

Safety coefficients were used following the ENV 1993-1-1 norm, Eurocode 3, corresponding to a 1.1 safety coefficient on yield strength of material, and a 1.35 safety coefficient on static load. The yield

strength of the 2024 alloy used for the laminated plates is 290 MPa and the yield strength of 42000 alloy used for cast parts is 180 MPa. Figs. 2.19 and 2.20 show the deflections and stresses for super modules in the 12 o'clock position and the 9:20 o'clock position.

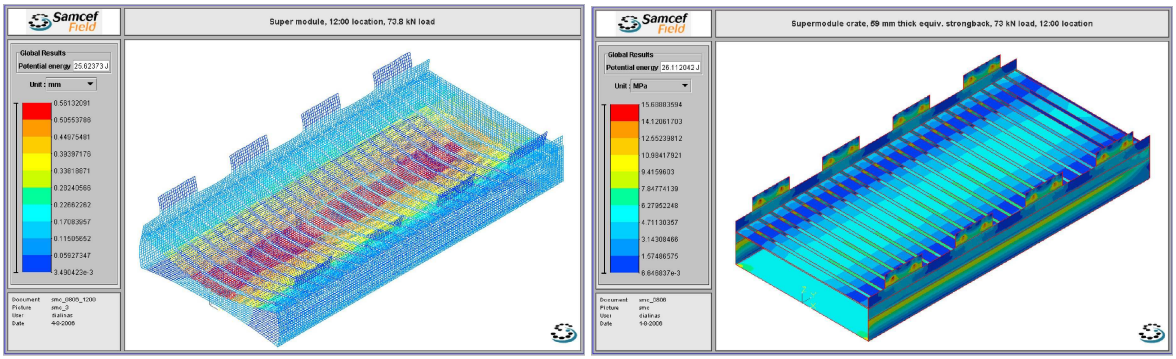

Figure 2.19: Deflection (Left) and stress (Right) of the super module at the 12 o'clock location.

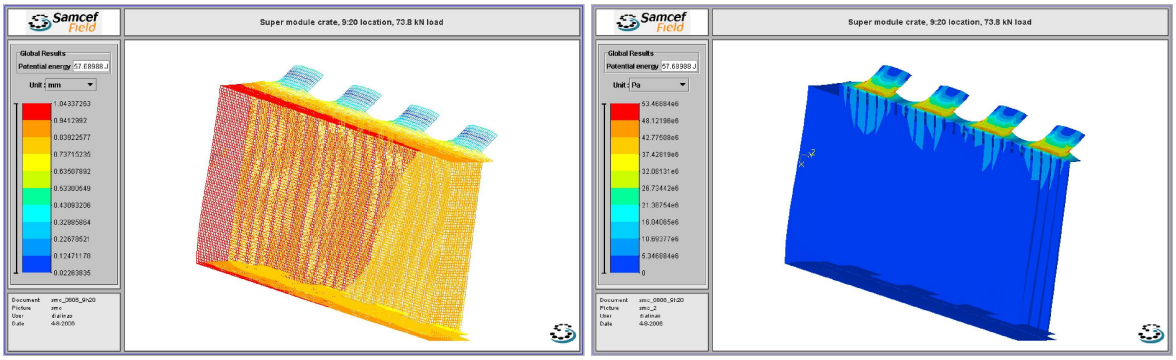

Figure 2.20: Deflection (Left) and stress (Right) of the super module at the 9:20 o'clock location.

The maximum stress in the super module crate for the 12 o'clock location is 22 MPa. The maximum stress in the super module crate for the 9:20 o'clock location is 73 MPa located at the interface between the carriages and the crate. The maximum stress on the support pads ranges from 17.5 to 18.3 Mpa depending on the location of the super module while the maximum stress on the carriage structure is 70 MPa.

3 Electronics

The readout electronics of the PHOS (PHoton Spectrometer) detector of ALICE have been adopted for the EMCal Front End Electronics (FEE) readout with only minor modifications. This is because the light yield per unit of energy deposit in the EMCal is similar to that of the PHOS [1, 2], and because the electronic noise performance requirements of the EMCal are less stringent than those of PHOS, because of the worse intrinsic energy resolution of the EMCal due to sampling fluctuations. The PHOS electronics readout is summarized in the next section and differences with the PHOS FEE are described in Section 3.2.

3.1 Front End Electronics Architecture

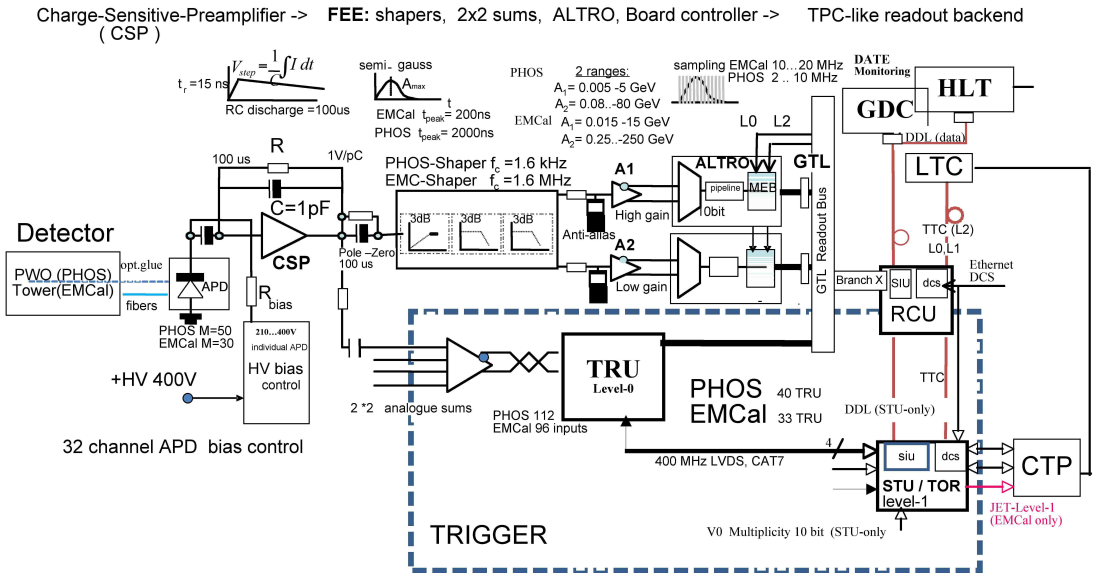

Figure 3.1: PHOS/EMCal Readout electronics overview.

The PHOS is a highly granular $PbWO_4$ calorimeter comprising 17920 crystals when fully implemented in 5 groups of 3584 crystals. The crystals are kept in a cold zone at -25° C and separated by an isolation layer from a warm volume immediately behind (radially) the crystals that encloses the electronics. A schematic overview of the EMCal (PHOS) Front End Electronics [3] is shown in Fig. 3.1. The interface of the FEE with the ALICE Data Acquisition and with the Trigger and High Level Trigger are described in further detail in Chapters 4 and 5.

3.1.1 APD and Preamplifier

The active readout element of the PHOS detector is a 5×5 mm^2 active area Avalanche PhotoDiode (APD S8148) [4] which is glued to each PHOS crystal. This APD was the result of a large R&D activity carried out by the CMS collaboration and Hamamatsu Photonics to arrive at the development of the APD S8664-55 (or S8148) [5, 6]. This is a large area Avalanche PhotoDiode with high quantum efficiency, low dark current, and very good stability and reliability. The main characteristics of this photo-detector are listed in Table 3.1. In particular extensive studies have been made to insure the radiation hardness of this device [7].

Table 3.1: Characteristics of the S8664-55 (S18148) Avalanche PhotoDiode.

Active Area	5×5 mm^2
Capacitance	90 pF
Wavelength min.	$\sim$ 320 nm
Wavelength max.	$\sim$ 1000 nm
Peak wavelength	600 nm
Quantum efficiency	$\sim$ 80% at 476 nm
1/M $\times$ dM/dT (M=30)	$\sim -1.7\%/^\circ$C
1/M $\times$ dM/dV (M=30)	$\sim 2.3\%/$V

The APD is connected directly to the back of a Charge Sensitive Preamplifier (CSP) with 0.83 V/pC sensitivity and a maximum range of about 5 pC. The APD and CSP are shown in Fig. 3.2. The APDs are operated at moderate gain for low noise and high gain stability in order to maximize energy and timing resolution. With a nominal APD gain of M=50, about 220 electrons are generated in the APD per MeV of energy deposited by showering electromagnetic particles (4.4 e^-/MeV at M=1) in PHOS.

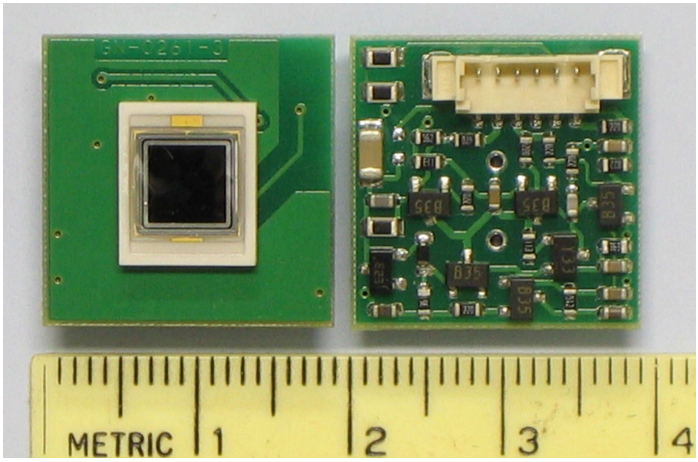

Figure 3.2: The Avalanche PhotoDiode (left) mounted on the back of the Charge Sensitive Preamplifer (right) used by PHOS and EMCal.

3.1.2 Front End Card: Shaper and Digitization

The CSP converts the charge signal over a 1 pF capacitor into a voltage step that is formed by the CR-2RC shaper of the FEE into a semi-Gaussian pulse shape. The FEE cards contain 32 remotely controlled precision High Voltage (HV) bias regulators [8], 64 shapers and digitizers, a board controller, and a power regulation system which prevents noise coupling between digital or High Voltage sections and the analog signal section. The APD bias voltages can be set individually to a precision of 0.2 Volt/bit. Each shaper channel is split via a low noise gain buffer into high and low gain shapers for a total dynamic range of 14 bits using two 10-bit digitizers. Four ALTRO (ALICE TPC ReadOut) [9] digitizer chips are required, each containing 16 10-bit flash ADCs and internal multi-event buffers, for a total of 32 high gain and 32 low gain channels per FEE card. The choice of the ALTRO chip, combined with a board controller FPGA, allows the PHOS and EMCal to re-use the readout back-end protocol of the ALICE TPC via an external Readout Control Unit (RCU) [10].
The FEE has an effective 14-bit dynamic range over the interval 5 MeV to 100 GeV for the PHOS, which has a measured energy resolution of 2% at 2 GeV. The ADC samples the waveform at 10 MHz

(programmable). An additional design goal for PHOS was timing resolution of about 1 ns at 2 GeV in order to reject low energy neutrons and anti-neutrons. The competing requirements of low noise (narrow bandpass) and good timing resolution (wide bandpass) have necessitated extensive tests of alternative PHOS shaper designs, with shaping times varying between 1 and 4 μs. As discussed below, the EMCal requirements dictate a shorter shaping time of about 100 ns. These shaping time modifications only require changes in discrete component values of the shaper and do not affect the layout of the FEE board.

3.1.3 Trigger Input

Each 32 channel FEE card forms 8 analog charge sums of 2×2 adjacent towers to provide fast Level-0 and deadtime-less Level-1 photon (or electron) shower triggers. The fast-OR signals are extracted from the input of the shaper, passed through a simple 100 ns RC-shaper, and sent via short differential cables of equal length to the Trigger Region Unit cards (TRU) [11]. One TRU card receives 112 (PHOS) or 96 (EMCal) analog sums from the 14 (PHOS) or 12 (EMCal) FEE cards connected via the short differential cables (TRU domain). The TRU digitizes the sums using commercial Flash ADCs and inputs the full space and time image of all channels it services into a single FPGA. In the case of PHOS, the FPGA trigger algorithm applies 4×4 sliding window algorithms for successive Level-0 and Level-1 trigger generation, with programmable thresholds for simultaneous low, mid, and high energy trigger outputs at a decision rate of 40 MHz.

3.1.4 Readout and Control

A group of 9 FEE cards (384 towers for EMCal) is read out by a custom 200 MByte/s GTL+ bus under mastership of an external RCU card. Each RCU card masters up to two readout domains via a separate custom GTL bus and transmits the FEE data to the Local Data Concentrator of the DAQ via an ALICE-standard Detector Data Link (DDL) [12]. An additional slot on each GTL bus is used for installation of a TRU card, or additional FEE card. Communication and control of the TRU are via the GTL bus.
Control and monitoring access to the FEE card resources are implemented in programmable firmware logic on the FEE cards. This slave logic allows RCU address-mapped access to both the control and data sections of the FEE cards. The address space includes ALTRO-chip internal registers, APD bias control registers, and registers for voltages, currents, and temperatures.

3.2 EMCal Readout Considerations

3.2.1 APD and Preamplifier

The PHOS decision to use the Hammatsu S8664-55 APD was made largely because, at the time, it was essentially the only commercially available large area APD. It was developed by Hamamatsu in collaboration with the CMS experiment. While a number of new APD products are now commercially available, and some of these products might be suitable replacements for the Hamamatsu S8664-55 APD, there is no expected performance benefit for the EMCal due to the dominance of the intrinsic resolution contribution, and potential cost savings would most likely be offset by the need to develop a new preamplifier and/or bias control in the case that the required bias exceeded the 400 V maximum of the PHOS FEE. For these reasons it was decided to use the same APD and preamplifier as used by PHOS (see Fig. 3.2).
The only significant difference with the PHOS readout then is the difference in the FEE amplifier due to the chosen dynamic range, the EMCal light yield, and the amplifier shaping time.

3.2.2 Dynamic Range

Based on the expected annual yield of photons and π^0 at high p_t (Fig. 1.4 of Chapter 1), the full scale energy range for an EMCal tower is chosen to be 250 GeV as compared to 80 GeV for PHOS, well beyond the expected maximum photon or π^0 energy. Setting the EMCal full-scale energy range to 250 GeV sets the Least Significant Bit (LSB) on the low gain range to 250 MeV (10-bits) with the corresponding maximum energy on the high gain range at 16 GeV ($\times$16) and least significant bit at 16 MeV.

3.2.3 Light Yield

Another important parameter of the EMCal readout is the light output to the APD per MeV of energy deposit in a tower. The PHOS produces 4.4 photo-electrons/MeV from the APD with gain M=1. The initial estimate for the EMCal from measurements with early prototype lead/scintillator assemblies with photomultiplier readout using cosmic ray muons gave a initial estimate of 2.5 photo-electrons/MeV for APD readout at gain M=1. The shaper gains discussed below and used in the first test beam measurements were based on this result and the assumption of an operational APD gain of M=50. As discussed in Chapter 7, analysis of test beam results indicates an EMCal light yield of 4.4 photo-electrons/MeV, i.e. the same as PHOS.

3.2.4 Shaper Time Constant Optimization

A substantial effort was made for PHOS to investigate alternative shaper designs and shaping times. In the case of PHOS, a primary consideration is optimum performance for measurement of low energy photons, in the region around 1 GeV, of interest for observation of thermal photon radiation from the hot initial phase of the heavy ion collision. With the good intrinsic resolution of $PbWO_4$, care must be taken to minimize the electronics contribution to the noise. This can be done by a judicious choice of the shaping time of the amplifier.
A general noise model of an amplifier reflects all noise sources to the input and represents them in an equivalent representation as Equivalent Noise Charge (ENC) which includes both the amplifier and the detector noise. There are in general 4 noise components:

- Current (or Parallel) noise: Shottky ($2qI_D$) + Shunt resistor thermal + equivalent input current
- Voltage (or Series) noise: $4kTR_S$ thermal + Johnson noise at amplifier input
- 1/f noise
- Pileup noise (negligible for EMCal).

The noise performance of the APD+preamplifier is shown in Fig. 3.3 [3] . These results are for a detector capacitance of $C_D = C_{APD} + C_{in} = 90 + 10 = 100$ pF as for the Hamamatsu S8664-55 APD. These results indicated an electronic noise minimum of about 300 e^- for a shaping time of about 2 μs. The competing consideration of a reasonably good timing measurement motivated a final choice of 1 μs shaping time for PHOS.
Several considerations motivate a much shorter shaping time for the EMCal. First, simulations of central Pb–Pb collisions with HIJING+AliRoot [14] (the ALICE implementation in GEANT3) indicate that the EMCal will be affected by a large slow neutron contribution that has a tail extending for hundreds of ns after the collision. Second, the number of ALTRO samples recorded is dictated by the total shaped pulse width. With the approximately ten times coarser EMCal granularity, the occupancies will be correspondingly higher in EMCal than in PHOS. With the goal to keep the total data volume per RCU similar to PHOS the number of EMCal samples should be reduced to keep the product of (occupancy)$\times$(No. samples) similar. This would argue for a shaping time of about 100 ns. With 100 ns shaping time the voltage noise would dominate such that one would expect a total electronics noise contribution of about

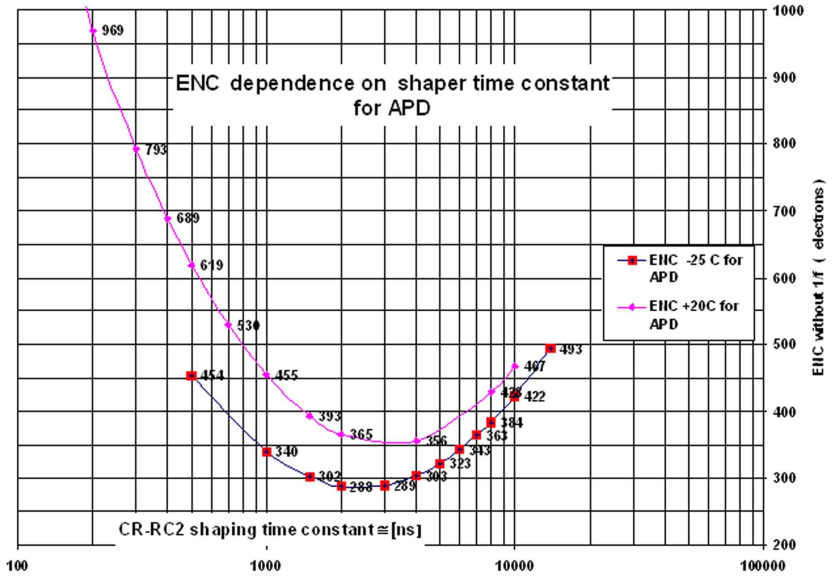

Figure 3.3: Electronic noise as a function of shaping time for PHOS at $-25°$C and EMCal at $+20°$C.

1500 e^- for the PHOS APD+preamplifier+shaper with 100 ns shaper time. This would correspond to an electronics noise contribution of about 12 MeV per EMCal tower. Due to the larger intrinsic energy resolution term of EMCal compared to PHOS (8.5% vs 3.6%) the importance of the electronics noise contribution is much less significant.

3.2.5 Late Neutron Background

Simulations of the EMCal response for central Pb–Pb collisions with HIJING+AliRoot have shown that there is a large background energy deposit predominantly from late neutrons produced in secondary interactions in the surrounding materials of the ALICE experiment [13]. The muon absorber is one of the major sources of this background. As shown in Fig. 3.4 the background has a long tail with arrival times extending for several hundreds of ns after the collision. (Note that this background is generated by the primary central Pb–Pb collision, and hence it is a centrality dependent effect, expected to scale with the multiplicity of produced particles). The result indicates that the shaping time used should be as short as feasible in order to minimize this background contribution to the energy measurement. Without any timing cut, the average background energy deposit in central Pb–Pb collisions is 36 MeV per tower, i.e., several times greater than the expected electronics noise contribution per tower with 100 ns shaping time.

3.2.6 EMCal Energy Resolution Contributions

The relative contributions to the total EMCal energy resolution are shown in Fig. 3.5. The assumptions have been discussed above and relevant parameters are compared to PHOS and summarized in Table 3.2. The intrinsic energy resolution has been assumed to be $6.9\%/\sqrt{E} \oplus 1.4\%$, based on GEANT3 simulations for the production module (see Section 2.2.1). The digitization resolution has been assumed to be determined by a maximum energy scale set to 250 GeV with 10-bits of digitization resolution and dual gain ranges separated by a factor of 16. The constant energy contribution due to calibration errors has been assumed to be 1%. Finally, the electronics noise contribution has been conservatively assumed to be $\sigma_{ENC} = 2000\ e^-$ for an integration time of 100 ns (see Fig. 3.3). With a light yield of 4.4 e^-/MeV, a gain of 30, and 3×3 modules included in the energy sum, this corresponds to an electronics noise

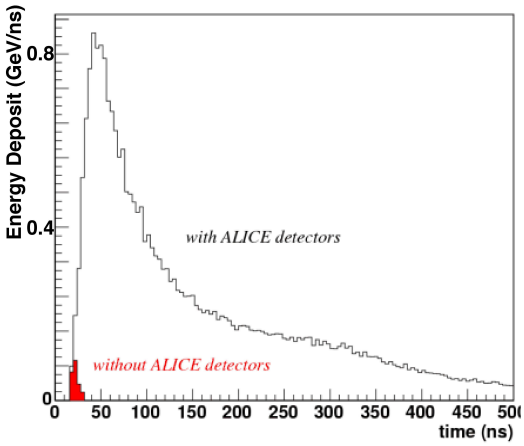

Figure 3.4: Rate of total energy deposit in the EMCal vs arrival time for central Pb–Pb collisions. Results are shown for arrival times greater than 30 ns with and without the other ALICE detectors. The background energy deposit is primarily from late neutron hits and comprises about a third of the total energy deposit.

contribution to the resolution of $c = 48$ MeV/E (Eq. 2.1). This contribution (dotted curve) is seen to be negligible compared to the intrinsic noise contribution (solid dark curve) except at photon energies much below 1 GeV.

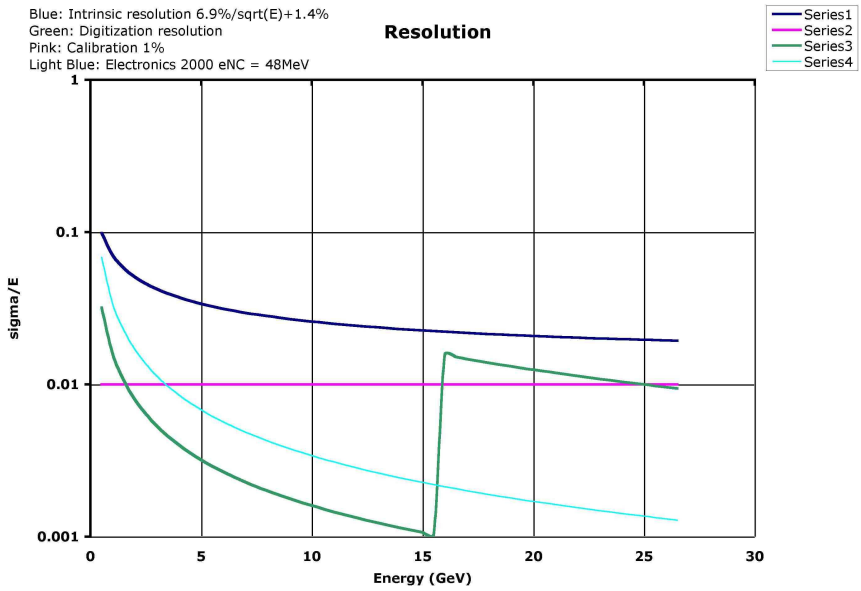

Figure 3.5: Contributions to the total EMCal photon energy resolution. Blue curve: $6.9\%/sqrtE \oplus 1.4\%$ intrinsic contribution, Green curve: digitization contribution, Light blue curve: electronic noise contribution.

3.3 The FEE Shaper

As discussed above, the only modification to the FEE used by PHOS for application to the EMCal readout is to modify the shaper to use a shorter shaping time. The CERN-Wuhan (CW) shaper, developed jointly by CERN and Wuhan, implemented on the FEE card, is shown schematically in Fig. 3.6. The shaper gain for each gain range is chosen such that the maximum CSP voltage (for the chosen APD gain) gives

Table 3.2: Summary of PHOS and EMCal readout parameters.

Quantity	PHOS	EMCal
Digitization Ranges x16 and x1 ranges 10-bits	High Gain: 5 MeV – 5 GeV Low Gain: 80 MeV – 80 GeV LSB=5 MeV	High Gain: 16 MeV – 16 GeV Low Gain: 250 MeV – 250 GeV LSB=16 MeV
Light Yield	4.4 e^-/MeV at M=1 220 e^-/MeV at M=50	4.4 e^-/MeV at M=1 125 e^-/MeV at M=30
Channel rate at E$>$ 30 MeV	$\sim$200 Hz	$\sim$2 kHz
APD	Hamamatsu S8664-55 5×5 mm^2, $C_{APD}=90$pF	Hamamatsu S8664-55 5×5 mm^2, $C_{APD}=90$pF
Charge Sensitive Preamp	JFET:2SK932 $C_{input}=10$pF 0.83mV/fC or 0.136μV/e^-	JFET:2SK932 $C_{input}=10$pF 0.83mV/fC or 0.136μV/e^-
CSP Output range	0.143mV – 2.34V (5 MeV – 80 GeV)	0.267mV – 4.27V (16 MeV – 250 GeV)
ENC	730e^- (3.3 MeV)	$\sim$ 1500e^- (12 MeV)
Shaper	CR-2RC type; Semi-Gauss $\tau_{int}=1$ μs; $\tau_{peak}=2$ μs	CR-2RC type; Semi-Gauss $\tau_{int}=100$ ns; $\tau_{peak}=200$ ns
Trigger signal shaping	FWHM=100 ns	FWHM=100 ns
ADC	ALTRO-16ST; 10-bit LSB$_{noise}<0.5$ mV	ALTRO-16ST; 10-bit LSB$_{noise}<0.5$ mV
Sampling Rate: $1/\Delta t$	10MHz; 15 presamples	10MHz; 15 presamples
Max.Nr. Samples/signal $5\cdot\tau_{peak}/\Delta t$	100+15	10+15
Data rate/Channel	58 kB/s (=200Hz*2*(115 samples)*10-bits)	=125 kB/s (=2kHz*2*(25 samples)*10-bits)
Power consumption	112 FEE*10W = 1.12kW 8 TRU*30W =0.24kW Total 1.36kW/Module (380mW/channel)	36 FEE*10W = 0.36kW 3 TRU*30W =0.09kW Total 0.45kW/SuperModule (390mW/channel)

the fullscale input voltage of the ALTRO ADC chip of 1 Volt maximum input (=1024 bit). Based on a nominal light yield of $4.4e^{-}$/MeV obtained with the PHOS crystals and an APD gain of 50 the following two gain ranges and gain values were implemented for PHOS:

High gain: 5 MeV – 5.12 GeV: V_{CSP} = 1.37 mV – 0.14 V: Shaper gain = 6.9

Low gain: 80 MeV – 81.9 GeV: V_{CSP} = 2.19 mV – 2.34 V: Shaper gain = 0.43

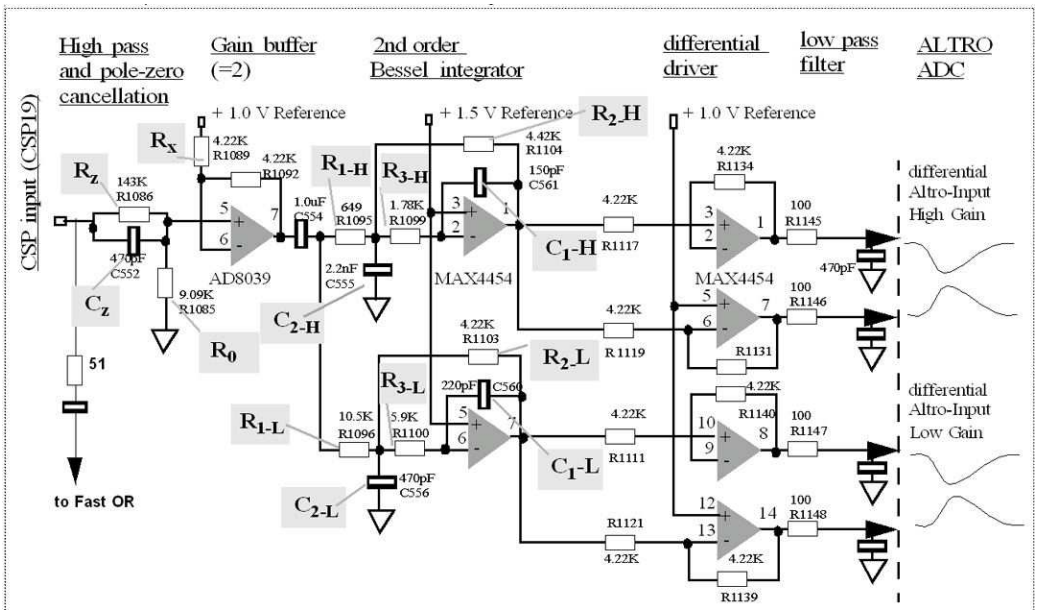

Figure 3.6: Schematic diagram of the shaper of the PHOS/EMCal FEE.

The CW shaper was developed for optimal noise performance with successive RC differentiator and dual Bessel integrator stages of common cutoff frequency and with gain ratio of 16 for low energy and high energy ranges. The RC differentiator is combined with a pole-zero cancellation, tuned for the CSP. The output stage to the ALTRO ADC is fully symmetrical and contains a high frequency RC noise filter.
Table 3.3 shows the results obtained with the Bessel calculation described in detail in Ref. [3] for the CW shaper RC components of 1 μs (PHOS) and 100 ns (EMCal) shaping times and gain ratio 1/16. R_Z has been determined empirically as the best non-overshoot value of the pole zero cancellation. For a change in the bandpass frequency (or shaping time) of the shaper, R_0 must be adjusted to correspond with C_Z to the new bandpass value (i.e., $\tau_{peak} = C_Z R$ where $1/R = 1/R_Z + 1/R_0$). All other values R_1,R_2,R_3,C_1, and C_2 can be calculated with the method described. The results for the 1 μs shaping time were calculated for the desired PHOS maximum signal of 1 Volt to the ALTRO input for 2.34V maximum preamplifier signal output corresponding to a low range gain value of 1/2.34=0.42 ($\times$16 gain range gain = 6.81) . The values for the 100 ns shaping time have been calculated for the 4V maximum preamplifier output for the EMCal (see Table 3.3) corresponding to gains of 1V/4.27V = 0.234 ($\times$1) and 3.75 ($\times$16) for the two gain ranges.
The first prototypes of the PHOS FEE electronics board (version v1.0) were produced in fall 2004 with second prototypes (version v1.1) produced in spring 2005. A photograph of the FEE card is shown in Fig. 3.7. The production of 130 PHOS FEE cards (sufficient to read out the first PHOS module of 3584 crystals) took place in December 2005, and first prototypes of the EMCal FEE (version v1.1e) were produced in spring 2007.
The test beam measurements with the EMCal prototypes described in Chapter 7 were performed with one FEE v1.0 card with the 1 μs shaping time used for PHOS, and a second FEE v1.0 card with 100 ns shaping time as planned for the EMCal, during the tests at the meson test beam at FNAL in 2005, The

Table 3.3: RC values for the CERN-Wuhan shaper with 2 μs, and 200 ns shaping times, peaking time $\tau_{peak} = 2\tau_0$ (buffer gain = 2, gain ratio =16).

τ_0	Gain	C_Z, R_Z	R_0	R_1	R_2	R_3	C_1	C_2
1 μs	2×3.35	470 pF,143 kΩ	4.22 kΩ	681 Ω	4.87 kΩ	1.96 kΩ	68 pF	1000 pF
1 μs	2×0.21	470 pF,143 kΩ	4.22 kΩ	4.02 kΩ	1.69 kΩ	5.36 kΩ	150 pF	470 pF
100 ns	2×2.00	470 pF,143 kΩ	213 Ω	78.7 Ω	316 Ω	205 Ω	100 pF	1000 pF
100 ns	2×0.125	470 pF,143 kΩ	213 Ω	590 Ω	147 Ω	442 Ω	220 pF	470 pF

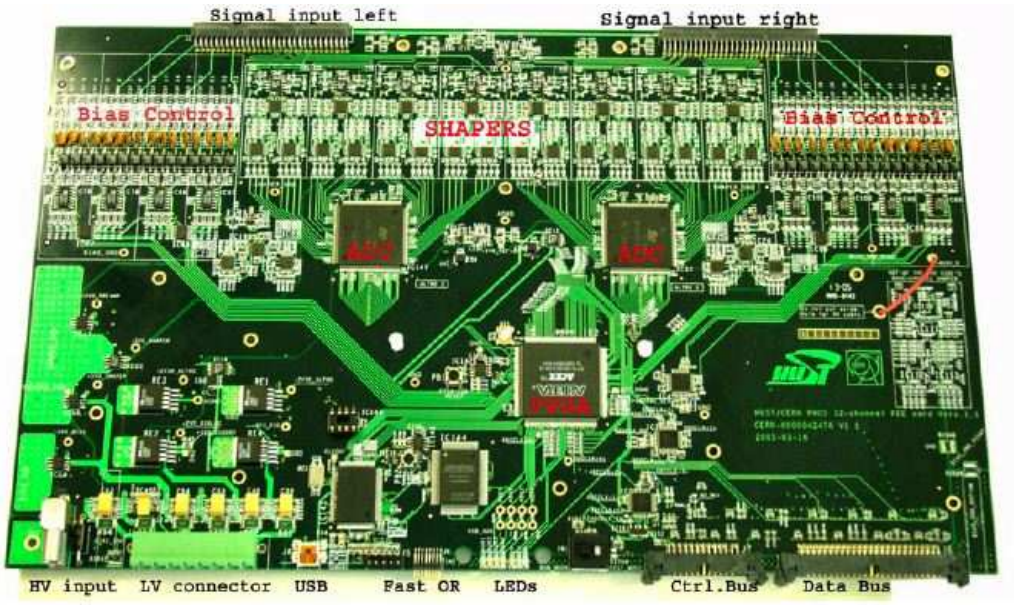

Figure 3.7: Photograph of the 32 channel PHOS/EMCal FEE card.

test beam measurements carried out at CERN in 2007 were performed with prototype EMCal FEE cards (FEE version v1.1e).

3.4 The EMCal Trigger

As described in Section 3.1.3 the PHOS readout includes a Trigger Region Unit card (TRU) [11] on each GTL readout bus that provides sliding 4×4 tower sums for generation of a Level-0 and three Level-1 triggers with programmable thresholds for simultaneous low, mid, and high energy shower trigger outputs. All of the trigger outputs generated locally from each TRU are logically ORed and input to the ALICE Central Trigger Processor. The PHOS trigger was designed to trigger efficiently on photons and can serve that purpose equally well for the EMCal. The PHOS TRU will be used for the EMCal with only minor modifications. First, because the EMCal input connections to the FEE cards do not have exactly the same geometrical mapping as for PHOS, the TRU FPGA code will need to be modified to take into account the different tower mapping of PHOS and the EMCal.
The PHOS TRU single shower trigger provides a good leading photon, or leading π^0 trigger that also triggers efficiently on high energy jets. However, because a single shower trigger will have a bias towards jets including a leading π^0, it is of interest to have the capability to trigger on larger regions of EMCal towers. For this purpose a Summary Trigger Unit (STU) that will take input from the TRU modules and

perform energy sums over larger regions of the EMCal is being built. The PHOS TRU has been upgraded for EMCal for this purpose to provide raw trigger sum output that can be input to the STU to form trigger sums over large jet-like regions of EMCal that cross TRU boundaries, and to provide improved single shower 4×4 tower sums that cross TRU boundaries. The TRU modifications for EMCal and the STU module are described in more detail in Chapter 5.

3.5 EMCal FEE Readout Mechanics

In the EMCal assembly four towers with APDs and preamplifiers are integrated into one mechanical-electronic EMCal unit, a so-called EMCal module. The ends of the fiber bundles, light guides, and APDs with preamplifiers are secured in a compact matrix unit on the back of the module. As part of the construction of an EMCal super module, 12 EMCal modules will be assembled onto a support backbone to provide one strip module. Twenty-four strip modules are stacked together in Z to comprise a super module. An EMCal transition card (T-card), located within the strip module, connects APD+preamplifiers of a group of 2×8 towers from a group of four modules adjacent in ϕ. The T-card is connected to the FEE via a 60-pin shielded ribbon cable. The mapping of the EMCal towers to FEE input channels will be accommodated on the T-card to preserve the geometrical grouping of 2×2 adjacent towers used to form the analog trigger sum primitives in the FEE.

3.5.1 EMCal Readout Crate

Owing to radial space restrictions for the EMCal, it is not possible to locate the EMCal FEE directly behind (radially) the EMCal, as is the case for PHOS. Instead, the EMCal FEE crates, with associated FEE and TRU boards, and GTL bus and RCUs, will be located at the outer end (large Z) of each EMCal super module, as shown in Fig. 3.8.

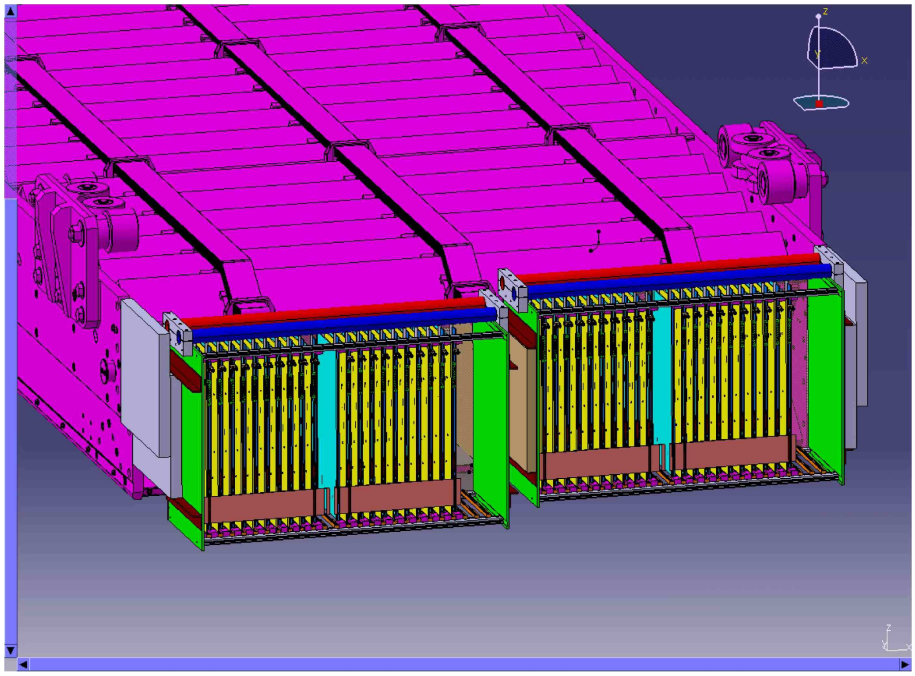

Figure 3.8: The arrangement of the two FEE crates mounted at the end of the EMCal super module. (Note that in Fig. 2.18 three FEE crate enclosures are shown at the end of each super module.)

A super module consists of $24 \times 48(\phi \times Z)$ EMCal towers with each FEE card connected to $8 \times 4(\phi \times Z)$ towers. Thus each full super module is read out by 36 FEE cards with two RCUs logically arranged as

shown in Fig. 3.9. Each RCU is connected to two GTL buses with 10 logical addresses for connection to either a FEE card or TRU card. Nine FEE cards are readout with each GTL bus and 3 TRU boards are installed on 3 of the 4 GTL buses. The extra GTL bus location is used for an extra FEE board that is used to readout the photodiodes that monitor the LED output of the LED monitoring system (see Section 3.6).

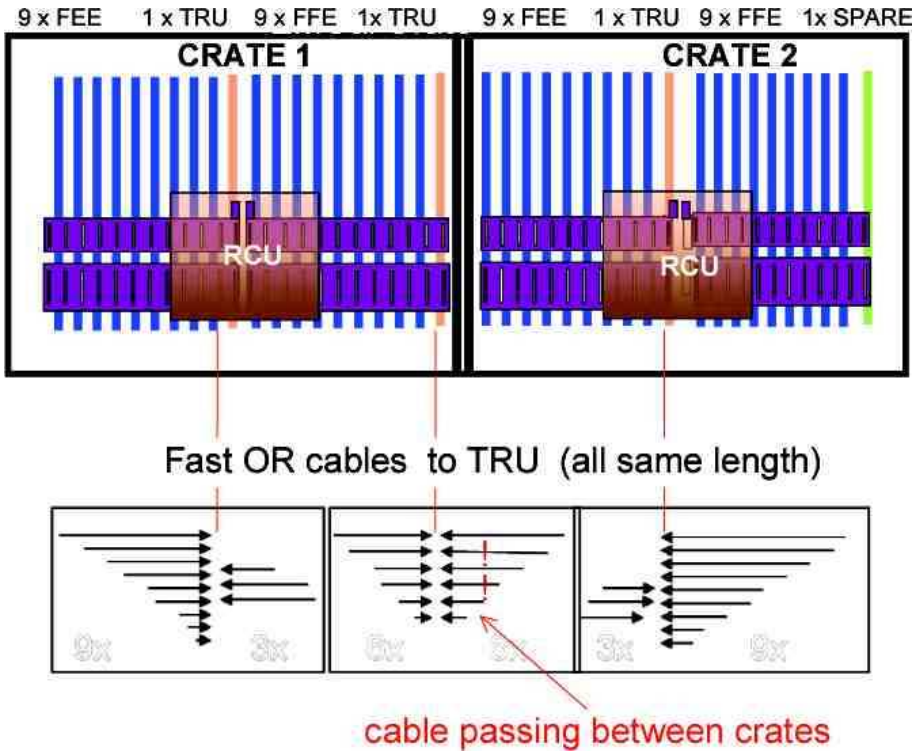

Figure 3.9: The arrangement of the EMCal readout electronics within the FEE crates.)

Physically, each RCU and GTL bus pair with FEE and TRU boards, is located within it's own mechanical crate. Figure 3.10 shows the arrangement of the two FEE crates attached to the end of the super module. The power dissipation per channel of embeded FEE/TRU electronics is 390 mW/channel. This gives an expected power dissipation of 450kW per super module. This heat is removed by a manifold of copper radiator plates connected to the ALICE negative pressure water cooling system (see Fig. 3.10).

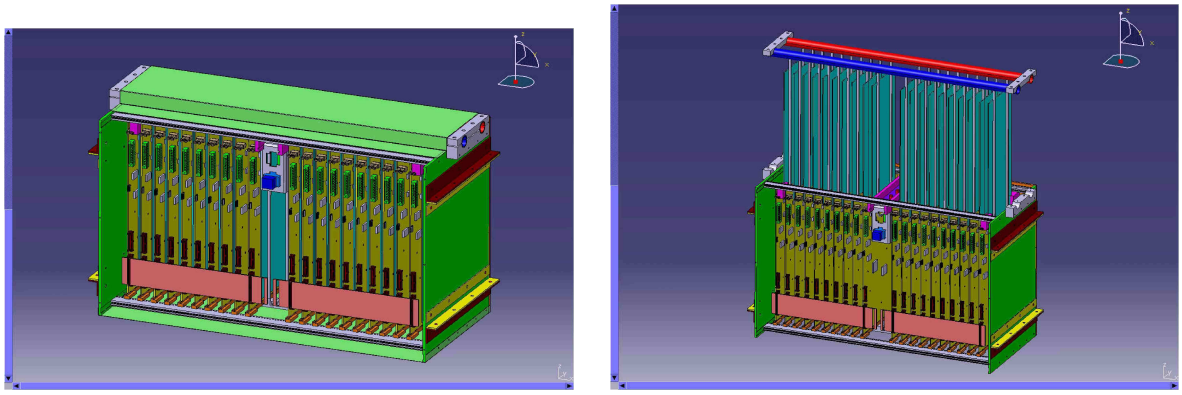

Figure 3.10: The mechanical details of EMCal readout crate. Right: With cooling manifold raised.

3.6 LED Calibration System

A LED calibration system will be incorporated into the EMCal detector in order to monitor and adjust the APD gains. A preliminary version of a LED system was incorporated in the first prototype modules used in the first test beam measurements performed at FNAL described in Chapter 7. In that system, a UV LED (part no. E7113UVC by eLED) was mounted in a small hole in the back enclosure of each module and irradiated a small piece of plastic scintillator that extended into the region of each tower where the WLS fibers were brought together to attach to the lightguide and APD. The scintillation light excited the WLS to provide the calibration signal. Although this system worked adequately for the purposes of the test beam measurements, the light yield was barely adequate, especially for the short shaping times intended to be used for the EMCal readout. Also, the close proximity of the LED to the APD and preamplifier resulted in electronic pickup in the APD+preamplifier from the large amplitude fast pulse necessary to pulse the LED. The electronic pickup was especially problematic for the short shaping time. As a result of these observations, the LED monitoring system was revised with the LEDs located outside of the EMCal super module and the LED light brought to the EMCal modules via light fibers, as illustrated in Fig. 3.11. The LED light is transported to each strip module via a 3 mm light fiber, where it is split in a fiber bundle (12×0.5 mm) with one fiber brought to each module of the strip module. A small diffusor sheet located at the center of the module, between the four towers, reflects the LED light up towards the WLS bundle of each tower. The 0.5 mm fibers are routed through a 1 mm diameter Al tube which has the same shape for all modules, assuring a uniform light source for all 48 towers of one strip module.
For the LED drivers, an avalanche pulser system has been used to provide ultra-bright LED light pulses of a few ns duration [3, 15]. Such fast ultra-bright LED sources have been used already for investigation of the timing characteristics of the PHOS/EMCal electronics [3] and will be used for the APD tests described in Section 6.2.

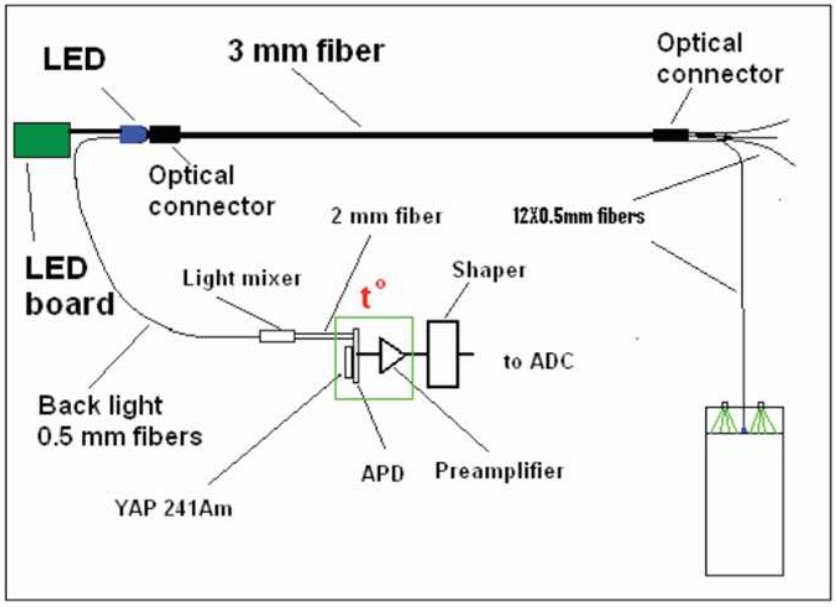

Figure 3.11: Scheme adopted for EMCal gain monitoring system. Note that the LED monitoring fiber will be viewed by a unit gain photodiode, without radioactive source. The photodiode will be readout through the EMCal FEE.

The LED pulser and light distribution system shown in Fig. 3.11 was implemented for the prototype EMCal modules used in the 2007 beam tests at CERN, described in Chapter 7. The prototype LED

system with planned fiber distribution scheme was confirmed in the test beam measurements to provide sufficient light per tower (about 30 GeVequivalent) for the EMCal requirements. Analysis of the beam test data has demonstrated the feasibility of this method, confirming the expected anti-correlation of gain with temperature (Fig. 3.12).

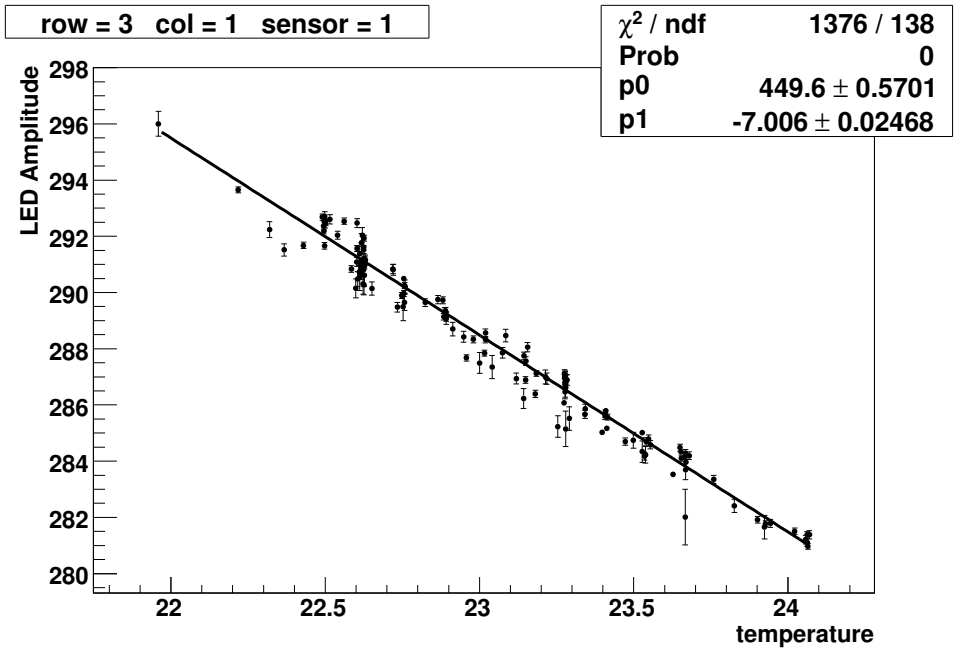

Figure 3.12: Measured LED peak amplitude versus temperature for a typical tower.

To avoid electrical pickup from the LED trigger pulse it is planned to place 8 LED drivers with LED trigger fan-out in a copper box as shown Fig. 3.13 with 3 boxes installed in the gap between two FEE crates (see SM electronic description in Section 3.5). A prototype has been tested showing good performance concerning the light output and the electronic isolation. Moreover, there is the possibility to add an additional cable delay to each channel within the box in order to have the same time of arrival of the light into the different modules, compensating for the different light fiber lengths from the distribution box to the modules. The possibility to construct new 8 or 12 channel boards with exactly the same functionality of the prototypes is under study. To have more flexibility inside the box, bundles of seven 1 mm light fibers will be used from the optical connector, where the LED is inserted, to the outside, where they will be glued to a 3 mm light fiber.
The stability of the light sent to the modules has to be monitored independently. For this reason the back light from the LED, collected by a 0.5 mm light fiber, will be measured by a photodiode that will be readout with an additional FEE card located in the extra position of the GTL bus without TRU card.

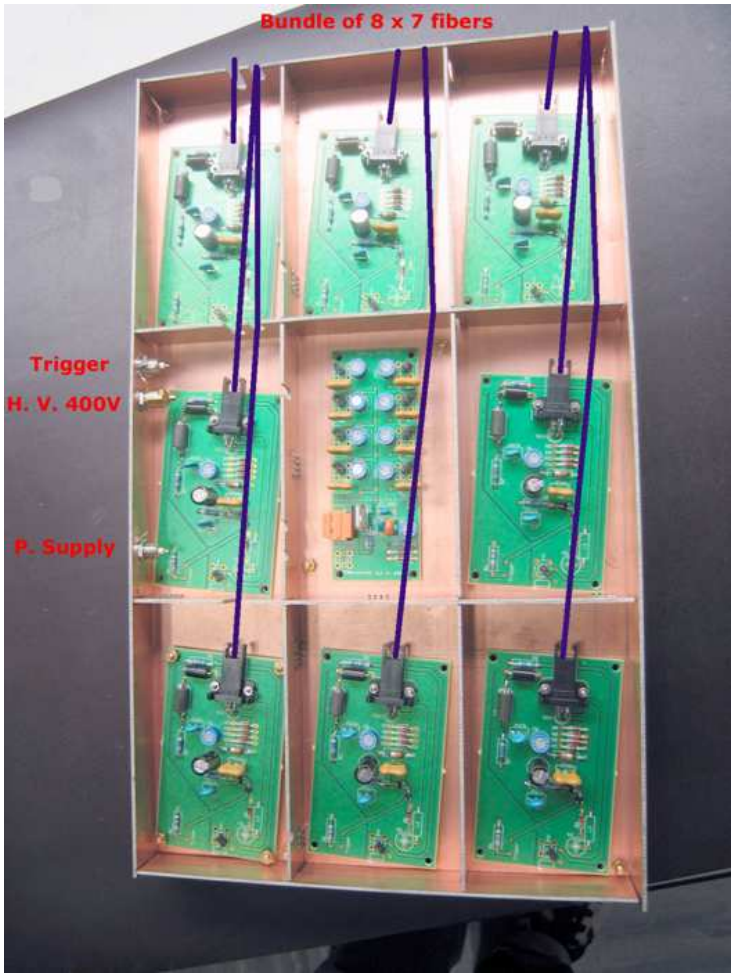

Figure 3.13: Copper box with 8 LED drivers.

4 Data Acquisition and Online

4.1 Requirements

The ALICE experimental program incorporates a wide variety of running conditions: heavy-ion collisions, p–p p-A, and lighter ion collisions. The heavy-ion run will last only a few weeks per year but this run will require the largest possible bandwidth to permanent storage. A large number of trigger classes will be used concurrently to select and characterize events relevant to studies of several physics topics. The rest of the running period will be used to acquire data produced by p–p interactions which generate five times less data. The selection of events in the ALICE experiment is performed by two trigger systems. The Central Trigger Processor (CTP) [1] is hardware-based and is always present as it delivers the trigger levels 0, 1, and 2. The High Level Trigger (HLT) [2] is software-based. Several running modes have been defined to permit its gradual activation. The ALICE Data Acquisition (DAQ) system is designed to be flexible enough to address this diversity of running conditions and of running modes.
The ALICE EMCAL readout uses the same components as the PHOS subsystem of ALICE and thus all needed parts of the readout chain have already been integrated into the ALICE data acquisition system.

4.2 DAQ Architecture Overview

The architecture of the ALICE Data Acquisition and its interface with the Trigger and the High Level Trigger are illustrated in Fig. 4.1 and detailed in the ALICE Technical Design Report on Trigger, Data Acquisition, High Level Trigger, and Control System [2].
The EMCal detector receives the trigger signals and the associated information from the CTP, through a dedicated Local Trigger Unit (LTU) [3] interfaced to a Timing, Trigger and Control (TTC) system [4]. The Front End Read Out (FERO) electronics of the EMCal is interfaced to the ALICE Detector Data Links (DDLs). The data produced by the EMCal (event fragments) are injected into the DDLs using a common protocol.
At the receiving side of the DDLs there are PCI-based electronic modules, called DAQ Readout Receiver Cards (D-RORCs). The D-RORCs are hosted by the front-end machines (commodity PCs), called Local Data Concentrators (LDCs). Each LDC can handle one or more D-RORCs. The event fragments originated by the various D-RORCs are logically assembled into sub-events in the LDCs.
The CTP receives a busy signal from each detector. This signal can be generated either in the detector electronics or from all the D-RORCs of a detector. The CTP also receives a signal from the DAQ enabling or disabling the most common triggers. It is used to increase the acceptance of rare triggers by reducing the detector dead-time. This signal is a function of the buffer occupancy in all the LDCs.
The role of the LDCs is to ship the sub-events to a farm of machines (also commodity PCs) called Global Data Collectors (GDCs), where the whole event is built (from all the sub-events pertaining to the same trigger). The GDCs also feed the Transient Data Storage (TDS) with the events that eventually end up in Permanent Data Storage (PDS). The PDS is managed by the CERN Advanced Storage Manager (CASTOR) [5].
All these hardware elements are driven and controlled by the Data Acquisition and Test Environment (DATE) software framework [6] developed by the ALICE DAQ project. The coherence of the whole system is ensured by this common software framework composed of different layers of modules. A bottom layer includes the memory handling, the process synchronization, and the communication modules. The application layer includes the data-flow applications (detector readout, event building, and data recording). DATE has been used for a number of years by many ALICE test beam users. The EMCal test

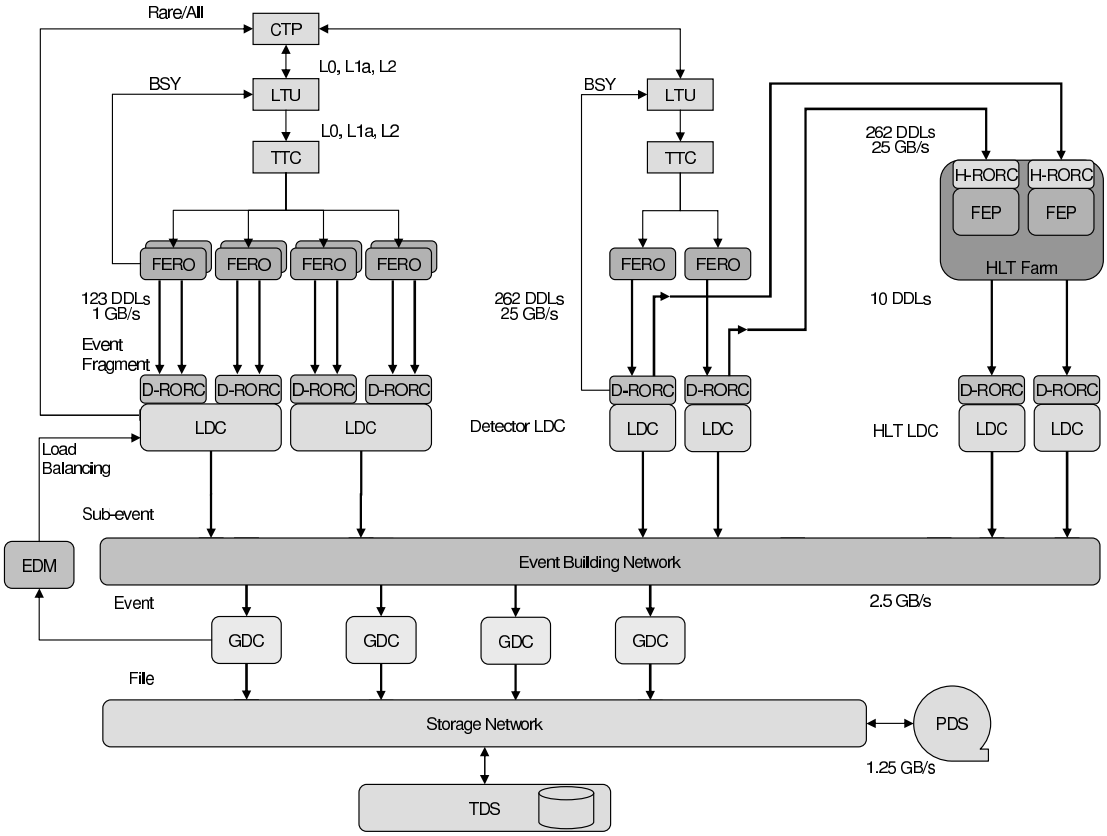

Figure 4.1: DAQ architecture overview.

beam measurements described below were realized using a completely integrated readout system with the DDL and the DATE software.
The HLT system receives a copy of all the raw data. The data and decisions generated by HLT are transferred to dedicated LDCs.

4.3 DAQ-High Level Trigger Interface

The overall architecture of the Trigger, DAQ, and HLT systems is illustrated in Fig. 4.1. The DAQ system takes care of the data flow from the DDL up to the storage of data on the PDS system. The task of the HLT system is to select the most relevant data from the large input stream and to reduce the data volume by well over an order of magnitude in order to fit the available storage bandwidth, while preserving the physics information of interest. This is achieved by a combination of event selection (triggering), data compression, or selection of Regions of Interest with partial detector readout. While executing either of these tasks, the HLT may also generate data to be attached to or partially replacing the original event. Care has been taken not to impose any architectural constraints which could compromise the HLT filtering efficiency, knowing that event selection will become more and more elaborate during the experiment lifetime. This way, filtering may be introduced in progressively more sophisticated steps without affecting the performance and the stability of the Data-Acquisition system.
The DAQ-HLT interface is based on the DDL and its DIU/SIU cards, the same components used to transfer data from the detector electronics to the DAQ system. The choice of existing components as interface between the two systems minimized the need for new R&D and avoided the development of a new type of link. Past experience shows that at the experiment startup the DAQ and HLT problems are of different nature and essentially independent. There is no benefit from not keeping them so. Therefore,

the DAQ system is implemented within a coherent hardware and software framework, with the HLT system operating as an external system [7], as shown in Fig. 4.2

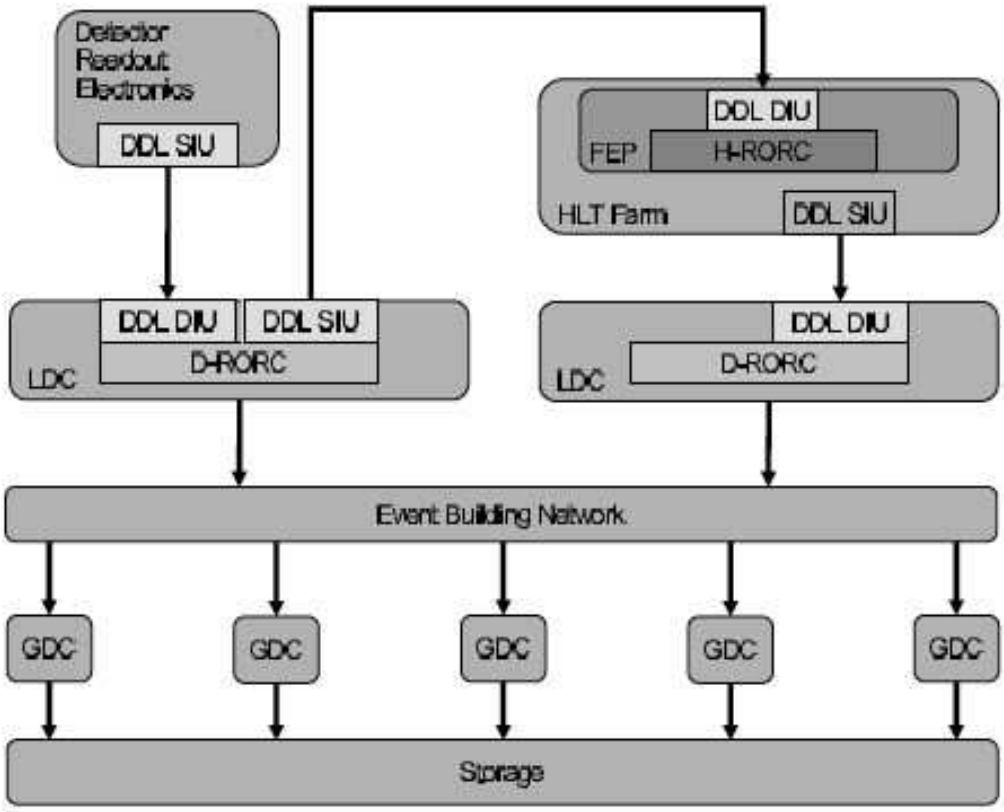

Figure 4.2: DAQ-HLT data flow overview.

Every D-RORC sitting in the LDC can host two DIUs. These on-board DIUs can be used in two ways: both can be connected to the front-end electronics and serve as two readout links, or one DIU can be connected to the front-end electronics while the other is able to transfer a copy of all the raw data to the HLT RORC (H-RORC) sitting in the HLT computers, through the standard DDL. The H-RORC receives all the raw data as they have been received from the front-end electronics. All the LDCs dedicated to the detectors which make use of the HLT system are equipped with D-RORCs working in the second mode. The interface between the DAQ and the HLT system is the DIU output on the H-RORC. The selected interface offers as much physics-selection flexibility as possible, since the H-RORC is granted full access to the sub-event and all the raw data are given to the HLT processors. Data will then be available in the HLT farm computers for pre-processing or co-processing in the H-RORC FPGA. The HLT computers will run the HLT algorithms and will transfer the result of the processing, the trigger decisions, and the compressed data to the DAQ system, using again standard DDLs. Using this scheme, the HLT system looks like any other sub-detector for the DAQ. The GDCs will receive the sub-events from the sub-detectors LDCs and any additional data generated by the HLT computers from the LDCs dedicated to the HLT. The DATE software is ready to accept as many data channels from the LDCs dedicated to the HLT as required, since it handles these channels as additional LDC data paths.
The HLT LDCs will also receive messages specifying whether to discard or accept a given event. Furthermore, for accepted events, the HLT decision can specify the pattern of sources for a given event, resulting in a partial readout of the raw data. A decision broker process, running in the HLT LDCs, will transfer the HLT information and decision to a decision agent process, running in the detector LDCs, as

shown in Fig. 4.3.

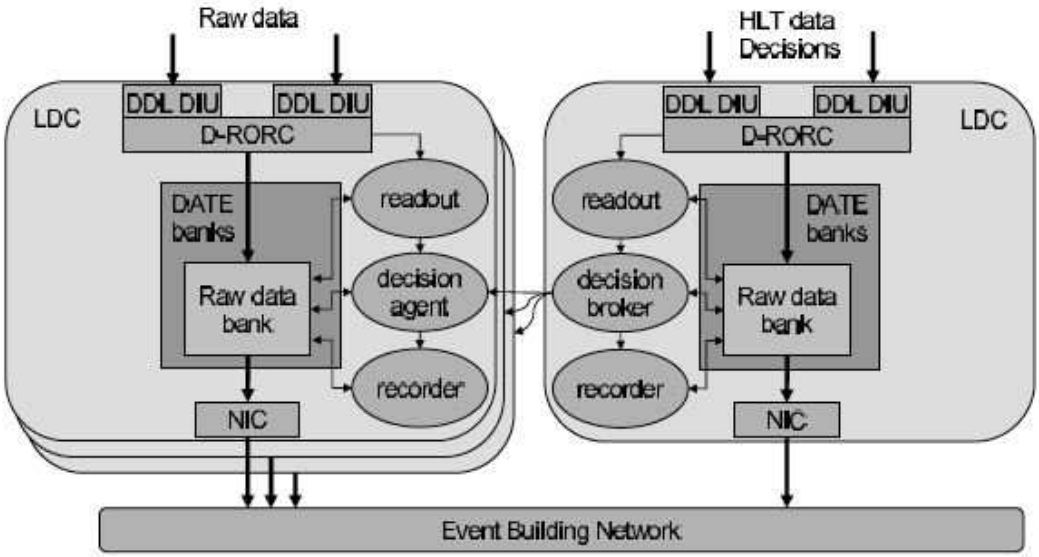

Figure 4.3: HLT decision into LDC to control data flow to DAQ.

4.4 Data Volume and Bandwidth

The ALICE EMCAL, as described in earlier chapters, consists of 1152 towers per super module (SM). Each tower has both a high and a low gain readout channel. The EMCal is configured with two readout crates for each SM. Two Readout Control Units, each with a DDL connection to a LDC will be used to readout each crate (one RCU services two GTL branches). Each GTL branch will transfer 9 Front-End Cards for a total of $32 \times 2 \times 9 = 576$ channels (288 towers) of 10-bit data. There are 10 SM + 2 one-third-size SM planned for the full EMCAL for a combined total of 24576 readout channels (12288 towers).

The data volume per channel is a function of how many ADC time-samples are read out from the ALTRO chip. With the 100 ns shaping planned for the EMCal shaper (see Section 3.3) and a 10 MHz sampling frequency, about 10 samples would adequately sample the peak. Up to 15 additional pre-samples may be taken for event-by-event pedestal measurement. Therefore 25 samples would be taken for each of the two shaper gain channels (see Section 3.3). Each sample is a 10-bit ADC word, and the data is formatted into 40-bit words in the ALTRO chip.

The granularity of the EMCal is about 10 times coarser than the PHOS with the result that the EMCal occupancy and tower hit rates are about 10 times larger than PHOS. The tower hit rate for the full 8 kHz min bias Pb–Pb collision rate from HIJING simulations is estimated to be 2000 Hz. This would correspond to a maximum data transfer rate of $2000 \times 2 \times 25 \times 10/8(\text{Bytes}) = 125$ kBytes/s/tower, or 36 MBytes/s/GTL with zero suppression (see Table 3.2). This is below the DDL data transfer limit of 200 MBytes/s allowing the EMCal to operate without deadtime at the full Pb–Pb min bias trigger rate. The data volume for readout of the full EMCal would be $(2 \text{ gain ranges}) \times (12288 \text{ towers}) \times (25 \text{ samples}) \times 10/8(\text{Bytes}) = 768$ kBytes per event. The 2 kHz tower hit rate corresponds to a 40 % average EMCal occupancy for Pb–Pb collisions at 8 kHz. The corresponding EMCal average total event size would be ~ 300 kBytes per event. This is much smaller than the 75.9 MBytes size of the average TPC event (Table 7.1 of Ref. [2]).

4.5 EMCal Detector Slow Control

The ALICE control system is responsible for configuring, monitoring and controlling the equipment of the experiment. This can be hardware devices such as power supplies, crates, but also more sub-detector specific equipment such as front-end chips, etc. It will also cover computing devices (such as PCs and PLCs) and the software processes running on them. This task is mainly accomplished by sending commands and settings to the equipment and reading information back from the equipment. The control system is designed to take pre-programmed decisions and automatic actions (without operator intervention) such as recovering from errors. The operator will be able to interact with the control system through user interfaces that will present the information from the system and allow issuing of commands. All information concerning any part of the equipment is stored in a configuration database. This information ranges from the physical location of the equipment, hardware addresses, to operational settings (that can be different for the various running modes). Also here the information is not only restricted to hardware but will also cover processes running on PCs, etc.
The ALICE online systems, namely, the Detector Control System (DCS), the Data Acquisition system, the Trigger system (TRG), and the High Level Trigger system (HLT) interface to each other through a controls layer, the so-called Experiment Control System (ECS), shown in Fig. 4.4.

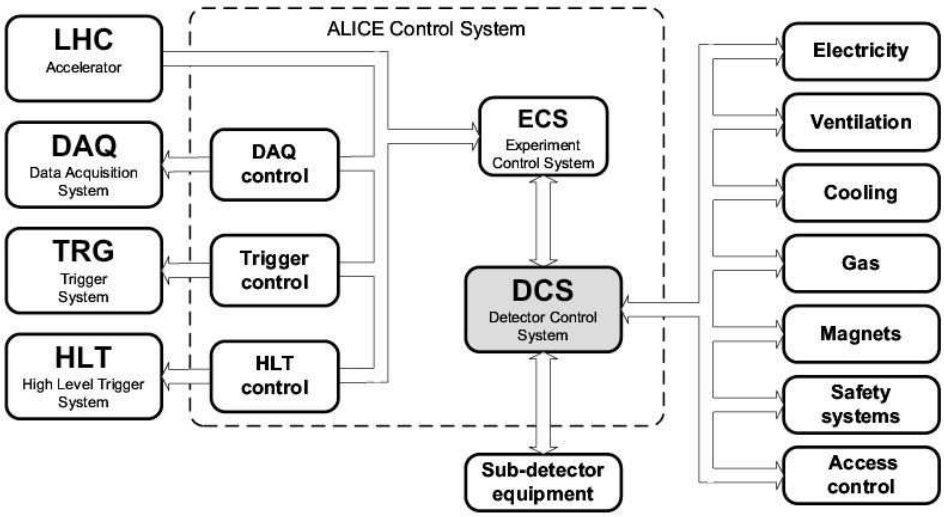

Figure 4.4: The ALICE online control systems.

The core software of the control system [2] is a commercial SCADA(Supervisory Controls And Data Acquisition) system called PVSSII. It will be used to connect to hardware (or software) devices, acquire the data they produce and use it for their supervision, i.e., to monitor their behavior and to initialize, configure and operate them. PVSSII has its own proprietary run-time database which is used to store the values that are read from the devices, information on the configuration of PVSSII itself and any information that is needed for the operation of the PVSSII system. This database is optimized for fast access, as it is an essential part in the operation of the PVSSII system. Data archiving is an integral part of PVSSII and is the mechanism to store the history of any data available in the system that the user decides to archive. The PVSSII archiving managers provide an efficient mechanism for storing, accessing, and manipulating historical data acquired by the control system. Alarms can be generated by defining conditions applying to new data arriving in PVSSII. The alarms are stored in an alarm database and can be selectively displayed by an alarm display. Alarms can be filtered, summarized, etc.
The EMCal detector control will be implemented within the ALICE PVSSII environment. The detector control system for the electromagnetic calorimeter consists of seven subsystems and a user interface. The low voltage, high voltage, and temperature monitoring control systems were validated during the

Fall 2007 CERN test beam.
Low voltages for the front end electronics cards are controlled by means of an OPC server for the Wiener PS 512 supply. The server communicates with the supply over CANbus.
The ISEG high voltage supply for APD bias is controlled using an OPC server written for the ALICE experiment. The server communicates with the supply over CANbus.
Individual APD HV bias demand values are controlled using software for the RCU adapted from software developed jointly by the ALICE PHOS and EMCal. The subsystem uses a DIM server and client communicating over Ethernet.
Temperature and voltage readback values on FEE cards are also accessed through the RCU using software based on that used by PHOS. The RCU board controls will also set and monitor ALTRO chip parameters (sampling frequency, number of samples, zero suppression thresholds, etc.) and the L0 and L1 trigger thresholds and masks. The subsystem uses a DIM server and client communicating over Ethernet.
Temperature sensors throughout the EMCal detector region are monitored using an ELMB and the related CERN framework software. The ELMBs are accessed using an OPC server communicating with the device over CANbus.
Development of the LED pulser software is expected to follow that used on a similar system for PHOS.
EMCal cooling water temperature and control are part of a system shared with PHOS, TOF, and CPV. It is monitored using the CERN framework software as implemented at ALICE. A software interlock for the cooling system to the low voltage supply will be implemented. Two pressure sensors will be used to monitor the system in case of leaks. The cooling system is controlled by a DIM server that is accessed by Ethernet.

5 Trigger

5.1 Physics Requirements and Design Overview

Full exploitation of the LHC luminosity delivered to ALICE requires fast triggers at Level-0 and Level-1 (denoted L0 and L1 below) that are both efficient for the signals of interest, and have sufficient rejection of background to meet the ALICE recording bandwidth requirements. ALICE will measure a wide range of collision systems (p–p to Pb–Pb), with widely varying physics environments. The trigger system must consequently be very flexible in order to accommodate the wide variation in interaction rates and complexity of backgrounds.
The EMCal will measure high p_{t} photons, electrons, and jets, and optimized triggers must be developed for all collision systems for each of these signals. The overall trigger strategy is to provide the minimum necessary rejection at L0/L1 with as many events as possible transferred to the High Level Trigger (HLT) (see Section 4.3). The full event information from all ALICE subsystems is available in the HLT, where event analysis with a precision approaching that of offline analysis can be carried out, and optimal decisions made about event rejection.
The rejection requirement at L0/L1 is driven for all collision systems by the maximum gating rate of the ALICE TPC ($\sim$ 500 Hz), whereas the total rejection (including HLT rejection) for some collision systems is determined by the HLT and DAQ throughput of about 1.5 GBytes/s. We estimate that the L1 rejection required for Pb–Pb collisions is 10-20, to reduce the data rate to the HLT to manageable levels. For lighter systems, the data volume per event is small enough that all TPC-triggered events can be written to tape. Consequently, rejection at the HLT level is ineffective and the entire rejection, corresponding to a factor 3000 for p–p. needs to be performed at Level 0/1.

5.1.1 Trigger Design Overview

5.1.1.1 Photon/Electron Trigger

The EMCal L0/L1 trigger for photons and electrons is provided by functionality already present in the PHOS Front End Electronics (FEE), which has been adopted without significant modification for the EMCal. The FEE generates fast analog 2×2 tower sums which are then summed in the FPGA of the Trigger Region Unit (TRU) into 4×4 regions for high energy shower trigger decisions at L1.
For p–p collisions, the ALICE interaction trigger will potentially be biased. Consequently, the EMCal - like the PHOS - will provide trigger input at L0 for p–p using a low threshold in order to record all events with EMCal activity (electrons and photons) without bias of other trigger detectors. Details of the L0 trigger are given below.

5.1.1.2 Jet Trigger

The EMCal L1 jet trigger requires additional considerations. As shown by the recent STAR measurement of jets in heavy ion collisions at RHIC, a PHOS-type tower cluster trigger for jets (which is effectively a hard π^0 trigger) generates significant trigger bias; while leading-particle jet trigger bias is known to be present in p–p collisions, its effects are evidently exacerbated by jet quenching in heavy ion collisions. Consequently, unbiased recording of rare, high E_T jets by the EMCal requires a specialized jet trigger designed to integrate energy over a large phase space area (denoted “jet patch” in the following), in order to measure a significant fraction of the jet energy as input to the L1 trigger decision.
The jet patch size is expected be about $\Delta\eta \times \Delta\phi \sim 0.3 \times 0.3$. However, optimization of this area requires

a compromise between suppression of background from the underlying event, which prefers small patch area for better signal/noise, and integration of a large fraction of the jet energy, which prefers larger patch area. Jet quenching at the LHC may generate significant broadening of jets in heavy ions relative to p–p collisions, but little is known about this issue at present and data are required to answer it. Consequently, the EMCal jet patch trigger design must be very flexible, with its optimal configuration established only after the first set of LHC heavy ion data has been analyzed.
The EMCal TRU (see Fig. 5.1) reads out 384 towers, corresponding to a fixed phase space area of $\Delta\eta \times \Delta\phi \sim 0.7 \times 0.1$. Its small phase space coverage in ϕ and fixed boundaries are not suitable for a jet trigger. Section 5.2.1 describes the Jet Trigger electronics which transports signals from the entire EMCal into a single FPGA, providing the most flexibility design for an optimized Jet Patch Trigger.

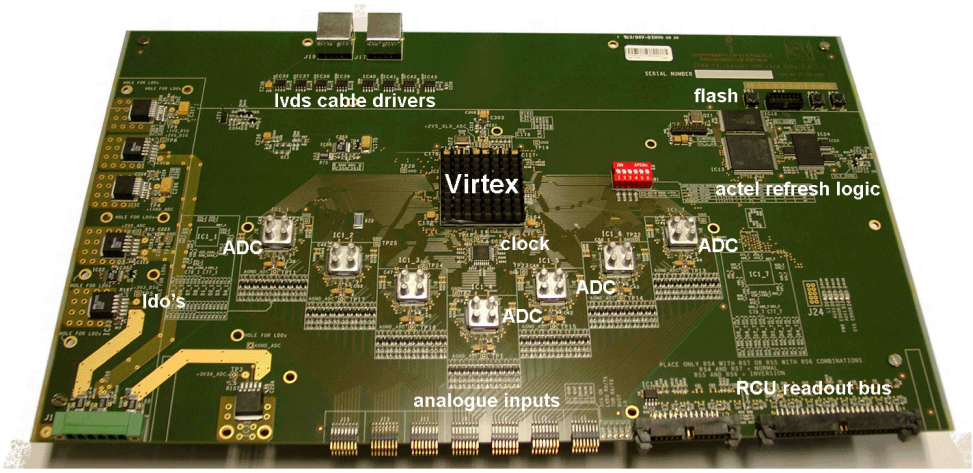

Figure 5.1: The EMCal TRU.

Additional complexity for triggering on jets in heavy ion collisions arises from the wide dynamic range of background energy density from the underlying event: the most peripheral Pb–Pb collisions at $\sqrt{s_{NN}} =$ 200 GeVhave backgrounds similar to p–p collisions, whereas the most central collisions have about 500 GeVof background energy in an area $R = \sqrt{\Delta\eta^2 + \Delta\phi^2} \sim 0.7$. From the standpoint of the L1 Jet Patch trigger, this background forms a fluctuating pedestal underneath the jet signal. A fixed trigger threshold with value set to discriminate jets from background in central collisions would therefore have negligible efficiency for the jet signal in more peripheral events. Section 5.2.1 also describes the solution to this problem, in which the signal with multiplicity information from a forward detector in ALICE (V0) is also transported to the Jet Trigger FPGA, to enable a centrality-dependent trigger threshold which will maintain approximately uniform Jet Trigger efficiency across event centralities.

5.2 Trigger Implementation

The trigger layout is shown in Fig. 5.2. Each 32 channel FEE card forms 8 charge sums from 2×2 towers. The charge sums are provided as fast analog signals to the Trigger Region Unit cards (TRU). There are 3 TRUs per SM that receive 288 charge sums via short analog cables from adjacent FEE cards. The 96 charge sum signals from each group of 12 FEE cards are connected via short differential cables to one TRU card where each input gets digitized at 40 MHz sampling rate derived from the LHC clock. The high frequency serial outputs of all 96 ADCs (112 max) are routed to the central Virtex-5 FPGA that de-serializes the ADC data and stores them in a 6.4 microseconds deep circular buffer (see Fig. 5.3). The input data rate to the FPGA circular buffer of each TRU is 5.7 Gbyte/s.
The L0 algorithm consists of Verilog code that is synthesized for the Virtex-5. It consists of 4 modules (see Fig. 5.4):

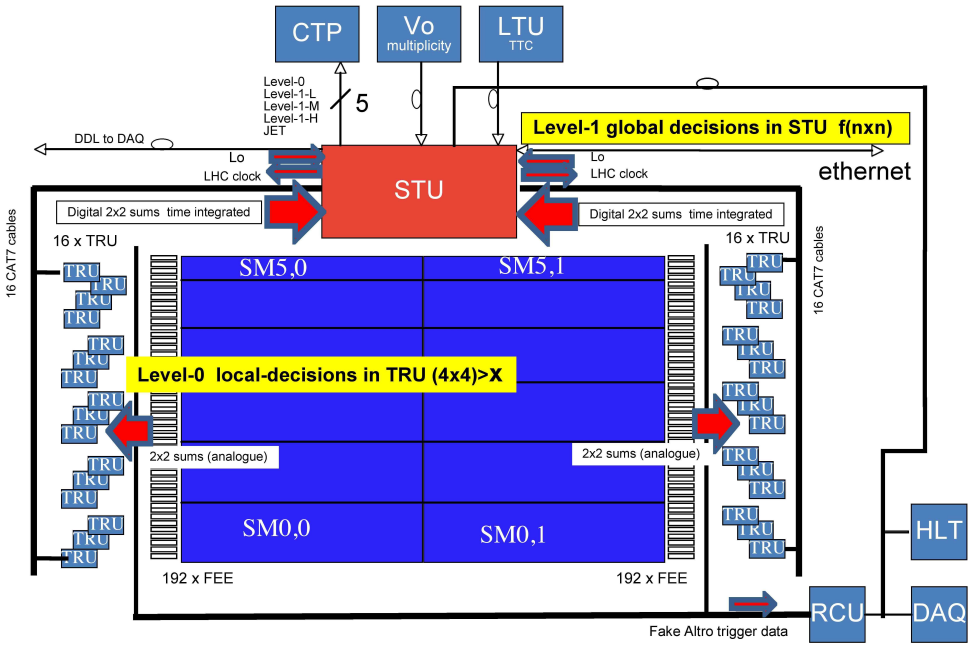

Figure 5.2: The EMCal trigger layout.

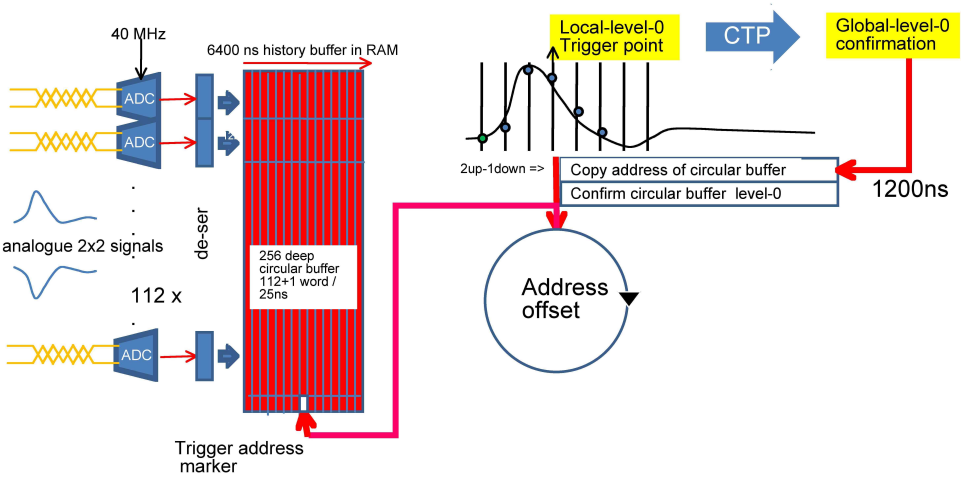

Figure 5.3: The EMCal trigger circular buffer.

- Time integration over the 2×2 signal envelope of 100ns FWHM.
- Pedestal subtraction
- Spacial 4×4 charge sums over all 91 possible combinations
- Programmable threshold on any of 91 (space $\times$ time) sums

The L0 algorithm requires about 10 clock cycles (250 ns) to produce a trigger decision with a new decision every clock cycle.
A single LVDS output line transmits the L0 decision at a decision rate of 40 MHz to the Summary Trigger Unit (STU) (see Fig. 5.5). All signals between a TRU and the STU are transmitted via quad LVDS lines contained in a CAT7 cable of 12 m length. The time-integrated 2×2 trigger data in the TRU is transferred upon receipt of a L0 decision via two parallel LVDS lines at a data rate of 800 MHz. The

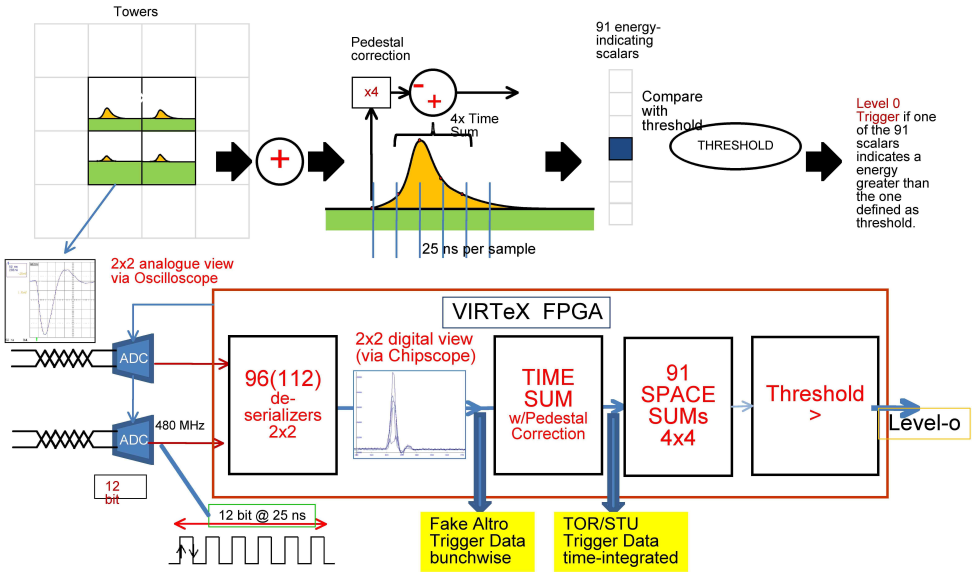

Figure 5.4: The EMCal trigger principle.

TRU receives the 40 MHz LHC clock from the STU via the remaining LVDS line. With this connection concept each of the 32 TRU's transmits both L0 decisions and 2×2 trigger data to the STU via a single CAT7 cable.
After the transfer latency of 1.44 μs, the FPGA of the STU card has received all L0 2×2 tower sum data from all SM's into a single FPGA. Its L1 algorithm then forms tower sums over larger overlapping regions to search for physics signatures (single showers and jets) within the L0-L1 latency of 212 bunch crossings (5.3 μs).
The STU sends both the the fast Level-0 decision and the 2 Level-1 decision for jet and photon via 40 m LVDS trigger cables to the ALICE Central Trigger Processor (CTP).

5.2.1 Jet Trigger

Computation of the triggers starts once the 3072 time-integrated data (96 values $\times$ 32 TRU) are received in the STU. Since there are significant computations to carry out with respect to the available latency and the granularity can be reduced without impairing the physics performance, the algorithm is divided in two consecutive stages.
The first stage of the algorithm builds 192 subregions by integrating the energy over squares of 8×8 towers. This is done in parallel for each region, yielding 6 subregions per region. The latency of this stage is expected to be ~ 1 μs (assuming processor clock speed of 120 MHz). The L1 jet trigger is then generated when the integrated energy over a sliding window of a n$\times$n subregion exceeds a multiplicity-corrected threshold. In order to keep some flexibility, n could be 2, 3, or 4. The three possibilities will either reside in a single FPGA configuration file or be implemented in three different FPGA configuration files (the FPGA being remotely reconfigurable). The latency of this last step is foreseen to be ~ 1.7 μs, thus the total delay for the jet trigger computation is expected to be 2.7 μs.
The threshold is recomputed on an event per event basis, thanks to the multiplicity information sent directly to the STU by the V0 detector via a dedicated optical line about 200 ns after a global L0 confirmation. The value received, which is a measurement of the integrated charge deposited on the V0A and V0C scintillator arrays of the V0 detector, is converted into a threshold level via a second order polynomial $Ax^2 + Bx + C$. The A, B and C parameters are adjustable via the DCS.

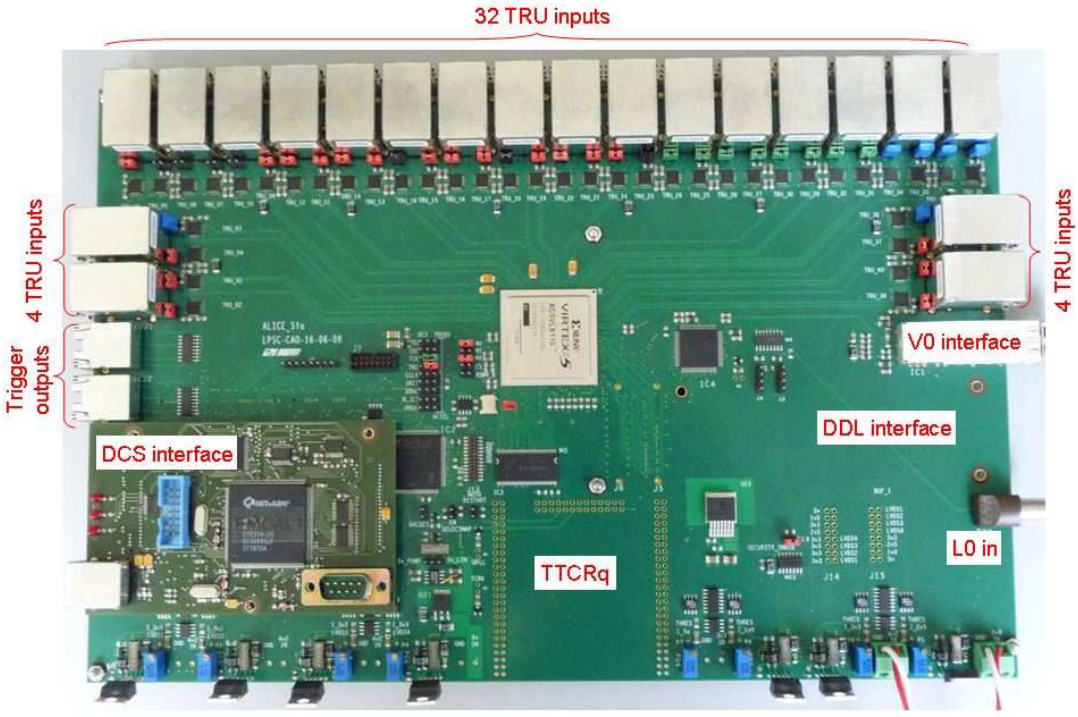

Figure 5.5: The EMCal Summary Trigger Unit.

5.2.2 Trigger Latency and Timing

The decision rate on all trigger signals is 40 MHz and the decision latencies are constant numbers of clocks cycles, respectively 40 for L0 and 260 for L1. Any L0 decision from the TRU-STU is to be validated at the CTP within 800 ns after the interaction. Within this latency are contributions from all analog and digital process delays from the preamplifiers, analog charge sums, ADC conversion, and sliding window pipeline in the TRU, and also significant cable delays (see Fig. 5.6).

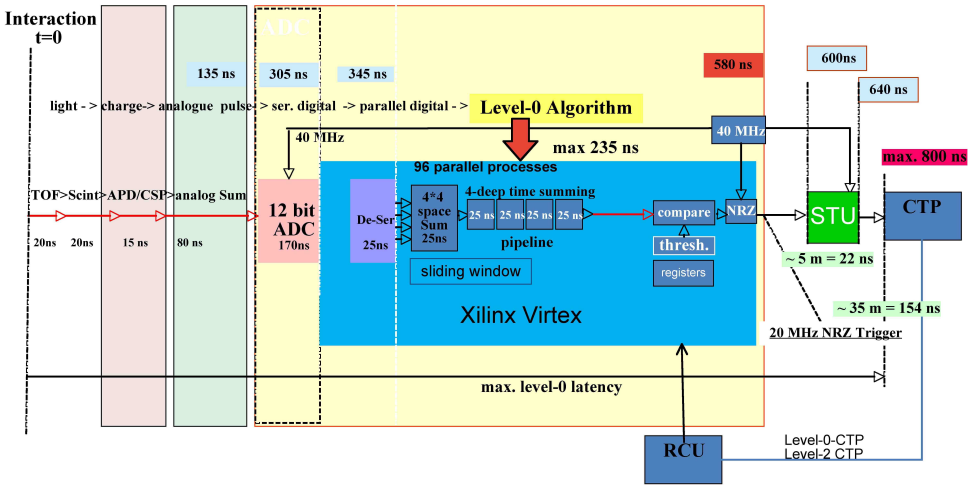

Figure 5.6: The Level-0 trigger latency.

Given the actual cable lengths of the experiment, the EMCal L0 decision must be formed at 580 ns after the interaction at the TRU level and at 640 ns at the STU level. The remaining time for the L0 algorithm of only 235 ns calls for a maximum of parallelism in all digital processes.
The L1 latency allows for a comparatively convenient processing time in the STU. However a major part of this time is used for

- Waiting for a L0 decision from the CTP (1.2 μs after the interaction)
- Transfer of trigger data from TRU's to the STU (finished about 2.915 μs after the interaction).

With an available L1 decision latency of 5.9 μs, the L1 processing time is limited to 2.985 μs (see Fig. 5.7).

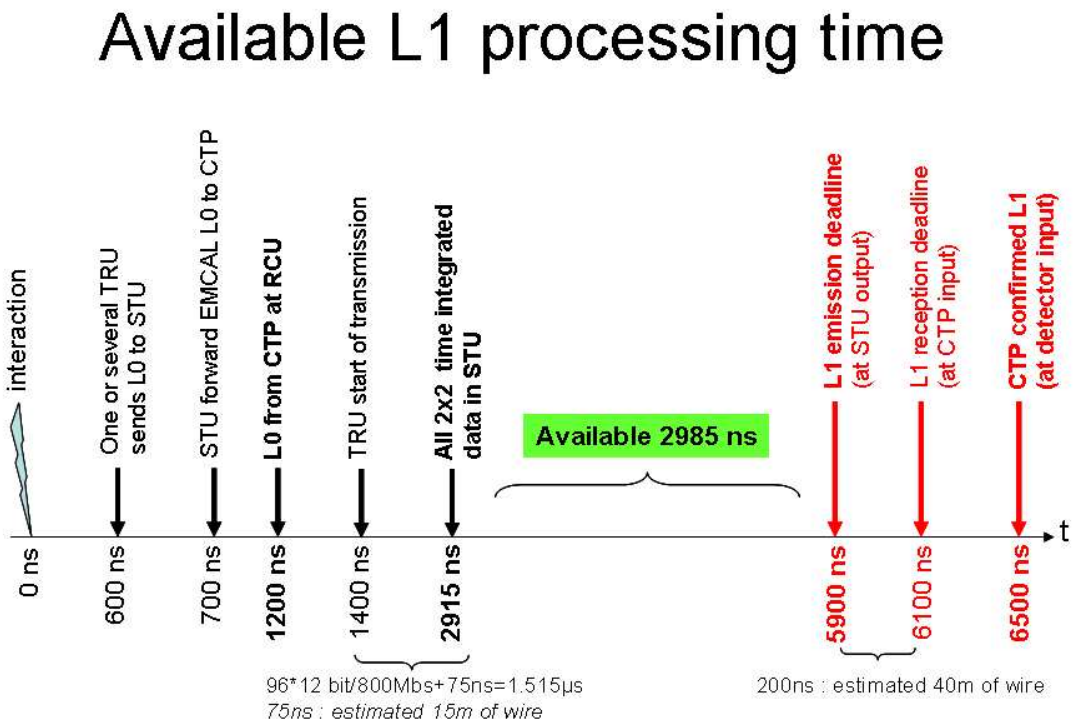

Figure 5.7: The Level-1 trigger latency.

5.2.3 Trigger Data

The type of trigger data that is used online in the TRU and STU are the digital samples of 2×2 analog charge sums of 100 ns FWHM. These are sampled at 40 MHz and time integrated over 6 samples in order to compensate for time differences in different channels (see Fig. 5.8). After subtraction of ADC pedestals, these are used for the 4×4 sum algorithm in the TRU. On reception of a L0 trigger from the CTP, the time-sums are transmitted serially from all TRU's in parallel, as 12-bit numbers to the STU. After the serial transfer latency of 1.515 μs, the STU has trigger data available that have the same 2×2 granularity as in the TRUs, however without local TRU boundaries, allowing the STU to start global trigger algorithms.
After a L2-Accept trigger, the STU will forward the jet and gamma trigger cluster indexes that satisfied the trigger threshold conditions via the DDL to the DAQ. In the commissioning phase it will be possible to transfer, in conjunction with the indexes, the time integrated data used for the trigger decision.

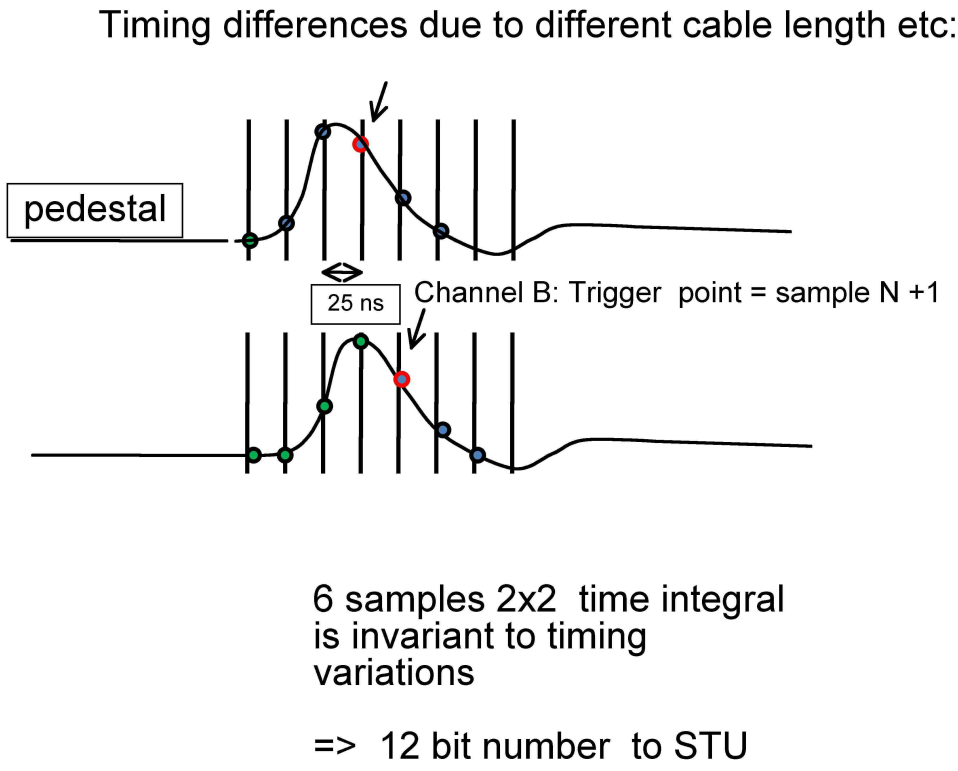

Figure 5.8: The sampling of the 2×2 charge sum trigger signals.

The raw ADC trigger data that are available offline are the non-time integrated ADC samples from the circular ADC buffers in the TRU's. These buffers can be read out via the "fake ALTRO" (F-ALTRO) protocol which effectively appends the raw trigger data to the RCU event data. For this purpose the TRU's have FPGA code that emulates the ALTRO chip readout protocol, such that it can be read out like a real ALTRO on the FEE cards. The format of the F-ALTRO data is depicted in (Fig. 5.9). A F-ALTRO emulates 16 Multi-Event Buffer (MEB) memory channels of 10-bit and up to 256 sample depth. The data from one F-ALTRO channel is sent to the RCU in block mode after the RCU has sent a readout command. The 16 channels correspond to 16 successive samples, or 400 ns of the charge-sum history around the L0 trigger point in the circular buffer. Each channels MEB memory contains the sampled ADC data of the 96 (112 for PHOS) ADC channels belonging to one single 25 ns sample. Consequently the N x 10-bit payload contained in the block that is sent to the RCU for each F-ALTRO channel is constant with N= 96 (112 for PHOS).
The raw trigger data are identified as having geographical (GTL) address zero and can be separated from the event data by the offline decoder that splits all blocks with geographical address field=0 into a trigger data file.

5.2.4 Trigger Board Prototypes

The EMCal Trigger is a derivative of the PHOS hierarchical trigger that was previously developed with TRU's for local L0 decisions and global L1 decisions in the Trigger-OR module (TOR) which receives 2×2 trigger data from the TRU's within a few μs after the L0 trigger. The TRU-1 of PHOS is based on Virtex-II Pro FPGA's and 12-bit, 40 MHz ADC's from Texas Instruments. The EMCal TRU has the same physical size as the FEE card and also connects to the RCU readout bus in the EMCal crate. The analog sums from the neighboring 9 FEE cards are connected via short, differential flat cables (see Fig. 5.1).
The TRU-2 of EMCal is an upgraded TRU-1 with more advanced Virtex-5 FPGA technology and newer

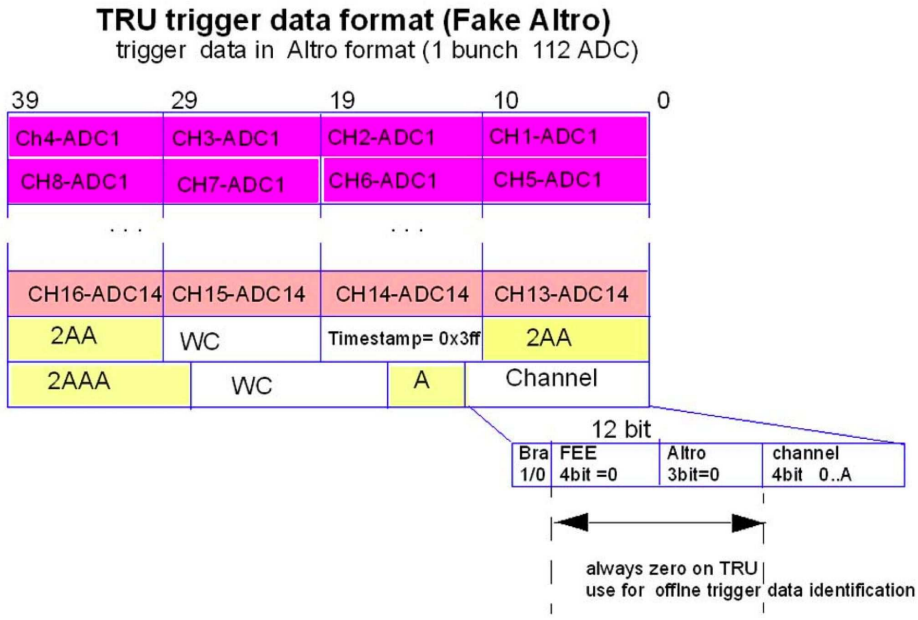

Figure 5.9: The Fake Altro trigger data format.

12-bit ADC's that include new features (like programmable gain and noise filters). In addition the board layout was revised in order to reduce cross-talk from the digital to the analog parts.
The readout and control of the TRU requires a board controller protocol that communicates with the RCU's for 3 different purposes:

- Configuration of registers
- Monitoring of voltages and temperatures on the TRU
- Readout of the "fake" ALTRO

The TRU-2 board controller is a firmware Verilog module that was developed by CCNU Wuhan for the PHOS TRU-1.
The STU is an upgrade of the PHOS Trigger-OR board (TOR), which was originally designed for PHOS in order to perform global OR of the Level 0/1 triggers generated by the TRU. The STU has been designed and optimized for high speed communication with the TRU and high performance computing thanks to the Virtex-5 FPGA. In order to fulfill all requirements, the card is equipped with:

- A custom made DCS interface for remote control that allows register configuration and distant FPGA reconfiguration
- A TTCrq mezzanine that receives the LHC clock and the L0 trigger decision
- An optical interface for the V0 detector that enables the reception of the centrality information
- A DDL link for interfacing with the DAQ/HLT readout system

Before building the STU, feasibility tests were performed on the TOR board, in order to validate the high speed communication link between TRU and STU. The tests demonstrated that extreme care had to be taken for the layout of both TRU and STU communication links and that the TRU side is slightly more sensitive. This is consistent with the fact that the synchronization reference clock is received by the TRU. Prototypes have been designed in accordance.

5.3 High Level Trigger

After a successful L0 and consecutive L1 trigger sequence, the HLT farm receives the following:

- A full copy of the EMCal FEE data from the FEE readout
- A list of the trigger clusters that have satisfied the trigger condition from the STU
- Optionally, the time-integrated trigger data from all 2×2 channels via the STU's DDL link together with dedicated trigger information from the STU algorithm.
- Optionally, via the F-ALTRO mechanism, the raw ADC samples from all 2×2 channels in 16 consecutive clock cycles.

The overall architecture of the Trigger, DAQ, and HLT systems is illustrated in Fig. 4.1 and is discussed in Section 4.3. The DAQ system transports the data from the DDL up to the storage of data on the PDS system. The task of the HLT system is to select the most relevant data from the large input stream and to reduce the data volume by well over an order of magnitude in order to fit the available storage bandwidth, while preserving the physics information of interest. This is achieved by a combination of event selection (triggering), data compression, or selection of Regions of Interest with partial detector readout. While executing any of these tasks, the HLT may also generate data to be attached to or partially replacing the original event.
The EMCAL HLT online software when run within the publisher-subscriber framework of the HLT incorporates the offline event reconstruction path. Dedicated processing components perform the local EMCAL reconstruction and after combining the reconstructed charged track information from the other sub-detectors (TRD and TPC) will deliver a physics trigger decision to a specialized trigger processing component responsible for a global HLT decision. In addition to triggering functionality the HLT has extensive monitoring capabilities. The built-in monitoring mechanism (HLT TCP publisher-subscriber) allows for monitoring of the detector performance as well as inspection of the event data at any level of reconstruction.

6 Detector Calibration and Monitoring

6.1 Requirements

In order to minimize the EMCal energy resolution for high energy electromagnetic showers it is important to obtain and maintain a tower-by-tower relative energy calibration of better than 1% in the offline analysis. The uncertainty in the tower-by-tower energy calibration contributes to the constant term of the total energy resolution which becomes most significant at high energy. Also, since analog tower energy sums provide the basis of the L0 and L1 high energy shower trigger input to the ALICE trigger decision, the EMCal should operate with APD gains adjusted to match the relative tower energy calibrations online to better than about 5%. This is desired in order to obtain sharp trigger energy threshold turn-on curves. Both of these goals will be attained through the use of a Light Emitting Diode (LED) calibration system in which all towers view a calibrated pulsed LED light source (see Section 3.6). Scans of the APD HV bias while taking LED pulser data will allow to determine the absolute APD gain for each channel. Once the LED light yield in each tower is calibrated, the LED itself can be used to track the tower gain in the case of APD bias adjustments, or in the case of APD gain drifts as might result from the known temperature dependence of the APD gain of about $2\%/^{\circ}\mathrm{C}$ (see Chapter 7 and Table 3.1).
The ALICE offline software will include a calibration database for each detector. The contents of the calibration database will all be ROOT objects and the overall database will be available in the AliRoot file catalog. In principle this is something that is only accessible during the offline analysis, and is not generally available online for the High Level Trigger (HLT) or the on-detector trigger logic. However, provision will be made for access to this general AliRoot resource, or to local copies of it that are accessible to the Experiment Control System (see Section 4.5) via PVSSII for the low level detector setup, such as for EMCal APD bias adjustments for gain matching, and as well to the HLT processors.

6.2 APD pre-Calibration

To ensure an optimal resolution for high energy electromagnetic showers, it is important to have a tower-by-tower relative energy calibration that is better than 1% in the offline analysis. This will be achieved by use of the Minimum Ionizing Particle (MIP) peak from cosmics and hadrons in ALICE, as well as identified electrons and the mass peak of reconstructed neutral pions in ALICE. During data-taking the APD gains need to be adjusted to equalize tower response within about 5%, due to trigger considerations. Prior to installation in the EMCal, each APD+preamplifier (CSP) has to be tested to verify its basic functionality and properties and to reject those APDs which do not meet the EMCal requirements. In particular, the voltage needed for the APD to obtain gain M=30 (V30) must be lower than 400 V due to the limitation in the EMCal FEE. Mass production tests will consist of measurement of the gain vs. voltage dependence of each APD at fixed temperature ($25^{\circ}\mathrm{C}$) and in the determination of V30. Such information will be recorded in a database and used to reject APDs with inadequate performance. Moreover, the information will be used to adjust the bias voltage individually for each APD to have a uniform APD pre-calibration of the EMCal towers for the calibration with cosmic ray muons.
In the following a brief description of the procedure adopted for this testing activity is given, together with results obtained from the characterization of a first batch of 170 APDs. More information can be found in [1, 2].
It is well known that the gain of the avalanche photodiodes is strongly dependent on the temperature: since the avalanche multiplication increases with the mean free path of electrons between ionizing collisions, the APD gain decreases with increasing temperature. An apparatus has been purpose-built to test

simultaneously 16 APDs directly connected to their Charge Sensitive Preamplifier (CSP), all maintained at a controlled temperature. It includes a copper mechanical plate with an internal cooling pipe connected to a chiller. The APDs are placed in direct contact with this plate and their temperature is continuously monitored by thermocouples placed on the APD surface. The use of this system allows a temperature control precision of $\pm 0.1^{\circ}$C. Figure 6.1 and Fig. 6.2 show a photograph and a sketch of the setup.

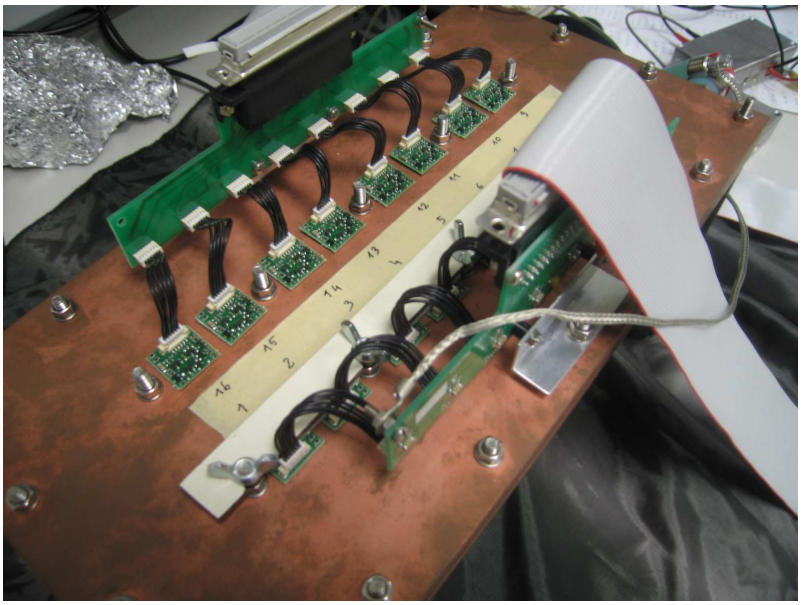

Figure 6.1: Photograph of the apparatus to simultaneously test 16 APDs.

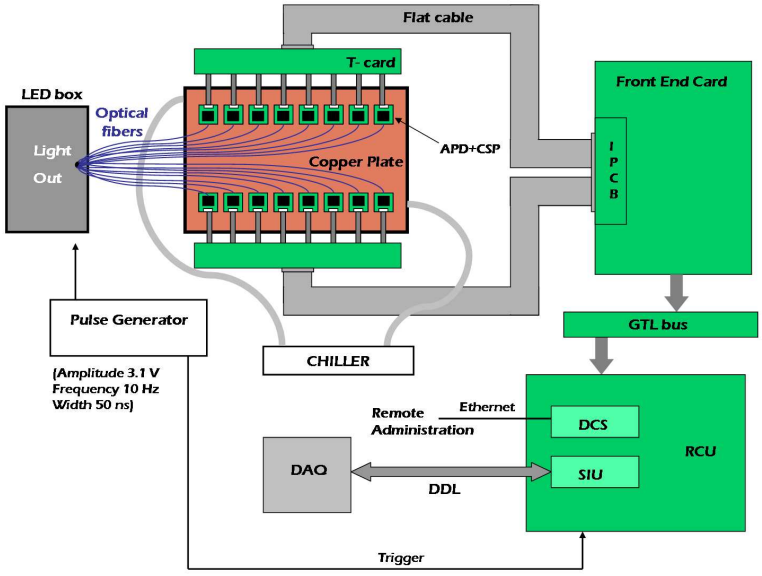

Figure 6.2: Sketch of the experimental setup used for the tests.

A highly stable blue LED from Kingbright (L7104PCB) [3] with $\lambda = 470$ nm, triggered by an external pulse generator (width 50 ns) with a frequency of 10 Hz is used as light source. To obtain the desired light intensity, a voltage of 400 V is applied. In Fig. 6.3 the basic scheme of the avalanche LED pulser

and a photograph of the LED driver are shown. More information can be found in [4]. The LED driver card is put in a metallic box to shield the apparatus from electromagnetic noise. The LED is inserted inside the optical connector and its light is delivered to the 16 APDs by a bundle of 1 mm fibers.

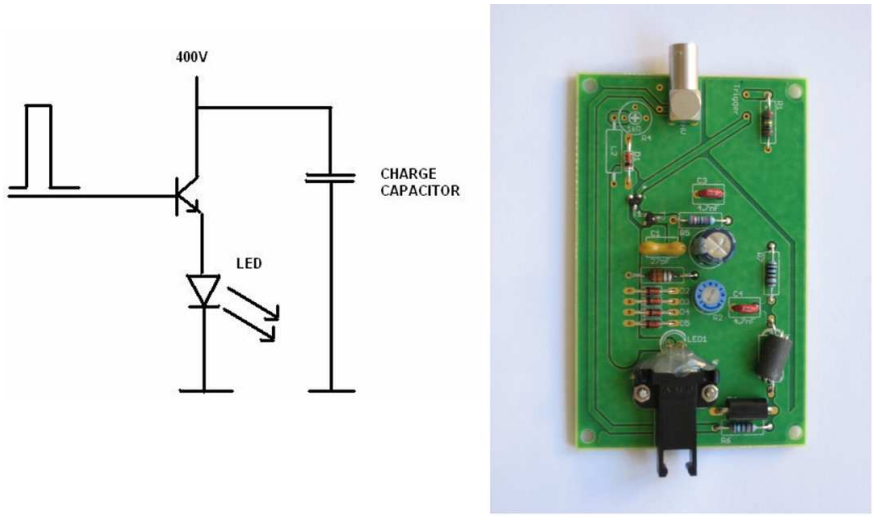

Figure 6.3: Scheme of the avalanche LED pulser (left) and a photograph of a LED driver (right).

The CSPs are connected to the standard EMCal electronics and readout (described in Chapter 3), and the digitized data are transferred via an optical fiber link to an offline computer running the ALICE DAQ (DATE) [5].
The test consists in the measurement, at a fixed temperature, of the gain dependence on the bias voltage to determine the voltage for which the gain M=30. The gain M(V) is defined as the ratio between the amplitude at the voltage V and the amplitude in the plateau. The shape of the gain vs voltage curve is an exponential function and may be well fitted with an exponential plus a constant:

$$M(V) = p_0 + p_1 e^{p_2 V}$$

where M(V) is the gain at the voltage V (see Fig. 6.4). The low gain plateau value can be determined in different ways. Accurate studies have shown that in our case the best reference value is the amplitude at 50 V.
The relative change of the gain with the bias voltage, (the voltage coefficient), is a linear function of the gain. In the present case such coefficient turned out to be $1/M \times dM/dV = 2.3\%/V$ at M=30. This voltage dependence has a significant effect on the energy resolution of the EMCal: if the voltage control step is 0.2 Volt/bit, a coefficient of 2.3%/V would limit the gain calibration to 0.46%.
Whereas the PHOS spectrometer will cool its APDs down to -25°C to work at higher gains, the EMCal will be operated at ambient temperature. Recent estimates of the temperature in the EMCal region inside the L3 magnet, made by the CFD (Computational Fluid Dynamics) group (see [6] and references therein) gave values around 20-21 °C and a temperature uniformity in the order of 1-2 °C across the large TPC volume, with an air flow of 10^4 m^3/h with the inlet temperature of 17 °C and a realistic air extraction scenario. Some variations may however be expected most likely on the high temperature side, according to the final choice of the air flow parameters. For this reason the APD behaviobehaviorur has been studied in the range around the room temperature (from 21°C to 29°C). Examples of gain curves, for the same APD, obtained at different temperatures are shown in Fig. 6.5.
The dependence on the temperature is especially evident at higher values of the bias voltage, where the gain undergoes a strong variation with temperature changes. As can be seen from Fig. 6.6, where the gain versus temperature is reported for four different APDs, the relation between gain and temperature

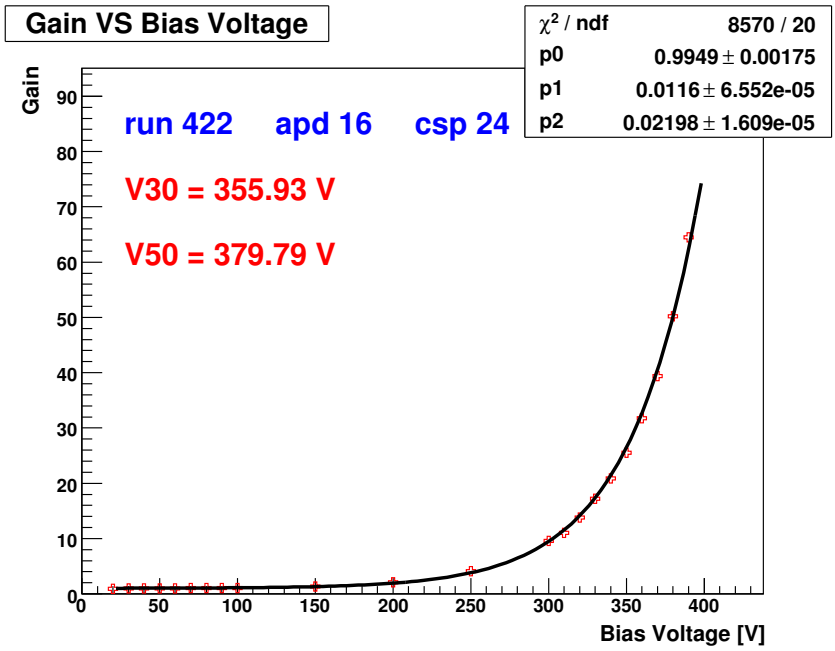

Figure 6.4: APD gain versus bias voltage.

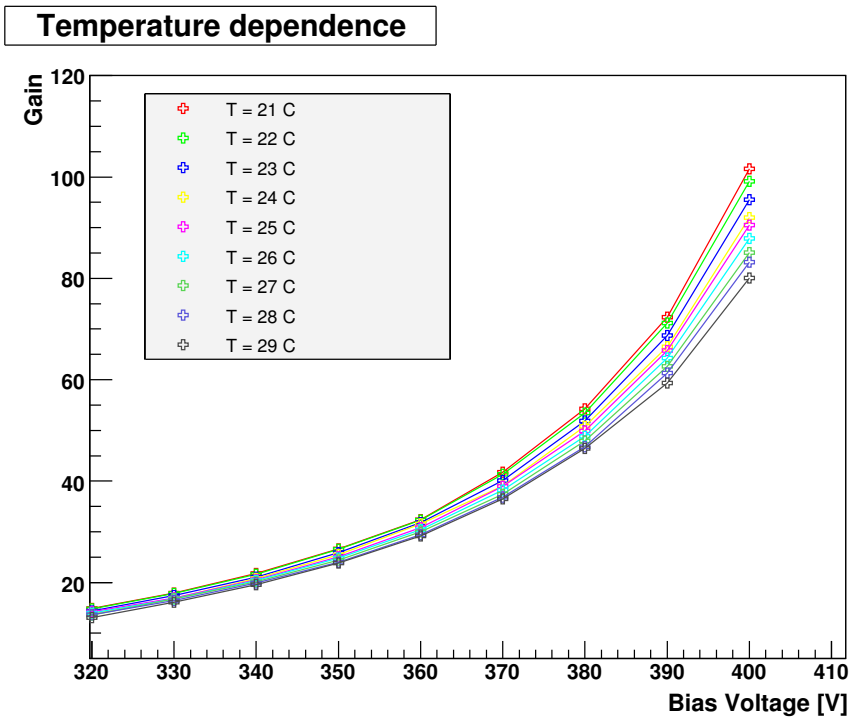

Figure 6.5: APD gain dependence for different operational temperatures.

is approximately linear at a fixed value of the bias voltage. The parameter from the linear fit allows to calculate for each APD, the temperature coefficient $1/M \times dM/dT$, which is the percentage change in gain per one degree change in temperature. In Fig. 6.7 the temperature coefficient as a function of

the APD gain is reported, showing that this quantity is strongly dependent on the gain. At M=30 the temperature coefficient is -1.7%/T; this means that for a variation of $+1^{\circ}$C, the gain of 30 will change to about 29.5.

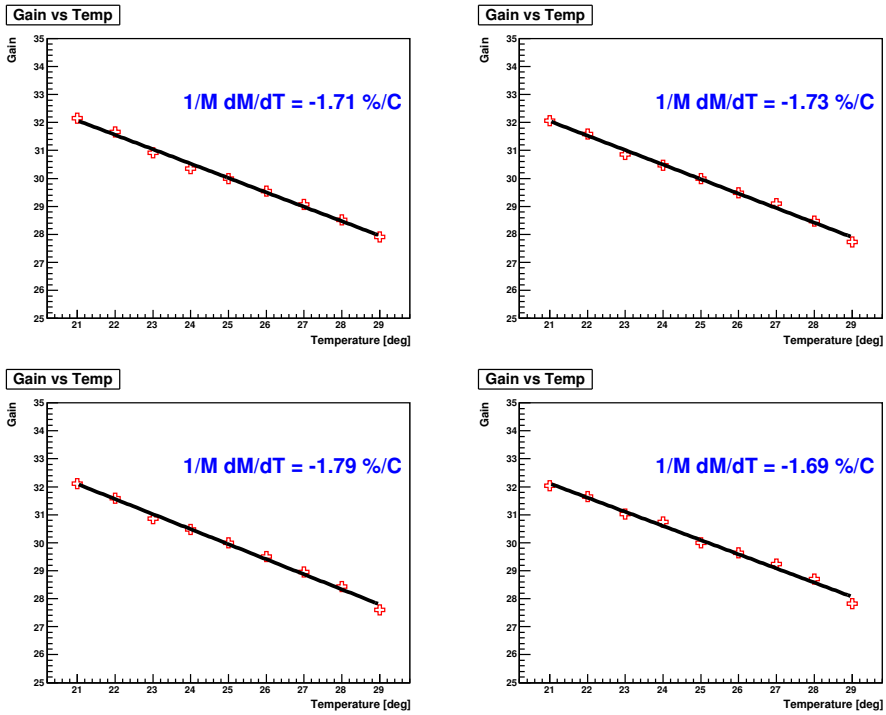

Figure 6.6: APD gain versus temperature for 4 different APDs.

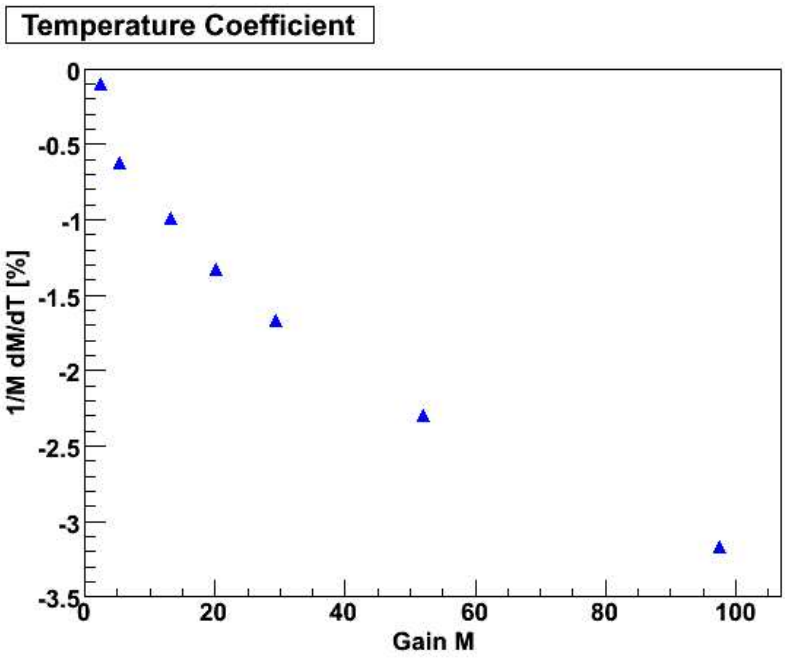

Figure 6.7: Temperature coefficient versus gain.

Measurements repeated on a significant number of APDs, show that the voltage and temperature coefficients (2.3%/V and -1.7%/°C at M=30) are quite similar for all APDs. For example, the RMS of the temperature coefficient distribution is 0.1%/°C. Conversely, at the same reverse-bias voltage a batch of 170 APDs showed considerable differences in the individual APD gain. For example, applying a bias voltage of 380 V, the distribution of gains ranged from M=20 to M=90.

6.3 Cosmic Ray Calibration

The EMCal super modules will be assembled at two sites. After their assembly, each super module will be calibrated to ensure that their integration in the ALICE detector will conform to specifications and allow for immediate functionality after installation. The calibration design goal is to achieve a relative (gain) calibration of all towers in a super module to better than 10%. The calibration procedure is based on measurement of the energy deposit of cosmic muons at the MIP peak as they pass through a single tower. The response of each tower to the known energy deposited by MIP muons will allow the relative calibration to be performed as well as to set the initial absolute energy calibration scale. This initial (pre-)calibration should be sufficient for the EMCal to have a uniform trigger response upon installation. The final calibration will then be done online using experimental data for MIP-particles, electrons, and π^0.

The pre-calibration will be performed at the two assembly sites, Grenoble and Yale, prior to shipment to CERN. In order to ensure the reliability of the procedure and to define a common procedure for both sites, a cosmic ray test was performed in December 2007 at CERN following test beam measurements. The prototype was made of 4 truncated strip modules, each one-third of a final strip module (4 modules), creating an array of 4×4 modules (8×8 towers). Since the energies of MIP particles from cosmic rays is too low to efficiently trigger with the EMCal, an external trigger based on scintillator paddles was necessary. The analysis of the cosmic tests at CERN focused on a comparison of the results with an EMCal tower based isolation procedure for two different trigger configurations, in order to define the most precise and reliable calibration procedure.

A coincidence trigger was arranged with scintillators above and below the EMCAL module. Two trigger configurations were compared. The first one covered a large acceptance over the entire setup (4×4 modules). The second configuration consisted of a small acceptance, i.e., covering 1 module (2×2 towers). In order to define a well calibrated signal associated with cosmic muons traversing only a single tower, an isolation procedure was applied offline by searching for the maximum signal amplitude in an event, then checking the neighboring towers to ensure their signals are smaller than a threshold value ("Q-cut parameter"). This cut parameter was chosen to be as low as possible and is defined by the electronic noise (in the present case 3 ADC channels). A typical MIP response of a tower is $\approx$23 ADC counts. Figure 6.8 shows the results of measuring the MIP peak for the modules used in the cosmic tests and applying both triggering conditions. Obviously, the isolation procedure is not applicable for "edge" towers, and therefore a "special" approach has been implemented to calibrate the edge towers with comparable precision. It consists of using a combination of an edge tower with a previously calibrated neighboring tower, combining the signal measured in both towers, and extracting a calibrated signal for the edge tower.

The analysis of the cosmic test data indicates that the small acceptance scintillator trigger configuration will provide the most reliable super module (SM) cosmic calibration. As a compromise between accuracy and the number of readout channels, the associated electronics cost, and the time required for calibration of a full SM, the trigger setup will consist of $12-16$ scintillators (dimensions $144\times12\times2$ cm^3) placed above and below the SM as shown in Fig. 6.9. Each scintillator pair will cover the full acceptance of one strip module. Each scintillator will be read out from both ends by photomultiplier tubes (PMT). A coincidence signal between the 4 PMT's of 2 corresponding scintillators for a given strip module will be required to start the readout of the EMCAL. Amplitude and timing information for each PMT will be processed in order to guarantee the selection of events when a single cosmic muon crosses only one

module. Position resolution along the length of the strip module will be achieved by analyzing timing differences between the two PMT's of each scintillator. This condition is necessary to successfully apply the off-line isolation procedure (described above) and extract a MIP peak. It has been estimated that within an $18-24$ hours long run, sufficient statistics can be accumulated for calibration of those towers under the area covered by the trigger. The trigger scintillator array is physically moved to cover the different portions of a SM. The scintillators will be placed on support structures and oriented to account for the different angle of the strip module being calibrated.

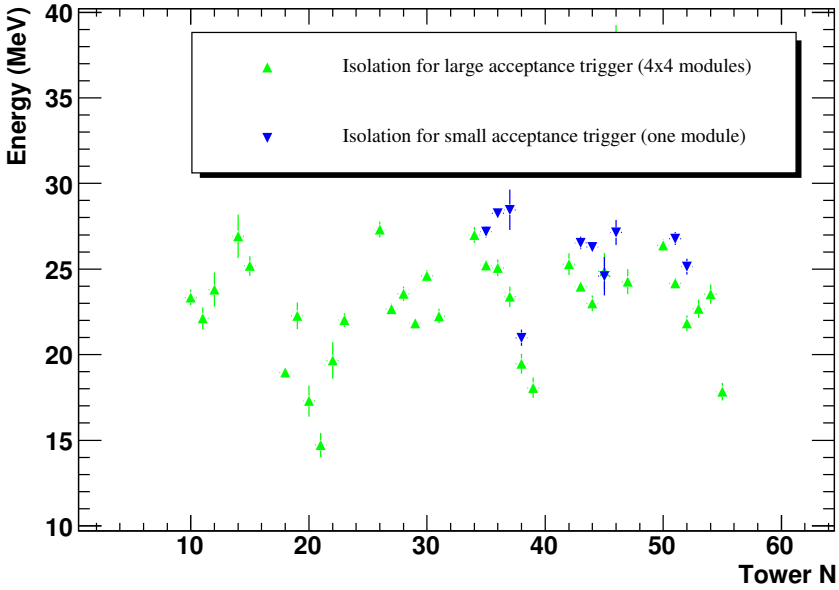

Figure 6.8: The mean energy deposited (in MeV) for several towers of the cosmic test setup obtained after application of the isolation procedure. The tower calibrations were taken as the 80 GeVelectron beam calibration factors, but without correction for the temperature dependence.

6.4 Gain Monitoring During Runs

As described in Chapter 4.5 of Ref. [7], it is foreseen to be able to take calibration triggers, such as the EMCal LED calibration trigger, during stand-alone EMCal operation, as during setup, as well as during physics data-taking. Calibration triggers would be taken during data-taking during the "long gap" of about 2.97 μs at the time when the orbit reset from the LHC machine is sent. A calibration "pre-pulse" is provided to trigger the LED pulser system followed by a L0 calibration event trigger. The pre-pulse is sent 1.3 μs after the last bunch before the gap, i.e., after the L0 trigger latency of 1.2 μs, to insure that no physics trigger has been issued from that bunch.
The LED calibration data will be analyzed online to monitor the status and track the gain of all EMCal towers. The LED calibration data stream will be split from the physics data stream in order that it can be processed directly to extract correction factors for any time-dependent gain drift. The time-dependent gain correction factors will be entered into the analysis database to allow immediate physics analyses with all time-dependent gain corrections applied.

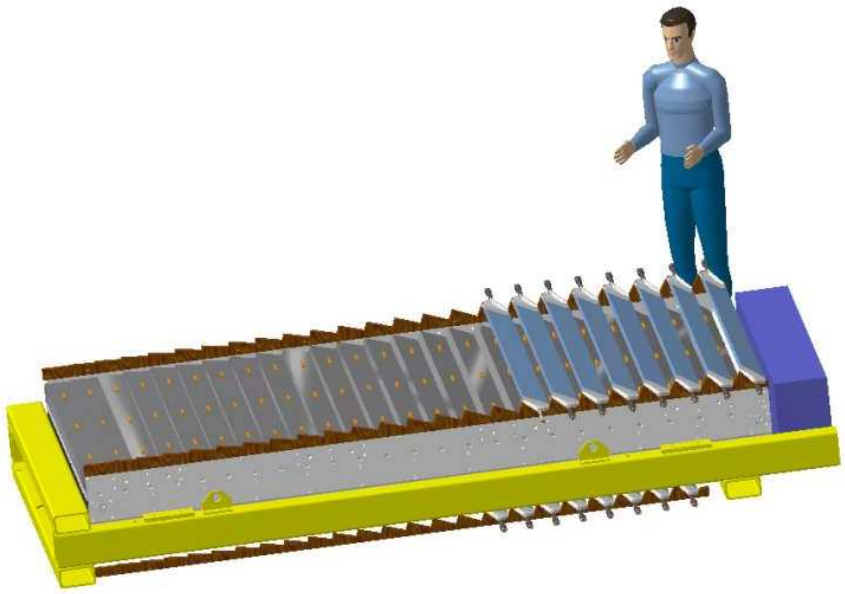

Figure 6.9: Illustration of a super module configured with 16 trigger scintillator panels for calibration of a portion of a super module. The scintillators are inclined according to the strip module angle and read out by photomultiplier tubes on each end. The yellow beams are the super module hoisting frame and only used for transport.

6.5 In-beam MIP, Electron, and π^0 Calibrations

The initial tower-by-tower gain matching based on cosmic muon data taken prior to the EMCal installation in ALICE, and the calibration of the absolute energy scale, will be improved using physics data. The high statistics data will allow to use the MIP peak in each tower to adjust the relative gain factors between towers. Identified electrons will be used to check the EMCal energy scale compared to the electron momentum measured by tracking in ALICE. Finally, the measured mass of the π^0 peak will also be used to confirm the absolute EMCal energy calibration.
With high statistics p–p or peripheral Pb–Pb collision data, two-photon invariant mass spectra can be accumulated for each tower that has either of the two photons centered on the tower and the position of the observed π^0 peak can be used to improve the tower energy calibration [8].
Full simulations of several π^0 per event in the ALICE analysis framework were used to quantify how much this method can improve the relative calibration of the EMCal towers. The same calibration constant was used for all towers. A 10% de-calibration was then applied to the tower calibration coefficients as expected from a pre-calibration based on cosmic muon data. For the ideal case (no uncertainty on the calibration coefficients), the reconstructed two-photon invariant mass for the full super module shows a peak which lies at the mass of the π^0 with a width corresponding to the intrinsic resolution of the electromagnetic calorimeter. For the 10% de-calibration case, the width of the two-photon invariant mass peak increases by 50% compared to the ideal case. The calibration coefficients were then corrected tower per tower with the help of the two-photon invariant mass spectra. For each tower i, the two-photon combinations were selected only if one of the clusters deposit at least 50% of its energy in the considered tower. The resulting two-photon invariant mass distribution was fitted and the extracted mean value m_i was used to correct the calibration coefficient cc_i of the tower through the following formula:

$$cc_i^{corr} = cc_i \cdot (1 + k_i^2)/2 \tag{6.1}$$

where $k_i = m_{\pi^0}/m_i$.

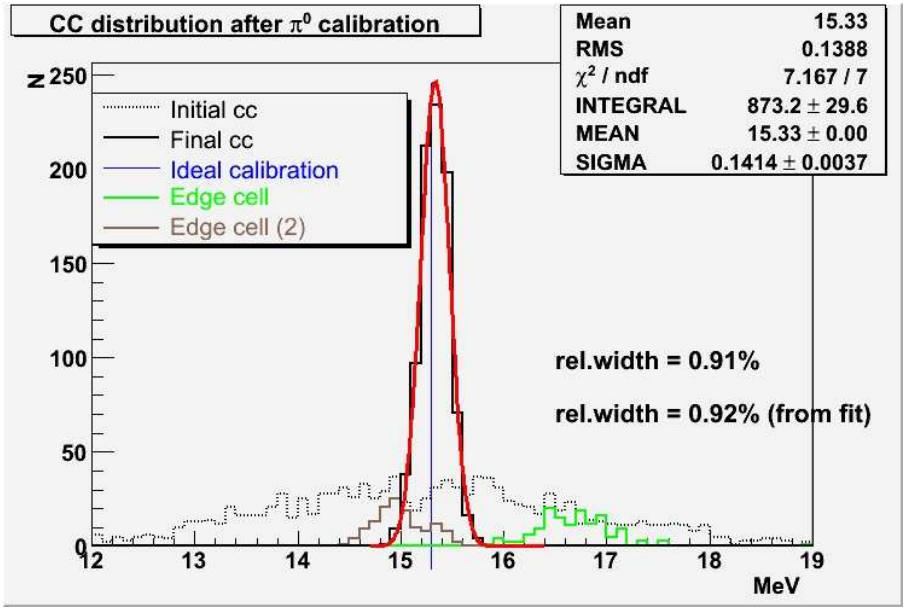

Figure 6.10: Distribution of tower relative calibration coefficients for one super module for an ideal calibration (blue line), for 10% de-calibration (dashed line), after corrections as explained in the text (full line). The latter distribution is fitted by a gaussian (red line). The green and brown lines shows the corrected calibration coefficients for the edge towers case.

The procedure was repeated several times in order to obtain an invariant mass distribution centered at the mass of the pion for each tower. Figure 6.10 shows the calibration coefficients distribution for one super module for the ideal case (blue line), for 10% de-calibration (dashed line) and after calibration coefficients correction (full line). In the latter distribution, the towers which lie at the edge of the super module were excluded. The corrected distribution is centered at the value of the ideal calibration with a 1% accuracy. The green and brown distributions show the corrected coefficient calibrations for the case of the edge towers: they are different from the inner towers due to shower leakage at the boundaries of the super module. The resulting final two-photon invariant mass for the full super module after applying the corrected calibration coefficients was found to be centered at the pion mass with a width which was only 5% higher than of the ideal case.
This study demonstrated that from a cosmic calibration with a 10% accuracy, it is possible to achieve a calibration uncertainty in the range of 1% using the π^0 invariant mass in p–p running. The statistics needed to obtain such accuracy is approximatively 700 π^0 per tower with the photon with highest energy of the two photons centered on the tower.

7 Test Beam Results

7.1 Goals and Setup

During a period of five weeks in autumn 2007 the first ALICE EMCal modules constructed according to final design were tested in the CERN SPS and PS test beam lines. The test utilized a stacked 4×4 array of EMCal modules (8×8 towers). All towers were instrumented with the full electronics chain with shapers and APD gains operated as planned in ALICE. A LED calibration system (see Section 3.6) was installed in order to monitor time-dependent gain changes. The readout of the front end electronics used the full ALICE DAQ readout chain.
Earlier test measurements were performed in November 2005 at the Meson Test Beam (MTEST) at FNAL utilizing a stacked 4×4 array of *prototype* EMCal modules (8×8 towers) of slightly different design than the final design described in Fig. 2.3. For this test in particular, measurements were made for comparison of the performance with two different signal shaping times in the front end electronics (see Chapter 3). Two front end electronics cards (32 towers each) were used for the readout of the modules; one had the nominal 1 μs signal shaping time which PHOS uses, and the other had a modified 100 ns shaping time as planned for EMCal [1].

The goals of the test beam measurements were:

- To determine the intrinsic energy resolution and the position resolution using electron beams.
- To investigate the linearity and uniformity of the response; in particular across towers and module boundaries and for tilted or recessed modules.
- To determine the light yield (signal) per unit of deposited electromagnetic energy.
- To study the effect of shorter shaping times as planned for the final design.
- To study the energy dependence of the response to electrons and hadrons to determine the particle identification capabilities of the EMCal by shower shape analyses.
- To develop and investigate the performance of monitoring and calibration tools (gain stability, time dependencies) using electron beams, MIPs from hadron beams, and LED events.
- To develop and test ALICE standard software for readout, calibration, and analysis.

The measurements at the SPS took place at the H6 secondary beam line located in the North area. A primary proton beam of 400 GeV and of intensity up to 10^{12} particles per spill is incident on the T4 primary target providing pion, electron, and muon secondary beams at the P0, H6 and H8 lines. The achievable maximal momenta at the three secondary beam lines are highly correlated. With the settings for the P0 and H8 lines the maximum energy for the H6 line was constrained to be less than 120 GeV. The electron beam had a purity of better than 99% and a typical momentum spread of $\delta p/p \sim 1.3\%$ (defined by the chosen aperture). The recorded number of triggers per spill was up to 1500 counts, depending on the momentum selected, over an area of a few square cm. The beam spill length was typically about 5 seconds every 10 seconds. By utilizing an absorber in the electron beam line hadrons in the momentum range of 5 GeV to 100 GeV have been obtained.
The measurements at the PS took place at the T10 beamline. A mixed electron/hadron beam was available with a momentum range of 0.5 GeV to 6.5 GeV.

The test measurements at Fermilab took place in the MTEST-MT6 secondary beam line [2]. The proton beam was resonantly slow-extracted from the Main Injector and focused onto the MTEST target for test beam use. The tests were made with mixed beams with good particle identification (e/π/p discrimination) over the full range of available momenta (3-33 GeV). The beam momentum selection bite was about $\delta p/p \sim 1\%$. The beam intensity was in the range of 0.2–10 kHz dependent on the momentum selected, over an area of a few square cm. The beam spill length was typically about 4 seconds every 2 minutes.

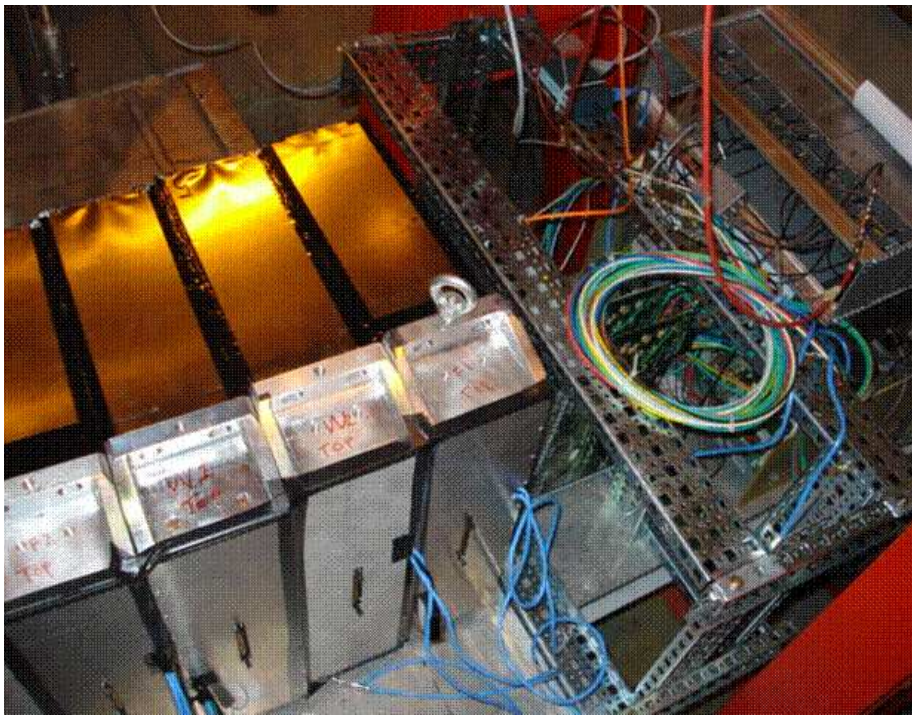

Figure 7.1: Rear view of the EMCal test modules in the H6 test beam at SPS CERN.

The setup of the EMCal test modules at the CERN SPS is shown in Fig. 7.1. For handling and stacking purposes, the modules were assembled on a strong-back in strip units of four modules in the vertical direction. In order to scan the entire surface of all four modules they were placed on a remotely controlled movable platform. The range of both horizontal and vertical adjustment allowed to scan the whole array of modules. The size of the stacked array was about $51 \times 51 \times 50$ cm with a weight of about 400 kg ($\sim$ 25 kg/module).
The EMCal readout electronics was attached to the back of the array of modules with the electronics cards and readout units (DCS/RCU) located on the same moveable table as the modules, together with the LV supplies.
In both setups at CERN and FNAL, a pair of scintillator paddles upstream of the EMCal was used for the beam definition trigger. In addition at the CERN-PS and at the FNAL-MTEST, the signal from gas threshold Cerenkov counters were used as electron trigger for electron/pion discrimination. A set of three MWPCs in front of the EMCal provided $x-y$ position measurement with better than 1 mm position resolution. The MWPCs were used to define the beam particle track which could then be projected to the front face of the EMCal modules.
The official ALICE DAQ (DATE v6.13) [3] was used for taking the EMCal data. The MWPC data was recorded with a CamacCrate-via-USB (CCUSB) readout system. For the CERN-PS and FNAL-MTEST, the data from the Cerenkov counters were also recorded via the CCUSB system. The EMCal data were combined with the data from the trigger detectors and from the MWPCs offline, aligning the information

from the different data streams spill-by-spill.

7.2 Measurements

At the CERN-SPS, 80 GeV electrons were used for gain-matching and for studies of the uniformity of the EMCal response with a scan through all module centers and through nearly all tower centers. In order to investigate in more detail the uniformity of the light collection, data were taken at a few positions of the beam across tower and module boundaries.
Further position and angle of incidence scans were performed with 5 GeV to 60 GeV electrons with modified geometries (tilted or recessed modules) to study the uniformity of the response for different incidence locations corresponding to the super module as installed in ALICE.
Energy scans were performed using electrons in the range of 5 GeV to 100 GeV at several different positions, chosen at tower centers and edges. The goal of these energy scans was to determine the intrinsic energy and position resolution of the EMCal and to investigate the linearity of the energy response.
In addition, 100 GeV hadrons were used for a scan through a large set of towers. At a few positions energy scans with hadrons in the range of 5 GeV to 100 GeV were performed. The goal of these measurements with hadrons was to utilize the response from Minimum Ionizing Particles (MIPs) for relative tower-to-tower calibrations and to investigate the EMCal particle identification capabilities by energy-momentum mismatch and by shower shape analysis.

At the CERN-PS, a 3 GeV mixed beam was used for gain-matching using the MIP peak with a scan through all tower centers. Energy scans with 0.5 GeV to 6.5 GeV mixed beams, using the signal from the Cerenkov counter as electron trigger, were performed at several different positions. These data allow to study the EMCal energy resolution at very low energies.

At the FNAL-MTEST 16 GeV electrons were used for gain-matching through all towers. Energy scans were performed using 3, 4, 8, 16, and 33 GeV electrons with standard as well as with modified geometries (tilted and with module offsets).

The analysis of the collected data is still ongoing. As described in the following sections, the already obtained results demonstrate a very satisfactory performance of the EMCal that compares well with simulations and design values.

7.3 LED Calibration Results

In order to reach the design EMCal energy resolution for high energy electromagnetic showers, a tower-by-tower relative energy calibration of about 1% has to be obtained and maintained in the offline analysis. In addition, since analog tower energy sums provide the basis of the L0 and L1 high energy shower trigger input to the ALICE trigger decision, the EMCal should operate with APD gains adjusted to match online relative tower energy calibrations to better than about 5%.
A LED calibration system, in which all towers view a calibrated pulsed LED light source, has been successfully tested to track and adjust for the temperature dependence of the APD gains during operation. The LED triggers where collected in parallel with the beam particle events throughout the entire CERN test beam measurements. These measurements were performed with the APDs operated at the nominal fixed M=30 gain. Figure 7.2 shows an online event display for the full 8×8 tower array for the high gain channels.
The LED signal is seen in nearly all towers. The differences of the signal height between the outer left/right and the central modules are due to different setups for the transmission of the LED light pulse in the modules. The histograms show ADC value versus time sample, where each time bin corresponds

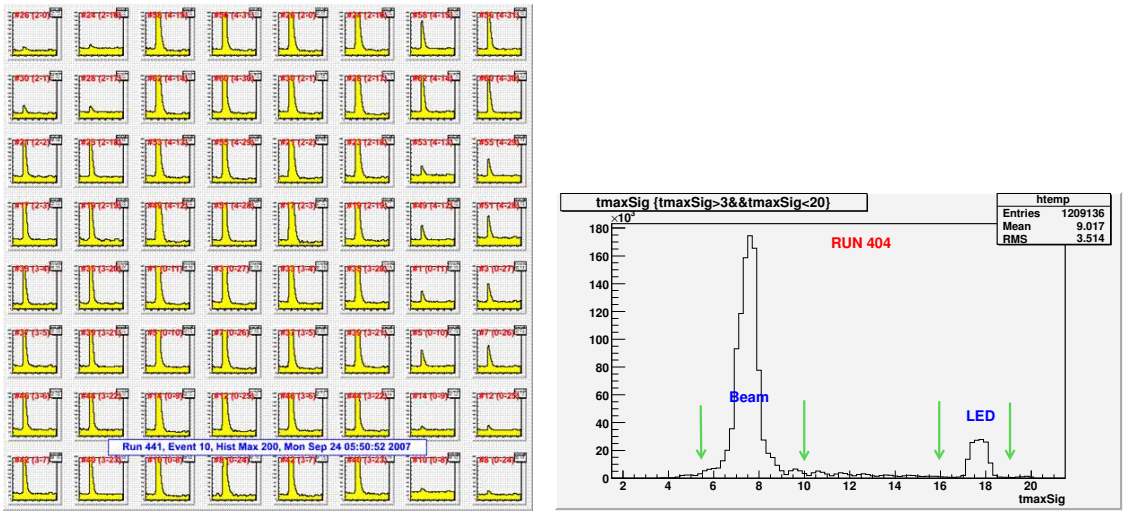

Figure 7.2: Left: Online event display for LED events in the 8×8 array of EMCal towers. The histograms show ADC value versus time sample at 100 ns interval. Right: A clear separation between beam particle and LED triggers is obtained.

to a sample at 100 ns interval. The right panel of Fig. 7.2 demonstrates that the LED events can be clearly separated from the beam particle events in the same run. LED events fire nearly all channels in the event and occur about 1 μs later than the physics triggers.

The variation of the LED signal amplitude with time and temperature was studied in order to test the system for calibration purposes. The temperature was monitored by a total of eight temperature sensors mounted at the top and bottom of each strip unit. The measured LED amplitude variation for a given tower as a function of time is compared in Fig. 7.3 for the same time interval with the temperature readings from the nearest sensor for the module in which the tower was located. A clear anti-correlation is observed.

Figure 7.4 shows the variation of the LED signal amplitude (low gain) over the entire period of test beam measurements at CERN, together with the temperature variation for the same period. Some of the sharp variations in the LED amplitude seen in Fig. 7.4 cannot be attributed to temperature changes but rather to LED light yield changes, as when the setup was reconfigured. These changes of the overall LED light were taken into account with an iterative extraction of the temperature coefficients. First, a new time interval was defined if an APD amplitude changed by more than 20 % from one hour to the next. For each such time interval, both low and high gain LED amplitudes were fit simultaneously as planes in space defined by APD amplitude, temperature, and the time interval. In a first iteration, all points deviating by more than $1.5\,\sigma$ from a predefined slope range ($0.015 < \mathrm{d}M/\mathrm{d}T < 0.025$) were excluded. In the next iteration, the cleaned sample was fit with free parameters for the slope in order to define the temperature coefficient. Figure 7.5 shows the LED amplitude for a typical tower as a function of the temperature and for a certain time bin.

The temperature coefficients obtained from the fits of distributions as presented in Fig. 7.5 were used to correct for the time dependence of the APD gain. As an example, the corrected LED amplitude is shown in the lower panel of Fig. 7.3 for the considered time interval.

A new class in the AliRoot calibration environment was introduced that stores the selected LED event amplitudes as well as the information from the temperature sensors as a function of time. Furthermore, an interface that allows for time-dependent calibration corrections in the offline AliRoot analysis was developed and tested.

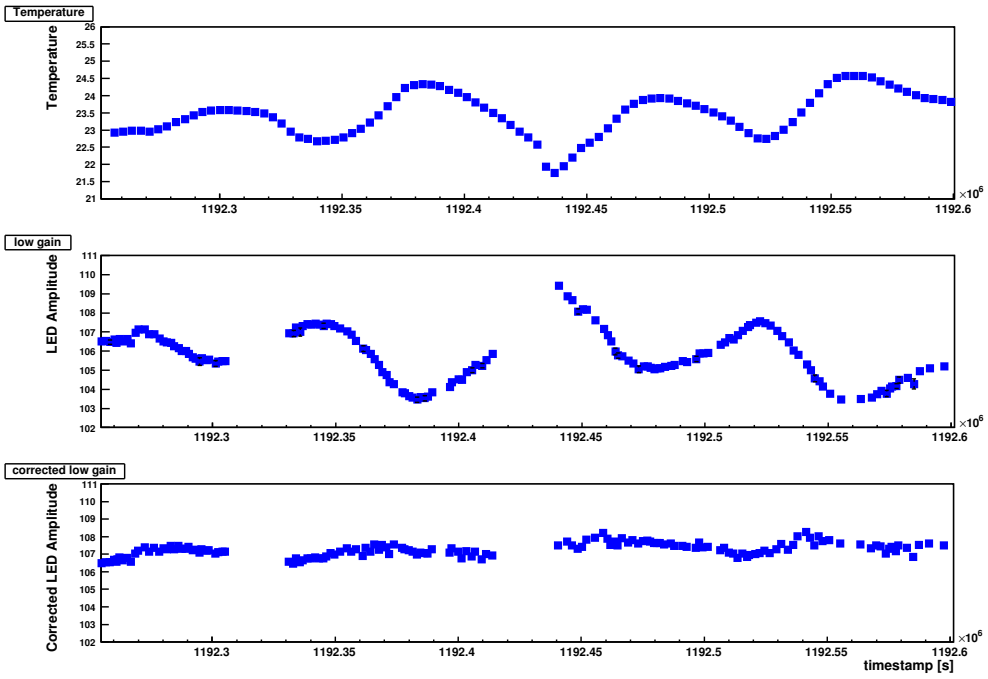

Figure 7.3: Upper panel: temperature measurement as function of time. Mid panel: LED peak amplitude for a typical tower for the same time interval. Lower panel: corrected LED peak amplitude.

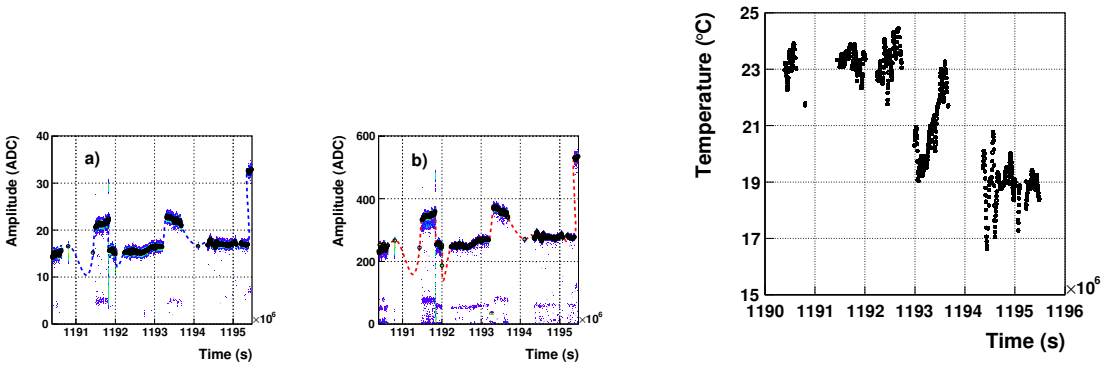

Figure 7.4: Left: LED peak amplitude variation (low gain) over the whole period of test beam measurements at CERN for a typical tower. Right: temperature variation for the same period

7.4 Analysis

Since the energy of an electromagnetic shower spreads over several EMCal towers, the energy deposited in the cluster of towers in which energy has been deposited must be summed, with proper relative calibration, in order to extract the total energy deposit in the EMCal. However, since the initial relative calibrations of the towers are unknown, the extraction of the calibration coefficients must be done iteratively.

Furthermore, energy may be missing from the sum energy peak as towers on the edge of the cluster may have signals which fall below the pedestal threshold of the towers. Also, the tower calibrations must be determined over a long period of time as the array of modules is scanned through the beam,

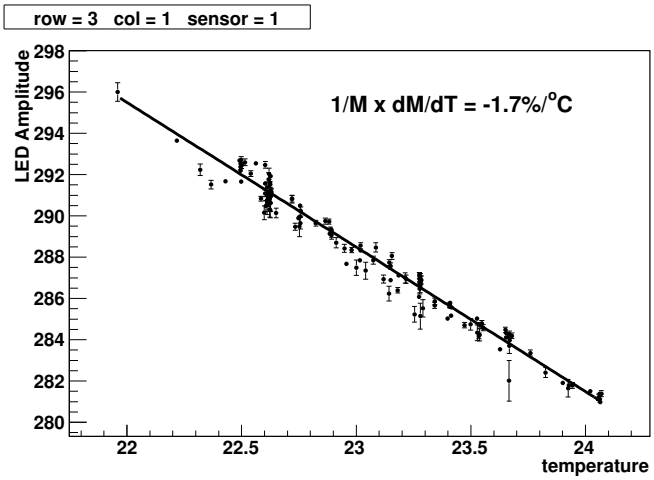

Figure 7.5: LED peak amplitude as function of the measured temperature.

with the result that the relative calibrations may be determined at different ambient temperatures with corresponding APD gain shifts.
As described in Chapter 3 and shown in Fig. 7.6 the digitized time samples have an amplitude as a function of time t that can be described with the form of a Γ-function as $ADC(t)$, where

$$ADC(t) = \text{Pedestal} + \text{A} \cdot x^{\gamma} \cdot \exp^{\gamma \cdot (1-x)} , \qquad (7.1)$$
$$x = (t - t_{max} + \tau)/\tau .$$

Here, t_{max} is the time value where the function peaks, τ is the decay constant and γ is the power parameter of the fit (typically fixed at $\gamma = 2$). The charge collected from the APD, and hence the energy deposited in the tower, is proportional to the value of the parameter A.
An important feature in the test beam analysis was to check if the parameters of the fit describe well the characteristics of the raw data. In particular, the amplitude and time values are used in all later steps of the analysis. A quality parameter was introduced, which represents the average value of the relative difference between the raw signal (ADC counts) and the fit function. This variable was studied for a large set of electron data. As a result, the AliRoot fit routine was further optimized. In addition, the High-Low gain correlation was studied using the electron data. The goal was to determine a threshold value for the amplitude for which the low gain rather than the high gain needs to be used due to saturation (at 1023 ADC counts). A good High-Low gain correlation with an average ratio of 16.3 between both gains was found up til 1050 ADC counts.
An overall inter-calibration procedure was carried out for all towers by normalizing the hadron MIP amplitudes in each tower, to one of the central towers. Isolation of the MIP peak was achieved requiring, for each tower, no energy deposit in the surrounding eight towers. An alternative inter-calibration map was also considered by using the information given by the electron beam peak in each tower.
An absolute calibration for each tower was obtained by comparing the nominal electron beam energy with the corresponding peak in the energy spectrum, as obtained by a sum over a 3×3 tower cluster. For this purpose, 3×3 local cluster inter-calibration coefficients were extracted from the overall map, by choosing each tower in turn as a reference. This allowed to evaluate the energy spectrum by a sum over the 9 towers in the cluster, with a proper calibration adjusted to match that of the central tower in each cluster. An example is shown in Fig. 7.7 for an 8 GeV mixed beam (from FNAL-MTEST) with the region of the MIP peak enhanced in the insert.
For a typical run, Fig. 7.8 shows the reconstructed energy for 80 GeV incident electrons obtained with the calibration procedure described above (left panel). The right panel shows the same data but using the

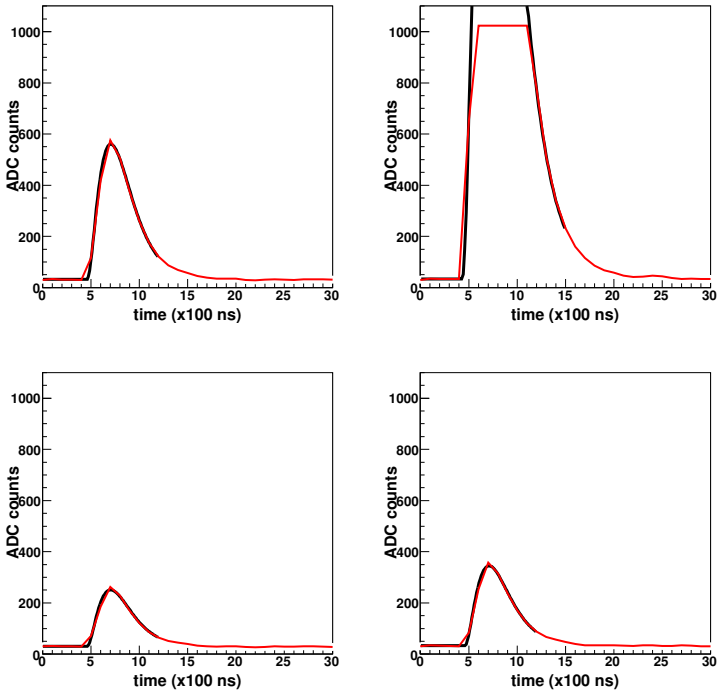

Figure 7.6: Pulse shape distributions in a 2×2 area of the EMCal where the electron beam hits roughly the center of the four towers. The red line represents the ADC counts and the black line the fit of the distributions according to Eq. 7.1.

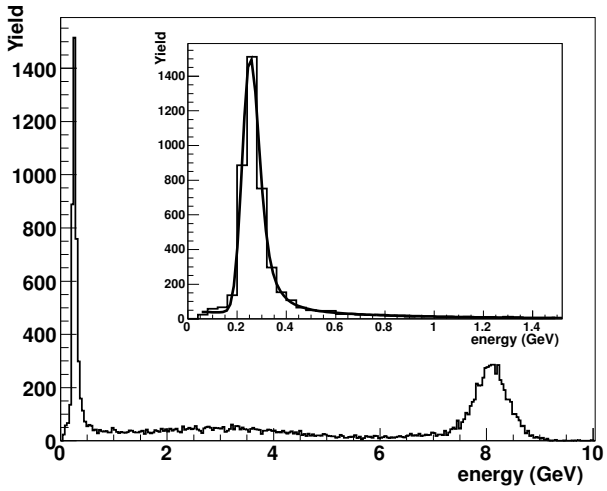

Figure 7.7: Reconstructed energy for 8 GeV mixed beam. The electron peak is well centered at the incident beam energy. The insert shows the energy spectrum in the region of the MIP peak. The continuum between both peaks results from showering hadrons.

full AliRoot standard EMCal reconstruction software with calibration coefficients obtained as before.

7.5 Light Yield

An important goal of the test beam measurements was to extract the average light yield, or number of photoelectrons at the APD per unit of electromagnetic energy deposit in the EMCal (photoelectrons/MeV).

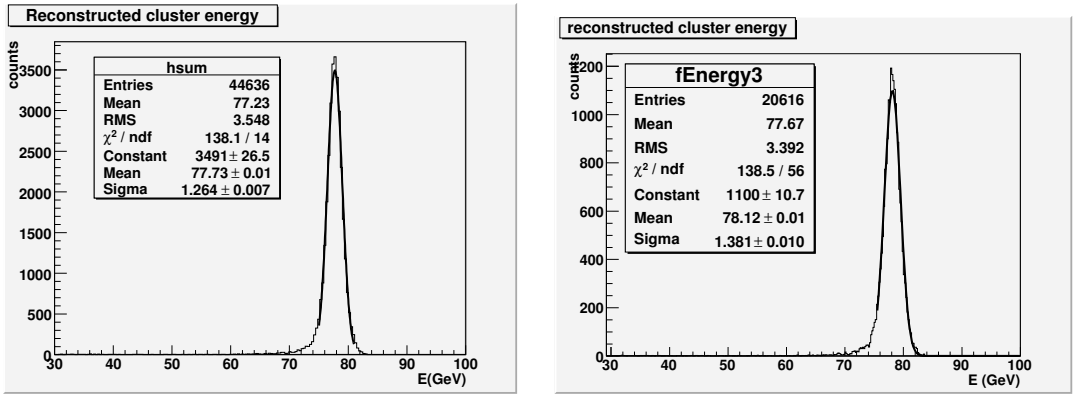

Figure 7.8: Left: Reconstructed energy for 80 GeV incident electrons using the 3×3 cluster algorithm. Right: Reconstructed energy for 80 GeV incident electrons using the AliRoot standard reconstruction algorithm.

This quantity determines the overall APD+shaper gain required to match the desired dynamic range in ALICE to that of the input signal to the digitization ALTRO chip. Due to the large number of individual towers planned for the final design of the EMCal, it is also important to estimate the tower-to-tower dispersion of the light yield.
Following the calibration procedure described in Section 7.4 an absolute calibration was obtained for a significant number of towers. Since measurements were carried out at several PS and SPS energies, from 0.5 GeV to 100 GeV, the light yield may in principle be extracted for each tower at several beam energies. However, the linearity of the energy response has been checked over the available energy range and a good linearity was found between the nominal beam energy and the corresponding numbers of ADC channels as shown in Fig. 7.9 (left) for four typical towers. A linear fit of the ADC vs. nominal beam energy gives the calibration coefficient (channels/MeV).

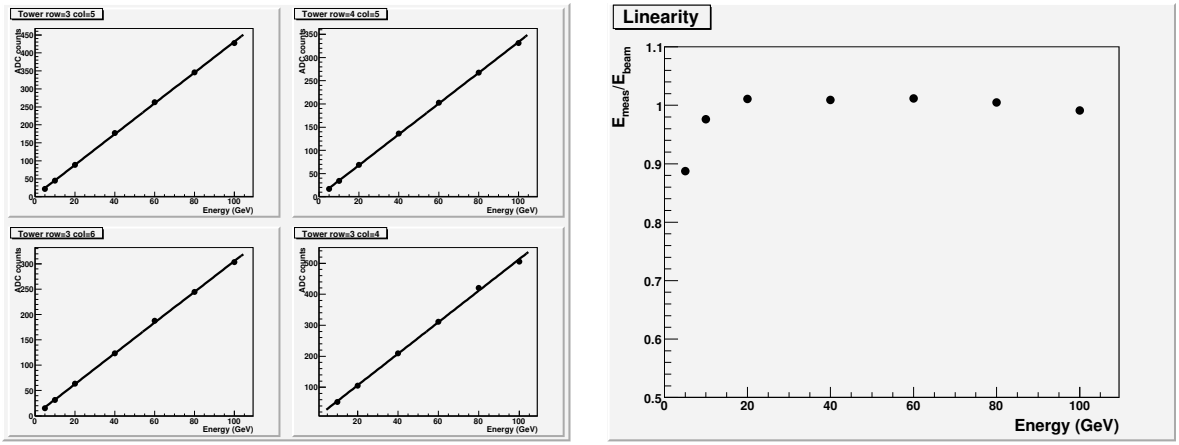

Figure 7.9: Left: ADC values (low gain channel), as obtained by a sum over the 3×3 cluster, versus the nominal SPS beam energy. Right: Average value of the measured to incident beam energy as function of the incident beam energy for several different positions taken at the SPS.

The average value of the measured to incident beam energy as function of the incident beam energy is shown in Fig. 7.9 (right) for several different positions and for the CERN-SPS energies. Deviations of this ratio from unity are expected at high energies due to leakage, or at very low energies due to tower thresholds being non-negligible with respect to the total energy, or due to light transmission losses in the WLS.
During the test beam, the APDs were all operating at gain M=30 with an individual voltage setting,

which was established by a procedure carried out on each APD prior to the test beam measurements, comparing the amplitude at a given bias voltage to the amplitude measured at low voltages, where the gain is assumed to be unity.
The light yield at the gain M=30, for each individual tower, may then be extracted following

$$LightYield(p.e./MeV) = (channels/MeV) \cdot (1/G_A) \cdot (1/P_G) \cdot (1/ADC_{conv}) \tag{7.2}$$

where the shaper amplifier gain G_A = 0.229, the charge voltage conversion factor of the CSP, P_G = 0.83 V/pC and the ADC conversion ADC_{conv} = 1024 channels/V, as discussed in Section 3.3 [1]. The light yield at unit gain (M=1) is obtained from this value divided by 30. As an example, with the above values, a light yield of 4.63 photoelectrons/MeV is obtained from the data reported in the upper left plot in Fig. 7.9.
A statistical analysis of the light yields obtained for several central towers was performed. This analysis will be extended to all central towers. As a preliminary result, the average light yield was found to be (4.3 $\pm$ 1.4) photoelectrons/MeV, essentially the same as the light yield value of PHOS and as the light yield found for the prototype from the FNAL measurements of (4.4 $\pm$ 0.6) photoelectrons/MeV. Figure 7.10 shows the distribution of the light yield for several towers in the FNAL test beam measurements with the prototype (left) and in the CERN measurements with the modules of final design (right).

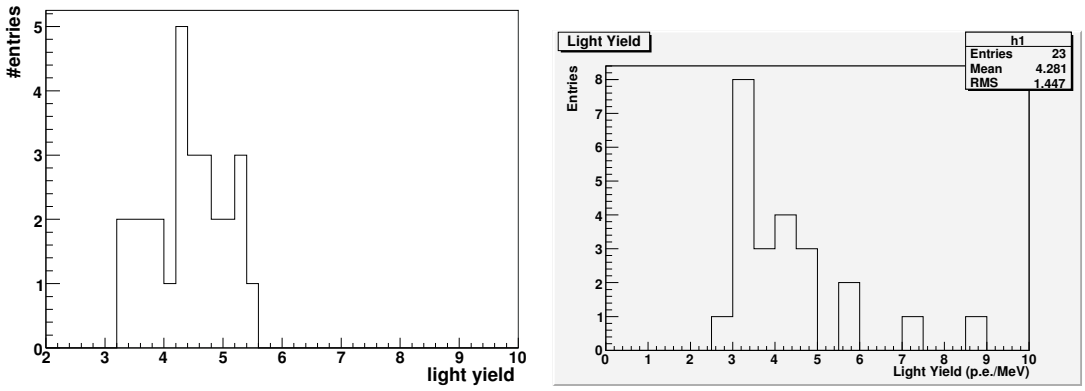

Figure 7.10: Distribution of extracted light yields in photoelectrons/MeV (for APD gain M=1) for several central towers from test measurements at FNAL with prototype modules (left) and at CERN with modules of final design (right). These results are preliminary.

7.6 Beam Results

7.6.1 Energy Resolution

A major goal of the test beam measurement was to investigate the energy resolution (δE/E) of the EMCal and its variation as a function of energy.
An absolute energy calibration of the test beam data was obtained as described in section 7.4 from the known incident electron energy using an iterative procedure. An initial relative tower-by-tower calibration was performed using the MIP peak from the hadron beam at the CERN-SPS or from the mixed beams at CERN-PS and FNAL-MTEST. The LED calibration system (see section 7.3) was used to track and adjust for the time dependence of the calibration coefficients. By combining data taken at the CERN-PS and SPS the energy range of 0.5 GeV to 100 GeV could be explored. Such energy scans were performed at several different positions, including tower and module edges. No systematic variation of the resolution depending on the position was observed. The resolution obtained at the different positions was combined

and the average values as a function of the incident beam momentum are displayed in Fig. 7.11. For the SPS data, the momentum spread of the incident beam of typically 1.3% was subtracted in quadrature.

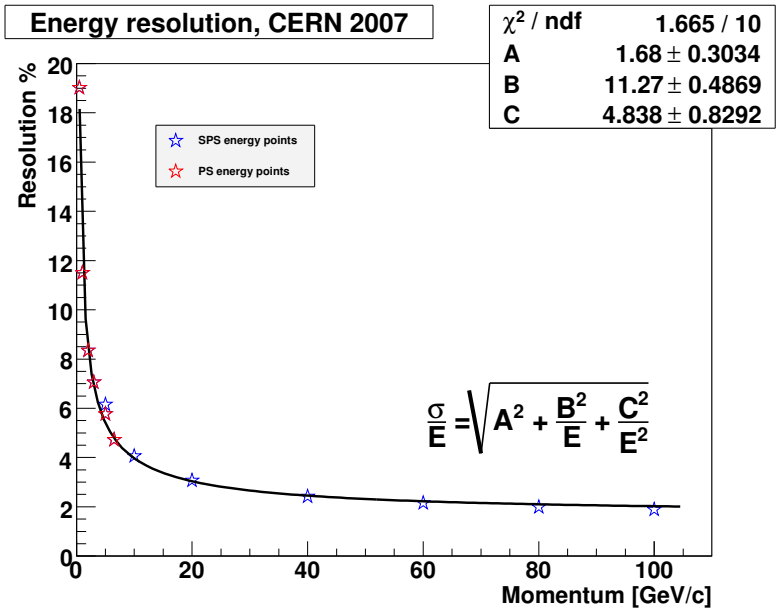

Figure 7.11: Energy resolution for electrons as function of the incident beam momentum. The beam energy spread was subtracted from the measured result.

A fit to the energy resolution as function of the incident energy is also shown in Fig. 7.11. The fit is made with the conventional constant, $\sqrt{E}$, and linear E terms, added in quadrature. The constant and $\sqrt{E}$ terms, respectively $a = 1.7 \pm 0.3$ and $b = 11.3 \pm 0.5$, may be compared with the GEANT3 simulation result for the EMCal module geometry (without light transport included in the simulation) shown in Fig. 2.3 that gave $a = 1.44 \pm 0.03$ and $b = 6.9 \pm 0.1$. The performance is quite similar to the PHENIX EMCAL [4] with similar physical characteristics and better than the stated requirements (see Chapter 3). Using the data from the FNAL test beam, possible effects of the shorter design shaping time for the EMCal of 100 ns (compared to 1 μs for PHOS) were studied. Figure 7.12 shows the energy resolution as function of the incident energy, where the fit is made to the conventional constant and $\sqrt{E}$ terms, added in quadrature. The results are shown separately for the long and short shaping time readout regions of the test setup, averaged over many runs in each region. There is some apparent difference in the resolution for low incident energies, with somewhat poorer resolution for the short shaping time. This is attributed to the lower gain and corresponding higher effective tower thresholds for the channels with the shorter shaping time. No significant difference is observed between the results with the two shaping times when the tower energy thresholds are raised in the analysis to be the same everywhere. Summing all data together gives a fit result with the two terms added in quadrature of $b = 10.8 \pm 0.7$ and $a = 2.0 \pm 0.3$. This may be compared with the GEANT3 simulation result for the prototype module geometry (without light transport included in the simulation) shown in Fig. 2.3 that gave $b = 7.91 \pm 0.05$, $a = 1.05 \pm 0.02$. The performance of the prototype modules is very similar to that of the final modules presented above.

7.6.2 Linearity and Uniformity of the Energy Response

Together with the energy resolution studies, the linearity of the energy response was investigated. Combining the measurements at the various different positions, the average value of the reconstructed to incident beam energy as function of the incident beam energy was already shown in Fig. 7.9 (right). A very good linearity is observed. As discussed earlier, deviations of this ratio from unity are expected at high energies due to leakage. This is not yet seen in the data. At very low energies, threshold effects

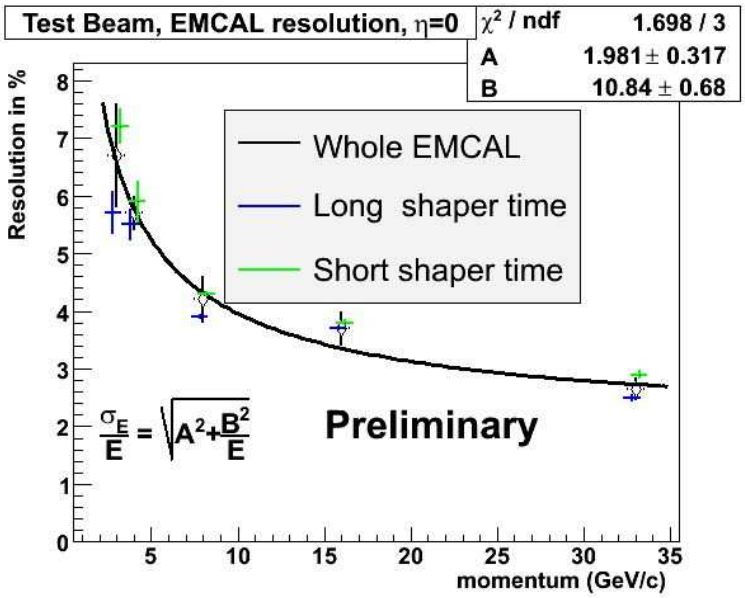

Figure 7.12: Energy resolution for electrons as function of the incident beam momentum for short (EMCal design) and long (PHOS design) shaping times. The fit result is given for the combined data set.

might be non-negligible compared to the total energy and light transmission losses might have an impact. In fact, the reconstructed energy is systematically lower than the incident one for energies equal or below 5 GeV. A drop of $\sim 10\%$ is observed at 5 GeV.

The uniformity of the energy response was studied for several different conditions. All module centers and a major part of tower centers were scanned using 80 GeV electrons. In addition, data were taken across tower and module borders as well as for tilted or recessed modules, as at the large Z end of a super module. The latter allow to study the uniformity of the response for incidence on towers in different locations within the super module as installed in ALICE. Figure 7.13 shows the reconstructed energy (upper panel) and resolution (lower panel) for the different configurations as listed before and indicated in the figure. At the corners and towers located at the edges (marked with red in the figure) significant losses are expected (which however are partially compensated by the calibration constants).

The presented results are still preliminary. No correction for time dependent effects have been applied yet. These might be important as data taken in very different time periods are compared. Also a full tower-by-tower recalibration has still to be completed. These preliminary results already give a response of the EMCal with an RMS better than 1 GeV, for 80 GeV incoming electrons (see upper, right plot of Fig. 7.13). This result implies a very good uniformity of the EMCal construction and readout. In particular, no systematic effect is observed for positions across tower or module boundaries. The still large variations of the energy resolution at different positions, varying from 1.5% to 4.3%, underline the need for a full tower-by-tower inter-calibration.

The energy resolution was also studied for different incidence locations corresponding to the super module as installed in ALICE. Most of the test beam data were taken with a configuration where the beam hits the EMCal modules perpendicularly, corresponding to $z = 0, \eta$=0 position of the modules. Data were taken also with configurations where the modules were tilted in ϕ by 6 deg or 9 deg at different surface positions. Figure 7.14 shows the energy resolution for such tilted configurations at two different positions obtained with electrons of 10 GeV to 60 GeV. These values are compared to the average resolution as function of energy already presented in Fig. 7.11. No significant difference with the average resolution at zero position was observed.

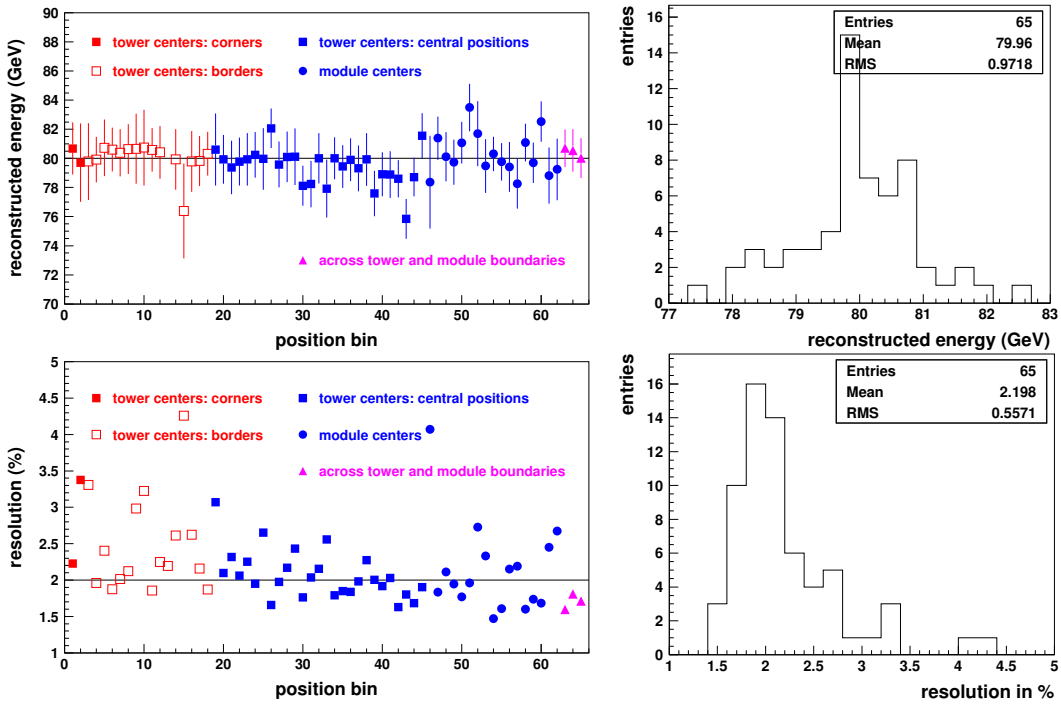

Figure 7.13: Upper panel: reconstructed energy for 80 GeV electrons at different positions as indicated in the figure and described in the text. Lower panel: the corresponding energy resolution for 80 GeV electrons at different positions as indicated in the figure.

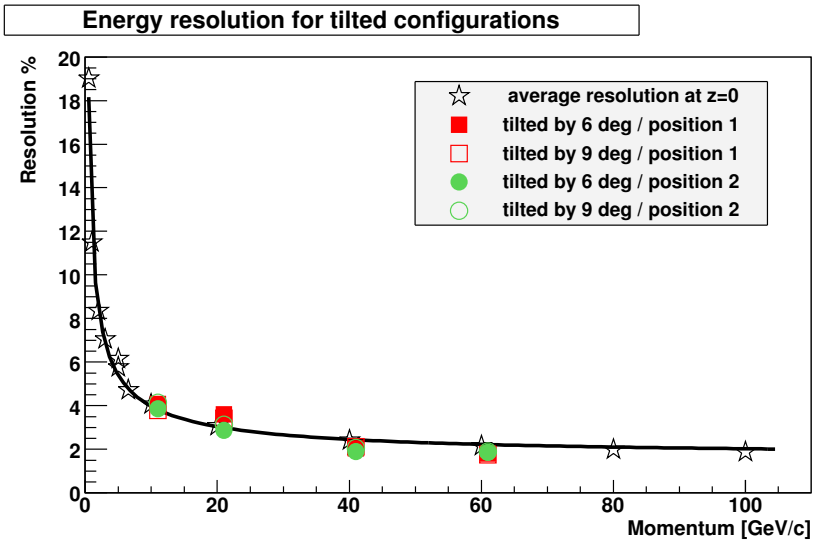

Figure 7.14: Energy resolution for electrons as function of the incident beam momentum for tilted configurations as labeled in the figure.

7.6.3 Position Resolution

The FNAL test beam data were also analyzed using the incident beam location projected from the tracking information from the MWPCs to investigate the position resolution of the EMCal. The x and y positions in the EMCal are calculated using distribution of energies in the towers of the cluster. The coordinate locations are calculated using a logarithmic weighting [5] of the tower energy deposits. The x and y position resolution as a function of incident momentum for electrons is shown in Fig. 7.15. As

expected no significant difference between the x and y position is observed. The electromagnetic shower position resolution is seen to be described as 1.5 mm + 5.3 mm/$\sqrt{E_{Deposit}}$.

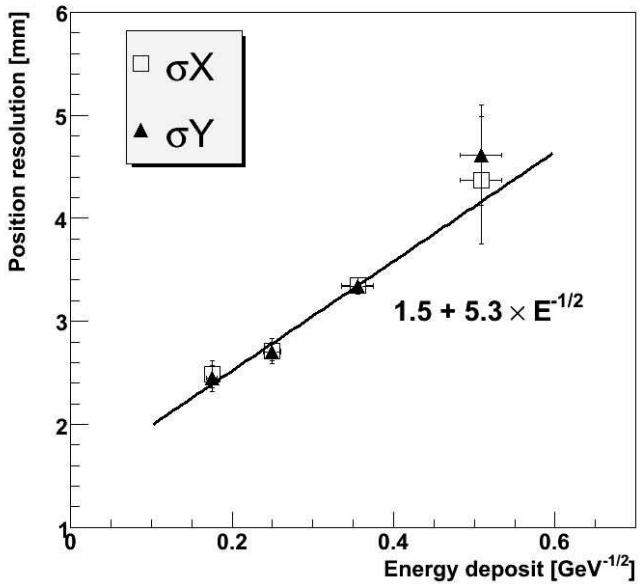

Figure 7.15: Dependence of the position resolution as a function of $1/\sqrt{E}$ (GeV) for electrons. The curve shows the best fit result.

Figure 7.15 showed the energy dependence of the position resolution averaged over many runs over much of the prototype detector. Figure 7.16 shows the position resolutions for individual runs with beam incident on different locations on the detector for 8 and 16 GeV electrons. While there is a clear systematic difference in the position resolution for the two incident energies, there is no apparent systematic dependence on the incident location, or on the long versus short shaping time FEE channels.

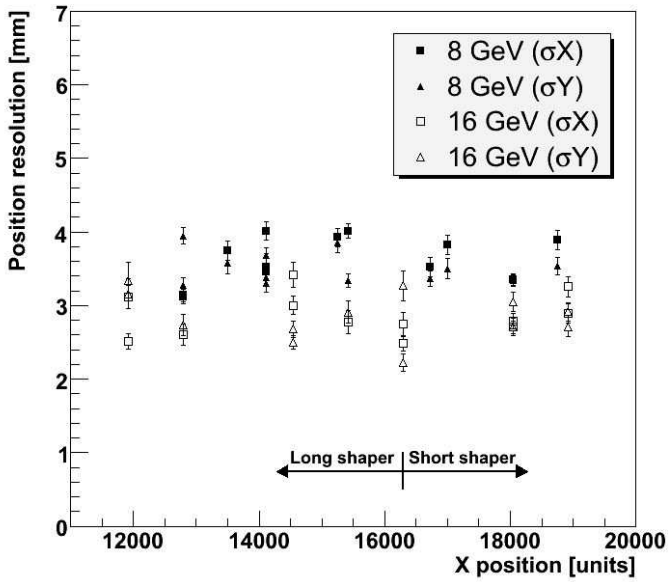

Figure 7.16: Dependence of the position resolution on the location of beam incident on the prototype detector for 8 and 16 GeV electrons.

The investigation of the position resolution for the final design modules tested at CERN is still ongoing.

First, very preliminary results indicate a similar performance as obtained for the first prototype.

7.7 Conclusions

Test beam measurements have been performed with an EMCal prototype at FNAL in November 2005 and with modules of final design and instrumented with the final electronics chain at CERN in autumn 2007. The readout of the EMCal front end electronics used the full ALICE DAQ readout chain.
A LED calibration system was installed in order to monitor time-dependent changes. It's operation was successfully tested and corrections for time-dependent effects were applied in the offline analysis of the test beam data. The AliRoot calibration routines were further developed in order to handle these time-dependent corrections.
The measurements at FNAL were in particular made for comparison of the performance with two different signal shaping times in the front end electronics (see Section 3). Two front end electronics cards were used for the readout of the modules; one had the nominal 1 μs signal shaping time which PHOS will use, and the other had a modified 100 ns shaping time as planned to use for EMCal [1]. No significant difference was observed for the energy resolution obtained with the two shaping times. Also, no effect of the shorter shaping time was observed for the position resolution.
The energy resolution of the final test modules was determined using electrons of 0.5 GeV to 100 GeV. A fit to the conventional constant and $\sqrt{(E)}$ terms gave $a = 1.7 \pm 0.3$ and $b = 11.3 \pm 0.5$, respectively. This performance is better than the stated requirements (see Chapter 3).
A very good uniformity of the energy response was found with a RMS better than 1 GeV, for 80 GeV incoming electrons. This value is still preliminary. In particular, no significant difference in the energy response was observed for configurations central to the towers and modules or across the boundaries. The energy resolution obtained for tilted configurations with 6 and 9 degrees in phi compares well with the average energy resolution stated above.
The electromagnetic shower position resolution for the prototype modules was seen to be described as 1.5 mm + 5.3 mm/$\sqrt{E_{Deposit}}$. As expected, no significant difference between x and y positions was observed.
The analysis of the CERN test beam data is still ongoing. In particular, the uniformity studies will be finalised after completing the full tower-by-tower re-calibration and the correction for time dependent effects using the information from the LED calibration system.
Furthermore, ongoing analyses are investigating the position resolution for the final EMCal modules as well as the response of the EMCal to hadrons by shower shape studies. The results from these analyses will be summarized in an upcoming publication.

8 ALICE EMcal Physics Performance

8.1 Physics Performance

ALICE is a large acceptance experiment with unique particle tracking and identification capabilities. ALICE measures charged particle momenta over three orders of magnitude, from 100 MeV/c to 100 GeV/c - a range that is unparalleled at the LHC.
Jet quenching can be considered to be the QCD analog to QED bremsstrahlung, where even a very high energy charged projectile in matter radiates dominantly soft photons. Jet quenching similarly couples high energy probes to soft radiation in the medium, thus a broad dynamic range in tracking is needed to fully explore the physics of quenching. This approach has been validated by the experience of the RHIC experiments.
The EMCal will complete ALICE's capabilities to measure jet quenching, by providing an efficient and unbiased fast jet trigger (Level 0/1) and measurement of the neutral portion of the jet. Jet measurements using precise charged particle tracking and EM calorimetry are well-suited to studying jet quenching: the jet energy resolution is comparable to that achievable with purely calorimetric jet measurements, and precise tracking is required for sensitivity to the physics signals of quenching.
A fast jet trigger increases the kinematic reach of ALICE substantially to enable measurement of jets beyond 200 GeV. QCD evolution will influence the physics of jet quenching [1], but its effects will be visible only with measurements over a large dynamic range in jet energy. While this issue is currently at the frontier of QCD theory, and calculations are highly uncertain at present, they suggest that quenching measurements over a broad kinematic range will provide unique and sensitive new probes of the structure of hot QCD matter.
The EMCal also triggers and measures high p_{t} photons and electrons. The photon trigger enhances ALICE's existing capabilities for measuring high p_{t} π^0, direct photon, and photon+jet coincidences. The electron trigger enables ALICE to measure heavy flavor jets at energies of 80 GeV and above, a crucial capability for elucidating the physics underlying jet quenching.
The following sections describe these various capabilities in more detail.

8.2 Simulation Framework

All results presented here are based on detailed GEANT simulations of the ALICE detector and the EMCal, incorporating all known detector material. Special attention was paid to accurate modeling of material within the geometric acceptance of the EMCal, which is a significant source of photon conversions and electron bremsstrahlung. The official ALICE simulations and software frameworks were used wherever possible.
Event generation utilized PYTHIA for p–p events (both minimum bias and with a jet trigger bias) and HIJING for the Pb–Pb heavy ion background. AliPyQuench was used to model jet quenching effects, whose magnitude is controlled by the in-medium transport coefficient $\hat{q} = \mu^2/\lambda$ [2], where μ is a typical momentum transfer in interactions between the hard parton and the medium and λ is the mean free path of soft gluons. Extraction of $\hat{q}$ from RHIC data has large uncertainties at present, but extrapolation to central Pb–Pb collisions at the LHC yields estimates in the range $\hat{q} \sim 20 - 50$ GeV^2/fm.
Figure 8.1, left panel, is the transverse projection of the ALICE central detector, showing the distribution of conversion vertices for photons within the EMCal acceptance. Figure 8.1, right panel, shows the cumulative fraction of high energy photons within the EMCal acceptance that convert within a given radial distance from the IP. The bulk of the conversions are seen to occur in the Transition Radiation

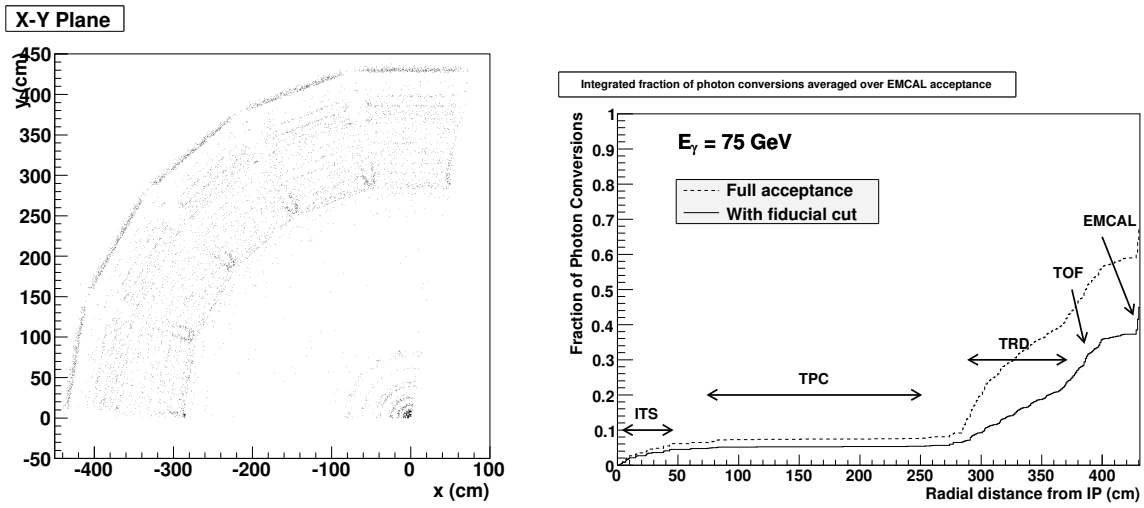

Figure 8.1: Left: Transverse projection of sources of photon conversion within the EMCal acceptance. Right: Integrated fraction of photon conversions as a function of radius from beamline, averaged over the EMCal acceptance. Dashed line is average over full EMCal acceptance, while the calculation for the solid line excludes phase space near the edges of the super modules that is subtended by the spokes of the TPC support structure. Radial positions of the major ALICE subsystems are indicated.

Detector (TRD) and Time of Flight (TOF), which are outside the TPC. Background electrons from such conversions can be rejected with high efficiency through the requirement that an electron shower match to a charged track of the correct momentum.
The cumulative conversion rate is shown averaged over the entire EMCal fiducial area (dashed line) and constrained to phase space that excludes the super module boundaries (solid line). The excluded region is subtended by the spokes of the TPC support structure and other material. This fiducial cut is applied in the photon and electron analyses.

8.3 EMCAL Trigger

8.3.1 Trigger Requirements and Design

Exploitation of the EMCal kinematic reach for inclusive jets requires an efficient, fast trigger (Level 1) that can discriminate the collimated energy flow in a jet from the heavy ion background. The core of jet energy is spread over a region larger than the phase space subtended by a single TRU, and additional trigger processing capability is required for efficient jet triggering.
The PHOS/EMCal TRU performs FADC digitization of 2×2 tower analog sums, which are input to the L1 photon/electron trigger. The "jet patch" trigger is implemented by transmitting all such 2×2 sums from all TRUs into a single FGPA on the Summary Trigger Unit (STU), via LVDS cables clocked at 40 MHz (see Chapter 5). A simple jet-finding algorithm is then applied over the entire EMCal acceptance, in which the energy is integrated within a patch of defined size (typically $\sim0.3\times0.3$) and the patch is stepped over the entire EMCal fiducial area. An L1 jet trigger signal is issued if a patch energy in the event exceeds a defined threshold.
Heavy ion events are characterized by background multiplicity and E_{T} production whose magnitudes are closely correlated with the impact parameter of the collision. The underlying background in a large jet cone may contribute hundreds of GeV in "central" events (small impact parameter). Such background can be estimated in offline analysis on an event-wise basis to correct the measured jet energy, but it must also be taken into account in the L1 trigger in order to achieve similar trigger efficiency for all heavy ion collision centralities. This correction is achieved in the EMCal jet trigger by adjusting the trigger

threshold in the STU FPGA by an amount proportional to the summed amplitudes of the V0 detectors. The V0 are forward scintillator detectors ($-3.7 < \eta < -1.7$, $2.8 < \eta < 5.1$) whose response is closely correlated with multiplicity and E_{T} in the ALICE central region. The fast V0 signals are digitized to 12 bits and transmitted to the EMCal trigger crate via fiber optic cable.
Due to TPC gating rate limitations and High Level Trigger and DAQ bandwidth constraints, the L1 jet trigger is required to achieve a rejection of 10 for minimum bias Pb–Pb and 2500-3000 for minimum bias p–p events. These two cases represent the extremes in terms of interaction rate vs. event size, and serve to bracket the required EMCal jet trigger performance.
The EMCal Jet Trigger hardware implementation is described in Chapter 5.

8.3.2 Jet Trigger Performance

The EMCal trigger architecture described in Section 8.3.1 has been modeled in full and its response analyzed using the detailed ALICE GEANT model. Modeling of the V0 response includes the contribution of interactions in the beam-pipe and other material subtending its acceptance.

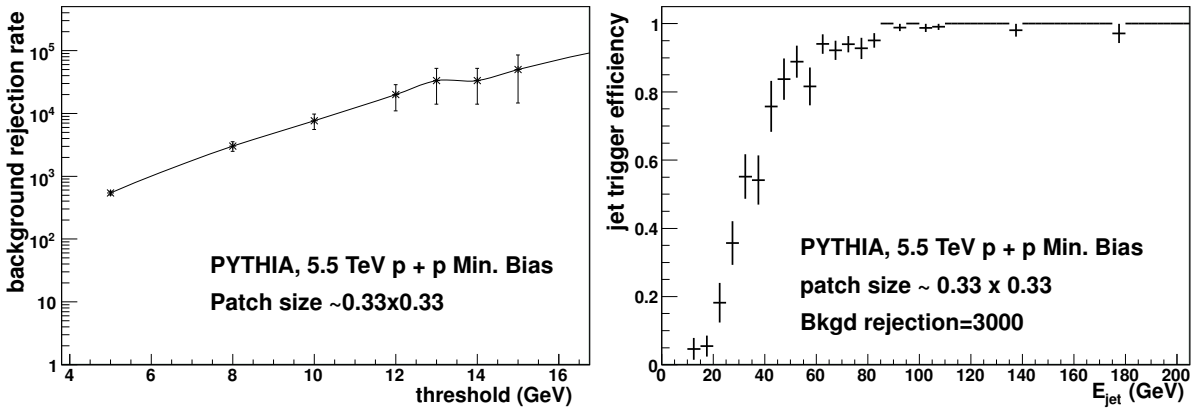

Figure 8.2: Jet trigger performance for 5.5 TeV p–p events. Left: Background rejection rate vs. trigger threshold. Right: Jet trigger efficiency vs. jet energy.

Figure 8.2, left panel, shows background rejection vs. threshold for 5.5 TeV minimum bias p–p events, for a jet trigger patch of size $d\eta \times d\phi = 0.33 \times 0.33$. The right panel shows the jet trigger efficiency for rejection 3000, achieved with a threshold ∼8 GeV. 90% efficiency is achieved at $E_{jet} \sim$ 60-70 GeV.
There is little theoretical guidance at present concerning angular broadening due to jet quenching. We therefore constrain our trigger studies to a conventional fragmentation model (PYTHIA), mindful that the trigger scheme must remain flexible in order to accommodate unanticipated new effects.
Figure 8.3 shows the same calculations for Pb–Pb collisions, incorporating the V0-based threshold correction. A rejection factor 14 generates ∼90% jet efficiency at $E_{\mathrm{T}}^{jet} \sim 90$ GeV. Trigger efficiency turn-on near threshold is not as sharp as in p–p - an effect related to the V0 threshold correction. Studies to optimize this threshold behavior are in progress.

8.3.3 Jet Trigger Enhancement Factors

Table 8.1 shows the expected enhancement, for various collision systems, in recorded jet events due to the EMCal jet trigger, compared to ALICE capabilities without the EMCal. The assumed luminosity and effective running time are shown. The comparison is between the rate of jets triggered by and reconstructed with the EMCal, and jets recorded using geometrical triggers only (minimum bias Pb–Pb or p–p, or central Pb–Pb) and reconstructed solely using charged tracks. The enhancement calculation takes into account the EMCal jet trigger acceptance relative to charged particle jets (17.3%) and trigger efficiency

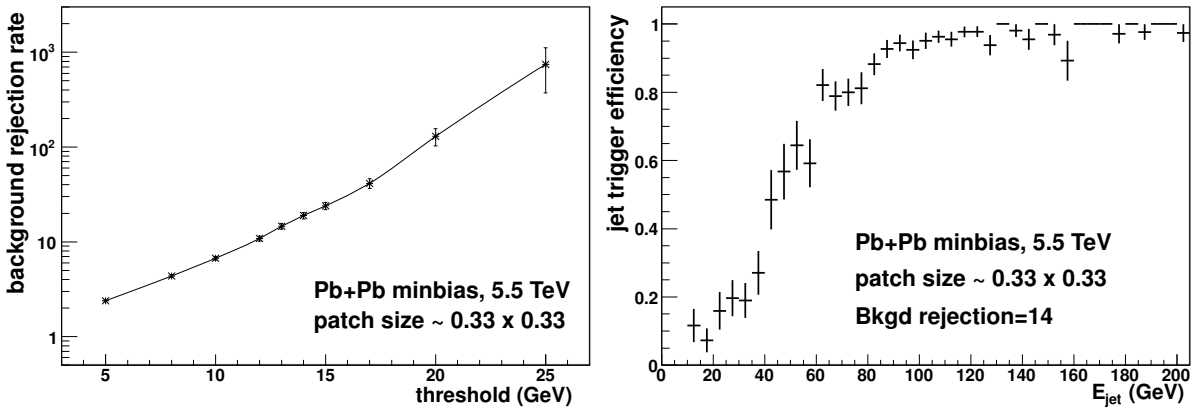

Figure 8.3: Jet trigger performance for 5.5 TeV Pb–Pb events. Left: Background rejection rate vs. trigger threshold. Right: Jet trigger efficiency vs. jet energy.

System	$\sqrt{s_{NN}}$ (TeV)	L_{mean} $(cm^{-2}s^{-1})$	Time (s)	DAQ rate (Hz)	EMCal Trigger gain
p+p	5.5	$5 \cdot 10^{30}$	10^6	500	110
p+p	14	$5 \cdot 10^{30}$	10^7	100	550
p+p	8.8	$1 \cdot 10^{29}$	10^6	500	110
Pb+Pb					
cent 10%	5.5	$5 \cdot 10^{26}$	10^6	20	5.3
periph 60-80%	5.5	$5 \cdot 10^{26}$	10^6	20	53

Table 8.1: Gain in recorded jet statistics for various systems due to EMCal Jet Trigger, together with assumed mean luminosity, annual running time and ALICE DAQ rate.

and live-time (combined factor 80%), together with event rate limitations due to DAQ bandwidth and maximum TPC gating frequency.
The enhancement factors in Table 1 are applicable for $E_{jet} >\sim 100$ GeV, where the trigger is efficient (see Figs. 8.2 and 8.3). The enhancement factor is seen to be greatest for the smallest systems (p–p, peripheral Pb–Pb). This is because the smallest systems have the largest interaction rate, while the ALICE DAQ rate is limited in all cases to ∼500 Hz.
The background rejection and jet efficiency shown in Figs. 8.2 and 8.3, calculated with full simulation of the trigger architecture and a detailed GEANT model of the detector response, is similar to trigger performance studies based on parametrized models shown previously. The jet trigger is seen to provide good background rejection and signal efficiency for $E_{jet} > 100$ GeV. Table 8.1 shows that this capability brings a significant enhancement to the ALICE physics program.

8.4 Jet Reconstruction

High-E_{T} jets that are clearly identifiable over the heavy ion background are produced copiously at the LHC [3, 4]. It is nevertheless challenging to achieve good jet energy resolution in the heavy ion environment. This section presents an overview of the main experimental considerations for jet reconstruction in heavy ion collisions, and discusses our current understanding of jet reconstruction performance in proton-proton and heavy ion events using the EMCal and ALICE tracking.
Jet reconstruction in elementary collisions is most commonly based on energy measurements using electromagnetic and hadronic calorimeters. ALICE takes an alternative approach, with hadronic energy measured using high resolution charged particle tracking and electromagnetic energy measured using the

EMCal. Hadronic calorimetry is preferred in elementary collisions because of systematic uncertainties due to unmeasured neutral hadrons in the tracking approach (primarily K_L^0 and neutrons). As detailed below, this effect is secondary in heavy ion collisions, where background fluctuations are large and a tracking approach allows a more targeted rejection of low-energy hadrons from soft backgrounds. Jet reconstruction incorporating charged particle tracking in place of hadronic calorimetry is the preferred method for heavy ion collisions.

Hadronic energy deposition in the EMCal is removed on average using the projection of charged particle trajectories to the EMCal front face together with a parameterized response to charged particle energy deposition [5]. This approach has been used successfully for jet reconstruction in elementary collisions by STAR [6] and ALEPH [7], with jet energy resolution comparable to traditional hadronic calorimetry methods. The charged particle momentum resolution of ALICE is about 10% at $p_{\mathrm{t}} = 100$ GeV/c, which is sufficiently good resolution for hard fragments of the most energetic jets generated in heavy ion collisions. The ALICE two-track resolution is sufficient to maintain this performance in the dense central core of high energy jets.

A UA1-type cone algorithm [8] is used for initial studies of jet finding in Pb–Pb collisions since such algorithms allow relatively simple correction of uncorrelated backgrounds.

8.4.1 Jet Background Reduction

The main consideration for offline reconstruction of jets in the heavy ion environment is the large background of uncorrelated particles. A recent estimate for central Pb–Pb collisions gives $dE_{\mathrm{T}}/d\eta \approx 3700$ GeV [9], or about 75 GeV of background energy in a small cone area of $R = \sqrt{\delta\eta^2 + \delta\phi^2} \leq 0.2$. The essential difficulty in correcting for this large background arises from impact parameter fluctuations, statistical fluctuations due to the finite number of tracks, and dynamical fluctuations due to low E_{T} jet production. The impact parameter fluctuations can largely be removed by an event-wise subtraction of background.

Jets measured in p–p collisions have a large fraction of their energy lying within a small forward cone: for a jet $E_{\mathrm{T}}$of $50-100$ GeV, about 80% of the charged track energy is contained in a cone of phase space radius $R = \sqrt{\delta\eta^2 + \delta\phi^2} \leq 0.2$ [10]. This suggests that a reduction in cone size below the commonly used value $R \approx 0.7$ will improve the signal/background in heavy ion events. A further reduction of the background can be achieved by imposing a lower p_{t} bound on the charged tracks used in the jet reconstruction. A study with the HIJING model shows that applying a track cut of $p_{\mathrm{t}} > 2$ GeV/c excludes 98% of the background tracks. The radius and p_{t} cuts are correlated, however, due to the well-known angle ordering in jet fragmentation (see Fig. 8.5).

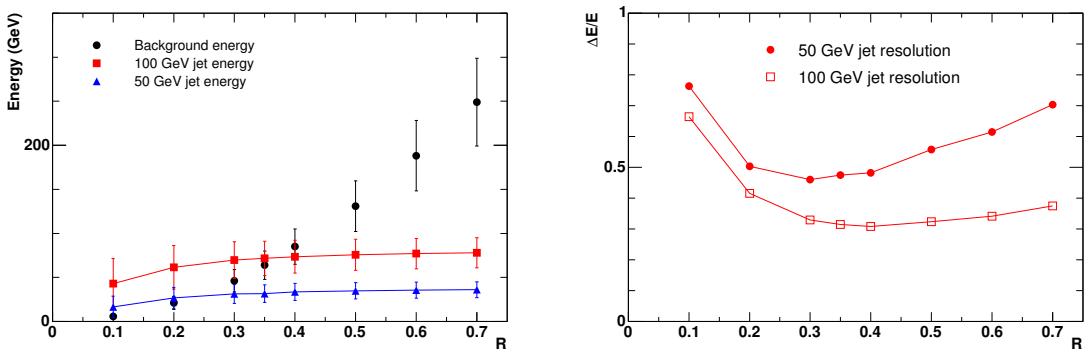

Figure 8.4: Left: Background energy (HIJING Pb–Pb central) and jet cone energy (PYTHIA) versus cone radius R [3, 4]. The vertical bars indicate the RMS of the distributions. Right: Jet energy resolution as a function of R. Only charged tracks with $p_{\mathrm{t}} > 2$ GeV/c are used for both panels.

Figure 8.4, left panel, shows the transverse energy measured with the track cut $p_t > 2$ GeV/c as a function of cone radius R, for 50 and 100 GeV PYTHIA jets and background due to central Pb–Pb events from HIJING. For a 100 GeV jet, the background E_T exceeds the measured jet E_T for $R > 0.4$. Figure 8.4, right panel, shows the resulting energy resolution from the cone algorithm for 50 and 100 GeV PYTHIA jets embedded into the HIJING background. A larger radius integrates more jet signal, improving the resolution, while also incorporating a larger background fluctuations which causes deterioration in the resolution. For 50 GeV jets these competing effects lead to an optimum cone radius of $R = 0.3$. For higher energy jets the background contributions become relatively less important, leading to a roughly constant resolution of about 30% for $E_T \approx 100$ GeV jets with $R > 0.3$.

8.4.2 Jet Energy Resolution

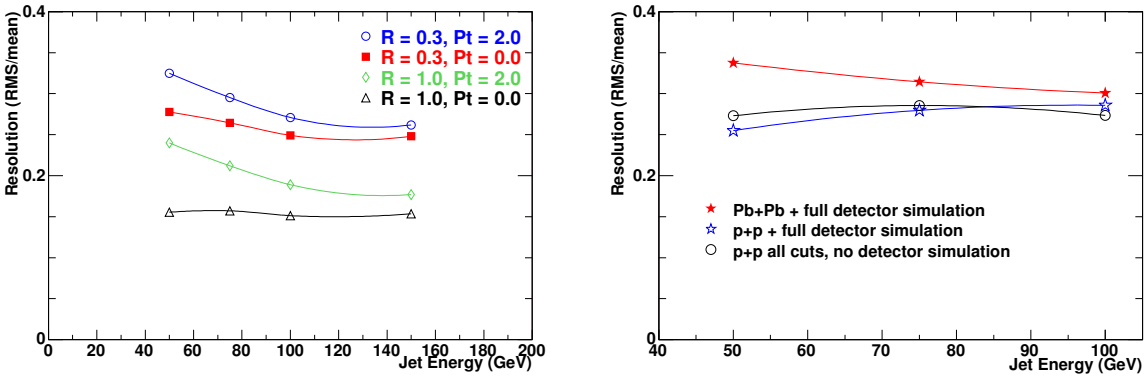

Figure 8.5: Energy resolution vs. jet energy for different reconstruction schemes [3, 4]. Left: Variation of cone size R and charged track $p_t$cut. Right: Effect of detector resolution and background fluctuations.

Figure 8.5, left panel, shows the jet resolution for various sets of cuts. The resolution is determined relative to reconstruction using all generated particles and a cone radius $R = 1$. It should be noted that other studies of jet energy resolution over heavy ion background use an alternative definition of resolution, in which reconstructed jet energy is compared with the same cone radius parameter $R \sim 0.4$, with and without heavy ion background. This alternative definition neglects the effect of out-of-cone radiation, and provides an apparently better resolution in the presence of background.
The triangular markers show the best achievable resolution with a real detector, using a cone radius of $R = 1$ and no track $p_t$cut. The loss of neutral particles, including neutrinos, neutrons and K^0_L, leads to an energy resolution of 15%. Successive application of the smaller cone radius cut $R = 0.3$ and the $p_t$cut for charged tracks leads to additional contribution to the resolution of 10% at high $p_T \approx 100$ GeV/c and 15% at $p_T \approx 50$ GeV/c.
Small jet cone radius and a track $p_t$cut are required to limit background in heavy ion events, but with the present algorithm they are the dominant factors in determining the jet energy resolution. As seen in Fig. 8.5, right panel, the additional contribution to the resolution due to background is modest. Charged tracking momentum resolution (about 10% at 100 GeV) (see Figure 5.4.3 of Ref. [11]) and EMCal energy resolution ($< 10\%/\sqrt{E}$) contribute negligibly to the jet energy resolution.
Figure 8.5 shows a significant deterioration in resolution as R is reduced. This effect is explored further in Figure 8.6 for $100 - 120$ GeV PYTHIA-generated jets. The generated jet is within the EMCal acceptance, excluding a boundary region to account for its finite size. For reference, curve (a) shows the optimum reconstructed energy distribution for large cone $R = 1.0$, with the shift in the peak relative to the simulation energy demonstrating the jet energy lost due to unmeasured particles and the track cut $p_t > 2$ GeV/c. Curve (b) shows the energy distribution for $R = 0.3$ jets, taking only the highest energy

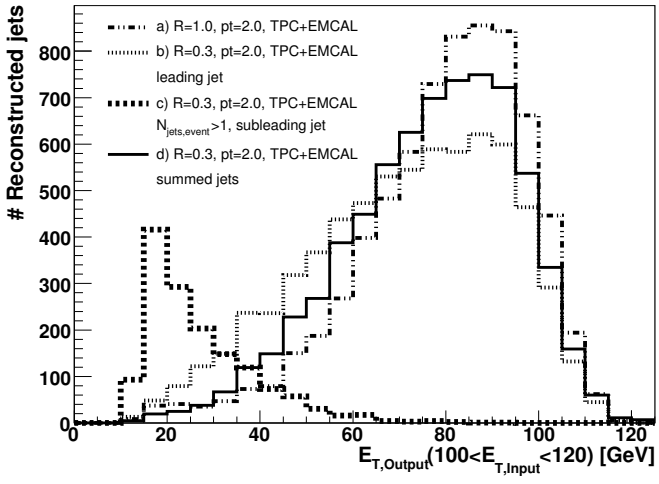

Figure 8.6: Effect of jet splitting due to small cone radius.

(leading) jet found in the event. Curve (c) shows the complement of (b), the energy distribution excluding the leading jet. The multiple jet rate is high for small cone radius, arising from splitting of a jet whose profile is relatively broad due to hard radiation. This results in a pronounced low-energy tail of the leading jet energy distribution which contributes to the resolution due to small cone size shown in Figure 8.5. A simple way to reduce the effect of jet splitting is to sum the energy of all small-R jets found in the EMCal acceptance. The resulting distribution, curve (d), shows a marked improvement in jet energy resolution. Figure 8.6 suggests that improvements in the reconstructed energy resolution shown in Fig. 8.4 are possible. Measurement of hard radiation may itself be an interesting probe of the medium, though this is as yet an unexplored issue.

Development of jet reconstruction algorithms for heavy ion collisions is in its beginning stages, and optimization of biases and resolutions will require a continuous interplay of experiment and theory. Recent analyses of jets in heavy ion collisions by the STAR collaboration at RHIC [12], utilizing infrared safe algorithms from the FastJet package [13], suggest that indeed unbiased jet reconstruction may be achievable in heavy ion collisions. This is a rapidly developing area of study.

8.4.3 Jet Reconstruction Performance

Based on the previous section one can conclude that the energy resolution for conventional jet reconstruction in heavy ion collisions is dominated by large background fluctuations of the underlying event and not by instrumental resolution. Experimental control of such fluctuations in cone reconstruction algorithms requires the imposition of relatively narrow cuts on jet cone radius ($R < 0.5$) and the $p_{\rm t}$ of tracks and EMCal tower energy ($p_{\rm t} > 1-2$ GeV), in comparison to jet reconstruction in p–p collisions. Alternative jet reconstruction algorithms are under development for heavy ion collisions, including k_t-type approaches with novel background subtraction methods (e.g., [13]).

A simple cone-type algorithm without mid-point merging or further corrections is utilized for these baseline jet reconstruction studies. The degree to which cone radius and $p_{\rm t}$ cuts suppress the influence of background on jet reconstruction is shown in Fig. 8.7. The left panel shows the reconstructed jet energy for the quenched-jet signal embedded into central Pb–Pb background ("Pb–Pb") vs. the quenched-jet signal only ("p–p"). Good correlation is evident for $E_{jet} > 50$ GeV, demonstrating that, with these cuts, the Pb–Pb background has only minor impact on the reconstructed jet energy. The energy difference distribution has a width less than 10 GeV for jet energy 100 GeV, decreasing for larger jet energy. The right panel shows the differential cross section for the quenched-jet signal only (p–p) and quenched-jet

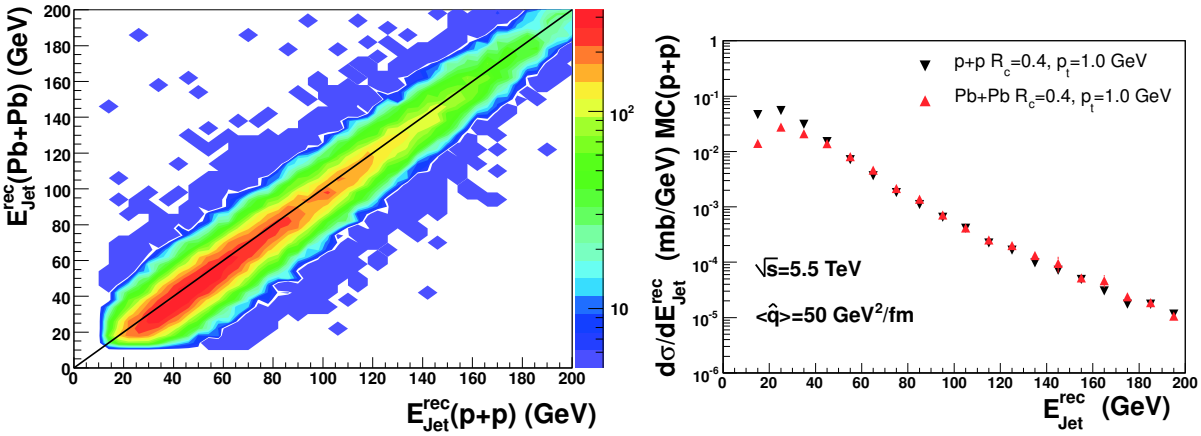

Figure 8.7: Influence of heavy ion background on jet reconstruction: "Quenched jets" are generated (AliPyQuench, $\sqrt{s_{NN}} = 5.5$ TeV, $\hat{q} = 50$ GeV^2/fm) and reconstructed without ("p–p") and with central Pb–Pb background ("Pb–Pb"). Jet reconstruction uses the radius and p_t cuts specified in the right panel to suppress background. Left: Reconstructed energy for jet plus central Pb–Pb background (Pb–Pb) vs. jet signal only (p–p). Right: Differential cross section of reconstructed jet energy without Pb–Pb background (black inverted triangles) and with background (red triangles).

signal embedded into central Pb–Pb background (Pb–Pb). The spectra are similar for $E_{jet} > 50$ GeV. For this model of background and quenching, and the corresponding cone radius and p_t cuts, background fluctuations in central Pb–Pb collisions have minor influence on jet reconstruction.

Jet reconstruction performance in the context of a jet quenching observable is shown in Fig. 8.8. The figure shows the distribution of charged hadrons with $R < 0.7$ from the reconstructed jet axis as a function of $\xi = \ln(E_{jet}/p_{hadron})$, where E_{jet} is the estimated total jet energy (i.e., corrected for reconstruction effects) and p_{hadron} is the magnitude of the hadron momentum projection on the jet axis. The inclusive distribution $dN/d\xi$, commonly known as the "hump-backed" plateau, is well-described by QCD-based MLLA (modified leading-log approximation) calculations for jets in e^+e^- collisions [14]. Jet quenching has been introduced into the MLLA formalism via modification of the radiation vertex coupling strength [14].

Figure 8.8 shows three different reconstruction schemes for quenched jets ($\hat{q}$=50 GeV^2/fm). The dashed blue line is for "ideal" reconstruction, with all generated particles measured over an arbitrarily large jet cone ($R < 1.0$) with no p_t cut. The black solid line shows reconstruction with standard background-suppression cuts but with no background present. The solid red line shows reconstruction of the same jet sample embedded into central Pb–Pb background. The jet sample is selected in each case, based on the measured (uncorrected) energy, to correspond to parent jet energy in a narrow bin around 150 GeV. The value of ξ is corrected for the estimated jet energy deficit due to the specific cuts of each method, based on unquenched PYTHIA simulations. This is a correction procedure that can be used in real data analysis, but assessment of the accuracy with which it corrects missing energy awaits the actual data.

Since ξ is an inclusive observable, the full multiplicity distribution can in principle be formed without regard to the specific p_t and radius cuts used in jet reconstruction. While the figure shows some biases, notably at low ξ (high p_t), due to the background-suppression cuts (p–p and Pb–Pb compared to ideal), the presence of background fluctuations has only minor influence for $\xi < 4.5$. However, above $\xi \sim 5$ ($p_t <\sim 1$ GeV/c) the background overwhelms the jet signal and the measurement loses sensitivity. It is not surprising that there is a p_t scale below which jet quenching signals cannot be measured reliably; similar conclusions are evident from correlation analyses at RHIC.

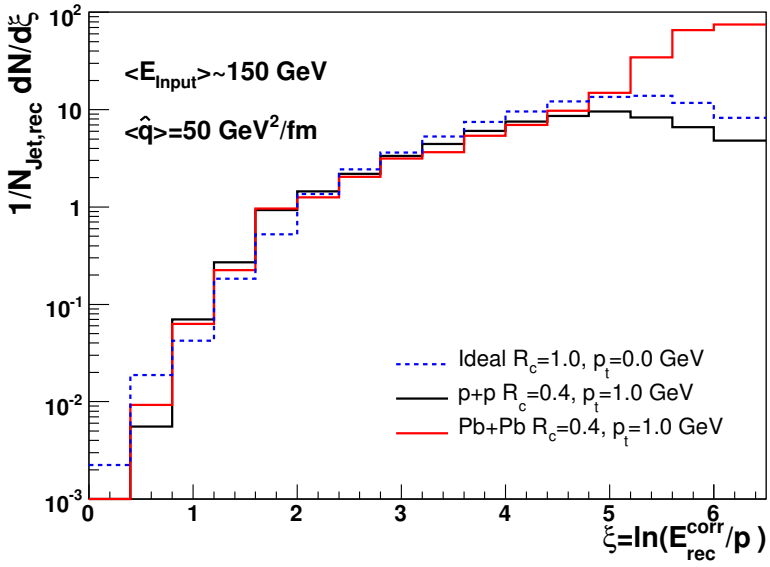

Figure 8.8: Charged hadron multiplicity in a jet vs. ξ. Variables and distributions are defined in text.

8.4.4 EMCal Kinematic Reach

The expected annual rates for hard processes in Pb–Pb running at the LHC were shown in Chapter 1. In this section we analyze a specific observable, to assess the EMCal measurement capabilities for high E_{T} jets in detail.

Figure 8.9 shows a projection for a jet quenching measurement: $dN/d\xi$ vs. ξ for ~ 175 GeV jets measured in central Pb–Pb collisions (quenched), normalized by the same measurement in p–p collisions (unquenched). The red data points correspond to the realistic reconstruction case using background-suppression cuts, while the black histogram corresponds to "ideal" reconstruction of the quenched jet including all generated particles but no background, with large cone radius and no p_{t} cuts. The $dN/d\xi$ distributions are for charged hadrons within $R < 0.7$ of the reconstructed jet axis. The error bars on the red data points indicate the statistical precision expected from one year of Pb–Pb and p–p running, combined in quadrature with 5% systematic uncertainty on the background subtraction.

The effects of jet quenching are evident in the ratio, through the suppression (below unity) of high p_{t} particles (low ξ) and the enhancement (above unity) of the soft multiplicity (large ξ). This behavior corresponds to the overall softening of jet fragmentation due to quenching observed at RHIC. There is good agreement between "ideal" reconstruction and the realistic case for $\xi < 4.4$, illustrating that the method works well for this model of quenching and background. There is significant disagreement for $\xi > 4.4$, however, indicating that background subtraction uncertainties are greater than the assigned 5% systematic. This is clearly an area that needs development. Among the LHC experiments, ALICE has by far the broadest set of tools that can be brought to bear on this problem.

The parent jet energy for Fig. 8.9 is in a narrow bin around 175 GeV. At this energy, the statistical precision is seen to be good compared to the magnitude of the quenching effect. Based on the rates shown in Chapter 1, we expect that a significant measurement can be made out to jet energies of ~ 250 GeV. This justifies our statement that the EMCal acceptance is sufficient to measure jet quenching over a broad kinematic range.

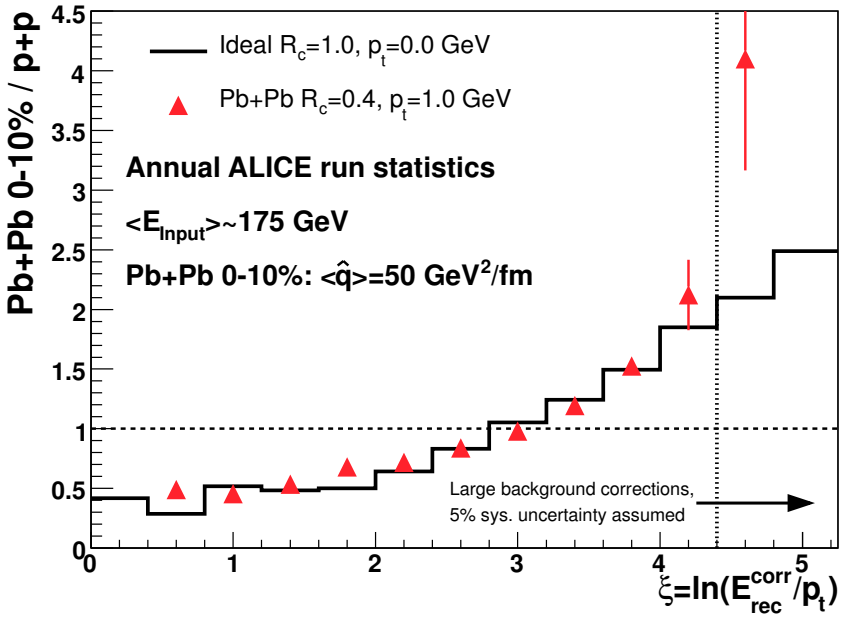

Figure 8.9: Projected ALICE measurements of the ratio of fragmentation functions for $\sim$ 175 GeV jets in Pb–Pb (quenched) and p–p collisions (not quenched), as a function of $\xi = \ln(E_{jet}/p_t)$. Error bars are quadrature sum of statistical errors for one year of LHC running and the systematic uncertainty due to background subtraction (see text). Red triangles show EMCal jet triggering and realistic reconstruction; black histogram shows "ideal" jet reconstruction including all jet particles for large cone, no p_t cut, and no background.

8.4.5 EMCal + ALICE PID Detectors Kinematic Reach

A unique feature of ALICE is its capability for reconstruction of identified hadrons over the kinematic range from 100 MeV/c to about 100 GeV/c through identification of π, K, and p in the TPC, strange, heavy flavor, and resonance reconstruction in the ITS and TPC, and e/h separation in the TRD and EMCal. These capabilities are unique at the LHC. Figure 8.10 shows the annual yields expected for identified hadrons in Pb–Pb collisions and in reconstructed jets with energies exceeding 30 GeV and 50 GeV, respectively.

Based on these simulations we expect that the measurement shown in Fig. 8.9 can be repeated for identified particles out to $\xi < 4$ for most of the particle species shown in Fig. 8.10. Detailed studies, taking into account the reconstruction efficiencies for rare hadrons from the full ALICE detector chain are in progress. Recent theoretical model calculations [15–17] indicate that the identified particle spectra in the high momentum region will probe the physics of hadronization and chiral symmetry restoration.

8.5 γ/π^0 Discrimination and Direct Photons

Photons do not interact with the medium and therefore provide an important calibration for jet quenching. At RHIC, the inclusive direct photon yield is a convincing cross-check for high p_t hadron suppression measurements of partonic energy loss. Even more significant would be the coincidence measurement of a direct photon with fragments of the recoiling jet. To leading order the photon energy gives the energy of the jet, allowing a controlled determination of the modified fragmentation function. Direct photon rates in the ALICE acceptance are significant up to $p_t \approx 50$ GeV/c, see Chapter 1. These measurements are challenging, however, due to the small γ/π^0 ratio and large fragmentation photon backgrounds, which drive the choice of the EMCal granularity. While the ALICE PHOS is by far the most finely granulated EM Calorimeter in the LHC heavy ion program, and will carry out the most precise direct photon measurements, there are strong reasons to carry out similar measurements in the EMCal:

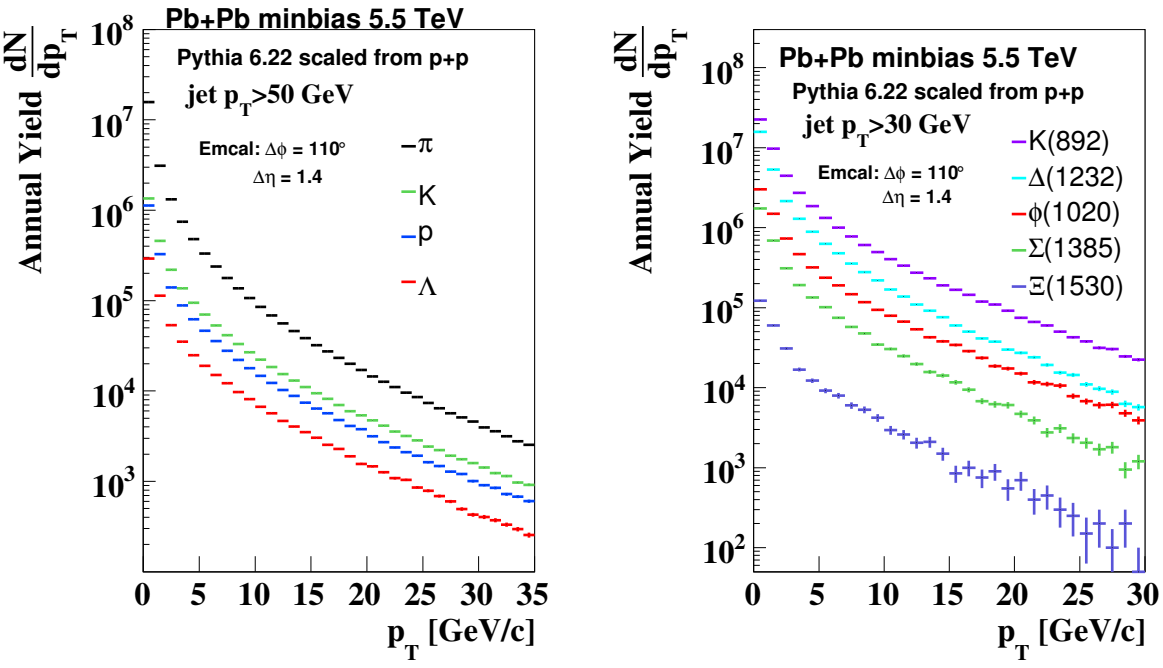

Figure 8.10: (a) Estimate of annual yield of hadrons, and (b) Hadronic resonances reconstructed in ALICE, as a function of transverse momentum based on a scaled PYTHIA simulation.

- The EMCal acceptance is a factor of seven larger than the full PHOS, with correspondingly greater measured yield for the statistics-hungry γ+jet measurements in the kinematic region in which the EMCal can discriminate π^0 from γ;

- Redundant measurements, with different systematic uncertainties, are crucial for precise measurements of direct photons. In PHENIX, the redundancy between the lead-glass and lead-scintillator calorimeters has proven decisive in this regard.

Direct photon measurements are subject to large backgrounds from neutral meson decay (π^0, η). At low p_t the decay photons generate separate calorimeter showers and mesons can be reconstructed based on the two-photon invariant mass spectrum. At higher p_t the decay photon showers merge, and shower shape observables are needed to separate π^0 from direct photon signals. Highly asymmetric decays will mimic the direct photon signal, thus the physical γ/π^0 yield ratio (a few times 10^{-2} in p–p collisions at the LHC) plays a crucial role in determining the practical p_t reach of a given measurement.
An additional background to direct photon production is hard bremsstrahlung from a quark jet ("fragmentation photons"), which at the LHC may dominate the real photon yield up to $p_t \approx 50$ GeV/c [18]. Such photons are accompanied by hadrons from the jet and can be suppressed by means of an isolation cut. Studies for the PHOS find hadron suppression due to isolations cuts of a factor about 20 in heavy ion collisions [11]. The effectiveness of isolation cuts for the EMCal is under study, and preliminary studies show that isolation cuts are effective in p–p and quenched Pb–Pb collisions for γ energies larger than 10-20 GeV. In this section we restrict our discussion to EMCal capabilities for discriminating direct photons and π^0 at high p_t using the shower shape, which discriminates two merged showers due to a π^0 from a single shower due to a direct photon. The shower-shape ellipsoid is calculated using logarithmic energy weighting, and the discrimination is based on the length λ_0 of the major axis of the ellipsoid.

To study the EMCal performance, π^0 and isolated photon distributions were embedded in p–p and Pb–Pb background events and subjected to full GEANT simulation, including conversions and showering in the material in front of the EMCal. The shower reconstruction algorithm applies appropriate tower thresholds to suppress backgrounds due to the underlying event (the threshold is higher in central Pb–Pb than p–p). PHENIX at RHIC has measured inclusive direct photon yields in p–p and heavy ion events with systematic uncertainties $\sim$10%. Direct photon measurements at the LHC will be substantially more challenging however, because of the marked decrease in the ratio of γ to π^0 yields with increasing $\sqrt{s}$ in the p_t range of measurement. The situation for 5.5 TeV Pb–Pb collisions is somewhat more favorable than 14 TeV p–p given the expected large suppression of π^0 yields due to jet quenching and the lower $\sqrt{s}$. Current theoretical calculations predict π^0 suppression factors of 5-10 in central Pb–Pb collisions at the LHC. In the studies reported here we assume a (conservative) π^0 suppression factor of 5.
Figure 8.11 shows the γ/π^0 yield ratio for 14 TeV p–p (left) and 5.5 TeV central Pb–Pb collisions (right). The open symbols are expectations from NLO pQCD calculations. The Pb–Pb case additionally includes the π^0 suppression factor of 5. (The Pb–Pb ratio is also larger because the NLO calculation predicts an increase of a factor $\sim$ 1.5 in this ratio at 5.5 vs. 14 TeV.) The filled symbols show the same ratio for the fully simulated events with the EMCal design granularity (tower size 6x6 cm^2), utilizing shower shape discrimination to reject π^0's. An enhancement of the ratio is seen for both systems up to $\sim$30 GeV, due to rejection of the π^0 yield which reduces the denominator. In the Pb–Pb case the ratio approaches unity over a significant p_t range.

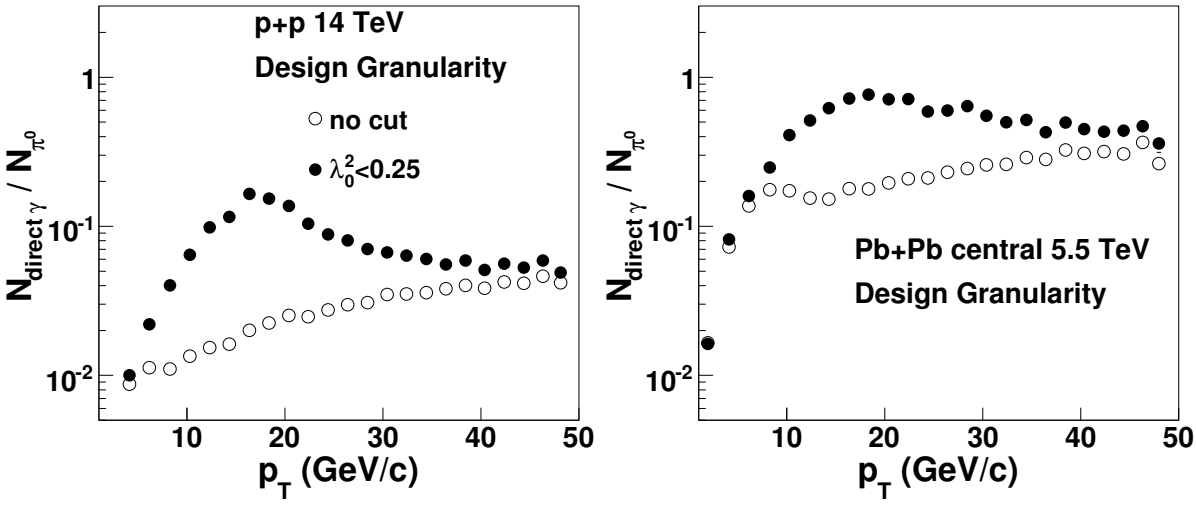

Figure 8.11: Performance of EMCal for γ/π^0 discrimination at design granularity: γ/π^0 ratio for 14 TeV p–p (left panel) and 5.5 TeV central Pb–Pb collisions (right panel). Open symbols are NLO pQCD predictions; a factor 5 π^0 suppression due to jet quenching is also assumed for the Pb–Pb case. Filled symbols show the same ratios from full GEANT simulations for the EMCal design granularity, including π^0 rejection by shower shape analysis.

The cut on λ_0 in this calculation is somewhat aggressive, favoring purity of the photon sample at the expense of a $\sim$ 10% relative reduction in the photon efficiency compared to the maximum achievable. Such an approach is appropriate for the γ+jet coincidence measurement, where precise control over the photon efficiency is not paramount, but careful systematic study and optimization of this cut must be carried out for the actual measurement. Figure 8.11 illustrates the discrimination power of the EMCal using this technique.
A study with the EMCal tower dimensions doubled in both directions (i.e., 12×12 cm^2), thus reducing the channel count by a factor of 4, shows that this granularity does not provide significant π^0/γ discrimination in the p_t region of interest, and such measurements would be severely limited by such a design. The p_t region over which the π^0's could be identified would be reduced by at least a factor of two compared to

the design granularity capabilities.

8.6 Heavy Flavor and High p_t electrons

The propagation of massive quarks in dense QCD matter is a very active area of research. Interest in this topic was initiated by the suggestion of Dokshitzer and Kharzeev that radiative energy loss for a charm or bottom quark may be suppressed due to the "dead cone effect", which also governs heavy quark fragmentation [19]. More recent theoretical studies have confirmed and refined this prediction [20], but measurements of high p_t non-photonic electrons at RHIC have found no evidence to date of anomalous "liberation" of high p_t heavy quarks [21].

At higher momentum the dead-cone effect is negligible but a difference in energy loss between jets led by B- or D-mesons (quark jets) and light hadrons (dominantly gluon jets) is still expected due to the difference in color charge of gluons and quarks (factor 9/4) [22]. The study of heavy quark jet production over a broad energy range therefore provides key tests of the mechanisms underlying partonic energy loss.

Speculative calculations of jet quenching in strongly-coupled gauge theories (but not QCD) using the AdS/CFT correspondence [23] predict observable differences at the LHC between massive quark propagation in a weakly coupled plasma, calculated using pQCD, and a strongly coupled plasma [24]. While such calculations are at present controversial in the theory community, they continue to provide new ways to look at QCD matter and new ideas for observables accessible to experiment.

The ALICE Transition Radiation Detector (TRD) has good electron/hadron discrimination in the region $p_t < 10$ GeV/c. The EMCal extends ALICE capabilities for electron identification and measurements in the region beyond $p_t \sim 10$ GeV/c. In this section we present the EMCal capabilities for electron identification, and for measuring electrons from b-quark decays.

8.6.1 Electron/Hadron Discrimination

Figure 8.12 shows the expected electron yield within the EMCal acceptance for one month of LHC heavy ion operation, calculated using PYTHIA simulations for p–p and scaling the cross section by A^2, assuming Pb–Pb luminosity of 0.5 $mb^{-1}s^{-1}$ and effective data-taking time of 10^6 seconds. Only "trackable" electrons that generate hits in the TPC are included (this excludes electrons from conversions in the TRD and TOF). The various components of the inclusive electron spectrum are shown. There is significant electron yield in the EMCal acceptance out to $p_t \sim 50$ GeV, setting the momentum scale over which electron/hadron discrimination must be carried out.

Figure 8.13 shows the ratio of hadron to electron yield vs. p_t predicted by PYTHIA, for trackable electrons from all sources (open symbols) and from B-decays only (filled symbols). It is evident that a hadron rejection factor greater than ~ 400 is required for robust electron measurements at high p_t. It is also clear from the figure that B-decays comprise a large fraction of the reconstructed electron population, a point we return to in greater detail below.

The principal tool for discriminating electrons from hadrons at high p_t is measurement of the ratio p/E, where E is the shower energy measured in the EMCal and p is the track momentum measured in the ALICE tracking system. To investigate the ALICE capabilities for electron/hadron discrimination, electrons and charged pions were embedded in central Pb–Pb events and passed through full GEANT simulation and complete event reconstruction. The analysis involves extrapolation of the charged tracks (helices) to the EMCAL, matching to the nearest EMCAL cluster with a maximum distance of $\Delta R = \sqrt{\Delta\phi^2 + \Delta\eta^2} < 0.02$. Figure 8.14 shows that electrons and hadrons are separable using p/E discrimination and that high efficiency can be obtained in the heavy ion environment.

Figure 8.15 shows the rejection factor for pions (inverse of efficiency) as a function of p_t for 80% and 90% electron efficiency. In light of Fig. 8.13, it is seen that sufficient hadron rejection can be obtained in heavy ion collisions for $p_t > 10$ GeV/c using the p/E technique.

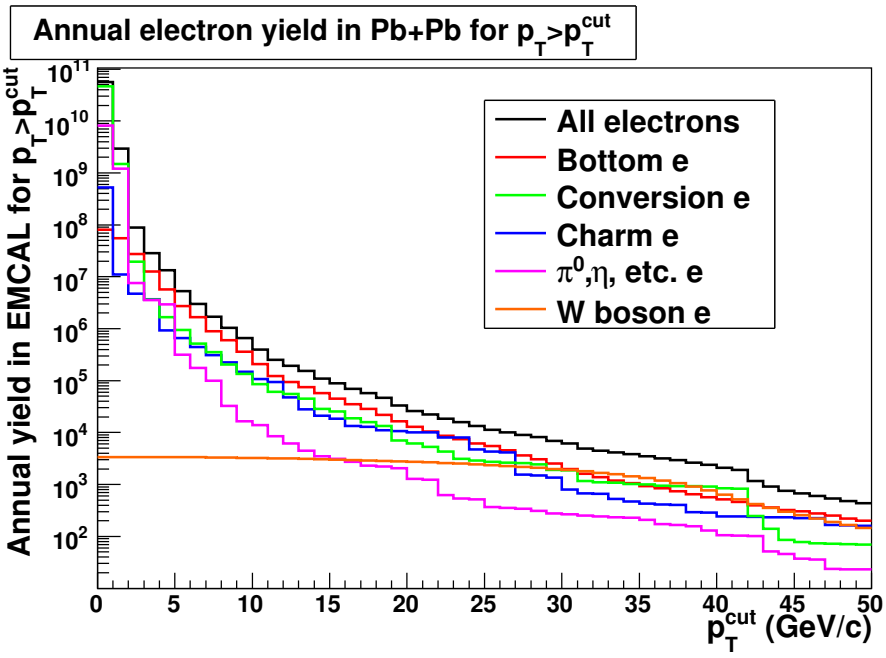

Figure 8.12: Cumulative annual yield in the EMCAL acceptance of electrons from 5.5 TeV minimum bias Pb–Pb collisions. Contributions from various sources, including B-decays (red) and "trackable" photon conversions interior to the TPC (green) are indicated.

8.6.2 Measurement of Heavy Flavor Electrons

Figure 8.12 shows the expected yield of identified electrons above a given p_t cut in one month of Pb–Pb running ($\sim 10^6$ seconds) at 5.5 TeV, including electron components from specific physics processes and from conversions in material. Electrons from B-decays dominate the electron spectrum in the p_t range $5-30$ GeV/c, while above this range W-decays dominate. There is a measurable yield of electrons from B-decays up to $p_t \sim 50$ GeV/c.

We have used a NLO-tuned PYTHIA simulation to investigate the kinematics of B-jets decaying semi-leptonically to electrons. Figure 8.16 shows the differential spectrum for electrons with $p_t < 10$ GeV/c, corresponding to the TRD capabilities, and $p_t > 10$ GeV/c, corresponding to unique EMCal capabilities. With the additional requirement that the leading electron be associated geometrically with the jet, falling within a cone $dR = \sqrt{\Delta\phi^2 + \Delta\eta^2} < 0.2$ of the jet axis, the cross section for $p_t > 10$ GeV/c dominates at high p_t.

The EMCal trigger and electron identification capabilities enable ALICE measurements of B-jets up to $E_{jet} = 80-90$ GeV in one month of Pb–Pb running. The good geometrical correspondence of a high p_t electron with the direction of the B-jet (note the similarity of the red curves in the two panels in Fig. 8.16) corresponds to a bias for given electron energy that the unobservable energy carried by the neutrino be small on average. In the case of significant energy loss, such a "fragmentation" bias will generate a geometrical bias familiar from leading particle-triggered jet quenching studies at RHIC (small path length in medium, corresponding to small energy loss). Interpretation of electron-trigger spectra in terms of heavy quark energy loss will therefore require careful theoretical modeling to assess these biases.

Isolation of electrons specifically from heavy quark decays requires additional discrimination by means of a displaced vertexing method ("DVM"). This method relies on the fact that bottom decays typically produce a large number of charged particles by decaying via charm mesons to lighter hadrons. Hadrons with the largest p_t are correlated in phase space and point back to a common, displaced vertex. Reconstruction of the semi-leptonic displaced vertex (using the electron and one additional hadron from

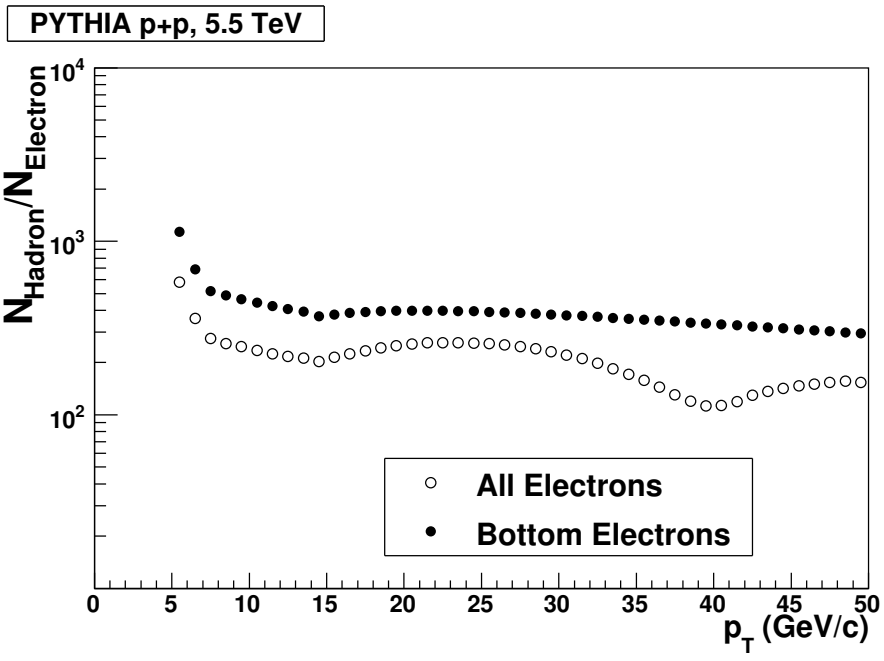

Figure 8.13: Ratio of charged hadrons to electrons vs. p_t from PYTHIA simulations of 5.5 TeV p–p collisions. The open symbols are electrons from all "trackable" sources (as in Fig. 8.12), while the filled symbols are electrons from B-meson decays.

the decay) consistent with the B-meson lifetime provides a powerful tool for discrimination of heavy-flavor electrons from non-heavy flavor electrons. This method has been used successfully by CDF in identifying bottom contributions in semi-leptonic muon decays [25].
The ALICE Inner Tracking System (ITS) has excellent vertexing capabilities. To implement the DVM method, a large p_t electron is used as a trigger. The algorithm searches for intermediate p_t hadrons (with $p_t > 0.5$ GeV/c) from a common, displaced (secondary) vertex within a cone of $dR < 1.0$ of the trigger. A minimum of 4 (of 6) ITS hits are required on each track to ensure sufficient spatial resolution of the secondary vertex. Once a pair is found and their displaced vertex determined, the bend-plane projection L_{xy} is calculated as

$$L_{xy} = \frac{r \cdot p_{e+h}}{|p_{e+h}|} = |r| \cdot cos(\theta) \tag{8.1}$$

where r is the vector between the primary and secondary vertex and p is the 3-momentum sum of the hadron + electron. The distribution of this quantity is symmetric around zero for random background, but strongly biased towards positive values for real decays. By isolating the non-symmetric (positive) component of the distribution one can further reduce backgrounds. Imposition of an invariant mass cut suppresses direct charm decays. More details can be found in Ref. [26].
We have studied the DVM method in a full GEANT simulation of ALICE, including ITS response. Figure 8.17 shows the relative fraction of various components of the identified electron spectrum vs. p_t, obtained from ratios of the electrons in Fig. 8.12. Without vertex constraints, B-decay comprises about 60% of the total. A displaced vertex cut of $L_{xy} > 600$ μm and electron-Kaon invariant mass threshold of 1.7 GeV generates the dot-dashed curve in the figure: this population is 99% due to B-decays, with $\sim 70\%$ efficiency. From this study we conclude that the DVM method, combined with the PID capabilities of the EMCal, provides efficient and pure identification of semi-electronic B-decays.

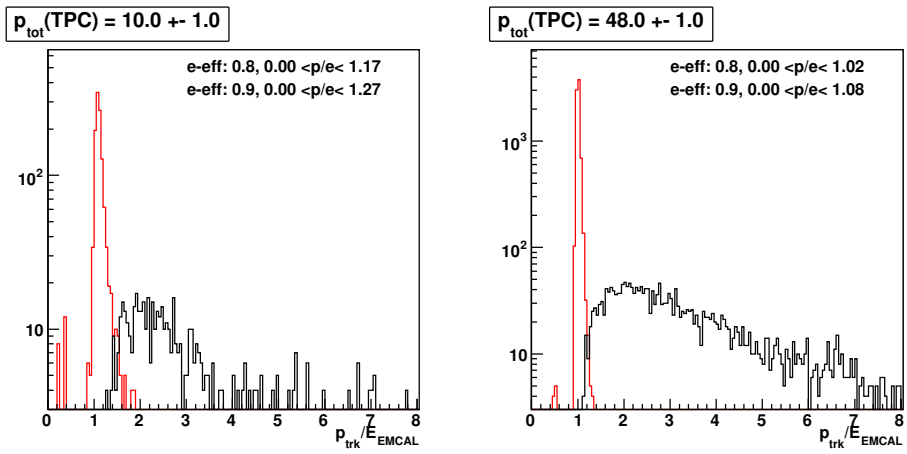

Figure 8.14: Electron/hadron discrimination: p/E distributions for electrons (red) and hadrons (black), for track momentum 10 GeV/c (left) and 48 GeV/c (right). Broadening of the electron peak due to bremsstrahlung is evident in the 10 GeV case. The MIP peak for hadrons is suppressed due to shower threshold cuts; it would lie off-scale to the right. The cut values for electron identification with 80% and 90% efficiency are shown.

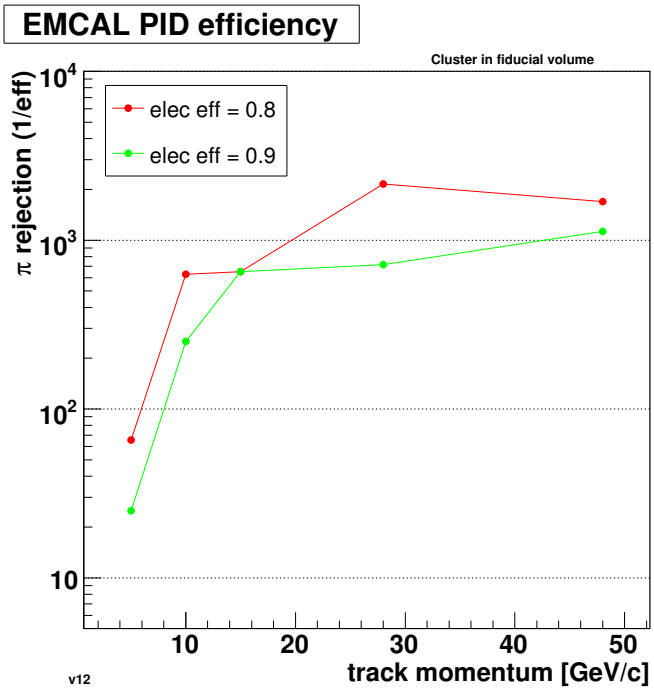

Figure 8.15: Hadron rejection vs. p_{t} for different electron efficiencies, in central Pb–Pb collisions. Cluster is within the EMCAL fiducial volume and cleanly associated with a track. Cuts on p/E vary with momentum.

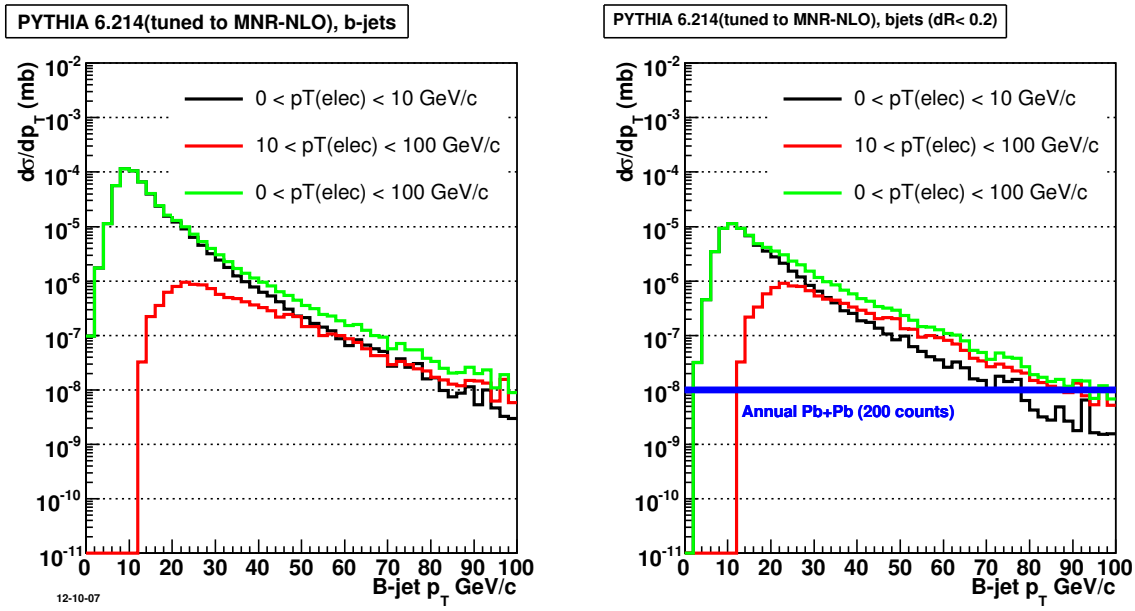

Figure 8.16: Differential cross-section for inclusive B-jet production as a function of p_t, requiring semi-electronic decay with the electron in the EMCal acceptance. Calculations from NLO-tuned PYTHIA simulations. Black histograms are for electron $p_t < 10$ GeV/c, red are for $p_t > 10$ GeV/c, and green are for all p_t. Left panel has no geometrical constraint on the electron relative to the jet, while the right panel requires that the trigger electron fall within a radius $= 0.2$ of the B-jet axis. The blue line indicates 200 counts in the EMCal acceptance in one year of Pb–Pb running.

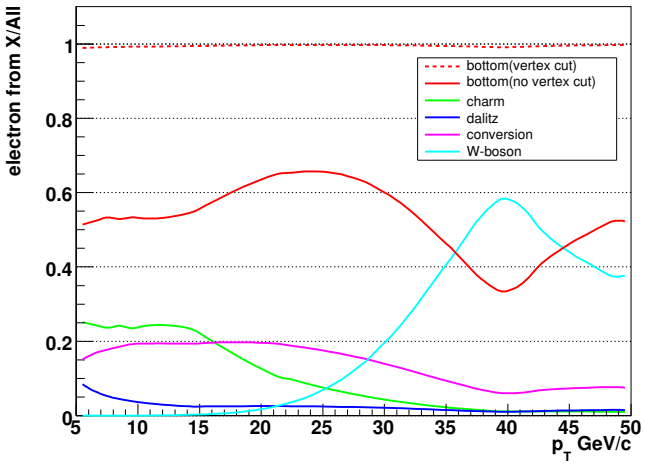

Figure 8.17: Relative fraction of various components of identified electron yield as a function of p_t. The electrons from B-decays are shown before (solid red) and after (dashed red) the displaced vertex cut.

9 Integration and Implementation

9.1 Mechanical Support Structure (CalFrame)

9.1.1 General

The EMCal weighs approximately 90 tons, or 8 tons per super module. It is supported on a support structure (CalFrame) that in itself weighs about 25 tons. The full weight of the EMCal and its support structure is transferred to the ALICE magnet via two pre-existing I-beams that span the length of the magnet as shown in Fig. 9.1. The CalFrame was fabricated at a manufacturing company in Italy and was completed in early 2007. Figure 9.2 is 3-D CAD model of the fully assembled CalFrame. Figure 9.3 shows a photograph of the CalFrame fabrication process.

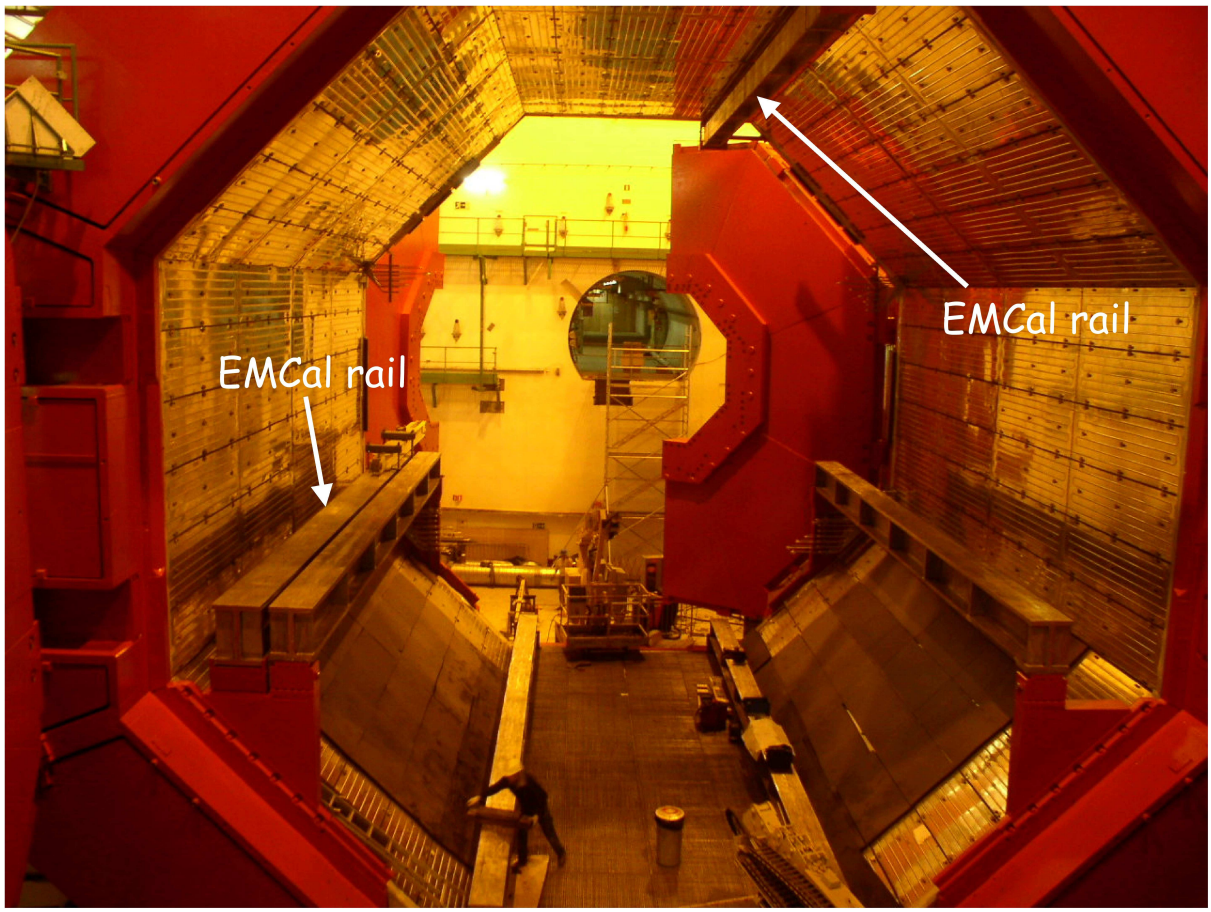

Figure 9.1: Photograph of the ALICE magnet showing the EMCal support structure I-beams. The lower and upper I-beams which support and position the CalFrame are visible at approximately 8 o'clock and 1 o'clock respectively.

The CalFrame was assembled and load tested at CERN prior to installation inside ALICE in May 2007. The CalFrame was designed to incorporate rails for the insertion and removal of super modules during later installation windows.

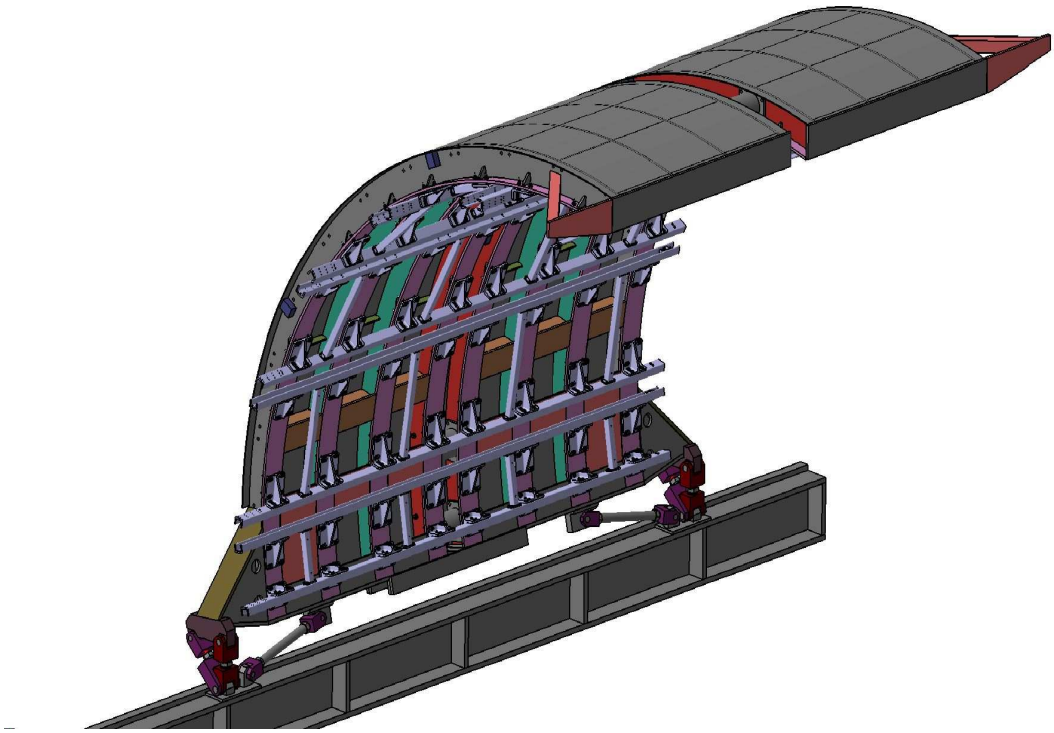

Figure 9.2: The EMCal mechanical support structure (CalFrame) fitted with rails, ready to receive super modules.

Figure 9.3: The CalFrame in the process of assembly (left) and fully assembled (right).

9.1.2 CalFrame Design Constraints

The volume of the EMCal and its support structure is bounded from the IP between 4320 mm and 5400 mm radially and $\pm$3500 mm axially. The azimuthal envelope is set by the two support I-beams as seen in Fig. 9.1. This envelope includes the stack up of all fabrication tolerances and deflection of the CalFrame and the support I-beams when the system is fully loaded with all super modules. The pre-existing I-beams are supported from their ends on the ALICE magnet return yoke with its support span of approximately 10 meters. The lower I-beam is designed to provide the full vertical and horizontal load reaction at the bottom of the CalFrame. The top I-beam is designed to provide limited horizontal reaction and no vertical reaction. Therefore, the CalFrame is designed to contact the upper I-beam via slip pads to eliminate vertical loading on the top beam.

Finite element analysis of the pre-existing I-beams indicated that the I-beams will experience excessive deflection and rotation if the EMCal load was applied at ± 3500 mm. Therefore, the design of the CalFrame was modified to add outriggers at the top and bottom to increase the load span and reduce the overall system deflection and rotation. This addition of outriggers increased the complexity and cost of the CalFrame.
The CalFrame itself was designed to occupy minimum radial space so as to maximize the radial space available for the super modules, and yet to keep the radial deflection of the CalFrame to a minimum. Since the CalFrame is radially thin, there was never any question of excessive material stresses, provided that the frame design does not exceed the maximum allowable deflection. The CalFrame is modeled after the fuselage of an airplane or the hull of a ship. Figure 9.4 shows a 3-D CAD model of the CalFrame without the external skin. The outer skin is attached to flanged ribs which are in turn separated by stringers which keep the skin from having large deflections between flanges.

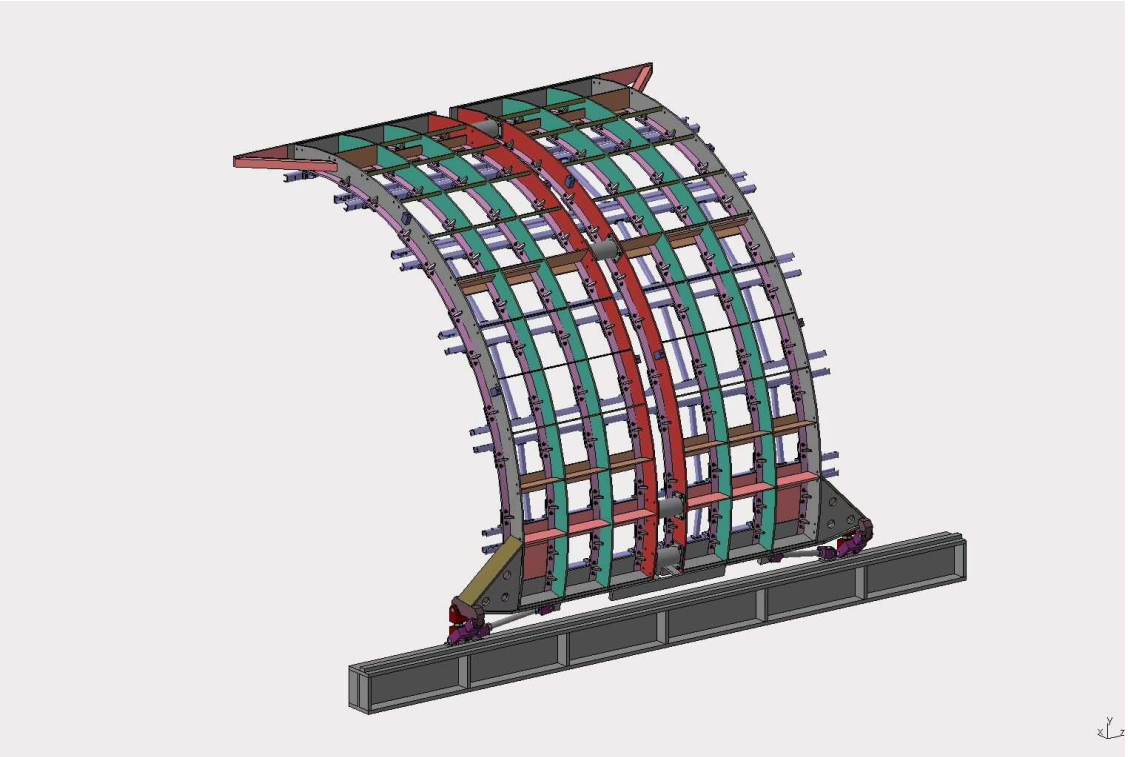

Figure 9.4: 3-D CAD model of the CalFrame without the external skin.

9.1.3 Super Module Crate and CalFrame Interface

The interface between the super module crate and CalFrame support structure is provided by rails mounted to the under surface of the CalFrame, and roller fitted carriages mounted on the super module crates. Each super module slides on 2 U shaped aluminum rails, and is fitted with 8 carriages. The U shaped rails are custom extrusions that have been made for the EMCal with dimensions $125 \times 92.5 \times 17.5$ mm^3. The raw material is 6106 T6 aluminum alloy which performs with a confirmed yield strength of 240 MPa. The extrusion process allows considerable savings on raw material cost and machining time for the rail fabrication. The full set of EMCal rails was delivered in June 2006.
The rails are fixed on the CalFrame through support pads which are L shaped and made from sand cast aluminum alloy (AC-42000). Support pads and fully equipped parallel rails were delivered already in 2006. Figure 9.5 shows the support pads used to mount the rails to the CalFrame and the first fully assembled set of rails. Figure 9.2 shows the final CalFrame design with all the rails in place and ready to

receive super modules.

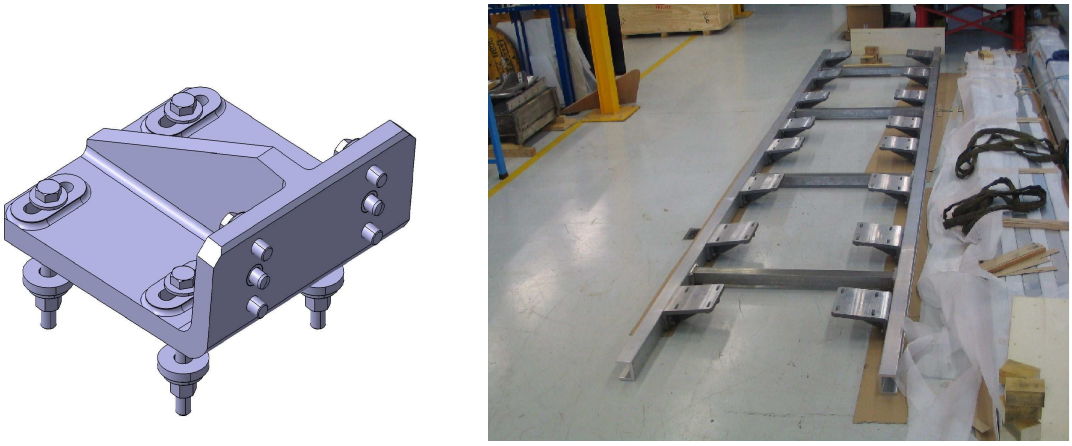

Figure 9.5: Left: Pad support used to mount rails on CalFrame. Right: Set of two rails before assembly on CalFrame.

The carriage parts that allow the super modules to slide into the CalFrame on the rail system are made from sand cast aluminum alloy (AC-42000). The wheels are made from stainless steel with bearings made from PEEK resin. Figure 9.6 shows a carriage assembly attached to the super module crate.

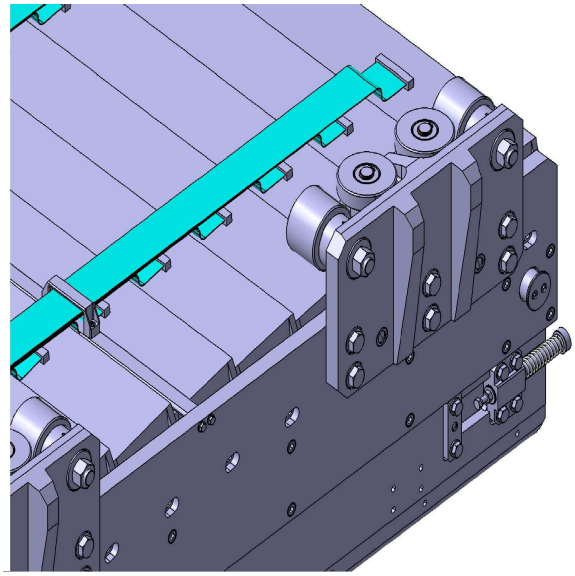

Figure 9.6: Carriage with rollers for installation of super modules into rails.

9.1.4 CalFrame Structural Analysis

A finite element model of the CalFrame was developed in ANSYS WorkBench to study the structural performance of the CalFrame and the support I-beams. The model was used to optimize the design to reduce material weight and fabrication cost. The FEA models were verified by a team of engineers. The boundary conditions applied to the support structure and the two support beams are:

1. The upper end of the CalFrame has only a horizontal reaction applied to it by a horizontally-oriented upper I-beam.

2. The lower end of the CalFrame has both vertical and horizontal reactions applied by a vertically-oriented lower I-beam.

Deflections and stresses were then calculated for static and seismic conditions as specified by the CERN site-specific vertical and lateral acceleration of 0.115 g. When the EMCal is fully loaded, the calculated maximum radial (actually vertical) deflection in the CalFrame alone is less than 25 mm and is located at the 12 o'clock location. This is an acceptable deflection; however, when initial deflections in the upper and lower support beams were considered, the maximum total system deflection and translation sums up to about 120 mm. The bulk of this deflection is due to the horizontal deflection and rotation of the support beams. Furthermore, the FEA results showed that the maximum stress in the lower support I-beam was close to the allowable stress for the 304LN material. In order to reduce this high deflection and stress several design changes were implemented:

1. Reduced the detector weight by approximately 15% by decreasing the EMCal radiation thickness by 15% with no impact on the physics performance. The full detector weight is now approximately 90 tons.
2. Moved the CalFrame I-beam interface points closer to the I-beam anchor locations by adding outriggers to the CalFrame to reduce overall deflection and stress in the I-beams.
3. Reduced the weight of the CalFrame itself by about 3 tons by using thinner SS plates.
4. Provided means for adjusting the position of the CalFrame after we complete the installation of the CalFrame in order stay within the assigned envelope.

9.1.5 FEA Model Description

At first, a general analysis of the frame was done using a relatively rough mesh as shown in Fig. 9.7. This model was used to determine the deflection of the model, as well as to highlight any areas of high stress. However, because of the coarseness of the mesh used in the model, the local stresses calculated with it were treated with caution.
Several more analyses were then done, where the mesh density was increased in the high-stress areas highlighted by the first analysis. Also, stand alone analyses of all welded joints with appropriate safety factors were performed. Combining the results of these analyses, it was possible to determine that the structure is safe. It should be noted that the frame was analyzed separately from the support beams.

9.1.6 Analysis Results - Static Case

In the final model, the maximum vertical deflection of the frame when loaded by gravity and 86,000 kg of detectors is 29.5 mm. The deflection of the frame and the supporting beams is shown schematically in Fig. 9.8. Adding all of these deflections together, the total vertical deflection of the CalFrame is estimated to be 63.9 mm.
The allowable stress in the structure under static loading, once all safety and load factors have been taken into account, is 118.5 MPa in the region of the welds, and 134 MPa elsewhere. The maximum stresses in the frame under static loading are compressive, and can be found at the top of the bottom outriggers, and in one of the shear plates. Figure 9.9 shows these areas (colored in blue). As can be seen, the stresses are all well within the acceptable limits.
As mentioned previously, a separate analysis was done for the support beams. The maximum global stresses calculated in the bottom support beam are in the region of 125 MPa. This value increases as the feet are adjusted in the x or y directions, but the stresses remain below the critical value.
The stresses in the top beam are calculated to be 112 MPa for the static case. The y-direction adjustment of the CalFrame anchors at the lower beam should ensure that the static load is always carried though the neutral axis of the upper beam.

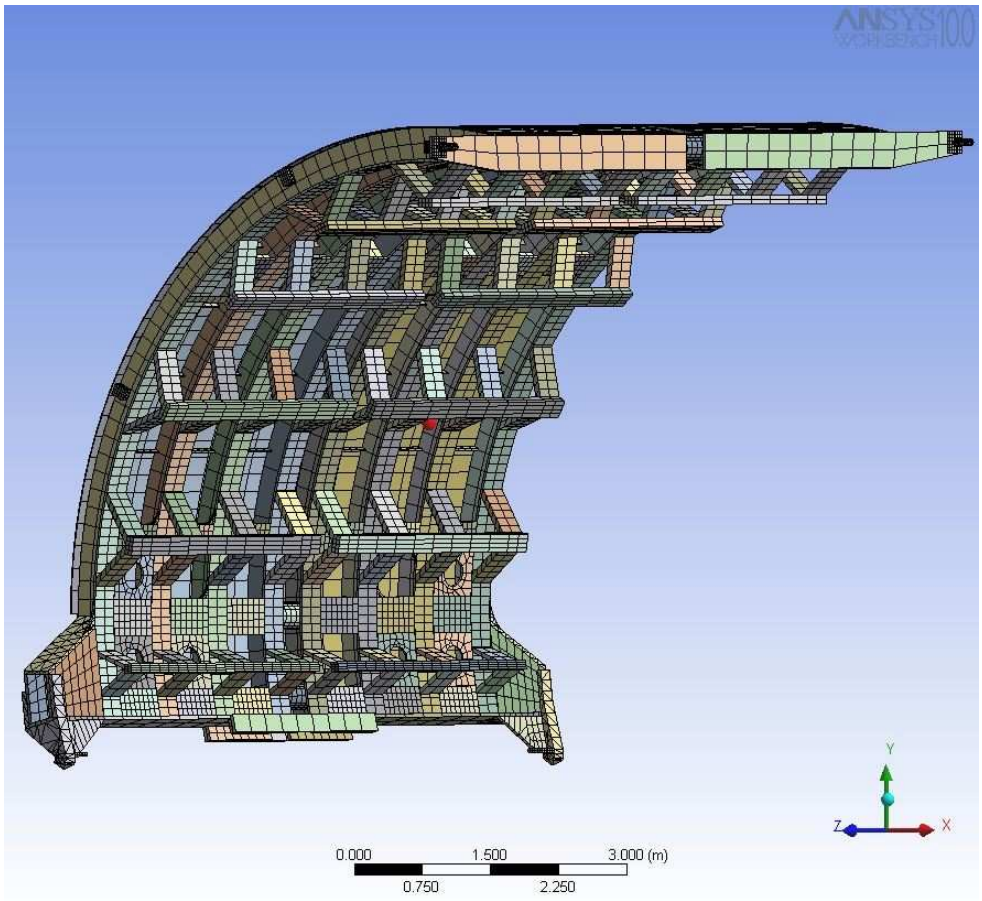

Figure 9.7: Coarse mesh FEA of the CalFrame.

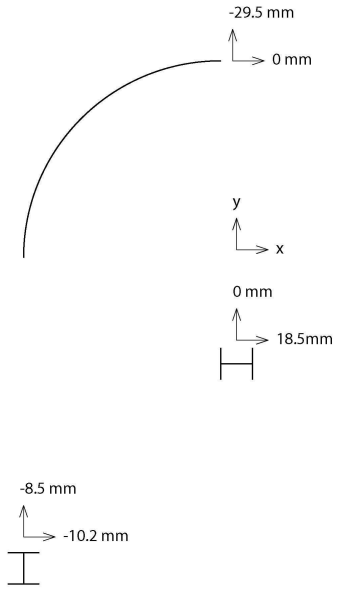

Figure 9.8: Deflection of the CalFrame and the supporting beams in the static case.

9.1.7 Analysis Results - Seismic Cases

With CERN being located in a seismically active region, the CalFrame and its support beams have to withstand seismic loading. Pseudo-static analyses were carried out to determine that the structure will

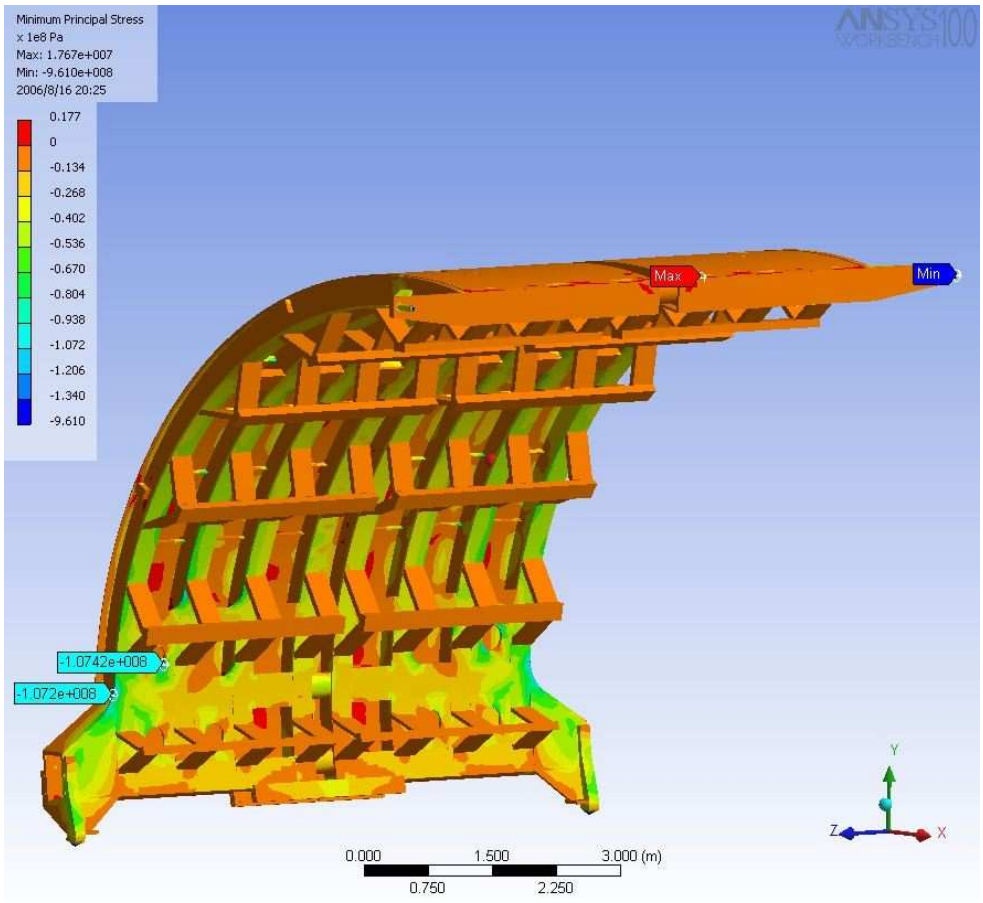

Figure 9.9: Maximum compressive stresses in the CalFrame under static loading.

not collapse in the event of an earthquake of normal magnitude for the region.

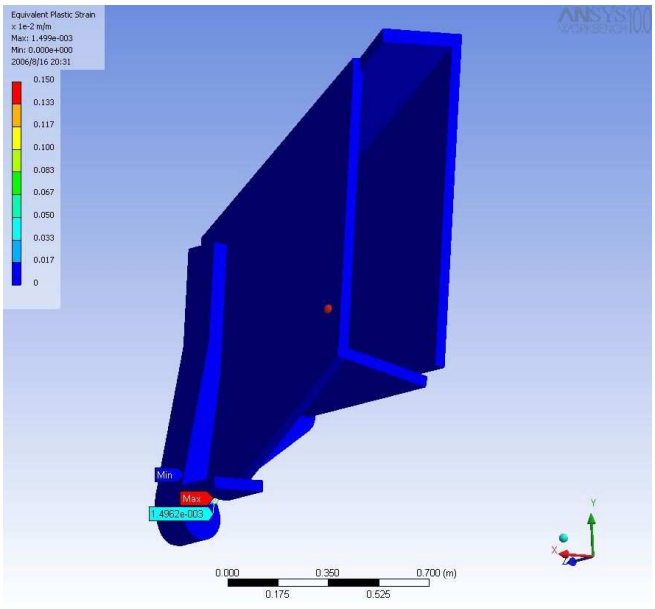

Figure 9.10: Plastic strain in the bottom outrigger during seismic loading.

Generally, the load in the CalFrame itself is relatively low, and the critical points are the support beams and the bottom outriggers. The bottom outriggers especially are severely affected by lateral excitation in the direction of the beam-axis. Thus, the three cases that cause the highest stresses in the aforementioned areas were analyzed:

- Bottom beam loading: The highest stresses developed in the bottom support beam during seismic analyses was 205 MPa. This is less that the yield stress of 304LN steel (270 MPa), and the beam is thus safe.
- Top beam loading: The highest stresses developed in the top support beam during seismic analyses was 194 MPa. This is less that the yield stress of 304LN steel (270 MPa), and the beam is thus safe.
- Bottom outrigger loading: The stresses in the bottom outrigger can reach a level where plastic deformation occurs. A plastic analysis was therefore carried out. Figure 9.10 shows the maximum plastic strain predicted in the outrigger, which is 0.0015. While it would be preferable to have no yielding at all, it is clear that the plasticity is local, and that the structure is safe.

9.1.8 CalFrame Load Test

Before the CalFrame was lowered into the ALICE cavern for installation inside the L3 magnet (November 2007) a number of assembly and test activities took place in the surface halls at Point 2.

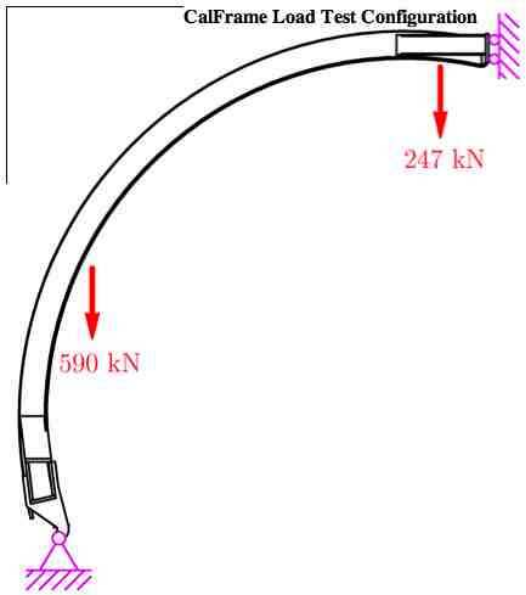

Figure 9.11: Configuration for the CalFrame load test.

Most of the CalFrame is not very highly stressed. The exceptions to this are the outriggers and the area of the frame near to them. A sketch of the load test configuration that can simulate the deflection of the CalFrame under full load is shown in Fig. 9.11. Figure 9.12 shows the load test setup using spreader bars and dead weight at the top and in the mid-section of the arch. The critical dimension that would indicate the deformation of the CalFrame when it is fully loaded is the cord dimension of the CalFrame. This dimension, shown in Fig. 9.13, was measured before, during, and after the load test. Two data points were recorded at different times before loading the CalFrame to set the zero reading. One data point was recorded when the CalFrame was loaded, and finally, a data point was recorded after the load was removed to see if the cord dimension would return back to its undeformed position. The total change of

Figure 9.12: Setup used for the CalFrame load test.

the CalFrame cord was measured between 8 and 16 mm, and the estimated value from FEA is 12 to 16 mm. This test confirmed the structural integrity of the support structure.

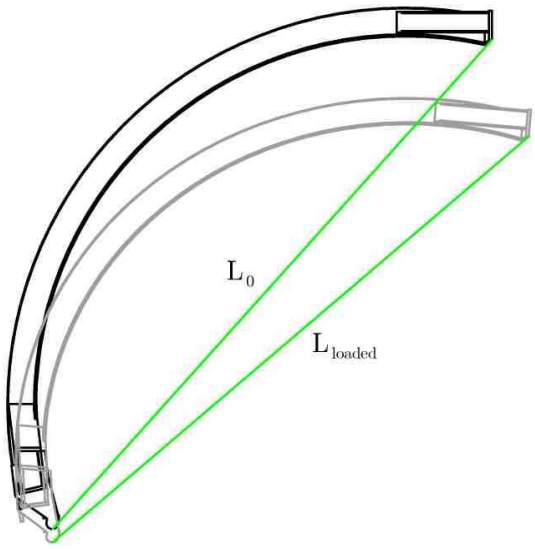

Figure 9.13: Cord dimension measured to record the CalFrame deflection during load test.

After the load test was completed, the Calframe was moved inside one of the surface buildings for the alignment test and installation of cable trays, electrical services, and water cooling manifolds.

9.1.9 Installation of the CalFrame Inside the L3 Magnet

Installation of the CalFrame inside the L3 Magnet is presented in Fig. 9.14 via several photographs that show the delicate process of lowering of the CalFrame into the Point 2 shaft and installation and alignment inside the L3 magnet.

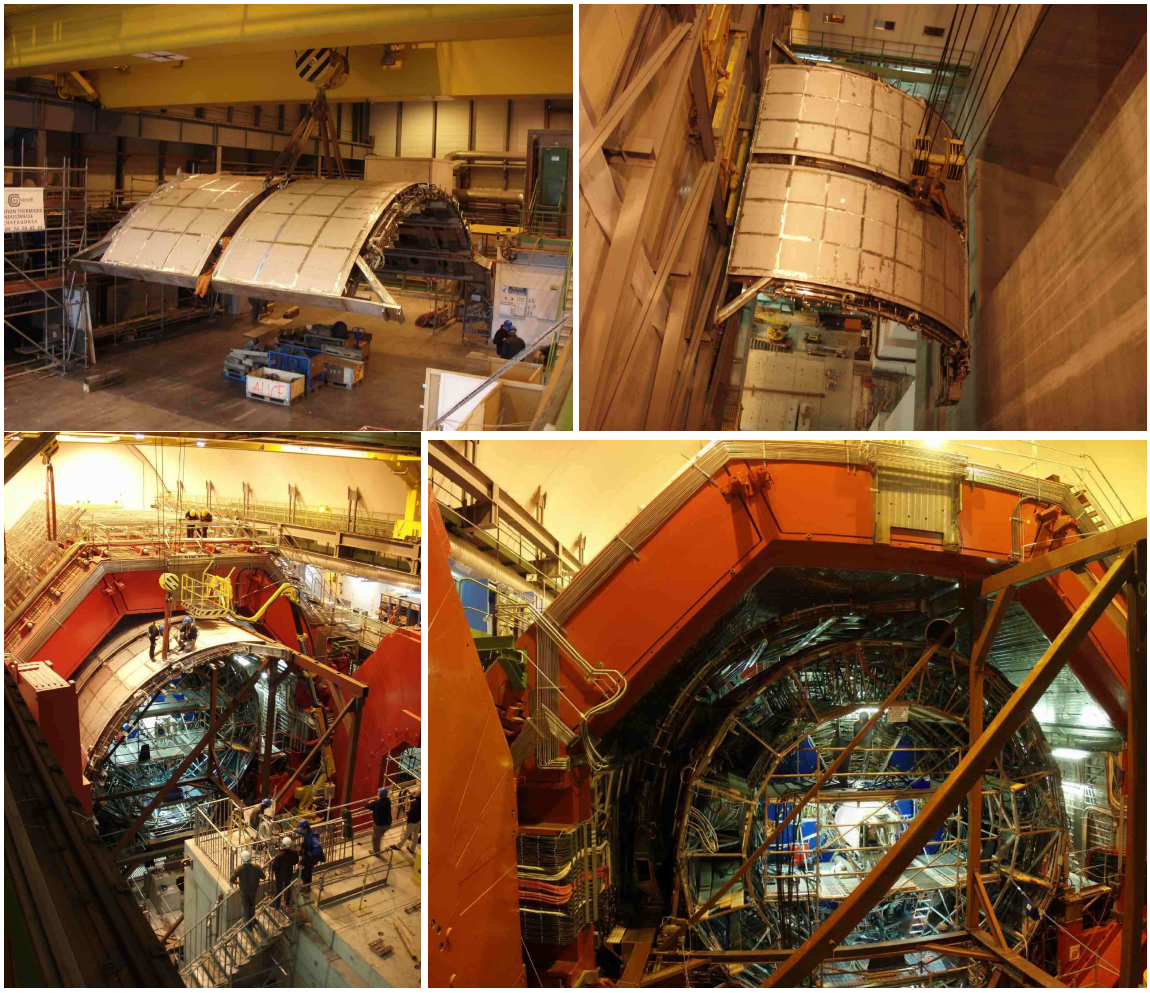

Figure 9.14: Photographs of various steps of the installation of the CalFrame.

9.2 Insertion of Super Modules into CalFrame

9.2.1 Mechanical Design of Insertion Tooling

Insertion of all of the EMCal super modules into the CalFrame takes place from the open end of the ALICE detector. An insertion tooling was designed to accomplish this task without impacting detector and beamline machine elements located in front of the EMCal support structure (CalFrame). Therefore, the insertion tooling allows for installation of the 8 tons super modules into 6 azimuthal positions inside ALICE, starting from a location outside of the L3 ALICE magnet and 3 m away from the sliding rails located on the CalFrame. The insertion tooling has to locate each super module at the correct x, y, z, (location accuracy better than 1 mm) and ϕ angle, prior to sliding the super module into the CalFrame. A dedicated tooling was designed for the purpose to insert EMCal super modules into ALICE. The super module insertion tooling shown in Fig. 9.15 features a handling device to put the super module into the insertion tooling, a rotator located outside of the ALICE L3 magnet for the ϕ angle orientation, a bridge to connect the rotator with the CalFrame, and a hydraulic system to move the super module into and out of the CalFrame. Figure 9.15 shows the CAD model of the insertion tooling connected to the CalFrame at the 12:00 o'clock position. The total length of the insertion tooling is 10400 mm and the total weight, including the super module, is 14 tons. The insertion tooling is mainly made from standard steel beams welded together and from U shaped rails similar to the ones installed inside the CalFrame.
A FEA analysis was done with cross check calculations made at CERN. Both calculations show a max

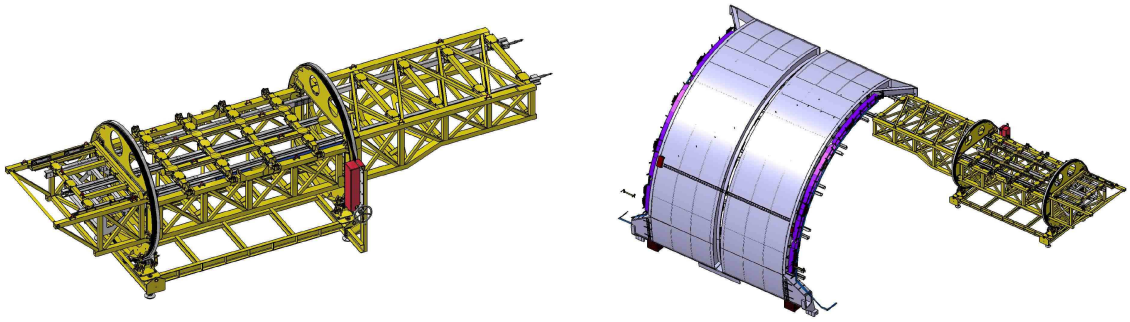

Figure 9.15: Left: Super module insertion tooling. Right: Attached to the CalFrame at 12 o'clock.

stress in the weld structure of 100 MPa for the 12:00 o'clock position, and 140 MPa for the 9:00 o'clock position. The insertion tooling design was completed in 2006 and fabrication drawings were edited through July 2007. The order was placed in August 2007. In order to reach the EMCal location without disturbing the detector and accelerator components, a platform constructed of concrete block will have to be erected. Figure 9.16 shows a schematic representation of the super module installation platform at the 12:00 o'clock position. The insertion tooling was delivered to CERN in February 2008. An insertion test inside ALICE was conducted in May 2008 to qualify the performance of the insertion tooling and insertion procedures. Figure 9.17 shows the super module crate insertion and removal test at the 9:20 o'clock location of the detector.

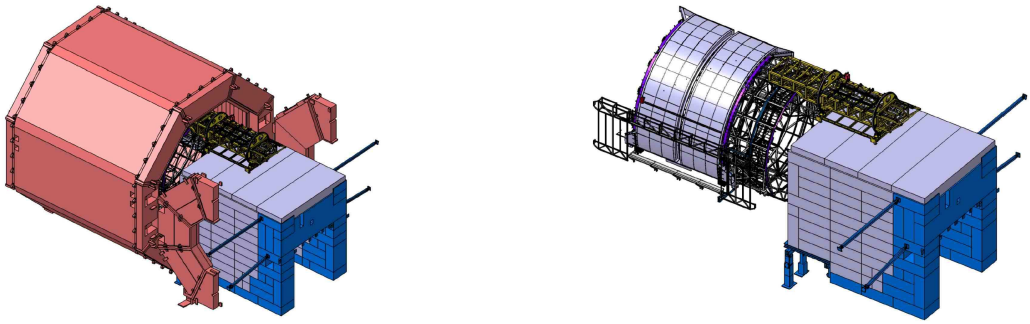

Figure 9.16: Two views of installation of a super module into the CalFrame at 12 o'clock with/without ALICE magnet shown.

9.3 Services, Access, and Maintenance

9.3.1 Services

In routine operation, the EMCal requires services consisting of LV DC power, HV (400V) DC power, and cooling water. The integration plan and hardware implementation for these services are complete. Figure 9.18 shows the schematic layout of the EMCal control circuit described in more detail in Chapter 4.

Cooling water is routed from the chiller to the two ends of the CalFrame where it branches to a manifold that runs along the end surfaces of the CalFrame. Leak-less outlets along the length of this manifold provide cooling water to the electronics crates located at the end of each super module described in Section 3.5.1. The electronics crates are the only locations where cooling water is used on the EMCal. In particular, no water is brought out onto the back surfaces of the super modules. The cooling water flow is sized to remove all power dissipated in the electronics crates.

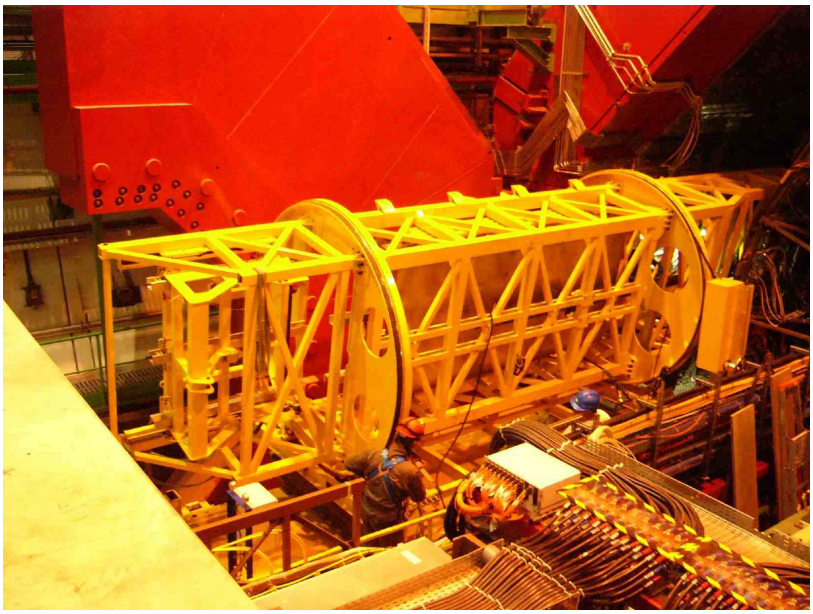

Figure 9.17: Photograph of the super module insertion tool attached at the 9:20 o'clock location.

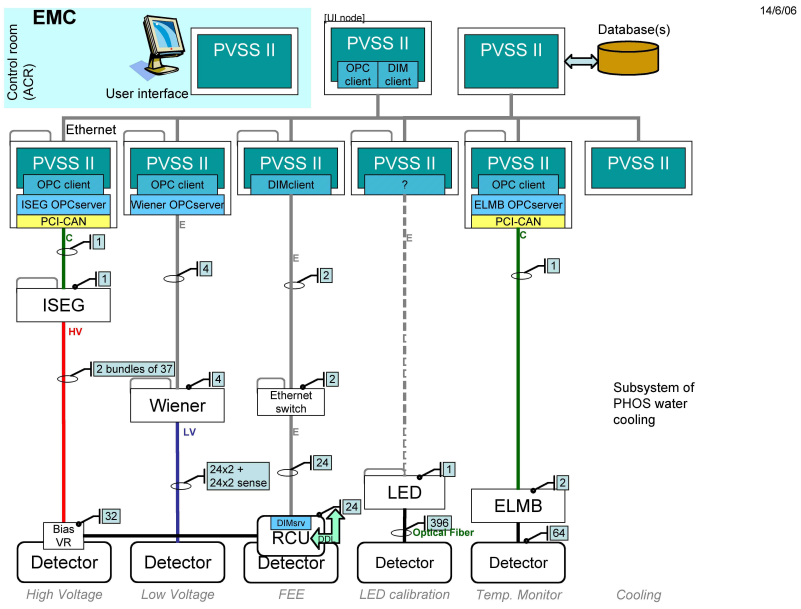

Figure 9.18: Schematic diagram of the EMCal Detector Control System.

Low voltage DC power is routed from allocated rack space to the two ends of the CalFrame. At that point the low impedance cables terminate in LV patch panels on the CalFrame. From there, secondary cables are run in cable trays along the end surfaces of the CalFrame to low voltage distribution blocks mounted adjacent to the electronics crates. Figure 9.19 shows the services installed on the CalFrame prior to insertion of the CalFrame into ALICE including the cable trays, water cooling manifolds, LV cables and distribution blocks, and other service cables.

The high voltage for the APD bias is supplied with a single channel of 400V supplied to each group of 9 FEE cards on an RCU branch. The individual bias to each APD is controlled and regulated on the front end boards located in the electronics crates (see Section 3.1.4).

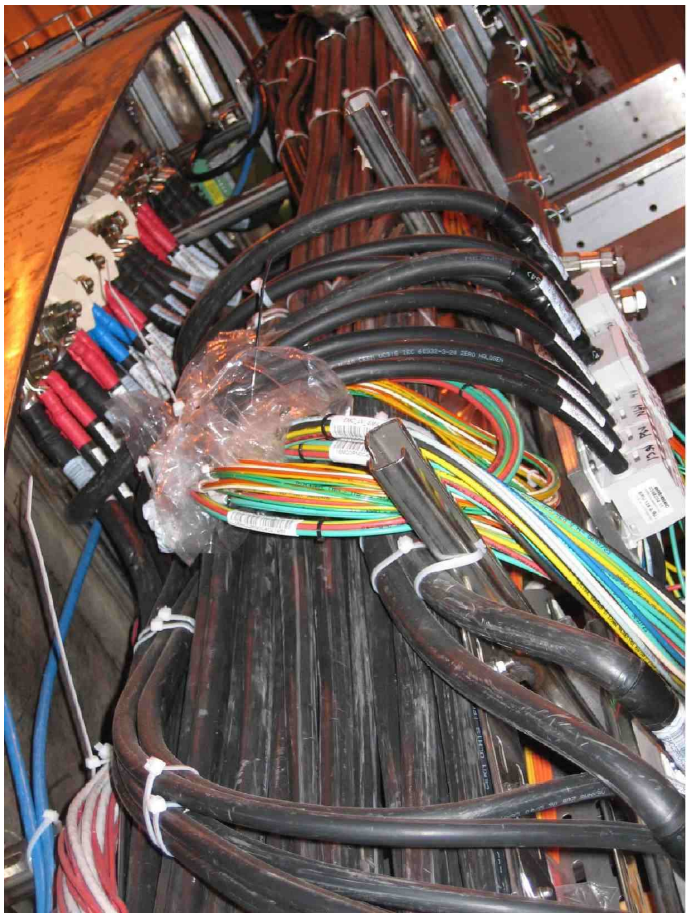

Figure 9.19: Cable tray showing low voltage cables and distribution boxes on CalFrame.

9.3.2 Access and Maintenance

Access to the EMCal is limited but sufficient for safe and reliable operation of the detector. Electronics crates, located at the ends of the super modules, are accessible for service even during relatively short access to the ALICE cavern. Front end electronics cards are easily removed for service. During short access, the ALICE doors will remain closed, and the ALICE volume will be a confined space (*cf.* Safety Code A4). Generally any access to the EMCal will require the use of a safety harness and the relevant safety training.
The back surfaces of the super modules, however, which contain the APDs, charge sensitive preamps, are not accessible once a super module is installed. Maintenance of components on the back surfaces of the super modules can only be performed during shutdown periods when sufficient time is available to withdraw a super module using its installation tooling. Fortunately, all of the components that are accessible only from the rear surface of the super module are robust and unlikely to need service.

9.4 Safety Considerations.

The EMCal project team is fully committed to the safe construction, installation, and operation of the EMCal as a component of the ALICE suite of detectors. Our primary goal is to ensure the safety of all personnel involved in the project but also to control risks, to the greatest extent possible, that might result in damage to the EMCal, other ALICE detector systems, or the environment.
The EMCal itself poses no safety hazards beyond those typical of other ALICE detector systems. Indeed, it presents far fewer hazards than most typical detector systems. No gasses of any kind are required for

EMCal operation and both HV and LVDC requirements are modest.
Temperatures on the critical components of the front end electronics - the only location of any significant power dissipation - are continuously monitored. In addition, located as they are within the ALICE magnet volume, the EMCal electronics crates are covered by ALICE's common smoke detection system (SNIFFER).
No flammable materials are used in the EMCal construction with the exception of polystyrene plastic scintillator. This material is, however enclosed in stainless steel containers within the detector in a manner that removes it from any source of oxygen for combustion.

10 Planning and Organization

10.1 Schedule

The schedule for the construction and the installation of the EMCal is driven by the startup of the LHC, and the shutdown periods to come, and by the physics which will be addressed in the first years of LHC operation. At present no heavy ion run at the nominal luminosity is foreseen before 2010. The installation of the EMCal support structure inside the ALICE magnet has been completed in 2007 and an insertion test of a dummy super module has been successfully performed in 2008 in the final position inside ALICE. All the services (cables, water) are already in place.
An extensive detector and electronics R&D program conducted during 2005, 2006, and 2007 described in this document has fixed all detector parameters and an integrated system test including final electronics has been conducted with hadron, muon, and electron beams. In particular, since the Technical Proposal of two years ago, the final detector design has been completed. Sixteen pre-production prototype modules have been tested at the CERN SPS and PS test beam areas. The final detector design has been completed and the massive production and module assembly is already started.
During the last few years, funds and resources for the R&D program, for the assembly and construction tools, for the prototypes, for the support structure, and for the services has been already assigned by DoE (2005-2007), IN2P3 (2006-2007) and INFN (2006-2008).
In mid of 2007 the scientific council of IN2P3/CNRS has already fully approved the French part of the project which is equivalent to about 1.5 super modules cost and labour. The US DoE has approved by end of 2007 the US part of the project which corresponds to about 8 super modules. INFN has supported up to now the equivalent of about 0.5 super module and the request for the final and full approval has been submitted.
Presently, two complete super modules are expected to be ready and likely to be installed in February 2009 to have them in ALICE during the first Pb–Pb run in 2009. This will allow to commision the EMCal and to obtain first physics results for γ, π^0, and electron production at high p_{t}.
Following this, physics opportunities suggest that at least half of the full EMCal should be completed and installed in the winter shutdown between 2009 and 2010 in order to have sufficient acceptance to begin the study of jet physics in the 2010 run. Finally, the complete EMCal should be ready for the 2011 run.
This construction and installation schedule is technically feasible within the present EMCal Collaboration, but it depends critically on the funding profile to the project. Any acceleration of funding will have a strong impact on the early potential of the project for jet physics since the jet acceptance strongly increases with angular coverage, and is optimal only for the full EMCal acceptance. The overall work program and schedule for the calorimeter project is summarized in Table 10.1.

10.2 Cost Estimate

The cost estimate for the full EMCal project scope is summarized in Table 10.2. The cost estimate is based on present quotations obtained from industrial vendors and on the already purchased material. A large fraction of the cost will be in the electronics whose cost evaluation is mainly based on the cost of the PHOS electronics, and includes spares and contingency. The support structure cost already installed is included. Only items which are exclusive to the EMCal are included in the table, while items common to all ALICE sub-detector (DAQ, offline, etc.) are not included. Labour costs are not included. The R&D money allocated by DoE, by INFN and by IN2P3 is not included. Also not included are the labour

Table 10.1: Milestones for the EMCal project.

Task	Milestone
Installation of services	done
Installation of support structure	done
Engineering design for the detector	done
Engineering design for the electronics	done
Mass production for the detector	started
Mass module assembly	started
Installation of first two SM	2/2009
Commissioning with p–p beam	4/2009
Start of γ, π^0, e physics	6/2009
Installation of next four SM	2/2010
Start of jet physics	2010
Complete installation	2/2011
Jet physics at full luminosity and acceptance	2011

work and the travel money already allocated by the funding agencies.

Table 10.2: Project cost estimate for the EMCal detector itself, electronics, conventional systems, infrastructure and installation, and calibration and test facilities.

Detector system	Cost (kCHF)
Mechanics	635
Working Tools	1050
Detector	4278
Electronics ($\sim$ 13 K channels)	2485
Conventional Systems	1246
Infrastructure and Installation	597
Cosmic and Beam Test Facility	344
Total Detector Cost	10635

10.3 Responsibilities

The EMCal is a common project shared and jointly managed by several US and EU institutions. WSU has scientific responsibility for the full project, and presently represents the project within the ALICE Technical Board. The EU responsibility is equally shared between LNF and SUBATECH, which also act with deputy responsibility for the project. The overall Technical Coordination is from LBNL. The EMCal project is administered by a Management Board which is responsible for the overall coordination of the three national efforts contributing to the project to insure the most efficient utilization of resources, monitor technical matters bearing on design, fabrication and quality control, and to nurture the development of the combined EMCal scientific program within the ALICE Collaboration.
Presently the project consists in 11 super modules (more precisely, 10 + two 1/3 super modules), 3 of them will be mainly provided by EU countries and 8 mainly by US. Several common items will be efficiently shared. A breakdown by institution of the responsibilities for the different subsystems of the

ALICE EMCal is shown in Table 10.3 below. The responsibilities will include all technical and financial aspects of the project, from R&D and design, to construction, assembly, and operation of the equipment.

Table 10.3: Primary institutional responsibilities within the EMCal project.

General Mechanics	Catania, LPSC, SUBATECH, WSU
Tooling	LPSC, LNF, SUBATECH, WSU
Module Construction and Assembly	Catania, LNF, SUBATECH, WSU
super module assembly	LPSC, LBNL, Yale
APD procurement and test	ORNL, Catania, Houston.
Readout Electronics	CERN, ORNL, SUBATECH, Knoxville
Trigger	CERN, LPSC, Jyvaskyla, Helsinki, LBNL, ORNL
Offline	Catania, LNF, SUBATECH, IPHC WSU, Yale, LBNL, ORNL, Jyvaskyla, Helsinki
Online	Creighton, IPHC, Knoxville, ORNL, WSU
Infrastructure and Integration	CERN, SUBATECH, LBNL

The participating national groups agree to make all effort to carry out their responsibilities as outlined above. Very recently a group from Finland joined the project. Additional US institutions and a group from Sao Paulo (Brasil) are in the process of joining the ALICE-EMCal collaboration. The project is also open to future collaborators from other countries.

References

Chapter 1

[1] F. Carminati *et al.* (ALICE Collaboration), J. Phys. **G30**, 1517 (2004).
[2] ALICE Collaboration, *Physics Performance Report, Vol 2*, J. Phys. **G** (2006).
[3] R. Baier, D. Schiff and B. Zakharov, Ann. Rev. Nucl. Part. Sci. **50**, 37 (2000).
[4] M. Gyulassy, I. Vitev, X. N. Wang and B. W. Zhang, Quark Gluon Plasma 3, 123 (ed. R. Hwa and X. N. Wang, World Scientific, Singapore); nucl-th/0302077.
[5] A. Kovner and U. Wiedemann, Quark Gluon Plasma 3, 192 (ed. R. Hwa and X. N. Wang, World Scientific, Singapore); hep-ph/0304151.
[6] P. Jacobs and X. N. Wang, Prog. Part. Nucl. Phys. **54**, 443 (2005).
[7] I. Arsene *et al.* (BRAHMS), Nucl. Phys. **A757**, 1 (2005).
[8] K. Adcox *et al.* (PHENIX), Nucl. Phys. **A757**, 184 (2005).
[9] B. B. Back *et al.* (PHOBOS), Nucl. Phys. **A757**, 28 (2005).
[10] J. Adams *et al.* (STAR), Nucl. Phys. **A757**, 102 (2005).
[11] J. D. Bjorken, FERMILAB-PUB-82-059-THY.
[12] M. G. Mustafa, Phys. Rev. **C72**, 014905 (2005).
[13] S. Wicks, W. Horowitz, M. Djordjevic and M. Gyulassy, nucl-th/0512076.
[14] S. S. Adler *et al.* (PHENIX), Phys. Rev. Lett. **91**, 232301 (2005).
[15] I. Arsene *et al.* (BRAHMS), Phys. Rev. Lett. **91**, 072305 (2003).
[16] S. S. Adler *et al.* (PHENIX), Phys. Rev. Lett. **91**, 072303 (2003).
[17] B. B. Back *et al.* (PHOBOS), Phys. Rev. Lett. **91**, 072302 (2003).
[18] J. Adams *et al.* (STAR), Phys. Rev. Lett. **91**, 072304 (2003).
[19] I. Vitev and M. Gyulassy, Phys. Rev. Lett. **89**, 252301 (2002).
[20] S. S. Adler *et al.* (PHENIX), Phys. Rev. **C69**, 034909 (2004).
[21] J. Adams *et al.* (STAR), nucl-ex/0601042.
[22] R. J. Fries *et al.*, Phys. Rev. **C68**, 044902 (2003).
[23] V. Greco, C. M. Ko and P. Levai, Phys. Rev. **C68**, 034904 (2003).
[24] R. C. Hwa and C. B. Yang, Phys. Rev. **C67**, 034902 (2003).
[25] C. Loizides, hep-ph/0507018.
[26] C.A. Salgado and U. Wiedemann, Phys. Rev. **D68**, 014008 (2003).
[27] K. Eskola *et al.*, Nucl. Phys. **A747**, 511 (2005).
[28] A. Drees, H. Feng and J. Jia, Phys. Rev. **C71**, 034909.
[29] A. Dainese, C. Loizides and G. Paic, Eur. Phys. J. **C38**, 461 (2005).
[30] J. Adams *et al.* (STAR), Phys. Rev. Lett. **95** (2005) 152301.
[31] M. Cacciari, G. Salam and G. Soyez, JHEP 0805:005 (2008).
[32] J. Putschke and S. Salur, talks at Hard Probes 2008.
[33] K. Zapp et al, arXiv:0804.3568.
[34] N. Borghini and U. Wiedmann, hep-ph/0506218.
[35] C.A. Salgado and U. Wiedemann, Phys. Rev. Lett. **93** (2004) 042301.
[36] X.-N. Wang and Z. Huang, Phys. Rev. **C55**, 3047 (1997).
[37] D. Buskulic *et al.* (ALEPH), Nucl. Instr. Meth. **A360**, 481 (1995).
[38] M. Miller *et al.* (STAR), proceedings of PANIC05, hep-ex/0604001.

Chapter 2

[1] ALICE Collaboration, *A Large Ion Collider Experiment*, CERN/LHCC 95-71, 15 December 1995.
[2] L. Aphecetche *et. al.*, (PHENIX), Nucl. Instrum. Methods **A499**, 521 (2003).
[3] A. Zoccoli for the HERA-B Collaboration, *The Electromagnetic Calorimeter for the HERA-B Experiment*, Nucl. Instrum. Methods **A446**, 246 (2000).
[4] LHCB Collaboration, *LHCb TDR2*, CERN/LHCC 2000-36, 6 September 2000.
[5] F.D. Brooks, *Development of organic scintillators*, Nucl. Instrum. Methods 162, 477 (1979).
[6] M. Beddo et al, *The STAR barrel electromagnetic calorimeter*, Nucl. Instrum. Methods **A499**, 725 (2003).

Chapter 3

[1] Photon Spectrometer PHOS, ALICE Technical Design Report, CERN /LHCC 99-4, 5 1999.
[2] D.V.Aleksandrov *et. al.*, *A high resolution electromagnetic calorimeter based on lead-tungstate crystals*, Nucl. Instrum. Methods A550, 169 (2005).
[3] H. Muller *et. al.*, *Configurable Electronics with Low Noise and 14-bit Dynamic Range for Photodiode-based Photon Detectors*, Nucl. Instr. and Meth. **A565**, 768 (2006).
[4] S8148 Silicon Avalanche Photodiode, Hamamatsu Photonics.
[5] K. Deiters *et. al.*, *Properties of the Avalanche Photodiodes for the CMS Electromagnetic Calorimeter.*, Nucl. Instrum. Methods **A453**, 223 (2000).
[6] K. Deiters *et. al.*, *Investigation of the Avalanche Photodiodes for the CMS Electromagnetic Calorimeter Operated at High Gain*, Nucl. Instrum. Methods **A461**, 574 (2001).
[7] J. Grahl *et. al.*, *Radiation Hard Avalanch Photodiodes for CMS ECAL.*, Nucl. Instrum. Methods **A504**, 44 (2003).
[8] I.Sibiriak, A.Tsvettkov, and A.Vinogradov, *APD power control for the ALICE PHOS prototype*, Alice Internal Note, ALICE-INT-2005-013.
[9] *The ALTRO chip: A 16-channel A/D converter and digital processor for gas detectors*, Proc. IEEE NSS/MIC, November 2002, Norfolk.
[10] Lien, J.A., *The Readout Control Unit of the ALICE TPC*, Thesis, CERN-THESIS-2005-013.
[11] *Trigger Region Unit for ALICE PHOS Calorimeter*, Proceedings LECC05,11th Workshop on Electronics for LHC and future Experiments, Heidelberg, September 2005.
[12] ALICE DAQ, ALICE DDL Interface Control Document, Internal Note ALICE-INT-1996-43 V9.1.
[13] Heather Gray, *The Reconstruction of High-p_T Photons with the Electromagnetic Calorimeter of the ALICE Experiment at the LHC*, PhD Thesis, University of Capetown, May 2005.
[14] R. Brun *et. al.*, *Computing in ALICE*, Nucl. Instr. Meth. **A502**, 339-346 (2003). http://aliweb.cern.ch/offline/
[15] B.K. Lubsandozhiev and Y.E. Vyatchin, *Stability Studies of Nanosecond Light Sources Based on Blue Ultra Bright LEDs*, physics/0403018.

Chapter 4

[1] The ALICE Trigger Project, ALICE Central Trigger Processor, User Requirement Document, Draft 1.0, 24 October 2001.
[2] ALICE Collaboration, *Technical Design Report of Trigger, Data Acquisition, High-Level Trigger and Control System*, CERN/LHCC/2003–062.
[3] The ALICE Trigger Project, ALICE Local Trigger Unit, Preliminary Design Review Document, Revision 0.1, 1 September 2002.

[4] B. G. Taylor, LHC machine timing distribution for the experiments, in *Proc. of the 6th Workshop on Electronics for LHC Experiments*, Cracow, Poland, 2000 (CERN 2000-010, Geneva, 2003).
[5] J. Baud *et. al.*, CASTOR status and evolution, in *Proc. Conf. on Computing in High-Energy Physics*, La Jolla, CA, USA, March 2003 (SLAC, Stanford).
[6] ALICE DAQ, DATE V4 User's Guide, Internal Note ALICE-2002-036.
[7] P.G.Innocenti *et. al.*, Report of the ALICE HLT and HLT-DAQ Interface Review Panel, Internal Note ALICE-EN-2003-009 v.1.
[8] http://aliceinfo.cern.ch/Collaboration/Documents/TDR/Computing.html
[9] http://www.nsf.gov/funding/pgm_summ.jsp?pims_id=6681&org=NSF&more=Y

Chapter 5

Chapter 6

[1] A. Badalá *et al.*, Proceedings of the International Conference on Large Scale Applications and Radiation Hardness of Semiconductor Detectors, Florence (Italy), (2007); to be published in NIM A.
[2] A. Badalá *et al.,* Proceedings of NDIP08 Conference, Aix-Les-Bains (France) (2008), to be published in NIM A.
[3] Kingbright, www.Kingbright.com
[4] H. Muller *et al.*, Nucl. Instr. and Meth. A565, 768 (2006).
[5] ALICE DAQ, DATE V5 User's Guide, ALICE Internal Note/DAQ ALICE-INT-2005-015.
[6] S.C. Eicher, CERN Report CFD-2005-09.
[7] ALICE Collaboration, *Technical Design Report of Trigger, Data Acquisition, High-Level Trigger and Control System*, CERN/LHCC/2003–062.
[8] S.S. Adler *et al.*, (PHENIX Coll.), Phys. Rev. Lett. **91**, 241803 (2003).

Chapter 7

[1] H. Muller *et al.*, *Configurable Electronics with Low Noise and 14-bit Dynamic Range for Photodiode-based Photon Detectors*, Nucl. Instrum. Methods **A565**, 768 (2006).
[2] ALICE Collaboration, *Meson Test beam experiment T951: ALICE EMCAL Prototype Test*, http://www-ppd.fnal.gov/MTBF-w/mtbf-mou.htm.
[3] ALICE DAQ, DATE V5 User's Guide, Internal Note ALICE-2005-015.
[4] L. Aphecetche *et al.*, (PHENIX), Nucl. Instrum. Methods **A499**, 521 (2003).
[5] T.C. Awes *et al.*, *A Simple method of shower localization and identification in laterally segmented calorimeters*, Nucl. Instrum. Methods **A311**, 130 (1992).

Chapter 8

[1] J. Casalderrey-Solana and X.-N. Wang, Phys. Rev. **C77**, 024902 (2008).
[2] C. A. Salgado and U. A. Wiedemann, Phys. Rev. **D68** 014008 (2003).
[3] S. Blyth *et al.*, J. Phys. **G30**, S1155 (2004).
[4] S. Blyth, nucl-ex/0510065.
[5] J. Adams *et al.* (STAR), Phys. Rev. **C70**, 054907 (2004).
[6] M. Miller *et al.* (STAR), hep-ex/0604001.
[7] D. Buskulic *et al.* (ALEPH), Nucl. Instr. Meth. **A360**, 481 (1995).
[8] G. Arnison *et al.*, Phys. Lett. **B132**, 214 (1983).
[9] K. Eskola *et al.*, Phys. Rev. **C72**, 044904 (2005).

[10] D. Acosta *et al.*, Phys. Rev. **D72**, 051104 (2005).
[11] ALICE Collaboration, *Physics Performance Report, Vol 2*, J. Phys. **G** (2006).
[12] S. Salur and J. Putschke, talks at Hard Probes 2008, A Toxa, Spain.
[13] M. Cacciari and G. Salam, Phys. Lett. **B641** 57 (2006).
[14] N. Borghini and U. A. Wiedemann, hep-ph/0506218.
[15] L. Maiani et al., Phys. Lett. **B645**, 138 (2007).
[16] S. Sapeta and U.A. Wiedemann, arXiv:0707.3494.
[17] C. Markert, R. Bellwied, I. Vitev, arXiv:0807.1509.
[18] F. Arleo *et al.*, JHEP **0411**, 009 (2004).
[19] Yu. L. Dokshitzer, D.E. Kharzeev, Phys. Lett. **B 519**, 199 (2001).
[20] M. Djordjevic, M. Gyulassy, S. Wicks, Phys. Rev. Lett. **94**, 112301 (2005).
[21] B. I. Abelev *et al.* [STAR Collaboration], Phys. Rev. Lett **98**, 192301 (2007); A. Adare *et al.* [PHENIX Collaboration], Phys. Rev. Lett. **96**, 032301 (2006); **98**, 172301 (2007).
[22] N. Armesto *et al.*, Phys. Rev. **D71**, 054027 (2005).
[23] Hong Liu, Krishna Rajagopal, Urs Achim Wiedemann, Phys.Rev.Lett. **97** (2006) 182301; Steven S. Gubser, Phys.Rev. **D74** (2006) 126005; J.J. Friess, S. S. Gubser, G. Michalogiorgakis, JHEP 0609, 072 (2006).
[24] W. A. Horowitz, M. Gyulassy, arXiv:0706.2336.
[25] D. Acosta et al. [CDF Collaboration], *Phys. Rev.* D **66**, 014003 (2002).
[26] Mark Heinz [ALICE Collaboration], Winter Workshop of Nuclear Dynamics, Big Sky MT.

Chapter 9

Chapter 10